MARTIN MARIETTA ENERGY SYSTEMS LIBRARIES
3 4456 0364425 1

CENTRAL RESEARCH LIBRARY
DOCUMENT COLLECTION

153

ORNL-3166
UC-80 – Reactor Technology

GAS-COOLED REACTOR PROGRAM

QUARTERLY PROGRESS REPORT

FOR PERIOD ENDING JUNE 30, 1961

CENTRAL RESEARCH LIBRARY
DOCUMENT COLLECTION
LIBRARY LOAN COPY
DO NOT TRANSFER TO ANOTHER PERSON
If you wish someone else to see this document, send in name with document and the library will arrange a loan.

OAK RIDGE NATIONAL LABORATORY
operated by
UNION CARBIDE CORPORATION
for the
U.S. ATOMIC ENERGY COMMISSION

Printed in USA. Price $3.50. Available from the

Office of Technical Services
Department of Commerce
Washington 25, D.C.

LEGAL NOTICE

This report was prepared as an account of Government sponsored work. Neither the United States, nor the Commission, nor any person acting on behalf of the Commission:

A. Makes any warranty or representation, expressed or implied, with respect to the accuracy, completeness, or usefulness of the information contained in this report, or that the use of any information, apparatus, method, or process disclosed in this report may not infringe privately owned rights; or

B. Assumes any liabilities with respect to the use of, or for damages resulting from the use of any information, apparatus, method, or process disclosed in this report.

As used in the above, "person acting on behalf of the Commission" includes any employee or contractor of the Commission, or employee of such contractor, to the extent that such employee or contractor of the Commission, or employee of such contractor prepares, disseminates, or provides access to, any information pursuant to his employment or contract with the Commission, or his employment with such contractor.

ORNL-3166

Reactor Technology
TID-4500 (16th ed.)

Contract No. W-7405-eng-26

GAS-COOLED REACTOR PROGRAM

QUARTERLY PROGRESS REPORT

For Period Ending June 30, 1961

Staff
Oak Ridge National Laboratory

DATE ISSUED

AUG 28 1961

OAK RIDGE NATIONAL LABORATORY
Oak Ridge, Tennessee
operated by
UNION CARBIDE CORPORATION
for the
U. S. ATOMIC ENERGY COMMISSION

MARTIN MARIETTA ENERGY SYSTEMS LIBRARIES

3 4456 0364425 1

CONTENTS

SUMMARY vii

PART 1. DESIGN INVESTIGATIONS

1. REACTOR PHYSICS 3
   Epithermal Neutron Absorption in EGCR Control Rods 3
   EGCR Power Distributions with Experimental Assemblies in Two Loops 7
   Criticality of EGCR Fuel Shipping Crates 8
   Fission-Product Decay Heat 9
   Power Distribution in 19-Rod Clusters 11
   Neutron Thermalization Calculations 12
   Reactivity Lifetime in Thorium Cycle 15
2. REACTOR DESIGN STUDIES 18
   Thermal Analysis of EGCR Core Components 18
      Fuel Assemblies 18
      Fuel Channel Pressure Losses 18
      Heat Transfer Correlation 19
      Gas Temperatures During Loss-of-Power Incident 24
   EGCR Control Rod Modifications 34
   Evaluation of EGCR Control Rod Drives 35
   Structural Investigations 36
      Temperature Distribution in EGCR Graphite Columns 36
      Structural Integrity of EGCR Through-Tubes 39
      Photoelastic Analysis of Model of EGCR Pressure Vessel 39
      Experimental Analyses of Perforated Plates 40
   Containment System for the EGCR 46
   Decontamination of EGCR Components 55
   Parametric Survey of Axial-Upflow Pebble-Bed Power Reactors 57
      Basis for Evaluating Effect of Size on Investment 57
      Correlation of Size and Cost 60

3. EXPERIMENTAL INVESTIGATIONS OF HEAT TRANSFER AND FLUID FLOW 63

Resistance-Heated-Tube Heat Transfer Experiment 63

Velocity Distribution Studies 68

Pressure-Loss Measurements in EGCR Clusters 71

PART 2. MATERIALS RESEARCH AND TESTING

4. MATERIALS DEVELOPMENT 77

Fabrication and Physical Properties Studies of Fuel Materials 77

Power Processing and Fabrication of UO_2 77

Thermal-Conductivity Studies 78

Fabrication of BeO 83

Coated-Particle Evaluation 84

Release of Fission Products from Coated Fuel Particles 86

Release of Fission Products from Hydrothermal Thoria 89

Uranium Carbide Fuels 89

Compatibility of UC with Beryllium 94

Structural Materials Evaluation 95

Coated Graphite Support Sleeves for EGCR 95

Dimensional Behavior of the EGCR Fuel Elements at Elevated Temperatures 101

Reactions of Type 304 Stainless Steel with CO and CO_2 in Helium 104

Studies of Pressure-Vessel Steels 106

Manufacturing and Inspection Methods Development 109

Fabrication of Instrumented Fuel Capsules for In-Pile Tests 109

Nondestructive Testing of Through-Tube Weldments 110

Diffusion of Carbon in Dissimilar-Metal Welds 111

Beryllium Investigations 112

Compatibility of Beryllium with Gases 112

Beryllium Pressure Bonding 113

5. IN-PILE TESTING OF COMPONENTS AND MATERIALS 117
Fuel Element Irradiation Program 117
Full-Diameter Prototype EGCR Fuel Capsules 117
Miniature-Capsule Irradiation Experiments in the LITR 123
Modification of GCR-ORR Loop No. 1 125
Fuel Element Testing in MTR 126
Evaluation of Radiation Effects 129
ORR- and ETR-Irradiated Prototype Capsules 129
LITR-Irradiated UC-Fueled Capsules 136
MTR-Irradiated UC_2-Graphite Dispersions 141
ORR-B9 Facility Irradiations 148
Instantaneous Fission-Gas-Release Experiment 153
Xenon and Krypton Release 153
Iodine Release 160
Radiation Effects on Structural Metals 160
Stainless Steel 160
Inconel 162
Beryllium 164
Pressure-Vessel Steels 166
6. OUT-OF-PILE TESTING OF MATERIALS AND COMPONENTS 167
Compatibility Tests of Graphite, Structural Materials, and Gaseous Coolants 167
Forced-Convection Loop Tests 167
Graphite-Metal Diffusion Studies 168
Evolution of Gas from Graphite 169
Transport of Gases Through Graphite 177
Development of Instruments for Analyzing Helium 178
Investigation of Adsorbers for Removing Fission-Product Gases from Helium 180
Removal of Iodine Vapor 180
Removal of Radioactive Noble Gases 181
Measurement of High Temperatures 184
Drift Studies in a Stagnant Helium Atmosphere 184
Drift Studies in a Graphite-Helium Environment 188

7. DEVELOPMENT OF TEST LOOPS AND COMPONENTS 191
EGCR In-Pile Loops 191
Through-Tube Design 191
Component Design 192
Design and Hazards Report 195
Loop Fabrication 195
EGCR Component Tests 196
EGCR Valve Tests 196
Through-Tube Bearing Test 198
Through-Tube Orifice-Plate Development Test 202
Mechanical Joint Service Testing 204
GCR-ORR Loop No. 2 207
Loop Design and Construction 207
Component Tests 213
Special Compressors 214
Compressors with Grease-Lubricated Bearings 214
Compressors with Gas-Lubricated Bearings 214
Compressors with GCR-ORR Loop No. 2 and EGCR Experimental Loops 216

SUMMARY

Part 1. Design Investigations

1. Reactor Physics

A simple two-group method has been developed for studying epithermal neutron absorption in control material. The predictions of the simple theory as applied to the B_4C of the EGCR control rods are in good agreement with experimental measurements. This two-group method is not limited to studies of the EGCR material and should be applicable to determinations of the effect on rod worth of changing the boron loading or annulus thickness, as well as to comparisons between B_4C and boron-loaded steel rods.

An analysis was made of the effect on the EGCR radial power distribution of operation with experimental assemblies in only two loops. Various enrichments of the experimental fuel and partial as well as full loading of the core were considered. Also, a "safe" arrangement for EGCR fuel shipping crates was established.

Fission-product afterheat in the EGCR was evaluated as a function of time after shutdown. Fission-product betas and gammas and the decay of Np^{239} and U^{239} were considered. Further, a study was initiated of the power distribution in beryllium-clad, UO_2-fueled, 19-rod cluster elements operating in the EGCR core.

Interlocking programs were written for the calculation of thermal-neutron spectra in infinite homogeneous media. Also, a series of calculations is being made for determining the reactivity lifetime of fuel elements consisting initially of U^{235}, thorium, and graphite.

2. Reactor Design Studies

The contract for the first core loading of the EGCR was awarded to the Westinghouse Atomic Fuel Division. The price for 1739 fuel assemblies of $786,897.50 does not include a protective coating for the graphite sleeves, which it now appears will be required.

The over-all pressure drop for the EGCR core was recalculated and was found to be 8.8 psi from plenum to plenum for the highest power

channel operating with a 1075°F exit gas temperature and a helium flow of 2280 lb/hr.

The variations of the local velocity and hydraulic diameter within the influence boundaries of an EGCR fuel channel were determined. The variations in the local Nusselt number at an L/d_e of 3.9 for typical tubes in the cluster were compared with the variations in the local mass transfer value. The circumferential variations of the mass transfer values and the calculated variations of the Nusselt number based on the axial velocity profile agreed within 8%.

The maximum or upper limit of the exit gas temperature to be expected from the EGCR core during a loss-of-power incident was determined using a combination of simulator data and analytical calculations. A number of operating conditions and values of design data were used in the study to determine their effect on the results. The study was limited to the case in which the loss-of-power occurred when the reactor was operating at full power. The maximum temperature for the conditions investigated was found to be 1115°F.

A mockup of an EGCR control rod was assembled, and coolant flow and pressure-drop tests were performed. The pressure drop agreed with the calculated value, but joint leakage was less than expected. Based on the test results, the clearance between the central rod and the internal spacers has been reduced by inserting an additional spacer above each joint.

Calculations were made to determine the acceleration capability of the proposed EGCR control rod drive mechanism, which consists basically of an electric-motor-driven cable drum arranged to rotate about a horizontal axis. The calculated acceleration was found to be acceptable in terms of the present specification. Uncertainties with respect to the inertias calculated for the alternator and brake can be resolved only through tests of an actual unit.

The temperature differentials in EGCR graphite columns during fuel-handling operations were calculated. The maximum differential based on conservative conditions was 400°F, which is to be compared with 8°F during design power operation. The stresses that are to be calculated from these temperature data will provide upper bounds for evaluating the conditions that will exist during fuel-handling operations.

Further tests were completed in the study of the structural integrity of the EGCR through-tubes. The fifth in a series of 4-in.-o.d., 5-ft-long, type 304 stainless steel tubes collapsed after 260 hr with an external pressure loading of 425 psi at 1200°F. A sixth, similar tube has been under test at the same conditions for 450 hr with no indication of collapse.

A model of the EGCR pressure vessel top head has been cast of epoxy resin and machined to a scale of 1 to 14.2 for a photoelastic analysis of the stresses. The stresses have been frozen in under a pressure loading and a simultaneous axial load on one of the control rod nozzles located at the outer edge of the nozzle cluster.

Experimental analyses of the stresses and deflections in perforated plates were continued. It has been noted that the principal stress directions are normal and tangential to the holes at the hole edges regardless of hole size. Deflections along a radius were found to be functions of hole pitch alone and not hole size combinations.

The study of the containment system for the EGCR has been continued. The most significant time for off-site exposure is the initial period following the maximum credible accident. Therefore only those emergency procedures in effect during normal operation will be effective in limiting the initial off-site exposure doses.

Studies in the development of procedures for decontaminating EGCR components were continued. Samples of piping from a helium-cooled loop operated at Brookhaven were decontaminated in oxalate peroxide and effectiveness of the treatment was indicated. The corrosion-inhibiting properties of hydrogen peroxide in oxalate citrate were found to be temperature dependent. Below 60°C corrosion of carbon steel in contact with the decontamination fluid was negligible, but at 65 to 70°C corrosion set in at a rate of 0.65 mil/hr. Corrosion rates of eight other metals were determined. In scouting tests, chromic acid was found to be impractical as a substitute for hydrogen peroxide.

The results of a parametric study made to correlate size and cost of axial up-flow pebble-bed power reactors are presented.

3. Experimental Investigations of Heat Transfer and Fluid Flow

Preliminary data were obtained for circumferential variations in tube-surface temperatures using a heat-transfer apparatus containing two electrically heated full-scale EGCR fuel element clusters. This system enables a close approximation of the temperature and flow patterns in the gas entering a typical fuel element in the reactor. Initial results obtained with the inlet cluster unheated and a 0-deg relative cluster orientation reveal a greater circumferential symmetry in the profiles in the upstream half of the cluster than observed in previous single-element experiments. In the downstream portion of the cluster, the data agree well with those of the earlier measurements.

The accumulation of data for delineating the velocity field in the downstream element of two seven-tube clusters as a function of relative cluster orientation was completed. The influence of spiders and cluster orientation was most noticeable just downstream of the cluster inlet. The effects of cluster orientation appear to be negligible downstream of the mid-cluster spacer, the velocity distribution being controlled by the mid-cluster spacer configuration and the general cross-sectional geometry of the flow channel.

The study of the contribution of the support spiders and mid-cluster spacers to the pressure loss in the EGCR fuel assemblies was completed. In the Reynolds modulus range of interest, the following pressure-loss coefficients were found to be essentially constant: $K = 0.43$ for a spider pair and $K = 0.34$ for the mid-cluster spacer. These values are in agreement with calculated values.

Part 2. Materials Research and Testing

4. Materials Development

Additional small samples of UO_2 with controlled grain size were prepared for irradiation. Specimens sintered for a long period in hydrogen developed a grain size of 90 μ, while other samples sintered at a minimum temperature in argon had a grain size of 20 μ.

The thermal conductivity of INOR-8 alloy was determined up to 800°C in the radial-heat-flow apparatus. The accuracy of the determination was estimated to be 5%. The apparatus has been reassembled with carefully prepared and characterized UO_2 disks, and measurements have been made at low temperatures.

High-density fueled BeO specimens containing 30 vol % UO_2 as 100- to 150-μ or 150- to 250-μ particles were fabricated by hydrogen sintering after preshrinkage of the fuel particles. Development work was initiated on the preparation of high-purity unfueled BeO samples for irradiation experiments. Varations in density are obtained by large additions of binders. The desired variations in grain size are controlled by varying the length of time at high temperature during sintering.

Preirradiation evaluation consisting of surface alpha-particle counting, thermal cycling, and acid leaching was completed on three batches of pyrolytic-carbon-coated UC_2. One batch from each of two vendors was selected as suitable for irradiation. The first in-pile capsule containing fuel from one of these batches is being irradiated, and the second has been prepared for irradiation. Metallographic and x-ray diffraction examination of particles disclosed that the extraneous material at the interface between the UC_2 and the pyrolytically deposited coating was mainly graphite.

Results from neutron-activation tests on one batch of UC_2 particles coated with pyrolytic carbon showed that the coatings were unharmed by thermal cycling and that no measurable amounts of Xe^{133} were released below 2000°C for times up to 140 hr. However, significant quantities of Ba^{140} were released at 1770°C in times as short as 2.5 hr.

Neutron-activation studies on a ThO_2–5 wt % UO_2 mixture prepared by the sol-gel process showed that the release of Xe^{133} occurred by a diffusion mechanism with an activation energy of 75.9 kcal/mole in the temperature range 1440 to 2015°C. At 2200°C the rate of release of Xe^{133} was constant. This suggests that the controlling mechanism of release at this temperature was sublimation of the ThO_2 instead of diffusion.

Uranium silicide-bonded uranium carbide bodies with high uranium density were fabricated by pressing and sintering. Bodies cemented with

5, 10, or 15 wt % USi_2 sintered to 97% of theoretical density at 1650°C in vacuum. The structure of the bodies consisted of UC plus α-USi_2.

The compatibility of UC with beryllium was determined at temperatures from 700 to 1000°C. The reaction between the two materials was found to increase rapidly above 750°C. At 800°C an intermetallic reaction zone 115 μ thick was produced in 160 hr. The intermetallic product was identified as UBe_{13}.

Oxidation tests of additional pyrolytic-carbon-coated graphite support sleeves indicated poor resistance after an initial 2-hr period. Four 901S graphite support sleeves coated with siliconized SiC were tested in an open furnace at temperatures up to 1000°C. Weight losses on a 10-kg sleeve ranged from 1 to 15 g; they resulted from oxidation through isolated defects.

Some thickness measurements on sections of samples coated with siliconized SiC could only be correlated with eddy-current measurements in the case of thin, fairly uniform coatings. The chemical compositions of coatings were determined in order to estimate their effect on the absorption cross section, σ_a, for the graphite sleeves. The calculated increase in σ_a ranged from 1.6 to 8.9 mb for various coatings, primarily because of the silicon and boron contents. In-pile measurements on specimens of moderator graphite before and after coating indicated that the increase in σ_a for a 1 wt % coating is approximately 10% higher than that estimated from the chemical analysis.

Studies of the dimensional behavior of simulated EGCR fuel elements were completed. These studies showed that plastic deformation of the cladding during thermal cycling can occur only if the cladding has collapsed onto the pellets. The total strain was determined to be a linear function of the number of cycles, and the strain per cycle was shown to be a function of the cooling and heating rates and the hold time at the upper temperature limit.

Type 304 stainless steel was observed to form a nonprotective oxide of Fe_3O_4 when exposed to CO_2 or atmospheres of CO_2 plus CO in which the CO_2-to-CO ratio is greater than about 0.7. Carburization of the metal in

CO_2 was restricted to a temperature range 1300 to 1700°C. The temperature dependence of the reaction rates could be correlated with the oxides produced.

The brittle-fracture characteristics of the weld heat-affected zones in ASTM A-212, grade B, steel are being studied. The cooling rates associated with a given weld energy input were found to be considerably more rapid in 4-in. plate than in 1-in. plate. The impact behavior of heat-affected zones in 1-in. plate derived from a 50 kj/in. energy input are similar to those in 4-in. plate derived from a 100 kj/in. energy input.

Improved procedures have been developed for fabricating in-pile instrumented fuel capsules. A modified thermocouple design was incorporated in which a 0.060-in.-o.d., stainless steel-sheathed, Chromel-Alumel unit was swaged down to 0.038 in. o.d. over the length which is located inside the capsule. Thus the part of the thermocouple which is subjected to damage during assembly has a fairly heavy cladding and an 0.060 in. o.d.

Radiographs were made of welds in mockups of the EGCR loop throughtubes under conditions that simulated the expected background radiation. No significant loss in detail was observed. The method is limited principally by the poor geometrical relationship of the source, specimen, and film. A film-reduction procedure was tested for use if the fogging background exceeds estimates. The original contrast of heavily fogged film could be restored under certain conditions.

The diffusion of carbon at elevated temperatures in dissimilar-metal welds is being studied on a subcontract. Diffusion coefficients were determined, and it appears that the major part of carbon diffusion occurred in the early stages of exposure and that after prolonged exposures the width of the decarburized zone will change very little.

The factors influencing the accelerated oxidation, "breakaway" reaction, of beryllium in atmospheres of CO_2, helium, and hydrogen were studied. In each case where breakaway occurred, $H_2O(g)$ was present in the carrier gas. The data show that Be_2C in the metal may be one impurity which promotes the breakaway reaction at temperatures up to 725°C.

The compatibility of UO_2 and various spacer materials with beryllium was studied during pressure-bonding experiments. A reaction layer 0.001 in. thick consisting of UBe_{13} was formed between UO_2 or graphite-coated UO_2 and beryllium during bonding at 1650°F for 4 hr. No reaction was observed with UO_2 coated with chromium or pyrolytic carbon. Of many metallic spacer materials tested under the same conditions, all but nickel reacted with the beryllium; however, all materials but nickel also separated readily from beryllium. Therefore, mild steel has been selected as a standard spacer material.

Inspection techniques are being developed for beryllium tubing having 12 straight or spiralled fins. Radiography of three such tubes detected pitting and foreign material. The critical areas, the root between the fins, could be examined in straight-finned tubes by three exposures with a sensitivity of 1%. Reference notches approximately 0.003 in. deep on the inner and outer surface of such tubes could be detected by the eddy-current technique using a bobbin coil.

Metallographic examination of beryllium tubes from burst tests disclosed defects that may contribute to failure. A preliminary study of the results of radiographic inspection on specimens showing premature failure indicates a definite correlation with defects.

Additional in-pile stress-rupture tube-burst data were obtained for type 304 stainless steel, boron-controlled heats of Inconel, and beryllium. The results of the tests of beryllium tubes at 700°C showed a definite reduction in strength. The relationship between the effect of exposure on the 100-hr rupture stress and the integrated fast flux was estimated. The data obtained at 700°C seem to bracket the data for tests at 600°C. Eight swelling specimens that were exposed to 3.6×10^{20} neutrons/cm^2 (>1 Mev) are being examined. Another test assembly containing swelling and tube-burst specimens was prepared and is being irradiated.

5. In-Pile Testing of Components and Materials

Eight group III experimental capsules were removed from the ORR following completion of the scheduled irradiation and eight group IV capsules were inserted. Four of the group IV UO_2-fueled capsules are stainless

steel clad and four are beryllium clad. The ORR irradiation facility was provided with a new mounting plate equipped with remotely operated screw-driven capsule positioners that permit individual adjustment of the capsules.

Irradiation was continued in the LITR of five miniature capsules. Two capsules contain $BeO-UO_2$ fuel, two contain $BeO-UO_2-ThO_2$ fuel, and one contains pyrolytic-carbon-coated UC_2 fuel.

Modification of GCR-ORR loop No. 1 was completed and operation was resumed. A set of pressure-vessel-steel weld-metal test specimens is being irradiated at 550°F.

The fourth graphite-encapsulated test fuel element irradiated in the MTR was removed for examination. Fission-gas release from this element became excessive after the first few hours of operation. The failure of this unit (ORNL-MTR-48-4) and the one irradiated previously (ORNL-MTR-48-3) almost immediately after startup of the reactor has indicated the need for improved leak testing of the graphite containers.

Examinations of group I and II ORR-irradiated UO_2-fueled EGCR prototype capsules were completed. Density measurements revealed no significant changes. Metallographic examinations showed that the group II pellet irradiated at the highest temperature showed the greatest tendency toward fracturing and was the only one that showed appreciable grain growth. A small amount of second-phase material, which is thought to be free iron, was found in both the irradiated and the control samples. Comparisons of the microstructures of solid pellets, hollow pellets, and hollow pellets with a central BeO rod showed no differences. Cladding samples showed voids at pellet interfaces that were not present in control samples, and small pieces of UO_2 were imbedded in the cladding at the inner surface. A second phase tentatively identified as sigma phase was found at grain boundaries. In comparison with the group I capsules, there was a marked difference in the integrity of the pellets in the group II capsules. The outer surfaces of the group II pellets were not fractured as were the surfaces of the group I pellets.

A capsule irradiated in the ETR under conditions similar to those for irradiations in the ORR was also examined. The fission-gas release was

several times that for the ORR-irradiated capsules. There were numerous microcracks in the pellets but no gross fractures.

Three bulk UC-containing tantalum capsules irradiated in the LITR were examined. A reaction at the UC-tantalum interface caused swelling of the can of the first capsule irradiated and rupture of the second and third capsules, which were irradiated for longer times at higher temperatures. Three distinct layers detected in the reaction zone are being studied by x-ray diffraction in an attempt to identify them.

The graphite capsules containing UC_2-graphite fuel matrices that were irradiated in the MTR are being examined. The outside dimensions of the graphite cans were unchanged, but there was an average decrease in the diameter of the fueled pellet of 4.5% and a length increase of 3%.

Modifications are being made to change the ORR-B9 facility from nitrogen cooling to single-pass air cooling. A special trap is to be provided in the helium sweep-gas stream to collect the solid daughters of short-lived fission gases. Pyrolytic-carbon-coated UC_2 spheres are being prepared for irradiation.

Metallographic examinations were made of irradiated capsules B9-3 and B9-4 which consisted of UO_2 pellets clad with low-permeability graphite. The ends of the originally hollow cylinders of capsule B9-3 were examined where UO_2 had deposited during irradiation. There was no evidence of reaction between the UO_2 and the graphite can. There was no movement of the UO_2 in capsule B9-4. The UO_2 was found to be composed of equiaxed grains about five times the size of those of the unirradiated control sample.

Analyses are being made of data obtained with tin-plate samples of UO_2 sandwiched between ThO_2 plates in the LITR facility for instantaneous fission-gas-release measurements. The data on the release of Xe^{138}, Kr^{88}, and Kr^{85m} have been found to divide roughly into those obtained before the sample was heated to 1110°C and those obtained after this maximum temperature was reached. The release-to-production ratio was increased about an order of magnitude by the irradiation at 1100°C. When the UO_2 was cooled from operating temperature to 100°C, there was a burst of fission-gas release. It has been demonstrated that this cooling burst releases a store of trapped gas and that the quantity of gas release in

the cooling burst is dependent on the temperature of irradiation. The iodine precursor of xenon was released with the same temperature dependence as the xenon and krypton.

6. Out-of-Pile Testing of Materials and Components

A forced-convection loop containing AGOT graphite, metal test specimens, and helium was operated to study the effects of H_2O inleakage on the EGCR materials. During the test, water-saturated helium was injected at a rate that was an order of magnitude greater than the maximum specified for the EGCR. The oxide films formed on the steel specimens were superficial, and the weight gains of steel specimens containing less than 7% chromium were lower than in similar tests with CO and CO_2 impurities in the helium. There was no soot deposition in the cold leg and no apparent adverse effect on the graphite.

Studies were initiated of the interaction of graphite and stainless steel in direct contact at 1300°F. In tests at 1300°F for 1000 hr at contact pressures in the range 500 to 2000 psi, the steel specimens were severely embrittled. There was heavy carburization at points of contact, but areas of the metal surface adjacent to voids in the graphite showed only grain-boundary carbides.

The degassing behavior of additional samples of needle-coke graphite produced for use in the EGCR was investigated. The results were essentially in agreement with those obtained previously. Data obtained for different size specimens indicate that geometry has no noticeable effect.

Data obtained in an experimental study of the interdiffusion and forced-flow behavior of helium and argon in Speer moderator No. 1 graphite and AGOT graphite were used to determine a mutual diffusion coefficient and to verify superposed flow equations. It was concluded that if the sweep rate of the gas is lower than the critical value for a given graphite in a gas-cooled reactor, the fission-product contamination will increase, whereas sweep rates greater than the critical value would require large reprocessing capacities without a decrease in contamination.

Modifications were made to improve the reproducibility of helium analyses with the Greenbrier Process Chromatograph. A third instrument was ordered for monitoring the blanket gases in in-pile loop tests.

Investigations of the removal of radioactive fission-product gases from helium were continued. In tests of a charcoal impregnated with salts of silver, copper, and chromium (Whetlerite ASC), iodine vapor was removed from high-temperature helium with an efficiency exceeding 99.99%. Long-term tests indicate that once iodine is adsorbed from a helium stream onto Whetlerite charcoal it becomes virtually immobilized. In one test, at 425°C, the iodine migration was no more than 0.07 in. over the test period of 897 hr. An experiment to measure dynamic adsorption of krypton by charcoal at liquid nitrogen temperature was initiated; no breakthrough of krypton has occurred during the eight weeks this test has been in progress. A basis for estimating effective diffusion coefficients for krypton and xenon in adsorbers operating at low carrier gas velocities was established.

Further tests of the stability of chromium-nickel alloy thermocouple wires in stagnant helium atmospheres have indicated that large negative emf drifts are to be expected when using 90% Cr–10% Ni alloys. Both regular and special Chromel-P were subject to selective oxidation, with resultant emf drift. The 80% Ni–20% Cr alloys were less susceptible to oxidative attack. Chromel-A, Chromel-AA, and Geminol-P had reasonably stable emf's for long periods of time.

Emf-drift tests at temperatures lower than 1000°C in stagnant helium substantiated previous results. The selective oxidative attack occurred in regions exposed to the atmosphere in the temperature range of 700 to 900°C.

Continuation of drift tests of stainless-steel-sheathed Chromel-P vs Alumel thermocouples in a graphite-helium atmosphere showed that the large negative errors were caused by products desorbed from the graphite. Thermocouples sheathed in type 304 stainless steel from vendor A were the least stable; they drifted a total of −50°C during six months of exposure. Thermocouples from vendor B drifted only −8°C during three months. Thermocouples sheathed in types 310 and 347 stainless steel from vendor B

were more stable. Tests on similar thermocouples in a pure CO atmosphere have shown only slight positive emf drift during 40 days of exposure.

7. Development of Test Loops and Components

The Title II detailed fabrication drawings for the top-nozzle tee sections of the EGCR in-pile loops were completed and work continued on through-tube and in-pile loop systems designs. A preliminary design and hazards summary report was completed. Fabrication of the bottom tee section components is under way.

Tests of valves for EGCR service were continued, and two tests of the through-tube bearings were completed. Considerable galling of the Stellite No. 6 occurred. Therefore parts coated with Linde Flame Plate LW-IN30 and Stellite No. 12 are being fabricated for further tests. Development test are being run on the through-tube orifice plate.

Proof tests of 5-in.-IPS double-seal Conoseal joints and 6-in.-IPS double-seal Grayloc joints were completed. Tests were also conducted on a spherical seal.

Work continued on the construction of GCR-ORR loop No. 2. Analyses were made of the hazards of the loop, and a design report was prepared. Tests of components are under way.

Two regenerative compressors that operated satisfactorily in GCR-ORR loop No. 1 for 3300 hr were examined. Some bearing wear and loss of lubricity of the grease lubricant were noted. Three regenerative compressors are being prepared for use in GCR-ORR loop No. 2. A small regenerative compressor was designed for use in the control-rod-drive test facility.

Tests of experimental compressors with gas-lubricated bearings continued at Bristol Siddeley and at ORNL. Bearing touching occurred in all tests of the ORNL-designed unit.

Part 1. Design Investigations

1. REACTOR PHYSICS

A. M. Perry

Epithermal Neutron Absorption in EGCR Control Rods

C. A. Preskitt D. R. Gilfillan

An experimental measurement of EGCR control rod worth[1] has been used as a basis for a study of epithermal neutron absorption in the B_4C control material of the rods. A previously reported theoretical check of the experimental results[2] showed that remarkable accuracy could be obtained with a four-group model in which the B_4C was assumed to be black to all neutrons in two groups below 4.5 ev and in which diffusion theory was applied to the B_4C in two groups above 4.5 ev.

Although four-group calculations may, in general, have more inherent accuracy, it is desirable to use less costly two-group calculations where possible. On the other hand the accurate treatment of the highly absorbing control material is more difficult in the two-group scheme, since the material properties vary by large factors within the single fast group. Accurate two-group calculations are made possible either by doing a detailed theoretical study to determine an effective fast group cross section or by adopting an empirical approach in which the boundary condition at the rod surface is varied to reproduce the control rod worth for a known condition.

The method adopted here for two-group calculations is basically the empirical approach, but an accompanying theoretical study has shown that a very simple model is consistent with the observed quantities. The boundary condition at the control rod surface consists of specifying a value of the current-to-flux ratio, C, at that point. If

---

[1]P. F. Nichols and R. E. Heineman, PCTR Measurements of Control Rod Strength, p. 105 in Nuclear Physics Research Quarterly Report for January, February, March, 1960, HW-64866.

[2]GCR Quar. Prog. Rep. Dec. 31, 1959, ORNL-2888, p. 9.

$$C = \frac{D}{\phi}\frac{d\phi}{dr} = \frac{j}{\phi} \quad ,$$

then it can be shown that

$$C = \frac{\lambda_{tr}}{3l} \quad ,$$

where l is the flux extrapolation length into the control rod, and λ_{tr} is the transport mean free path in the material outside of the rod.

In order to determine the average value of C, a system in slab geometry containing a nonscattering absorber of thickness t is considered. If the angular neutron flux is expanded into its spherical harmonic components and the first two terms of the expansion are kept,

$$\Phi(x,\mu) = \phi(x) + \frac{d\phi(x)}{dx}\mu \quad ,$$

where $\phi(x)$ is the total flux, and μ is the cosine of the trajectory angle measured from a vertical axis. Then the total entering current, J, on both faces of the slab, by the same approximation, is

$$J_+ + J_- = \frac{\phi(s)}{2} + D\left.\frac{d\phi(x)}{dx}\right|_s \quad ,$$

where s denotes evaluation on the surface of the slab.

If A_n is the ratio of captured neutrons to entering neutrons for a flux with a μ^n angular distribution, the total number of captures in the slab is given by

$$\text{Captures} = A_0\frac{\phi(s)}{2} + A_1 D\left.\frac{d\phi(x)}{dx}\right|_s \quad .$$

When this expression is set equal to the sum of the net currents into the two faces of the slab,

$$2D\left.\frac{d\phi(x)}{dx}\right|_s \quad ,$$

it can be seen that

$$C = \frac{D}{\phi} \left. \frac{d\phi(x)}{dx} \right|_s = \frac{A_0}{2(2 - A_1)} \quad .$$

The general expression for A_n in slab geometry is

$$A_n = 1 - \frac{\int_0^1 \mu^n e^{-\Sigma_a t/\mu} \mu \, d\mu}{\int_0^1 \mu^n \mu \, d\mu} \quad ,$$

from which it follows that

$$A_n = 1 - (n + 2) E_{n+3} (\Sigma_a t) \quad ,$$

where the E_n are the familiar exponential integrals.

The variation of C with energy is shown in Fig. 1.1, together with the average C as a function of the upper energy limit for a 0.25-in.-thick slab of B_4C. This thickness was chosen because it is the thickness of the B_4C annulus of the EGCR control rods. For neutron energies below about 5 ev, the slab absorbs all incident neutrons, and C(E) is equal to the

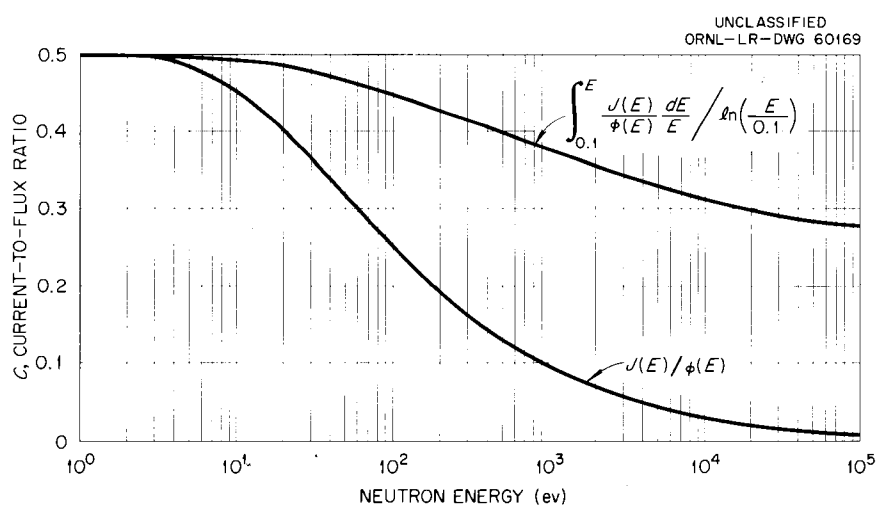

Fig. 1.1. Variation of Current-to-Flux Ratio with Neutron Energy for a 0.25-in.-Thick B_4C Slab.

familiar diffusion theory value of 0.5. As the neutron energy increases, the transmission becomes important, and the asymptotic value of the average C is 0.28 for this system. Thus an average epithermal current per unit flux is obtained that is a fraction 0.56 of that for a black slab.

In applying this result to the EGCR, use is made of the fact[3] that the value of C given by transport theory for a black cylindrical rod of EGCR dimensions is 0.37. Based on this analysis, a value of 0.207 would be expected for the epithermal current-to-flux ratio at the surface of this control rod.

Calculations of Δk versus the value of C in the fast group have been done for the lattice arrangement for which the EGCR control rod worth was measured at the PCTR.[1] The results of these calculations, plotted in Fig. 1.2, show that the predictions of the simple theory are in good agreement with the experimental measurements. The calculations indicate that the sensitivity of rod worth to the epithermal boundary condition is

[3]B. Davidson and S. A. Kushneriuk, Linear Extrapolation Length for a Black Sphere and a Black Cylinder, MT-214, March 1946.

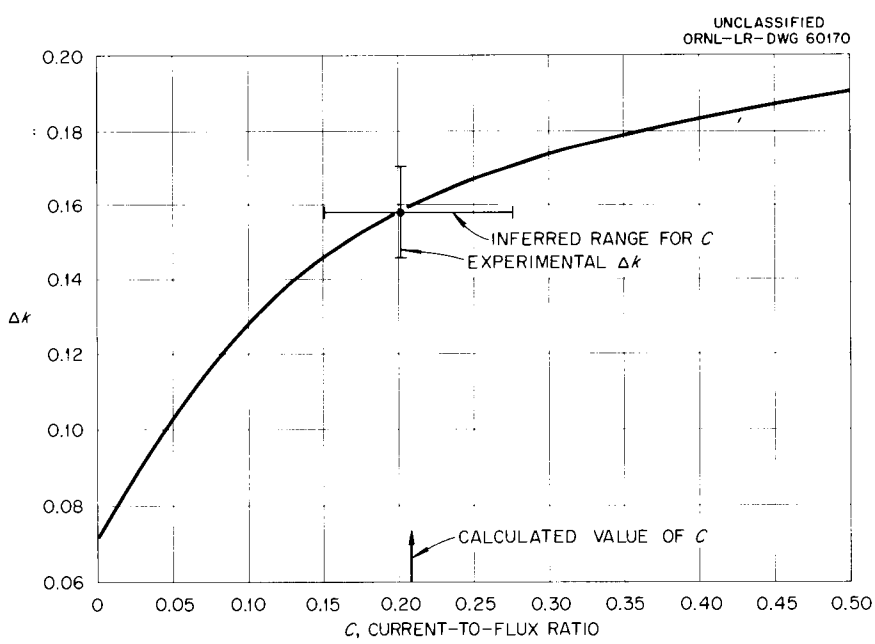

Fig. 1.2. Comparison of Calculated and Experimentally Inferred Values for the Current-to-Flux Ratio.

relatively low until the current-to-flux ratio falls to intermediate values. This results from the increased flux depression in the control rod supercell as the blackness of the rod increases.

It is important to note from Fig. 1.2 that complete neglect of epithermal absorptions in the EGCR control rods would result in an underestimate by approximately a factor of 2 in the rod worth.

Since these calculations are a straightforward extension of the highly successful four-group calculations reported previously,[2] it is expected that the accuracy of the simple treatment of epithermal absorption is not specialized to the particular problem at hand and should provide a satisfactory means for determining the effect on rod worth of changing the boron loading or annulus thickness of the rods. Comparisons between B_4C and boron-loaded steel rods should also be handled accurately, although in the case of solid rods the expression for A_n should be generalized to cylindrical geometry.

EGCR Power Distributions with Experimental Assemblies in Two Loops

C. A. Preskitt

The analysis of the EGCR radial power distribution with experimental assemblies in the loop facilities has been extended to include the case of the unsymmetrical configurations that result when only two loops are loaded. In this study the experimental assemblies were taken to be UO_2-fueled clusters with approximately 1.2 times the fuel volume of an EGCR fuel element. The range of enrichments considered for the fuel was from 5 to 20 wt % U^{235}. Calculations were done for partially loaded cores, as well as for full core loading of the 234 channels. For the partial loadings the absolute loop power could not be determined without a complete flow analysis of the core, and therefore in the summary of the results, presented in Table 1.1, the loop power is tabulated as a fraction of the total core power.

In all the calculations the loaded loops were two of the central facilities on the same side of the core axis. The results of the

Table 1.1. EGCR Core and Loop Parameters for Two Loaded Experimental Loops

Experimental Fuel Enrichment (wt % U^{235})	Control Rods Inserted	Number of Loaded Core Channels	k	P_{max}/P (see footnote a)	Loop Power (Mw)
Empty loops	None	234	1.099	1.314	0.000
5	None	234	1.106	1.350	0.741
10	None	234	1.113	1.418	1.350
20	None	234	1.128	1.680	2.914
10	N	234	1.097	1.324	1.146
20	N	234	1.109	1.500	2.540
5	X, P, C	234	1.084	1.681	0.881
20	P	234	1.124	1.784	3.107
5	None	166	1.101	1.184	0.0113[b] P_c
10	None	166	1.109	1.252	0.0202[b] P_c
20	None	166	1.127	1.456	0.0423[b] P_c
Empty loops	None	68	1.039	1.208	0.0000
20	None	68	1.104	1.237	0.0888[b] P_c

[a]Ratio of maximum channel power to average power per channel.

[b]Loop power is expressed as a fraction of core power, P_c.

calculations indicate that the previously noted nearly constant ratio of loop power to maximum channel power is not characteristic of these asymmetrical configurations. This is due to the effect of the control rods in moving the position of the peak power channel away from the loops for some configurations. It may also be noted that the experimental assemblies may each generate about 400 kw more power than in cases with four central loops loaded, without exceeding the maximum allowable power in any fuel channel.

Criticality of EGCR Fuel Shipping Crates

D. R. Gilfillan

Criticality of the EGCR fuel shipping crates has been examined for dry, immersed, and flooded configurations. In the immersed configuration, it is assumed that the insides of the crates remain dry when the crates are submerged in water; and in the flooded configuration, it is assumed that all voids within the crates are filled with water when the crates are submerged. The multiplication factor is calculated to be highest for the immersed configuration. For 18 crates containing 288 fuel assemblies the multiplication factor is near unity (~0.99) if the array is

immersed. It has been determined, however, that a "safe" configuration results if the crates are arranged in a single-layer array for all three cases. The calculated multiplication factor is 0.88 for an immersed infinite array of this height. This array should provide an acceptable configuration for either shipping or storage, even if the immersed condition is possible. When kept dry, the shipping crates cannot be made critical in any size array.

Fission-Product Decay Heat

J. G. Delene

An analysis of fission-product afterheat as a function of time after reactor shutdown was made with emphasis on its application to the EGCR. The results of this study are shown as curves 1, 2, and 3 of Fig. 1.3.

The data for the infinite operation curve (curve 1) between 10^2 and 10^7 sec were taken from a report by Avery et al.[4] The analysis showed that for infinite reactor operation the fission-product decay heat represents 7.3% of the total reactor power. This figure was based on an equilibrium value of 7.0 Mev/fission (ref. 5) for fission-product gammas and 7.6 Mev/fission (ref. 6) for the fission-product betas. The total energy per fission was taken to be 200 Mev. Within 1 sec after shutdown, the decay heat has decreased to approximately 95% of the equilibrium value. Curve 1 was completed by drawing a smooth curve between the data points at 1 and 100 sec. The curve was extended (not shown here) beyond 10^7 sec by using the data of Stehn and Clancy.[5]

The curve for one year of operation (curve 2) was computed using the infinite operation curve and the formula

---

[4]A. F. Avery et al., Method of Calculation for Use in the Design of Shields for Power Reactors, AERE-R-3216, February 1960.

[5]J. R. Stehn and E. F. Clancy, Fission-Product Radioactivity and Heat Generation, 1958 Geneva Conference Paper (A/Conf. 15/P/419).

[6]J. F. Perkins and R. W. King, Energy Release from the Decay of Fission Products, Nuclear Sci. and Eng. 3, 726 (1958).

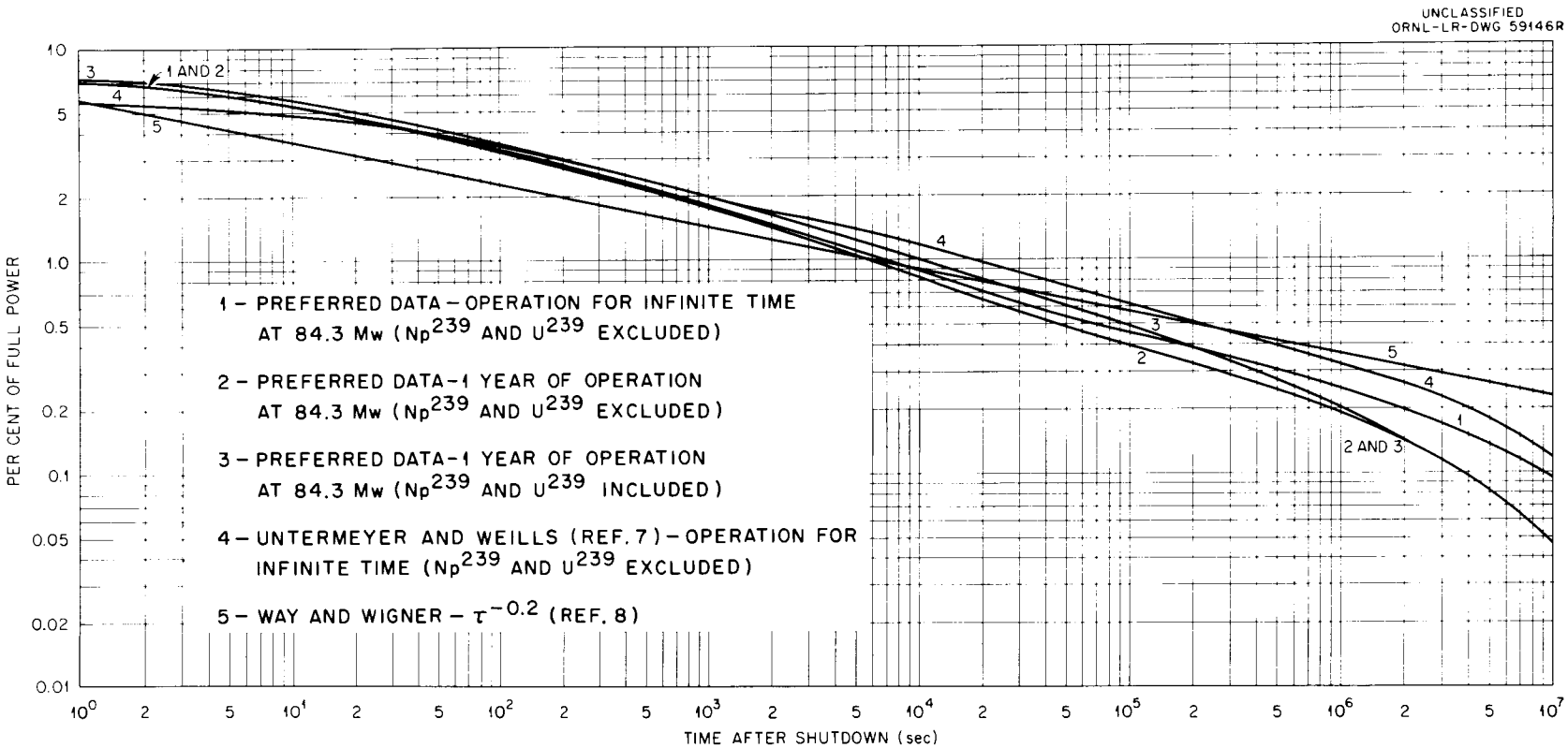

Fig. 1.3. Fission-Product Afterheat in EGCR.

$$\Gamma(1\ \text{yr},\ T_s) = \Gamma(\infty,\ T_s) - \Gamma(\infty,\ 1\ \text{yr} + T_s) \quad ,$$

where $\Gamma(A,B)$ is the power level at time B after shutdown for a reactor that was operated for a time A.

For the EGCR at equilibrium it is estimated that another approximately 0.28% of operating power comes from the decay of Np^{239} and U^{239}. This contribution is added to curve 2, and the sum is shown on curve 3.

Curve 4 is the Untermeyer and Weills[7] curve for heat production in U^{235} for infinite exposure. It is lower than the EGCR infinite operation curve for small times after shutdown. The two curves cross at approximately 1300 sec, and after approximately 10^4 sec the Untermeyer and Weills curve stays approximately 30% higher than the comparable curve 1. Curve 5 is the so-called Way-Wigner $t^{-0.2}$ approximation.[8] It tends to be out of line both with Untermeyer and Weills and with this analysis. It is recommended that curve 3 be used in any study involving afterheat in the EGCR.

Power Distribution in 19-Rod Clusters

D. R. Gilfillan

A study is being made of the power distribution in beryllium-clad, UO_2-fueled, 19-rod cluster elements operating in the EGCR core. Individual rods are 0.5 in. in diameter and have a 40-mil-thick beryllium cladding. In addition, each rod has six beryllium fins that increase the effective thickness of the cladding for the purpose of these calculations to approximately 61 mils. The rods within a cluster form a hexagonal array having a pitch of 0.79 in. between individual rods. In the calculations, a cluster was represented as a central rod with two rings of rods around it in the form of an inner annulus and an outer annulus. The fuel volume in a cluster was taken to be nearly the same as the fuel volume in an EGCR fuel element.

---

[7] S. Untermeyer and J. T. Weills, Heat Generation in Irradiated Uranium, ANL-4790, Feb. 25, 1952.

[8] S. Glasstone, Principles of Nuclear Reactor Engineering, p. 119, D. Van Nostrand Co., Inc., New York, 1955.

Results of the calculations are given in Table 1.2. Some additional preliminary calculations suggest that the power and the variation of power density across the central rod or rods in one of the two annuli may be independently controlled to some extent by varying the fuel enrichment in the three regions relative to one another.

Table 1.2. Power Distributions in Beryllium-Clad 19-Rod Cluster Fuel Elements

Fuel Enrichment (%)	Ratio of Power Generated in Individual Rods to Power Generated in the Cluster			$P_c/\overline{\phi}_m$ (see footnote a)	Ratio of Flux at Outer Edge of a Rod to Flux at Inner Edge of a Rod Along Radius of Cluster		
	Central Rod	Inner Annulus	Outer Annulus		Central Rod	Inner Annulus	Outer Annulus
2.46	0.045	0.049	0.055	1.0	1.04	1.07	1.05
3.0	0.043	0.048	0.056	1.17	1.05	1.07	1.06
4.0	0.041	0.047	0.056	1.44	1.07	1.10	1.08
5.0	0.039	0.046	0.057	1.68	1.09	1.13	1.10
6.0	0.036	0.044	0.058	1.88	1.12	1.17	1.12
7.0	0.034	0.043	0.059	2.07	1.15	1.20	1.14
8.0	0.032	0.042	0.060	2.23	1.18	1.24	1.17

[a]Ratio of power in cluster to average flux in moderator normalized to 1.0 for an enrichment of 2.46%. These values indicate how the power in the cluster varies with enrichment in an open lattice of the EGCR.

Neutron Thermalization Calculations

E. A. Nephew M. E. Tsagaris
C. A. Preskitt

A group of interlocking programs for the IBM-7090 has been written for the calculation of thermal-neutron spectra in infinite homogeneous media. These codes are all compatible with MONITOR operation and will be described in detail in a report to be issued at a later date. A brief description of the completed programs follows.

1. IMS – Infinite Media Spectra. The IMS program solves the space independent Boltzmann transport equation by means of a normalized extrapolated Gaussian iteration method. A generalized Simpson's rule using unequal energy intervals is used to perform all the necessary integrations, and a provision has been included which prevents the points of discontinuity in an energy transfer matrix from occurring inside a three-point

integration subinterval. The energy dependence of the absorption cross section may be specified as 1/v or an arbitrary energy dependence may be supplied. In the latter case, a special subroutine interpolates linearly between ln E and ln σ to obtain the absorption cross section for the particular energy mesh of the problem. The interpolation is thus exact when the cross-section variation is any power of the energy. The energy-transfer kernel is read from a library tape and may either be one calculated by the GTP program described below or by a more exact model that takes into account the molecular binding of the moderator. In addition to a listing of the computed flux values for each point of the energy mesh, a deck of cards containing the fluxes for each energy point is produced by the IMS program. This FLUX deck is of the correct format for use as input to the ACS program described below.

2. GTP – Gas Transfer Probabilities. This program evaluates the Wigner-Wilkins[9] energy-transfer matrix for the free gas approximation to a moderator. The kernel with a maximum size of 161 × 161 energy points is stored on tape for subsequent use as input to the IMS program. Features of the numerical methods used include a rational approximation to evaluate error functions and the use of the condition of detailed balance for the calculation of all upscattering. The program contains several checks which prevent loss of significance when two nearly identical numbers are subtracted.

3. ACS – Average Cross Section Code. The ACS program computes spectrum-averaged cross sections and uses as input the fluxes which have been calculated directly by the IMS code or arbitrary forms for the flux, such as the Campbell-Freemantle model. Both thermal and epithermal reaction rates are computed within specified energy limits.

4. Other Related Programs. Several other satellite codes have been written. A program, TKS, reads a kernel from the library tape and calculates the slowing-down source terms appearing in the finite-interval Boltzmann transport equation of the IMS program. A handling routine, THR,

---

[9]E. P. Wigner and J. E. Wilkins, Jr., Effect of the Temperature of the Moderator on the Velocity Distribution of Neutrons with Numerical Calculations for H as Moderator, AECD-2275, Sept. 14, 1944.

permits modification or inspection of the kernel library stored on tape by GTP. A decomposition code, DCOM, fits a Maxwellian, by the method of least squares, to the IMS fluxes and thus determines the effective neutron temperature. In addition, it is planned to write a code to compute group transfer cross sections for use with space-dependent transport-theory calculations in the thermalization range.

Some of the results which have been obtained by fitting a Maxwellian flux to the IMS fluxes computed for different conditions of moderator temperature and absorption cross section are presented in Table 1.3. It is planned to re-examine the parameters of the Coveyou-Bate-Osborn[10] expression relating moderator temperature and neutron temperature, since the value obtained for T_n clearly depends upon the range of the attempted fit. Also, the residue flux obtained by subtracting the fitted Maxwellian component from the total computed flux will be examined to obtain the best joining function between the Maxwellian and 1/E regions. It is also planned to study the perturbing effects on the spectral distribution in the moderating region of the presence of varying concentrations of Pu^{239} and U^{235} and to attempt to formulate from this study a set of effective cross

[10]R. R. Coveyou, R. R. Bate, and R. K. Osborn, J. Nuclear Energy, Vol. 2, pp. 153–67 (1956).

Table 1.3. Effective Neutron Temperatures Obtained with DCOM Code

$\sigma_a^{2200\ m/s}$ (1/v) (barns/carbon atom)	Effective Neutron Temperature (°K) at Graphite Temperature of		
	300°K	600°K	1200°K
0.05	324	632	1243
0.10			1287
0.15	373	694	1334
0.40	511	869	1565
0.50		946	

sections for plutonium and uranium. A typical perturbing effect of the large Pu^{239} resonance at 0.3 ev in a graphite reactor is shown in Fig. 1.4.

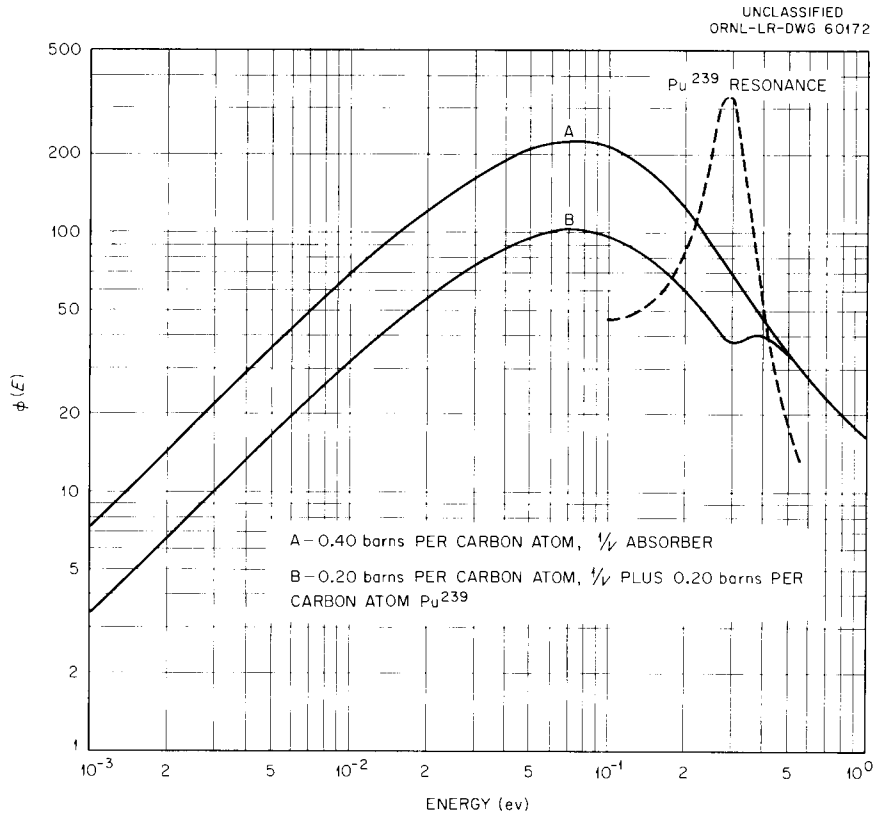

Fig. 1.4. Typical Effect of Pu^{239} on the Thermal-Neutron Spectrum in a Graphite Reactor at a Graphite Temperature of 600°K. Flux normalization is to one net slowing-down neutron per cm^3 per second at 5 ev. Cross section values given are at 2200 m/s neutron velocity.

Reactivity Lifetime in Thorium Cycle

R. S. Carlsmith

A series of calculations is being made for determining the reactivity lifetime of fuel elements consisting initially of U^{235}, thorium, and graphite. The conditions of the calculation were (1) an equilibrium fuel cycle, (2) a core neutron-leakage fraction of 0.05, (3) an absorption fraction in the structure of 0.01, (4) a moderator temperature of 1000°K, and (5) a feed-fuel moderator-to-uranium ratio of 4000. As shown in Fig. 1.5, there is an optimum thorium-to-uranium ratio for a given specific power. At low

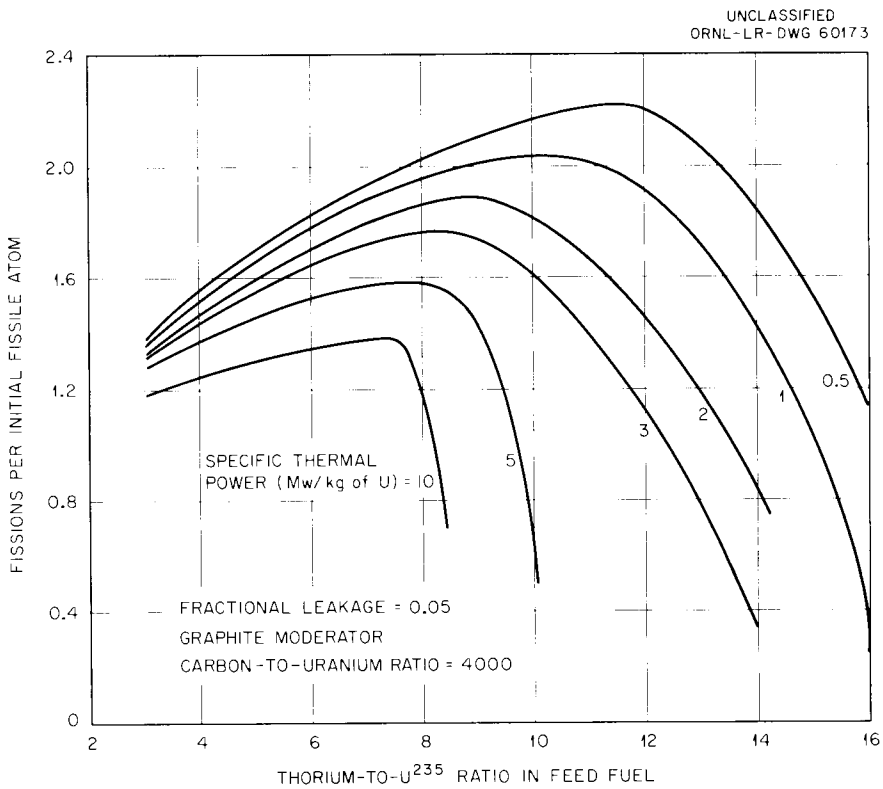

Fig. 1.5. Fissions per Initial Fissile Atom as a Function of Specific Power and Thorium-to-Uranium Ratio.

thorium-to-uranium ratios the conversion ratio is relatively low, resulting in short reactivity lifetimes. Increasing the thorium concentration increases the conversion ratio and initially increases the lifetime, but eventually the reactivity importance of fission-product buildup is greater than that associated with the increase in conversion ratio and the maxima shown in Fig. 1.5 result. The lifetimes are less at higher specific powers because of more absorption in Pa^{233} and Xe^{135} and the necessity of providing greater reserve reactivity for overriding peak Sm^{149} poisoning after shutdown.

The results of similar calculations at different moderator-to-fuel ratios are shown in Fig. 1.6. In this case only the results for optimum thorium-to-uranium concentrations are plotted. It may be seen that a moderator-to-fuel ratio of about 4000 gives generally the highest number of fissions per initial fissile atom under the stated conditions. At carbon-to-uranium ratios greater than 4000 there are generally more

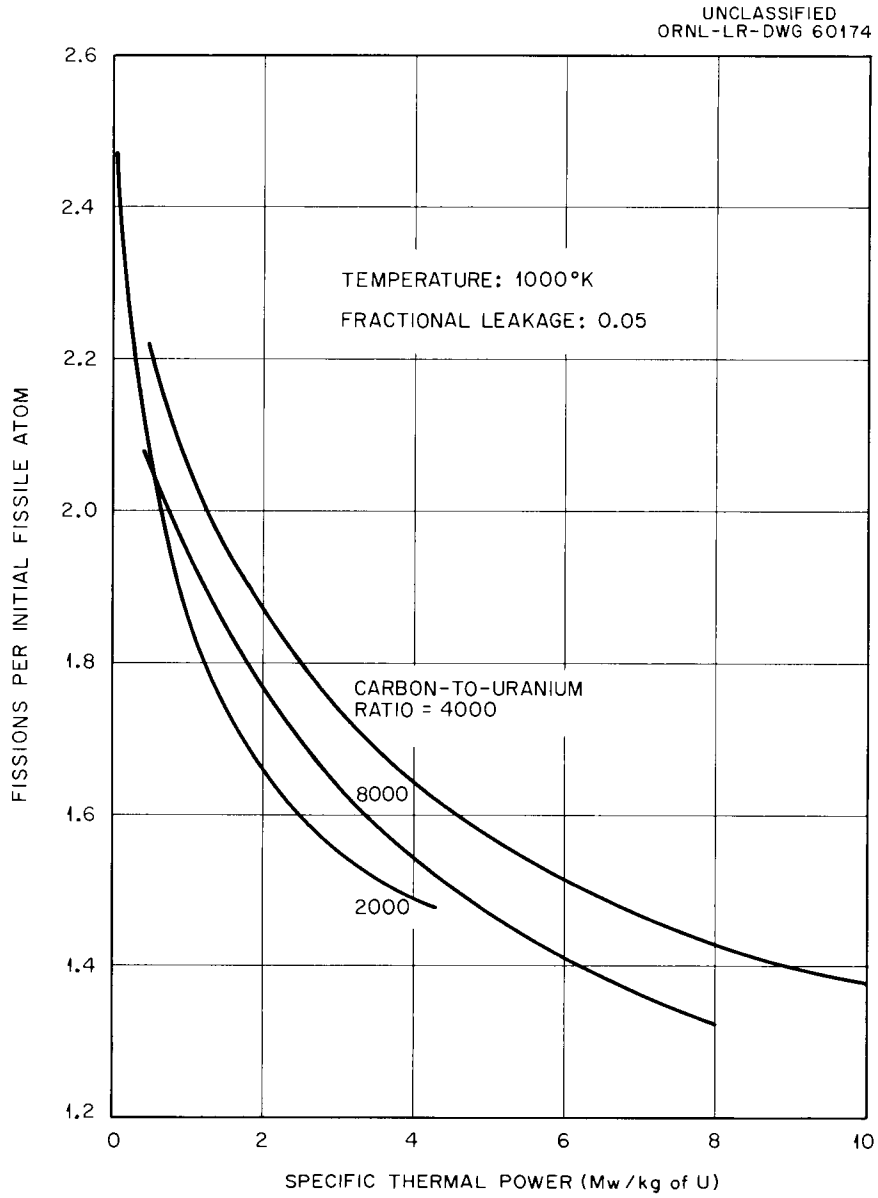

Fig. 1.6. Fissions per Initial Fissile Atom as a Function of Specific Power and Carbon-to-Uranium Ratio at the Optimum Thorium-to-Uranium Ratio.

absorptions in the moderator, leading to lower conversion ratios and shorter reactivity lifetimes. At ratios less than 4000, the fraction of absorptions that occur in the resonance region becomes quite large; the fissile-material characteristics are less favorable; and fission-product poisoning is relatively greater.

2. REACTOR DESIGN STUDIES

Thermal Analysis of EGCR Core Components

G. Samuels C. S. Walker

Fuel Assemblies

The contract for the first core loading of EGCR fuel assemblies has been awarded to the Westinghouse Atomic Fuel Division, Cheswick, Pennsylvania. The price for 1739 fuel assemblies is $786,897.50, which is approximately $52.00 per kg of uranium metal. This cost does not include a protective coating for the graphite sleeves. It now appears that the protective coating will be added to the sleeves to prevent oxidation of the sleeve and graphite moderator structure in the event of a rupture of the primary system.

Fuel Channel Pressure Losses (M. E. Lackey)

The over-all pressure drop for the EGCR core has been recalculated using the latest available pressure-loss data. The pressure drop from plenum to plenum for the highest power channel operating with a 1075°F exit gas temperature and a helium flow of 2280 lb/hr was found to be 8.8 psi. It was assumed in this calculation that each bundle was misaligned 30 deg relative to the adjacent bundles. The friction-factor equations and the loss coefficients at a Reynolds number of 50 000 that were used in this calculation are given below:

	Equation or Coefficient
Friction factor upstream of bundle mid-cluster spacer	$4f = 0.164/Re^{0.180}$
Friction factor downstream of bundle mid-cluster spacer	$4f = 0.214/Re^{0.199}$
Entrance dummy loss coefficient evaluated with the variable orifice completely open	3.82
Bundle entrance loss coefficient	0.183
Mid-cluster-spacer loss coefficient	0.339

Hanger-spider loss coefficient	0.425
Bundle exit loss coefficient	0.32
Exit dummy loss coefficient	0.98

Heat Transfer Correlation (R. S. Holcomb, M. E. Lackey)

The variations of the local velocity and hydraulic diameter within the influence boundaries of an EGCR fuel channel have been determined by graphical integration of the previously reported velocity profile[1] for tubes 1, 2, 3, and 7 at an L/d_e of 3.9 and 0-deg orientation. These variations are shown in Figs. 2.1 and 2.2. The angular measurements are taken clockwise when looking upstream with 0-deg on an outside tube (Nos. 1–6) being taken at the outermost point of the tube. The central tube (No. 7)

[1]GCR Quar. Prog. Rep. Dec. 31, 1960, ORNL-3049, pp. 114–7.

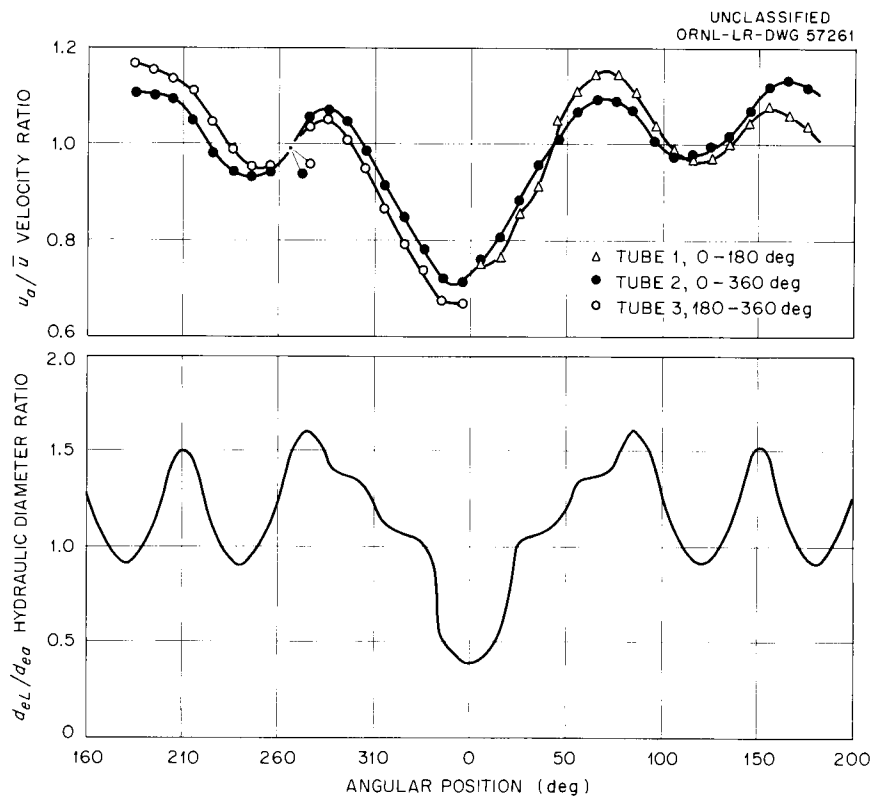

Fig. 2.1. Comparison of Circumferential Velocity Profiles Obtained on Tubes 1, 2, and 3 with Circumferential Variation in the Hydraulic Diameter.

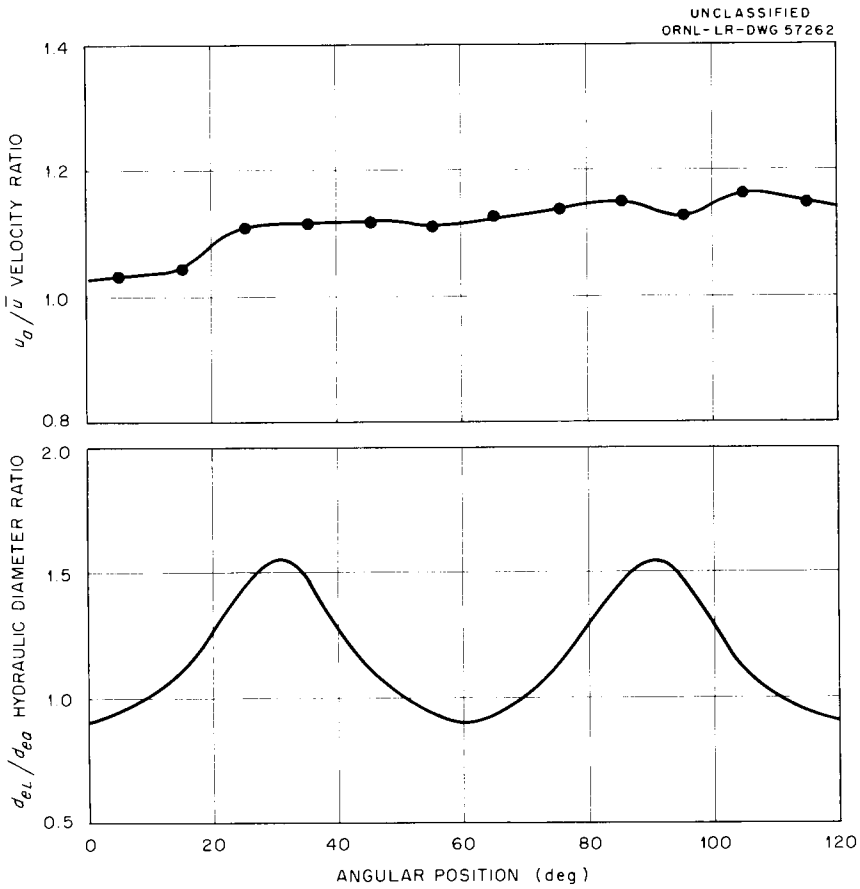

Fig. 2.2. Comparison of Circumferential Velocity Profile Obtained on Tube 7 with Circumferential Variation in the Hydraulic Diameter.

is noted in a similar manner, with 0-deg being taken as the point directly opposite 180 deg on tube No. 1.

The variation of the local Nusselt number at an L/d_e of 3.9 was calculated for tubes 1, 2, 3, and 7 with the equation[2]

$$Nu_{sx} = 0.0975\ Re_{sx}^{0.724}\ Pr_{sx}^{0.4} \left(\frac{x}{D}\right)^{-0.5576\ Re_{sx}^{-0.109}} \qquad (1)$$

and the velocity and hydraulic diameter variations given in Figs. 2.1 and 2.2. These variations of the local Nusselt number were compared with the variations in the local mass transfer value, j_M.[3] Both the local Nusselt

[2]GCR Quar. Prog. Rep. March 31, 1961, ORNL-3102, p. 20.

[3]GCR Quar. Prog. Rep. Sept. 30, 1960, ORNL-3015, pp. 53–62.

number and the local mass transfer values were normalized on the basis of the values found for one-half of tubes 1, 2, and 3 and one-third of tube 7. These comparisons are shown in Figs. 2.3 through 2.7. The circumferential variations of the mass transfer values and the calculated variations of the Nusselt number based on the axial velocity profile give agreement well within 8%.

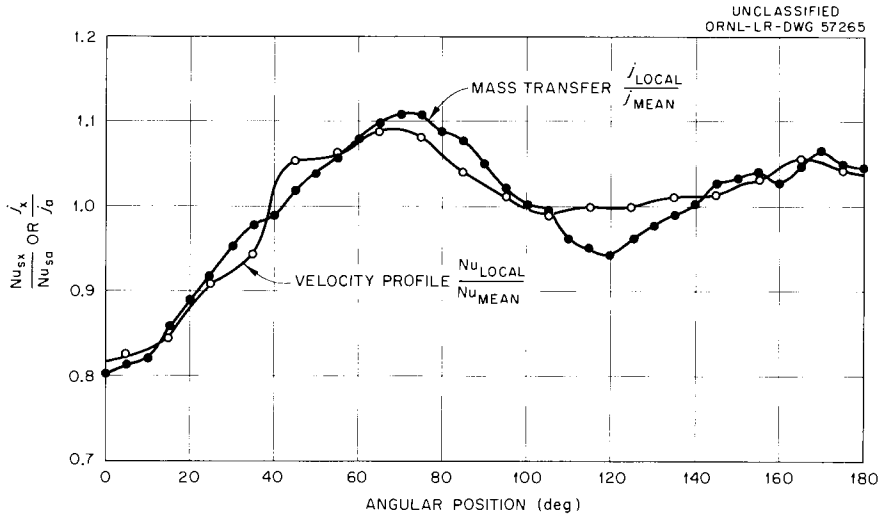

Fig. 2.3. Comparison of the Variation of the Local Heat Transfer Performance with the Local Mass Removal Rate for Tube 1 from 0 to 180 deg.

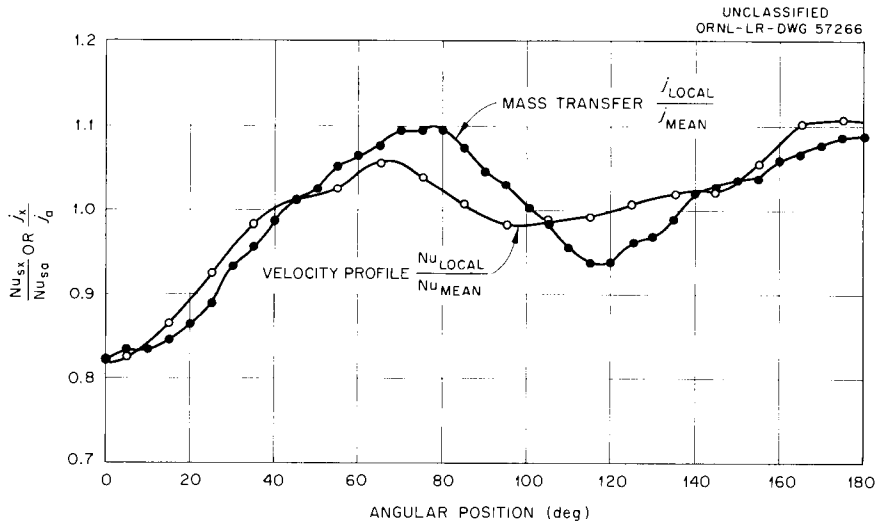

Fig. 2.4. Comparison of the Variation of the Local Heat Transfer Performance with the Local Mass Removal Rate for Tube 2 from 0 to 180 deg.

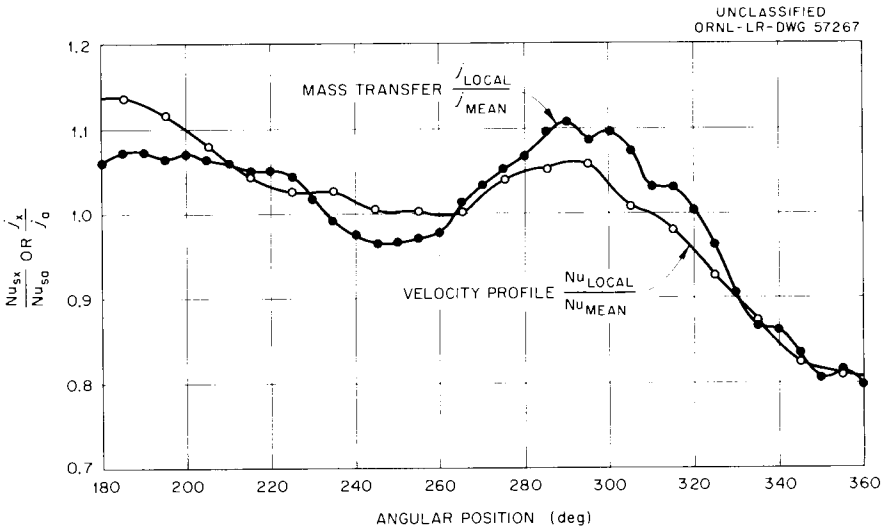

Fig. 2.5. Comparison of the Variation of the Local Heat Transfer Performance with the Local Mass Transfer Removal Rate for Tube 2 from 180 to 360 deg.

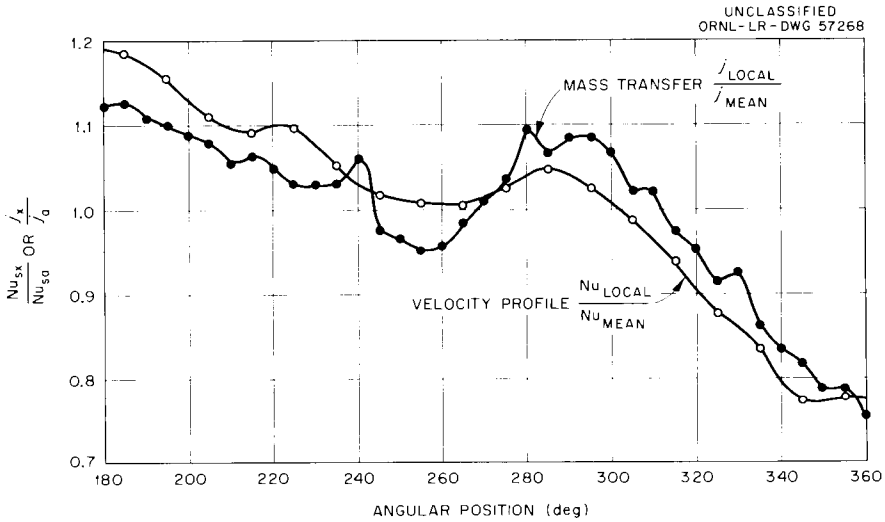

Fig. 2.6. Comparison of the Variation of the Local Heat Transfer Performance with the Local Mass Transfer Removal Rate for Tube 3 from 180 to 360 deg.

An equivalent j value (j_V) was calculated from Eq. (1) in order to effect a comparison of the absolute value of the mass transfer and heat transfer coefficients. These values are given in Table 2.1.

The absolute values of mass transfer at an L/d_e of 3.9 are in general higher than the j_V values calculated from the velocity profile. The distribution of the absolute values indicates that the flow is not purely axial,

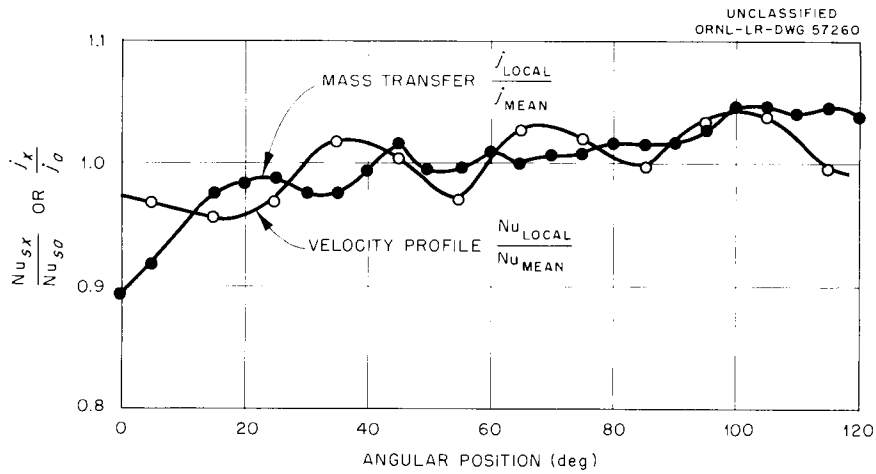

Fig. 2.7. Comparison of the Variation of the Local Heat Transfer Performance with the Local Mass Transfer Removal Rate for Tube 7 from 0 to 120 deg.

Table 2.1. Calculated and Experimental j Values for Tubes 1, 2, 3, and 7 with an L/d_e of 3.9 and 0-deg Orientation

Tube No.	Angular Position (deg)	j_M (Experimental)	j_V (Calculated)	j_M/j_V
		$\times 10^{-3}$	$\times 10^{-3}$	
1	0-180	4.42	3.83	1.15
2	0-180	4.38	3.87	1.13
2	180-360	4.71	3.74	1.26
3	180-360	4.90	3.74	1.31
7	0-120	3.92	4.07	0.96
1 and 2	0-180, 180-360	4.56	3.79	1.20
2 and 3	0-180, 180-360	4.64	3.81	1.22

but instead it has comparatively strong circumferential components, particularly in the outer regions of the channel. The close agreement of the average values of the adjacent halves of tubes 1 and 2 and 2 and 3 indicate that the circumferential velocity has a comparatively regular pattern. The close proximity of the measuring station to the starting point of the tube coating, which may have resulted in a disturbance in the boundary layer, could be the reason for the apparently high absolute values of mass transfer. If the mass transfer entrance length were measured from the beginning of the coating and the L/d_e effect normalized to 3.9, the mass

transfer values would be reduced by approximately 15%. The agreement of the absolute values would then be approximately 5% for tubes 1, 2, and 3.

Gas Temperatures During Loss-of-Power Incident

Thermal Model (K. T. Jung, G. Samuels). The primary concern during a loss-of-power incident has been reduced to the question of the temperature of the gas leaving the reactor and its effect on the piping and the steam generators. In order to evaluate this problem a series of combined simulator runs and calculations was made to determine the gas exit temperature for several cases in which various design factors were treated as parameters. The factors varied were (1) the thermal conductivity of the UO_2, (2) the blower coastdown time, and (3) the afterheat generation rate. All runs were made for the case in which the loss-of-power occurred with the reactor at full power.

In order to set up the model for use with the simulator, a number of assumptions and design conditions were used for determining the steady-state temperatures. The major assumptions and conditions are listed below:

1. The gas and cladding temperatures and the heat generation rate are based on an average power channel.

2. The axial power generation variation corresponds to the case in which the central control rod is fully inserted and the remaining rods are operated as a bank at an insertion depth of 62 in. This case gives the maximum temperatures for the proposed program of operating the control rods.

3. Two values for the thermal conductivity of UO_2 were used to calculate the internal temperatures. One value was that of Hedge and Fieldhouse[4] corrected to 95% of the theoretical density and the other value was 80% of the first value.

4. The value of q/L (Btu/hr·ft of element) was computed for 232 loaded channels, 42 elements per channel, an effective length per channel of 26 5/8 in., and a total heat generation in the elements of 80 Mw.

---

[4]J. C. Hedge and I. B. Fieldhouse, Measurement of Thermal Conductivity of Uranium Oxide, Armour Research Foundation Report G022D3 (1956).

The results of applying these conditions to the reactor at full power are shown in Fig. 2.8. Since the simulator computes the temperatures during a transient by finite differences, the system must be divided into a number of sections and a mean or effective temperature assigned to each section. For the present study the channel was divided into three axial sections and the fuel elements into three cylindrical sections. The axial sections were taken so that the two bottom assemblies were the bottom section, the third assembly from the bottom was the middle section, and the

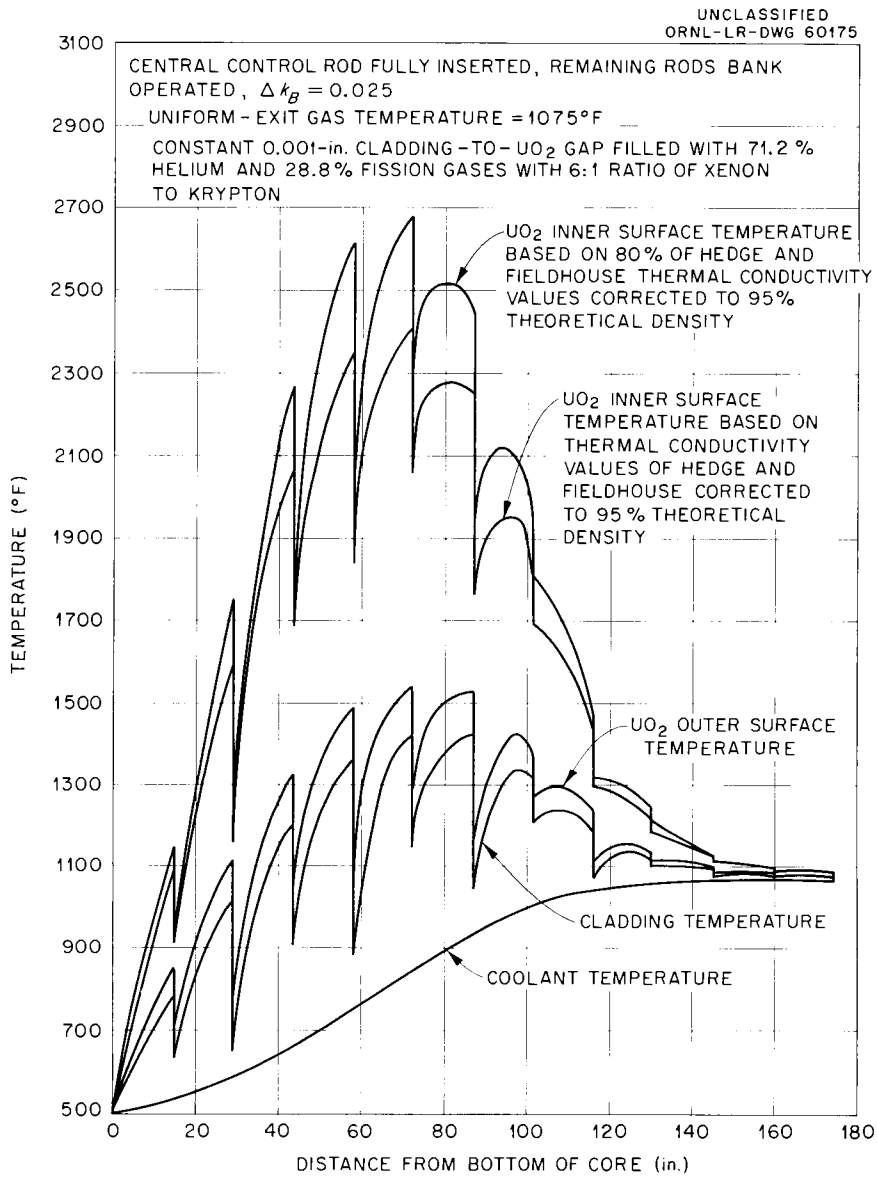

Fig. 2.8. Fuel, Coolant, and Cladding Axial Temperature Distribution for Average Power Channel.

three upper assemblies were the top section. The radial, or cylindrical, sections were subdivided so that the volumes of each of the three sections were the same. The mean inner and outer UO_2 temperatures were found by graphically integrating the curves of Fig. 2.8. Knowing the inner and outer UO_2 temperatures and the average heat generation rate, the mean temperatures of the radial sections were found by integrating the temperature over each of these sections. The mean temperatures of the sections are given in Table 2.2.

Table 2.2. Mean Temperatures in UO_2 Sections with Reactor at Full Power

Radial Section	Mean Temperature (°F)		
	Bottom Axial Section	Middle Axial Section	Top Axial Section
Inner[a]	1457	2191	1343
Inner[b]	1558	2408	1378
Middle[a]	1311	1950	1289
Middle[b]	1379	2096	1313
Outer[a]	1117	1628	1218
Outer[b]	1141	1680	1226

[a]Temperature calculations based on thermal conductivity values of Hedge and Fieldhouse corrected to 95% theoretical density.

[b]Temperature calculations based on 80% thermal conductivity values of Hedge and Fieldhouse corrected to 95% theoretical density.

The graphite sleeves were included in the simulator model. The sleeves were divided into the same three axial sections as the fuel, but only two radial, or cylindrical, sections were used. The radial sections were chosen so that one section included the inner 10% of the sleeve and the other section the outer 90% of the sleeve. The moderator structure was not included in the simulator model, and the thermal radiation between the fuel elements and sleeves was neglected. The effects of the thermal radiation and the moderator structure were included in the hand calculations for the long periods of time at which they become the controlling

factors. For the short time period in which simulator results are considered to be accurate, the omission of the thermal radiation and moderator structure effects has little bearing on the results.

The afterheat generation rate used for this study is shown graphically in Fig. 2.9. In applying these data to the reactor after shutdown, the energy deposition factors for the core components were taken as follows:

Fuel and cladding	0.82
Sleeve	0.06
Moderator	0.12
	1.00

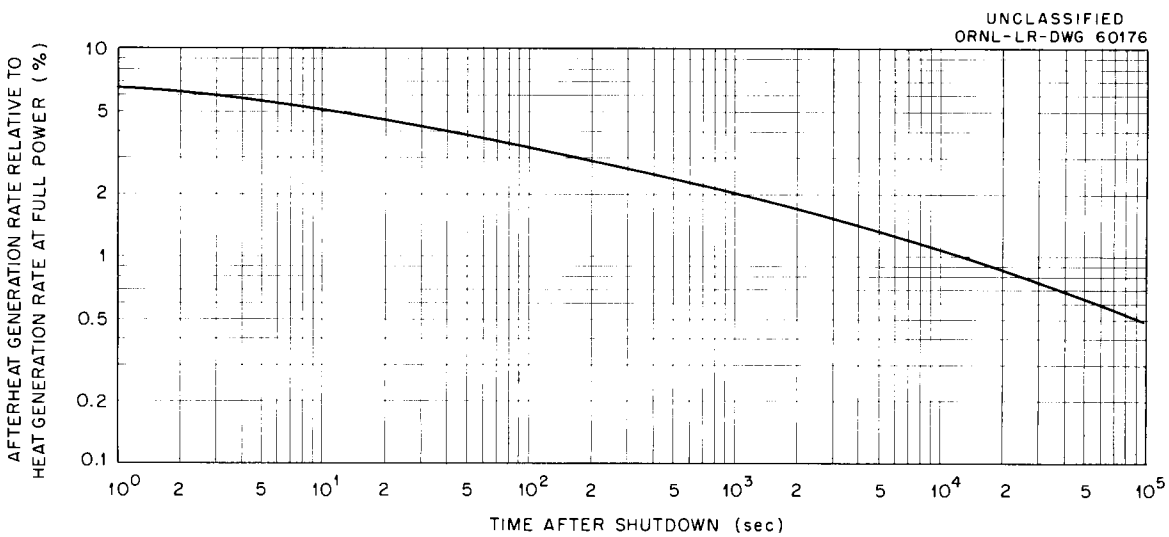

Fig. 2.9. EGCR Afterheat Generation Rate as a Function of Time After Shutdown.

Maximum Gas Temperatures (K. T. Jung and G. Samuels). In calculating the maximum gas temperature expected from the reactor, the results of the analogue computer calculations (see next section, this chapter) were considered valid for short periods of time, as mentioned above, the time period being either 5 or 7.5 min, depending on the blower coastdown rate. The results of the computer calculations for the 5- or 7.5-min period were then used as the starting point for analytical computations to determine outside limits for the gas exit temperature. The methods used in the

analytical calculations were identical to those described previously,[5] except that the moderator structure was included.

Although the simulator runs were made for only one position of the control rods, the analytical calculations were carried out for two conditions. The case for the control rods inserted 62 in. into the core was used in the simulator runs because this operating condition results in the highest fuel element temperature and also results in the largest amount of stored thermal energy in the fuel elements, sleeves, and moderator. The second case considered in the computations was for the control rods withdrawn from the core (0-in. position). This condition results in the afterheat rate being a maximum near the position where the moderator structure has the highest temperature. As shown below, this condition leads to calculated gas exit temperatures slightly higher than for the case with the control rods inserted 62 in.

The analytical work was also done for gas inlet temperatures to the reactor of 400, 450, and 490°F. Data obtained recently by Allis-Chalmers from simulator studies of the steam generator indicate that the gas inlet temperature to the core will be about 400°F for the time periods of interest. The gas temperature rise through the core was computed from the equation

$$\Delta t = 540 \times \frac{\%\ \text{afterheat}}{\%\ \text{flow}} \times 0.82 \quad .$$

The 540 factor comes from the initial operating conditions in which the temperature rise from the bottom plenum to the top plenum is 540°F for 100% flow and 100% power. The 0.82 factor results from the fact that only the fuel elements are at a high enough temperature to be a heat source for the gas and only 82% of the afterheat is generated in the elements. The gas flow for the various temperature conditions after shutdown was taken from Allis-Chalmers study IV-311.

In determining the temperature of the various components it was assumed that the heat was transferred from the fuel elements to the sleeve by radiation only and from the sleeve to the moderator by both radiation

[5]GCR Quar. Prog. Rep. Dec. 31, 1960, ORNL-3049, pp. 107–12.

and conduction. The results of these calculations are presented for two cases. The conditions which are identified as case A correspond to the afterheat generation rate shown in Fig. 2.9, the Hedge and Fieldhouse thermal conductivity values for UO_2, reactor scram on a flow decrease of 10%, and a blower coastdown rate that corresponds to the fastest that will meet specification. Case E_2 is identical with case A, except that the blower coastdown rate is much slower and corresponds to a value which can be obtained by adding inertia to the blower. The values used for case A are considered to be conservative.

The results of analyses for cases A and E_2 for both the 0- and 62-in. rod insertion cases are presented in Fig. 2.10. Each of the four

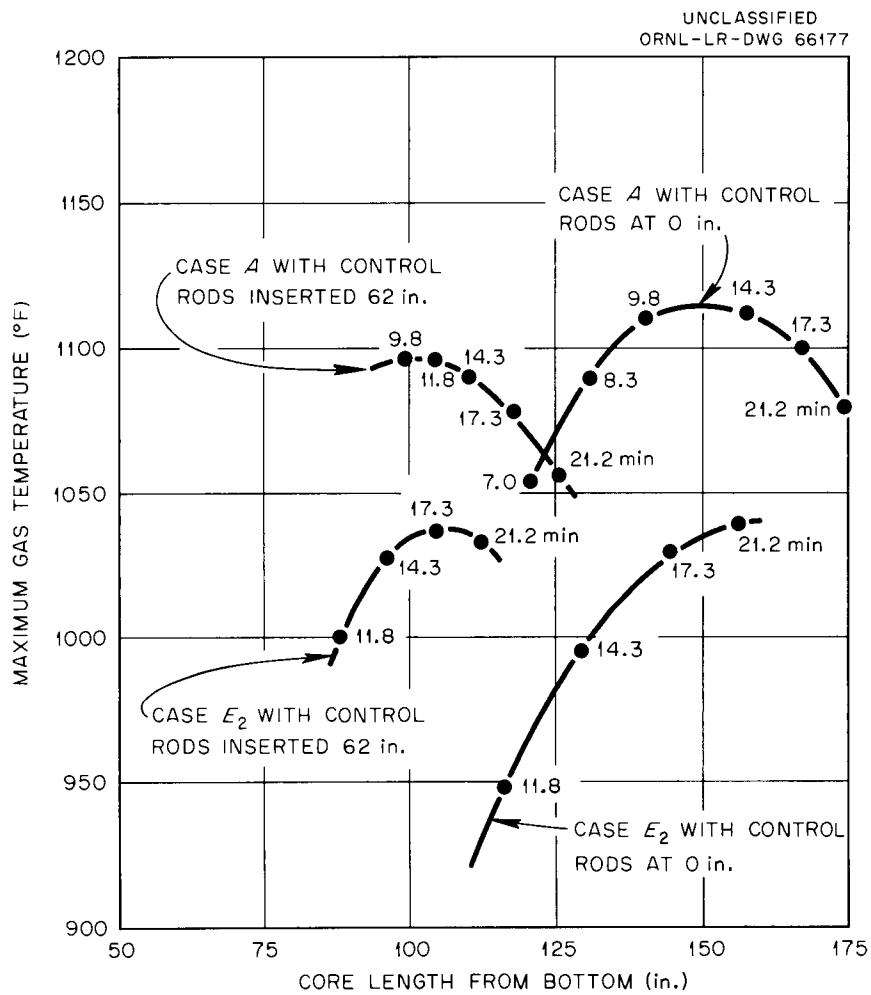

Fig. 2.10. Maximum Gas Temperature Versus Time and Position Along Channel.

curves gives the upper limit that the gas temperature may reach at the axial position shown. The numbers shown with each point represent the time after loss of power at which this temperature limit may be reached. Case E_2 with the longer blower coastdown time reduces the maximum gas temperature by 60 to 70°F, while the 0-in. rod position increases the maximum gas temperature and shifts the peak toward the top of the core. A rough check on the sensitivity of the maximum gas temperature to the natural convection flow indicates that a 10% reduction in the flow rate will cause an increase of about 20°F in the maximum gas temperature.

Simulator Calculations (S. J. Ball, R. M. Pierce, C. S. Walker). The results of the analog computer calculations of the reactor gas outlet temperature for several situations are shown in Fig. 2.11. These curves provide a graphic comparison of the effect of the results of changes in the scram signal, the afterheat generation rate, the gas inlet temperature, and the blower coastdown rate. Curve A presents the normal conditions obtained using a blower coastdown rate that is the quickest allowed by the

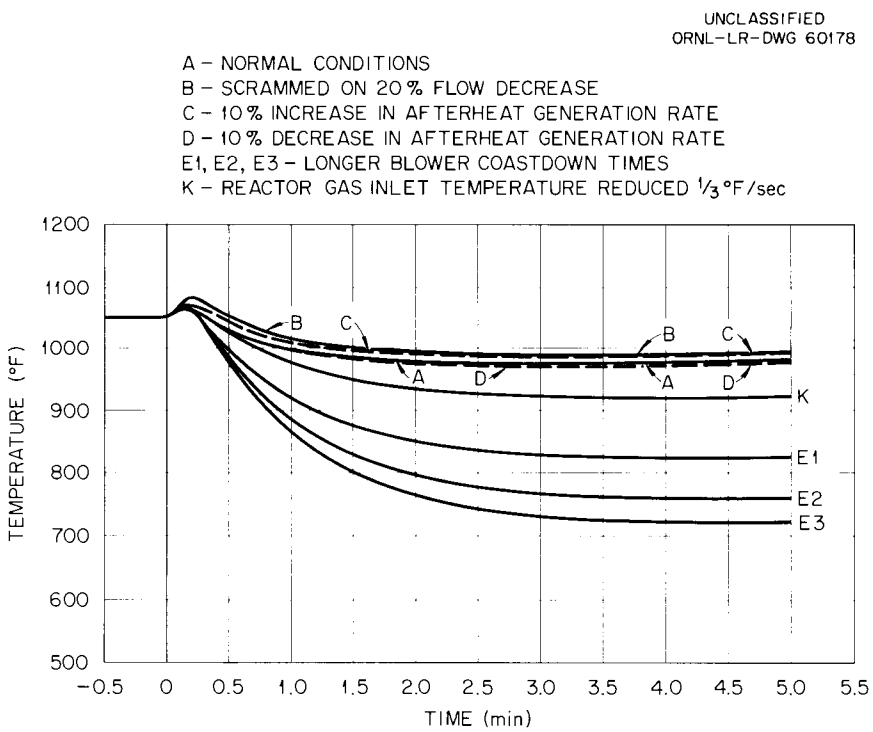

Fig. 2.11. Reactor Gas Outlet Temperature Following Loss of Power Under Various Conditions.

blower specifications, the afterheat generation rate given in Fig. 2.9, initial temperatures as given by the lower values in Table 2.2, a reactor scram initiated by a 10% reduction in gas flow, and a constant reactor gas inlet temperature of 510°F. The difference of 10 to 20°F between curves A and B arises from the additional heat generated during the time interval required for the gas flow to decrease by 20% rather than by 10%. Curves C and D illustrate that a 10% increase or a 10% decrease in the afterheat generation rate will produce approximately 10°F or less change in the gas temperature. A continuous reduction in the reactor gas inlet temperature of 0.333°F/sec will produce a decrease in the reactor gas outlet temperature of 60°F at the end of 5 min, as shown by curve K. The effects of longer blower coastdown times are shown by curves E_1, E_2, and E_3. The blower coastdown curves which were simulated were all of the form

$$W_g = A_1 e^{-t/\tau_1} + A_2 e^{-t/\tau_2} + B \quad ,$$

where W_g is the gas flow in per cent, t is time in seconds, and A_1, A_2, B, τ_1, and τ_2 are constants. The constants for the four coastdown curves are listed in Table 2.3. The constant B was used to simulate the effect of natural circulation by providing for gas flow that does not asymptotically approach zero with increasing time.

The detailed behavior of the temperatures in the EGCR for the loss-of-power accident under normal conditions is shown in Fig. 2.12. The symbols used on the curves of Fig. 2.12 are identified in the fuel element thermal model shown in Fig. 2.13.

Table 2.3. Constants Used for Blower Coastdown Curves

Case	A_1 (%)	A_2 (%)	B (%)	τ_1 (sec)	τ_2 (sec)	Time to Reach 20% Flow (sec)
A	58.8	40.1	1.1	52.0	11.1	60
E_1	58.8	40.1	1.1	78.0	16.7	90
E_2	58.8	40.1	1.1	104.0	22.2	120
E_3	58.8	40.1	1.1	130.0	27.8	150

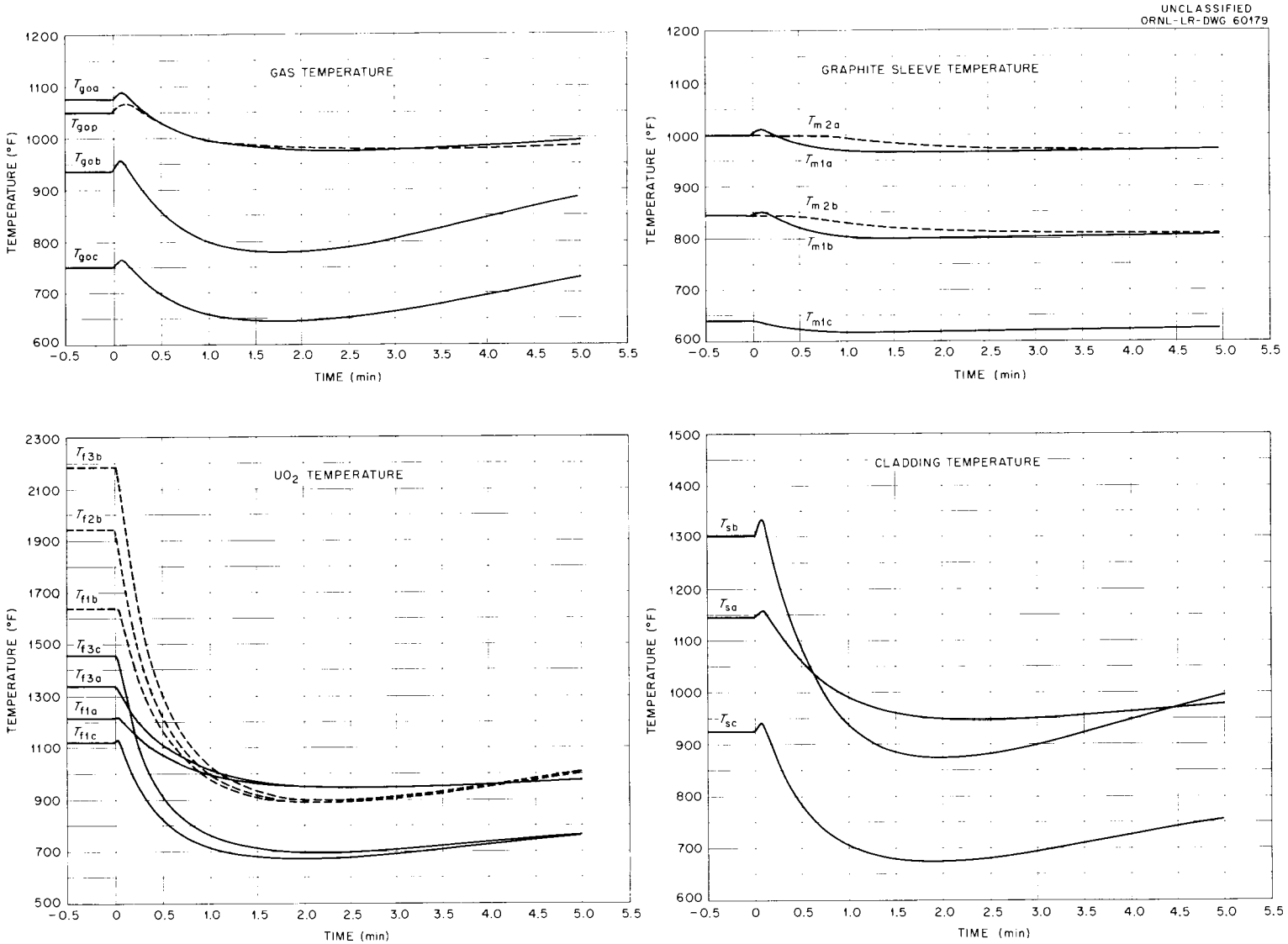

Fig. 2.12. Temperature in EGCR for the Loss-of-Power Accident Under Normal Conditions.

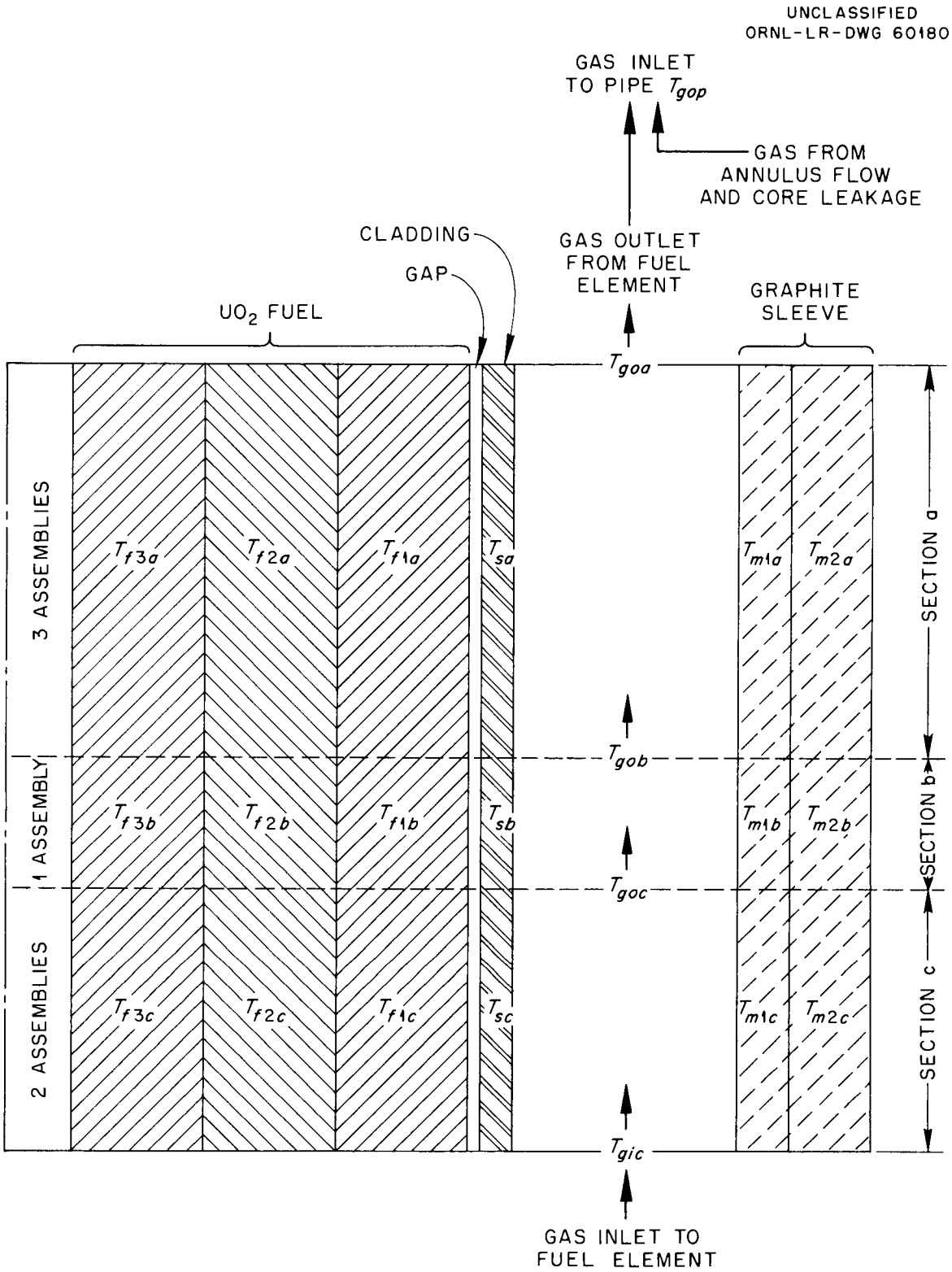

Fig. 2.13. Fuel Element Thermal Model.

Seven significant temperatures for different blower coastdown rates are listed in Table 2.4. The increase in time for the gas flow to decrease to 20% reduces the reactor temperatures considerably between case A and case E_1, with another appreciable reduction between cases E_1 and E_2. Although the reduction in temperatures was apparent between cases E_2 and E_3, the gain in temperature reduction had become markedly smaller.

Table 2.4. Gas Outlet, Fuel Element Cladding, and Graphite Sleeve Temperatures After 5 min for Blower Coastdown Case A and After 7.5 min for Blower Coastdown Cases E_1, E_2, and E_3

Blower Coastdown Case	Temperature (°F)[a]						
	T_{gop}	T_{sa}	T_{sb}	T_{sc}	T_{mla}	T_{mlb}	T_{mlc}
A	980	975	990	757	970	805	620
E_1	835	872	968	754	795	760	607
E_2	772	791	866	700	735	720	593
E_3	738	739	795	660	697	693	582

[a]See Fig. 2.13 for position for which the temperature is given.

EGCR Control Rod Modifications

J. W. Michel G. Samuels

The EGCR mockup control rod was assembled and coolant flow and pressure-drop tests were performed. The pressure-drop measurements confirmed the calculated values; however, the joint leakage was less than expected. The rod weight of 137 3/4 lb agreed with the computed value of 138 lb.

One questionable feature of the design was apparent in that the rod segments would not stay centered on the central support rod. The control rod has been modified by reducing the clearance between the central rod and the internal spacers and by inserting one additional spacer just above each joint. This modification allows the segments to be aligned while maintaining sufficient rod flexibility and has therefore been incorporated in the final control rod design.

Evaluation of EGCR Control Rod Drives

J. Foster

The EGCR control rod drive mechanism consists basically of an electric-motor-driven cable drum arranged to rotate about a horizontal axis. In order to conserve space within the control rod shield plug, the motor is located within the cable drum, which it drives through an epicyclic gear train designed for a 4096:1 reduction ratio. Additional gearing further reduces the drive speed at the cable drum. An electrically actuated magnetic clutch serves to disengage the cable drum from the gear train and the motor to permit the rod to scram under the action of gravity. There are, however, additional gear trains coupled to the cable drum that do not disengage upon scramming and which must, therefore, be accelerated as the rod makes its gravity descent. The energy required to accelerate each of these permanently engaged gear-driven systems as a rod scram occurs is extracted from the falling control rod, and the result of this energy conversion is a tension load in the control rod cable which acts to restrain the rod as it falls. The magnitude of the restraining force is a function of the number of rotating parts to be accelerated, the inertia of each, the angular acceleration of each (which is a function of the gear ratios), the system friction, and certain electromagnetic loads imposed upon rotating parts.

Calculations were made to determine the acceleration capability of the proposed system by identifying the four rotating components of the scram system that represent the major inertial restraint upon the falling control rod and then determining control rod acceleration assuming no friction and no electromagnetic restraining forces. These calculations were "optimistic" for the reasons stated above. The four rotating components taken into account were the cable drum, the 7-in. internal gear, the alternator, and the magnetic brake. Because each of these parts is not fully detailed and dimensioned on the drawings, some scaled or assumed dimensions were used and noted in the calculations. The calculated acceleration of the control rod during a scram was found to be 19.1 ft/sec^2. This value appears to be acceptable in terms of the presently stated

requirement that the scram acceleration be not less than approximately 10 ft/sec^2.

The four rotating components included in the calculation were selected because they represent the major contributors of inertial resistance to control rod acceleration; the inclusion of all the smaller gears should not appreciably affect the calculations. There is considerable uncertainty, however, in the inertias calculated for the alternator and brake, for which dimensions of rotating parts were assumed. It remains for the vendor to fabricate and test a drive unit as described in the specifications.

Structural Investigations

B. L. Greenstreet

Temperature Distribution in EGCR Graphite Columns (S. E. Moore)

The largest temperature differentials in an EGCR graphite column are expected to exist during fuel-handling operations. In order to compare the temperature distribution during design power operation with that during fuel-handling operations, calculations were made using the GHT IBM code[6,7] and the heat dissipation data described earlier.[8] The isotherms for a cross section at the top of a column just prior to refueling when 90 lb/hr of coolant at 1050°F is flowing through the annuli between the fuel element sleeves and the channel walls in all four channels are shown in Fig. 2.14, and in Fig. 2.15 are shown the isotherms for the same cross section at a time approximately 30 min after the gas seal at the bottom dummy is broken and the gas flow rate in the annulus of the one channel in which fuel-handling operations are being carried out has increased to 1400 lb/hr at 648°F. For these calculations the outer surface of the column was assumed to be insulated and the thermal conductivity of the graphite was taken as

---

[6]T. B. Fowler and E. R. Volk, Generalized Heat Conduction Code for the IBM-704 Computer, ORNL-2734, October 16, 1959.

[7]T. B. Fowler, Generalized Heat Conduction Code for the IBM-7090 Computer, ORNL CF-61-2-33, February 9, 1961.

[8]GCR Quar. Prog. Rep. March 31, 1961, ORNL-3102, pp. 50–51.

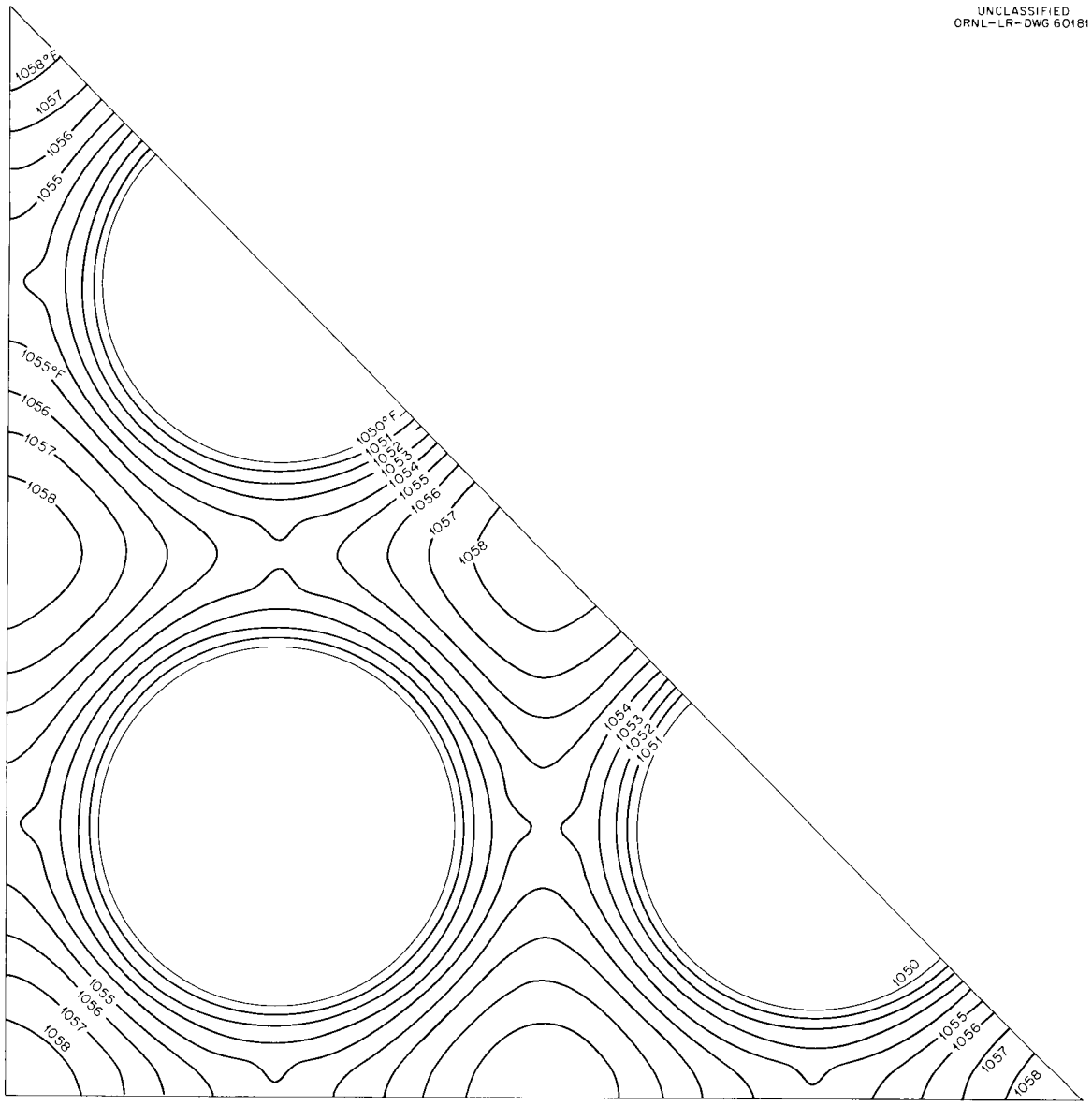

Fig. 2.14. Temperature Distribution at Top of Graphite Column During Design Power Operation.

15 Btu/hr·ft^2 (°F/ft). In both cases the temperatures are symmetrical about the diagonal.

It may be seen from Fig. 2.14 that the maximum temperature differential in the block during design power operation is about 8°F. During fuel-handling operations this difference increases to about 400°F under the conditions assumed, with the steepest gradients occurring between the surface of the channel being refueled and the surfaces of the immediately

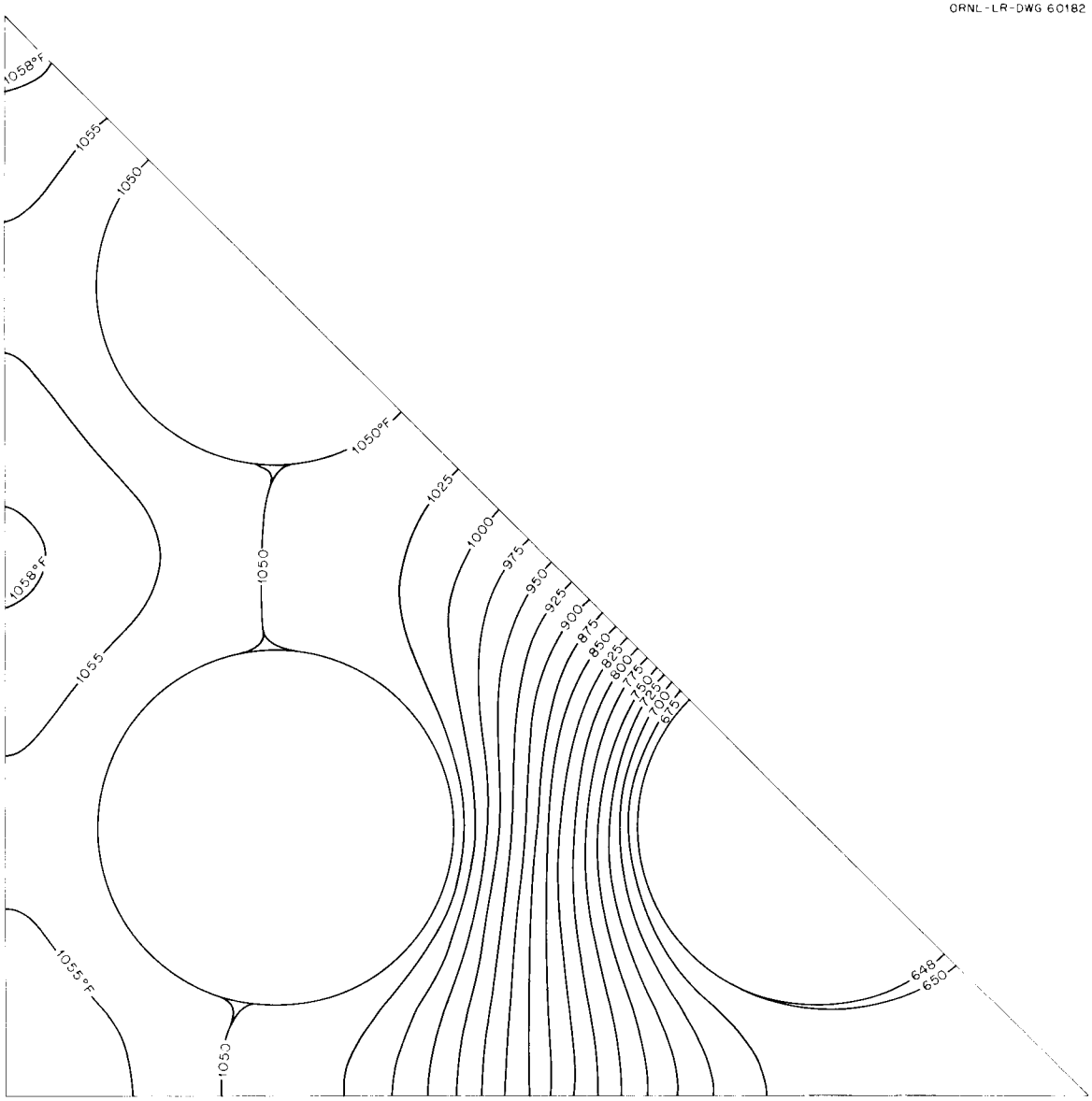

Fig. 2.15. Temperature Distribution at Top of EGCR Graphite Column During Fuel Handling Operations.

adjacent channels. The stresses associated with the temperature distribution of Fig. 2.15 will be calculated using the Battelle 7090 machine code.[9]

The temperature distribution in the reactor will differ from that shown because of the simplified boundary condition used in the calculations

[9]Robert F. Redmond, Lewis E. Hulbert, and Richard W. Clark, Numerical Solution of Reactor Stress Problems, BMI-1503, February 28, 1961.

(i.e., an insulated outer boundary on the column) and because the gas temperature used was the lowest that could exist under the conditions described. However, the stresses calculated from these temperature data will provide upper bounds for assessing the severity of conditions associated with fuel-handling operations.

Structural Integrity of EGCR Through-Tubes (R. L. Maxwell, J. M. Corum)

The experimental tube collapse investigation being conducted to provide both instantaneous and time-dependent collapse data applicable to the experimental through-tubes in the EGCR includes tests being performed by the University of Tennessee on 4-in.-o.d., 0.12-in.-wall tubes, as previously reported.[10,11] The fifth in the series of 4.0-in.-o.d. tubes was subjected to an external pressure loading of 425 psi at 1200°F, and it collapsed after 260 hr. The specimen was type 304 stainless steel tubing purchased in accordance with ASTM A312-58T specifications and was approximately 5 ft long. The average measured mean radius-to-thickness ratio was 15.32 and the ovality ratio was 0.969. The tube collapsed in the region of minimum wall thickness, which was near one end of the tube. After the initial collapse at 260 hr, the test was continued to 680 hr. At the end of this time, the collapsed section of the tube was found to extend axially along the specimen for a distance of approximately 1 ft.

The sixth in the series of 4-in.-o.d. tubes is of the same material and has the same nominal dimensions as the fifth tube. The sixth tube has been under test at the same conditions as the fifth tube for 450 hr with no indication of collapse. The tube has an average measured mean radius-to-thickness ratio of 15.32 with an ovality ratio of 0.9975.

Photoelastic Analysis of Model of EGCR Pressure Vessel (R. L. Maxwell)

The structural behavior of the top head of the EGCR pressure vessel was examined through the strain-gage analysis of a 1 to 5.533-scale

---

[10]GCR Quar. Prog. Rep. Dec. 31, 1960, ORNL-3049, pp. 144–54.

[11]GCR Quar. Prog. Rep. March 31, 1961, ORNL-3102, pp. 32–37.

aluminum model.[12,13] In order to gain more information on the stresses in the top head, a three-dimensional photoelastic analysis is also being carried out. This analysis should amplify the information gained from the strain-gage analysis previously made, serve as a check on that analysis, and give additional information as to the stress concentrations at the junctions between the nozzles and the hemispherical head. A photoelastic model of epoxy resin has been cast and machined to a scale of 1 to 14.2. The stresses have been frozen in under a pressure loading and a simultaneous axial load on one of the control rod nozzles located at the outer edge of the nozzle cluster. Figures 2.16 and 2.17 are photographs of the exterior and interior of the plastic model ready for the freezing of the stresses.

Calibration strips with stresses frozen in at the same time that the model was loaded have been observed through a polariscope, and good results are indicated. The model is now ready for slicing into sections so that the various stresses can be analyzed photoelastically.

Experimental Analyses of Perforated Plates (R. L. Maxwell, J. M. Corum)

Experimental investigations of the stresses and deflections in perforated plates are being made by the University of Tennessee. In each case, a flat, circular plate is clamped around the outer edge of the plate and subjected to a hydrostatic pressure loading. The hole pattern for a given specimen is specified and remains the same throughout the test program for the unit. Measurements are first made for the solid plate, and then the holes are drilled, with the hole size being increased after each test. The portion of the pressure loading corresponding to the area of the holes is carried by a thin plastic film stretched over the entire plate.

The results for a perforated plate which had an equilateral triangular hole pattern with a pitch of 1 1/4 in. were reported earlier.[14] The plate was 15 1/16 in. in diameter, 1/4 in. thick, and was made of aluminum. The

[12]GCR Quar. Prog. Rep. Sept. 30, 1960, ORNL-3015, pp. 35–42.

[13]GCR Quar. Prog. Rep. March 31, 1961, ORNL-3102, pp. 26–32.

[14]GCR Quar. Prog. Rep. June 30, 1959, ORNL-2767, pp. 28–30.

study of a second plate, which was identical to the first except for the hole pattern, will be completed when the stresses corresponding to one

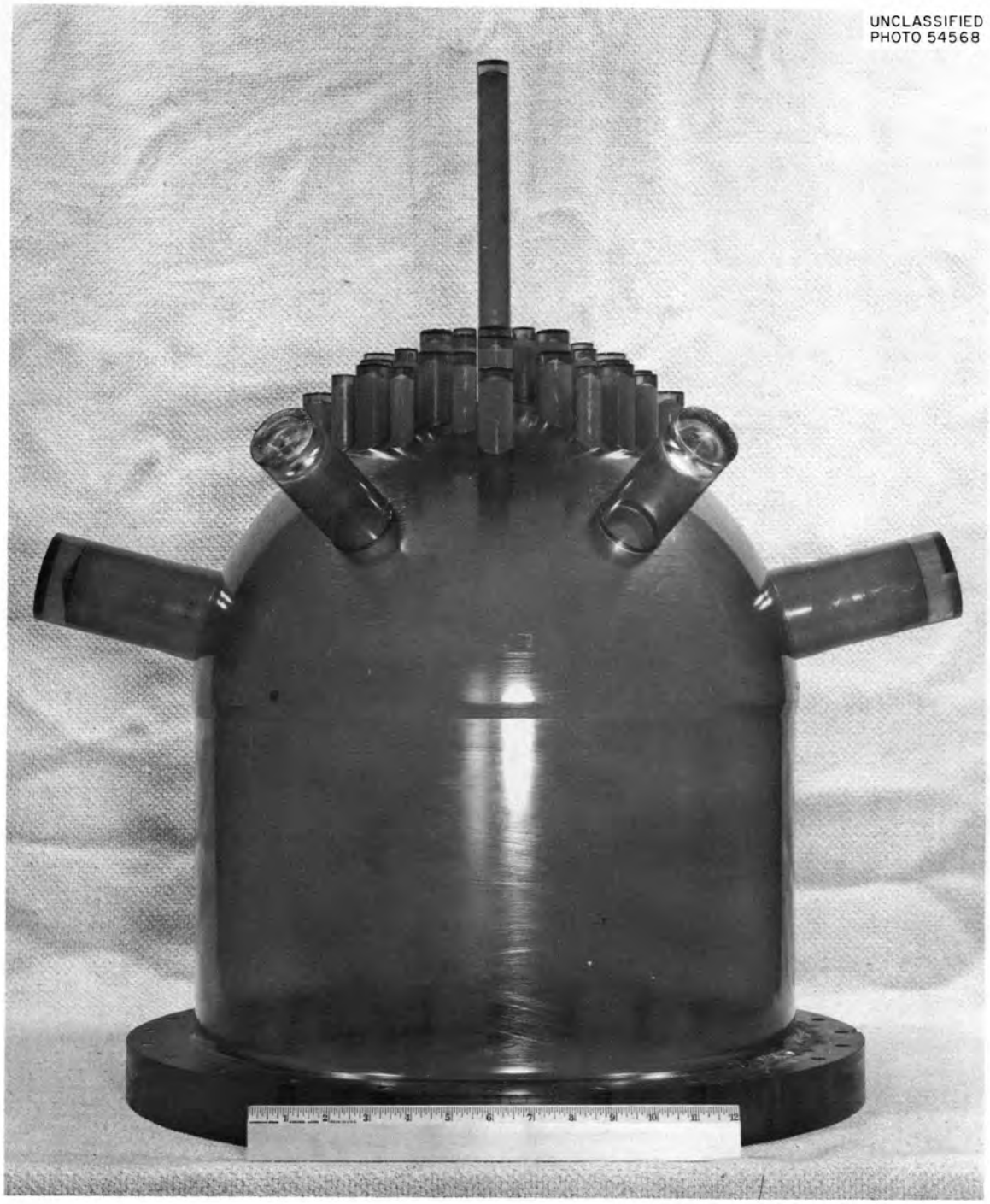

Fig. 2.16. Model of EGCR Pressure Vessel Head Prepared for Photoelastic Analysis of the Stresses.

remaining uniform hole size (1/2 in.) are determined. The study of the second plate is discussed here.

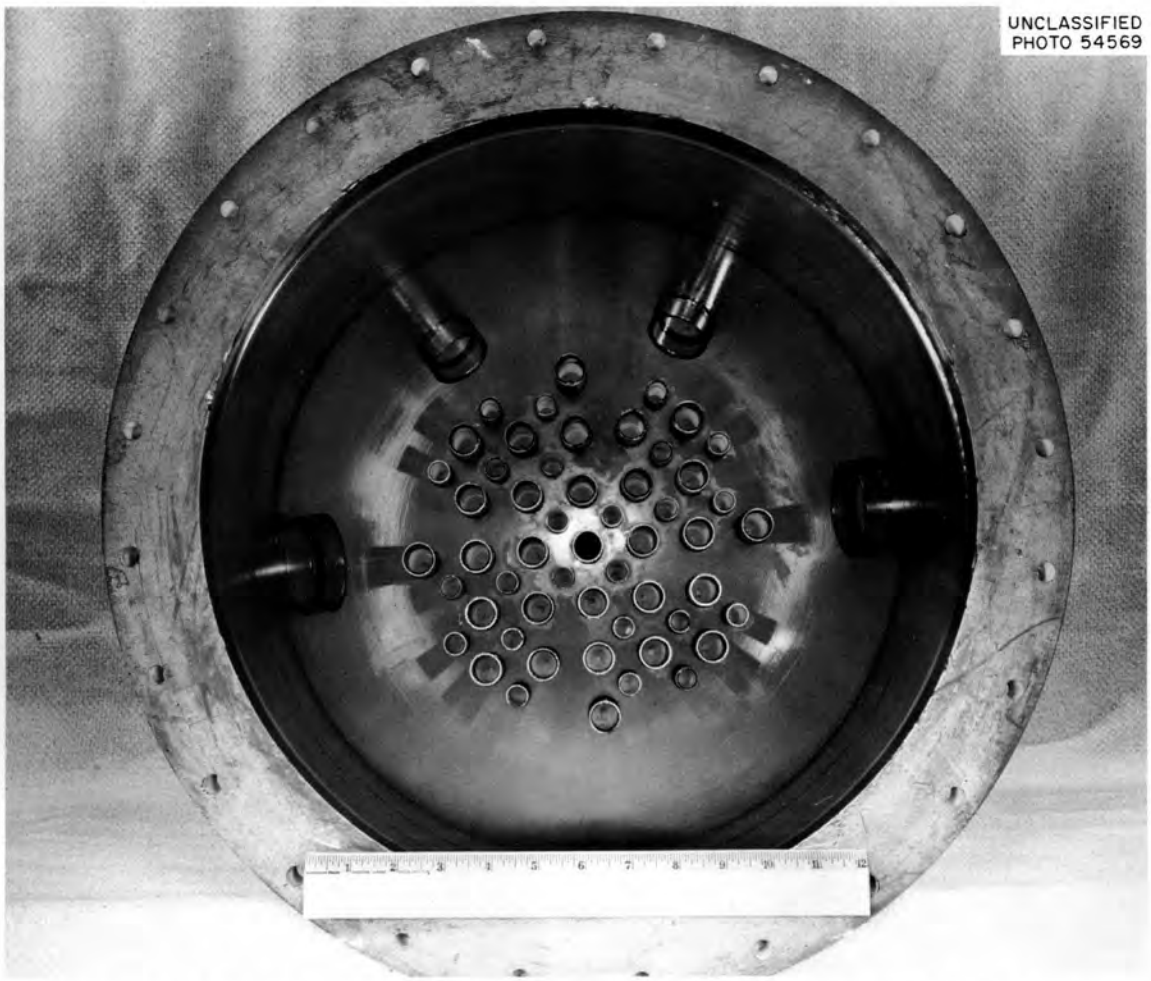

Fig. 2.17. Interior of Model of EGCR Pressure Vessel Head Prepared for Photoelastic Analysis of the Stresses.

There were two basic differences between the hole configurations used for the first and second plates. First, the equilateral triangular pitch was 5/8 in., rather than 1 1/4 in., in the second plate; second, only uniform hole sizes were used in investigating the behavior of the first plate, but tests of the second plate were made with two sizes of hole present concurrently. The diameters used in the constant, or uniform, hole-size tests of the second plate were 1/8, 1/4, 3/8, and 1/2 in., and the hole-size pairs were 1/8 and 1/4 in., 1/4 and 3/8 in., and 3/8 and 1/2 in., with the holes of a given diameter being on a 1 1/4-in. pitch. There were 475 holes. When a combination of hole sizes was used, 354 holes had the smaller diameter and 121 had the larger diameter.

The magnitudes of the stresses, as determined from strain-gage readings, are not discussed here. A discussion of the stress pattern for each configuration will be included in a forthcoming report covering the entire investigation, and comparisons will be made between the data from this study and those from the study made earlier.

A quadrant of the plate for the case in which the 1/4- and 3/8-in.-diam hole combination was used is shown in Fig. 2.18. The cracks that may be seen are in a brittle lacquer sprayed on the surface of the plate prior to loading. The cracks in the lacquer are normal to the maximum principal stress direction at all points and are present only in the more highly stressed areas. In all cases in which the strains were sufficient to crack the lacquer, the crack pattern indicates that the principal stress directions are always normal and tangential to the holes at the hole edges. This was true for all hole sizes, regardless of whether a single or two-hole-size pattern was used.

The measured deflections along a radius are shown in Fig. 2.19, with hole size as a parameter. The theoretical deflection curve for a solid plate with a fixed edge is also shown in Fig. 2.19. The small difference between the theoretical and experimental curves for the solid plate can be attributed to a lack of rigidity at the clamped edge.

The maximum deflection and area ratios were calculated using the solid plate as a basis, and the results are given in Figs. 2.20 and 2.21. An examination of Fig. 2.20 shows that the deflection ratio increases with

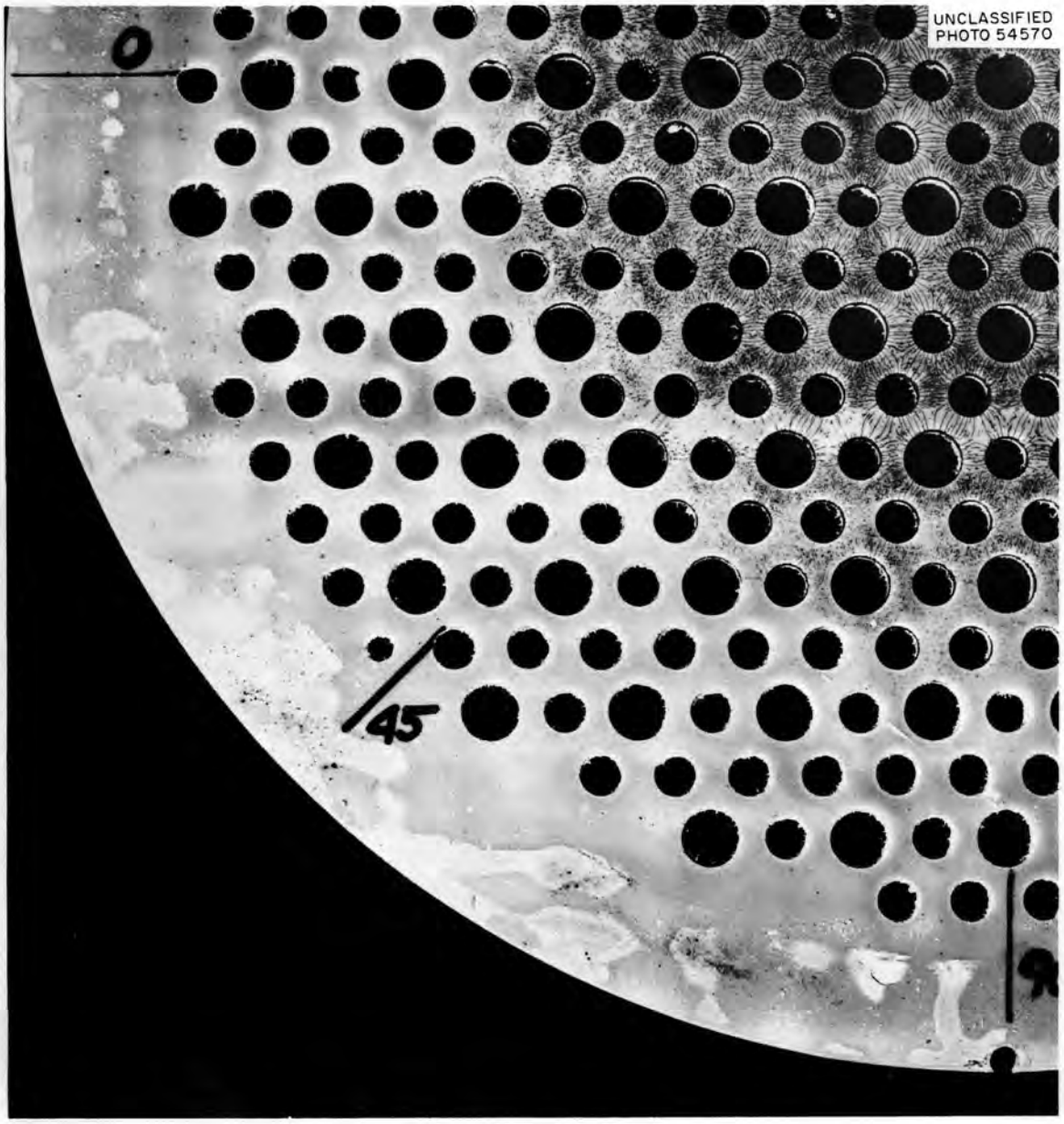

Fig. 2.18. Perforated Plate with 1/4- and 3/8-in.-diam Holes Showing Brittle Lacquer Crack Pattern.

hole size much more rapidly than the area ratio, as before. The curves in Fig. 2.21 were drawn so that comparisons can be made between the deflection characteristics for the plates with holes of uniform size and plates with combinations of hole sizes. The 1 1/4-in.-pitch curve represents data obtained from the first plate. The data presented in Fig. 2.21 appear to follow a straight line correlation in each case. Furthermore,

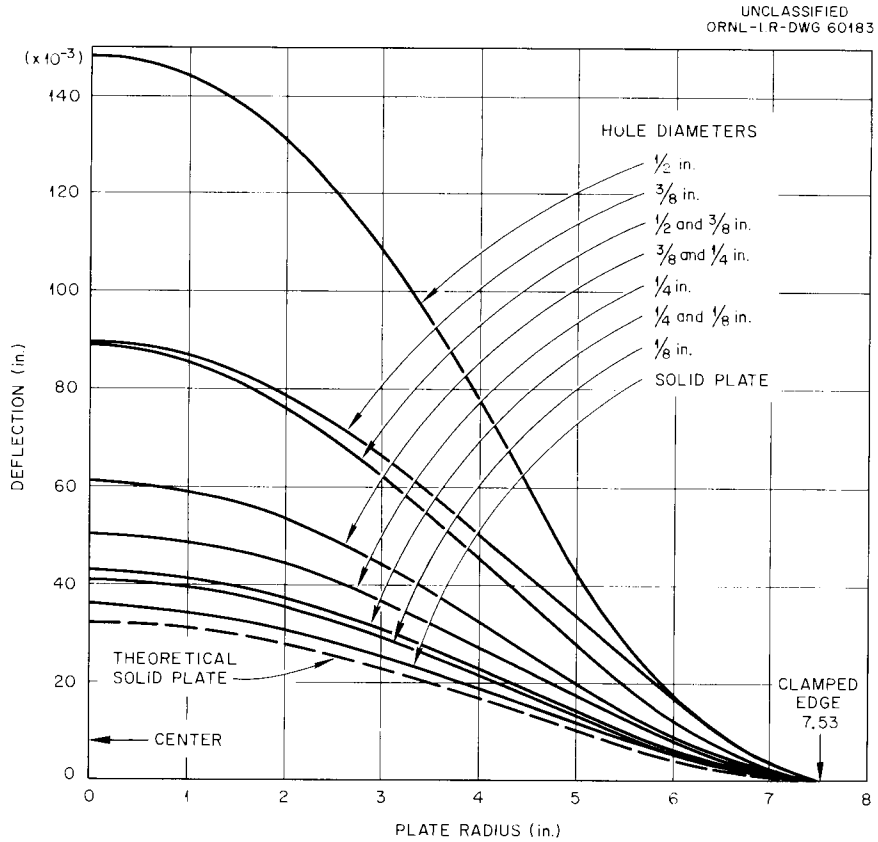

Fig. 2.19. Deflections of Clamped, Perforated, Circular, Aluminum Plates, 15 1/16 in. in Diameter and 1/4 in. Thick, Under a Test Pressure of 20 in. Hg.

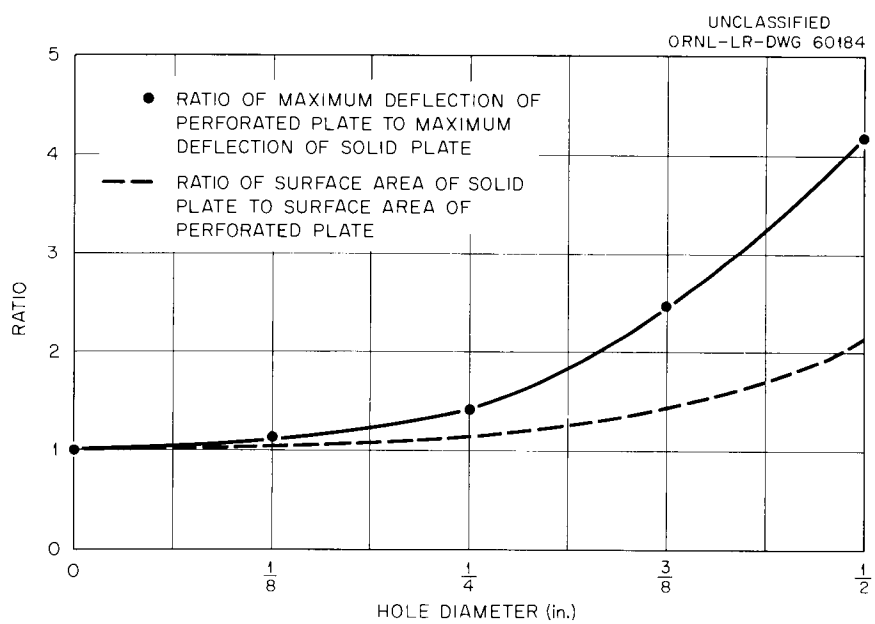

Fig. 2.20. Comparison of Deflection and Area Ratios of a Perforated Plate with Uniform Hole Size with Those of a Solid Plate Under the Same Total Load (A Maximum Test Pressure of 20 in. Hg).

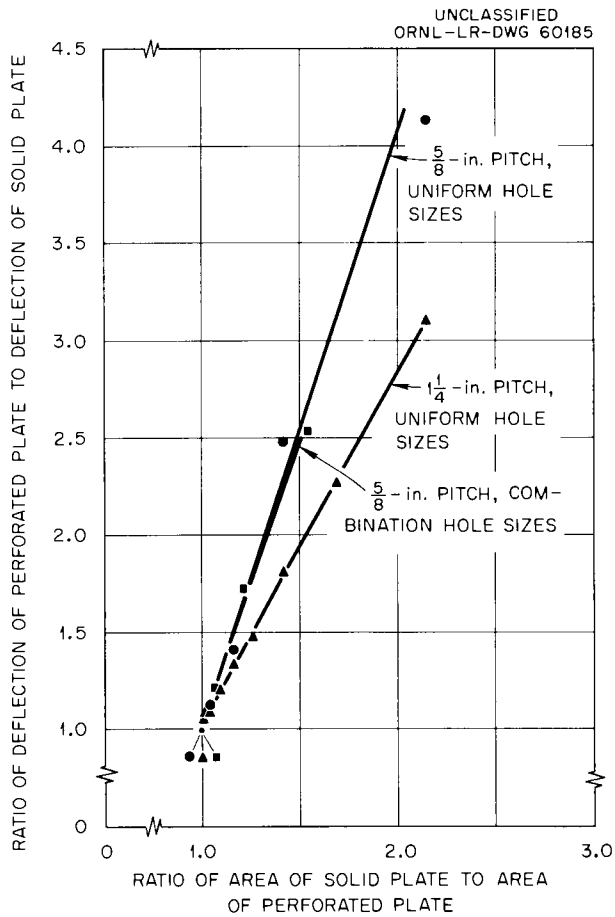

Fig. 2.21. Deflection Ratios Versus Area Ratios for the Two Plates Tested.

the slope appears to be a function of the hole pitch alone and not the particular hole-diameter combinations. This latter observation follows from the fact that all the points for the 5/8-in.-pitch plate fall within a single scatter band.

Containment System for the EGCR

H. N. Culver W. B. Cottrell

The analytical study of the expected performance of the EGCR containment system has been continued, and because of refinements in techniques and data, as well as changes in basic assumptions, the results differ

from those presented previously.[15] The particular factors responsible for the difference in the results[16] include an increase in the activity release per fuel assembly, an increase in the exposure dose per inhaled microcurie, and a decrease in the activity release based on consideration of the radial power distribution. The rate of release of fission products from the oxidized fuel was decreased on the basis of experimental measurements. The source term for activity being released during the second interval was increased to include the residual activity from the initial depressurization, and the correct formulation of the exposure dose as a function of distance from the point of continuous ground-level release was employed.

As in the previous report,[15] the exposure dose resulting from activity release in each of the following time intervals was examined separately: (1) the initial period of depressurization before the containment vessel is sealed, (2) the period after the initial depressurization but still before the containment vessel is sealed, (3) the period after the containment vessel is sealed. It is axiomatic that the contributions of different release mechanisms must be considered over the different release intervals. Accordingly this study was based on the known data on fission-product release from UO_2 and the performance of the EGCR reactor and containment systems. Additional information may be developed, however, that will change the results presented here, since every reasonable effort has been taken to assure that the results are conservative. The further refinements that may result in a reduction of the activity release and subsequent exposure doses are noted.

Case 1. The exposure doses from the activity released during the initial depressurization are shown in Fig. 2.22 for an assumed closure time of 15 sec for the containment penetration isolation valve. If the time to close this valve is significantly reduced, the activity released will also be reduced. On the other hand, if the magnitude of the failure in the primary system is appreciably less than that of a single-ended

[15]GCR Quar. Prog. Rep. March 31, 1961, ORNL-3102, pp. 54–63.

[16]H. N. Culver, EGCR Containment System Performance, ORNL CF-61-6-6, June 1, 1961.

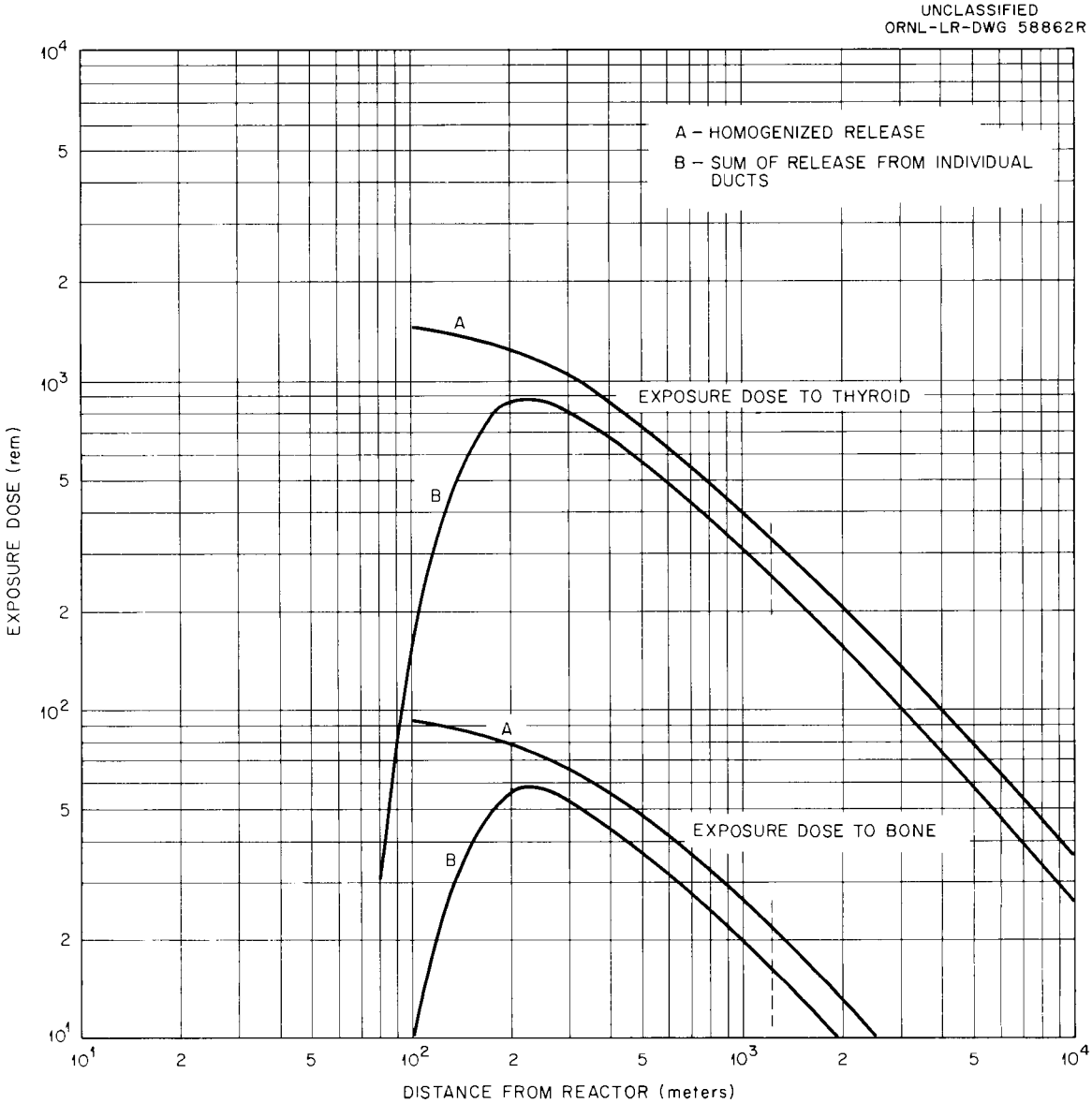

Fig. 2.22. Inhalation Exposure Dose from Activity Release During the Period of Depressurization of the Primary System. (Case 1).

failure, the time required to depressurize the primary system will increase. This increase in time to depressurize will significantly affect two important factors that influence the exposure doses. First, with relatively slow depressurization of the primary system, it will be possible to seal at least the inlet ventilation ducts in the containment vessel before significant activity release occurs. Second, if the magnitude of the primary system rupture is less than the large-size failure considered

here, the temperature of the fuel elements may be decreased before the system pressure is reduced to near atmospheric. This will result in a large reduction in the number of fuel element failures.

Case 2. The thyroid exposure doses from activity released following the initial depressurization of the primary system but at a time when activity from defective fuel elements is being discharged to the stack are shown in Fig. 2.23 for three different fuel element oxidation rates and as a function of the time required to seal the containment building. The exposure doses given are for the point of maximum exposure, which corresponds to a distance of 6.83 miles. Exposure doses at other distances may be obtained by using correction factors for the height of release, as given in Fig. 2.24. The values shown are based on the assumption that 99% of the iodine and the particulate matter is removed by the filter and the iodine-removal unit. The exposure dose at a given location for any other efficiency of activity removal may be obtained by multiplying the

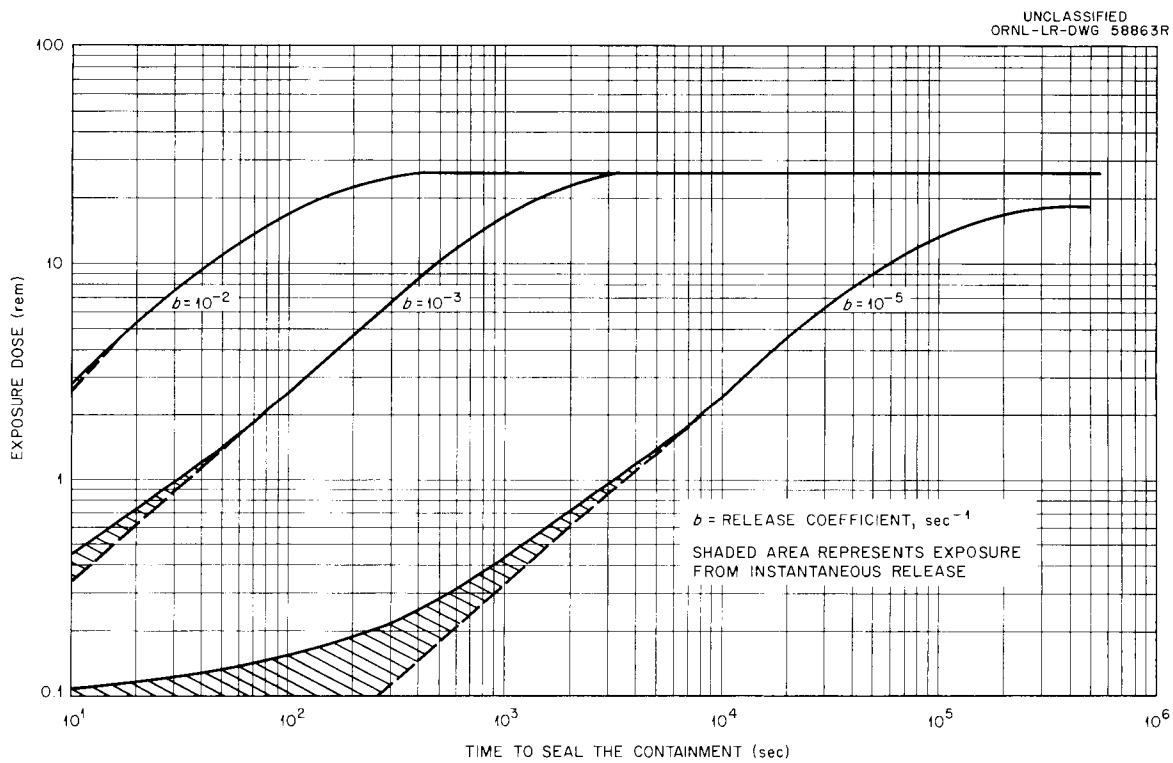

Fig. 2.23. Inhalation Exposure Dose to the Thyroid at 11 000 Meters for Activity Release Following Depressurization of the Primary System but Prior to Sealing of Containment Building.

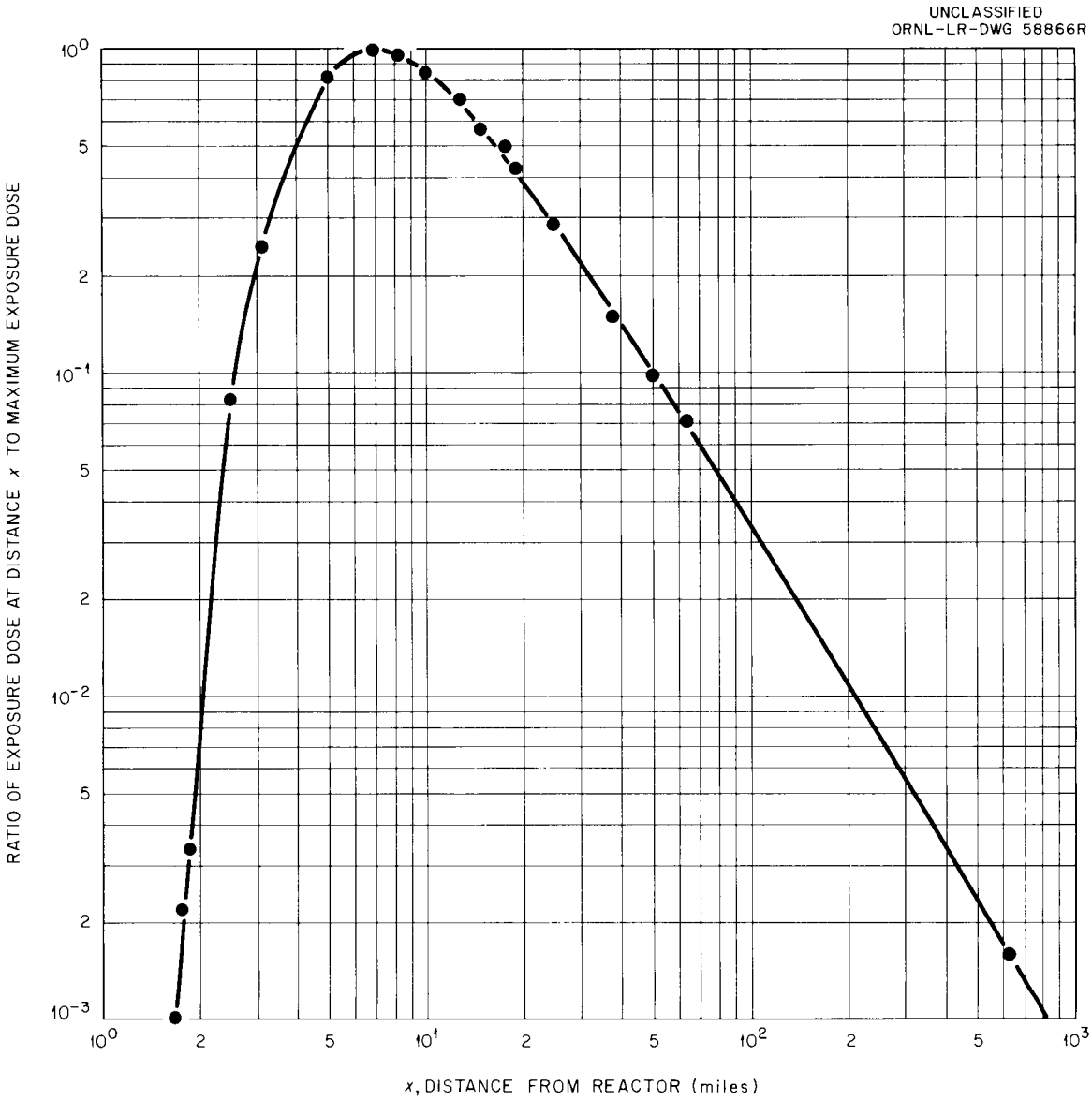

Fig. 2.24. Fraction of Maximum Exposure Dose as a Function of Distance Downwind from the Reactor.

values of Fig. 2.23 by the ratio of the removal efficiency. The data of Fig. 2.23 indicate the importance of the release coefficient. A value of the release coefficient of $\sim 10^{-2}$ sec^{-1} corresponds to 100% release in approximately 9 min and therefore would correspond to near-instantaneous release. It may be seen that for values of the release coefficient up to about 10^{-5} sec^{-1}, the maximum exposure dose will vary with the time required to oxidize the fuel completely. In the case of a release coefficient of 10^{-5} or less, the maximum exposure dose to the thyroid decreases,

since the release of fission products from the fuel is so slow that radioactive decay in the fuel reduces the amount of activity released from the building. In Fig. 2.23 it may be seen that only when the release coefficient is small will the instantaneous release of activity influence the results appreciably, and then only for short periods.

Case 3. The exposure doses following the sealing of the containment vessel are shown in Fig. 2.25 for 1- and 2-hr exposure times, t, and for $t = \infty$. The exposure values shown are for 4000 ft, and it was assumed that

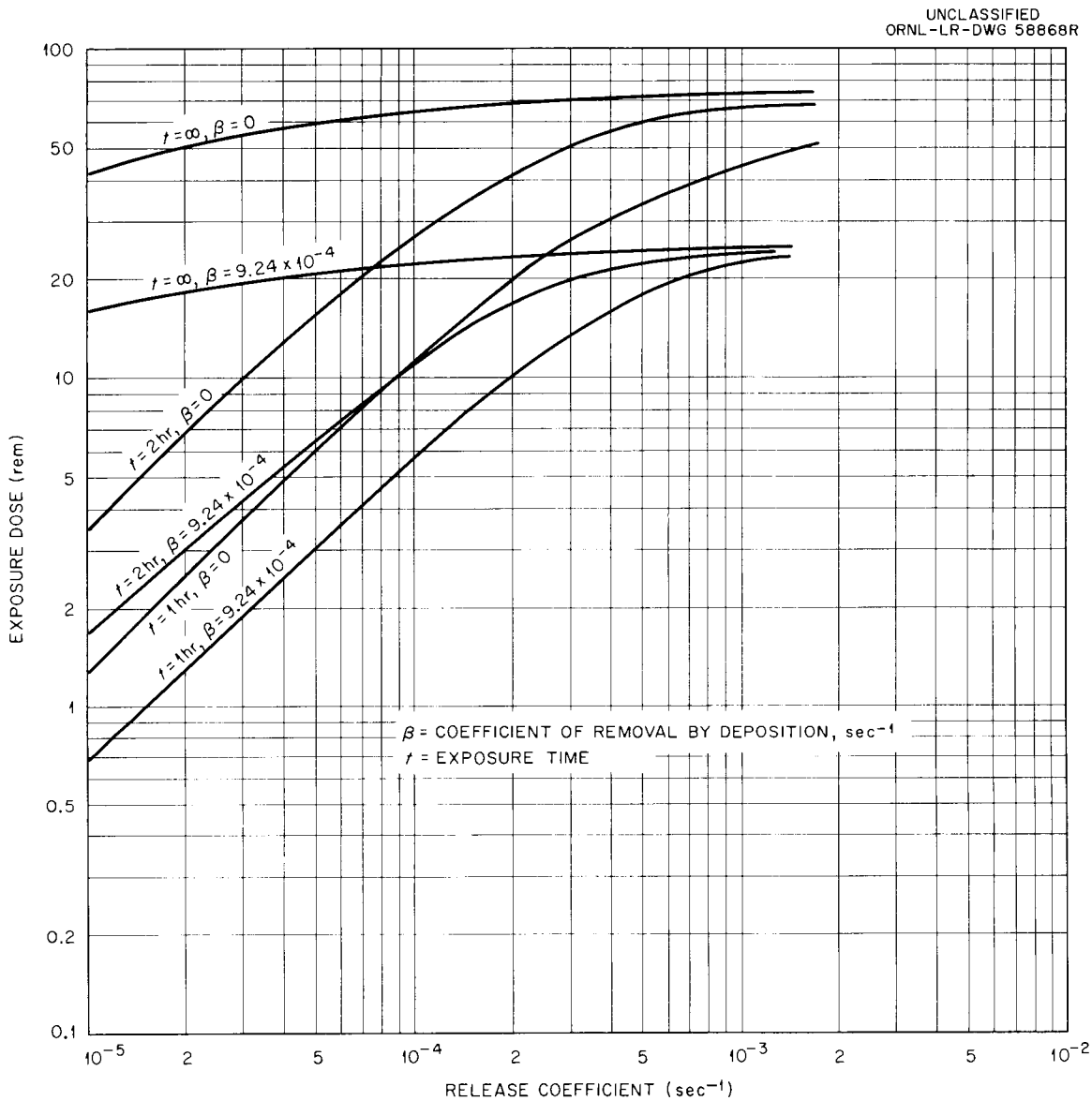

Fig. 2.25. Exposure Dose to the Thyroid at 4000 ft from Activity Released Following the Sealing of the Containment Building.

there was dilution of the activity adjacent to the containment building as a result of the turbulence of the air. Exposure doses at other distances, with and without the mixing at the containment building, are shown in Fig. 2.26. The importance of deposition within the containment vessel, as illustrated in Fig. 2.25, is quite pronounced.

The effect of varying the removal coefficient by recycle filtration is illustrated in Fig. 2.27. For these cases it was assumed that there was no deposition and that the efficiency for removal by recycle filtration

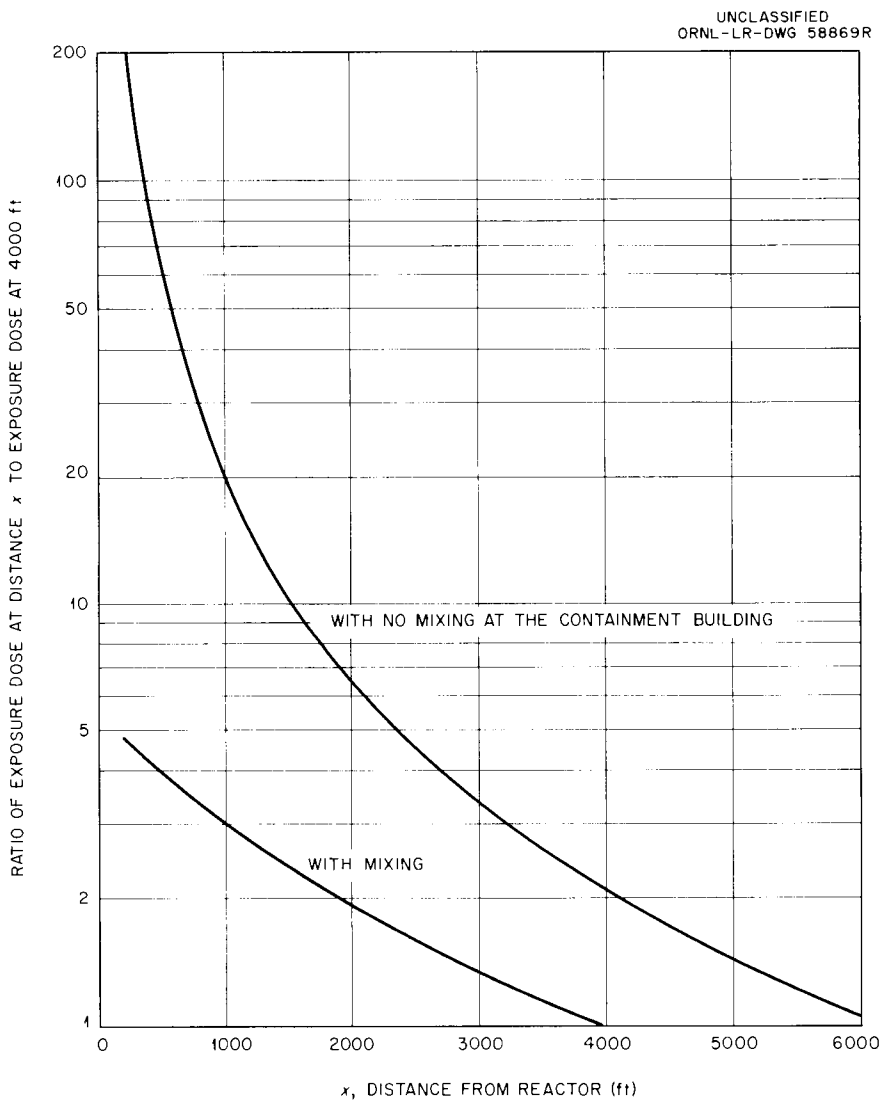

Fig. 2.26. Ratio of Exposure Dose at Various Distances to the Exposure Dose at 4000 ft.

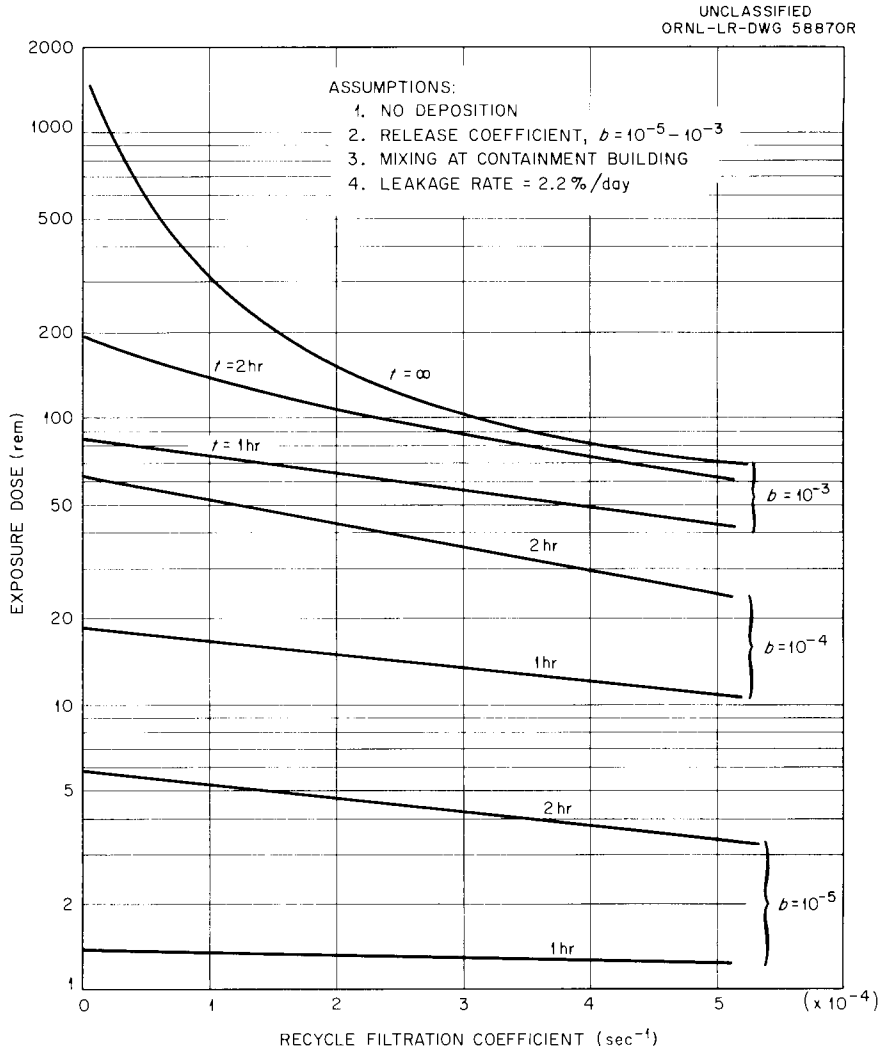

Fig. 2.27. Effect of the Recycle Filtration Rate on the Exposure Dose to the Thyroid at 4000 ft.

varied between 0 and 90%. The data of Fig. 2.27 indicate that the importance of the recycle filtration removal rate decreases as the release coefficient decreases. For 1- and 2-hr exposure periods, the recycle system is effective in reducing the exposure dose by a factor of between 1.07 and 2.94 for values of a release coefficient between 10^{-3} and 10^{-5}. Although these reduction factors are not as important as the reduction in exposure dose brought about by the decrease in the release coefficient, it may be seen in Fig. 2.27 that the real importance of the recycle filtration system lies in the ability of this system to limit the exposure dose for the lifetime of the accident, as indicated by the curves for $t = \infty$.

Conclusions. The results presented here indicate that the maximum off-site exposure dose following the maximum credible accident at the EGCR would depend on a large number of factors. Many of these factors are influenced by the design of the reactor and by the site, but some significant factors depend upon the method of operation or the actions taken during an emergency situation.

The maximum exposure doses to the bone and thyroid for the three time periods considered are listed in Table 2.5. The data reported here were based on a release coefficient of 10^{-5}, which on the basis of experimental results is conservative, that is, high. The values given should not be added directly, because the assumptions which were used in each case are not consistent when the cases are combined. For example, in order to obtain the exposure values given for case 3, it is necessary to seal the containment vessel during reactor operation; however, if the building is sealed during normal operation, the exposure values shown for case 1 do not exist.

From the exposure doses listed in Table 2.5, it is apparent that the most significant time for off-site exposure is the initial period when activity is able to escape from the containment vessel before the isolation valves are closed. The exposure doses for the two remaining periods

Table 2.5. Maximum Off-Site Exposure Doses for Three Cases of Release of Activity From the EGCR

Case	Exposure Time	Exposure Dose (rem)		Remarks
		Bone	Thyroid	
1		22	330	
2	15 min	0.03	0.4	Based on removal of 99% of the particulate matter and iodine activity by the cleanup system.
	∞	3.0	19.0	
3	1 hr	0.2	1.26	Based on no deposition, a leakage rate of 2.2%/day, and 90% efficiency for removal of particulate matter and iodine.
	2 hr	0.6	3.4	
	∞	7.6	42	

are of somewhat less importance, not only because of the magnitude of the exposure dose, but also for the reason that action may be taken to decrease these exposure doses, either by the emergency operating procedures or by evacuation of the areas where exposure is expected. The initial exposure dose will result, however, from activity released within an extremely short time, and therefore only those emergency procedures which are in effect during normal operation will be effective in limiting the initial off-site exposure doses.

Decontamination of EGCR Components

A. B. Meservey

Samples of piping from a helium-cooled loop operated at Brookhaven were decontaminated in oxalate-peroxide. Twelve samples contaminated with irradiated UO_2 and with Sr^{89}, Y^{91}, Zr^{95}, Ru^{106}, Ba^{140}, and Ce^{144} were decontaminated in 20 min at 95°C by an average factor of 73. The solution was 0.3 M ammonium oxalate, 0.1 M ammonium citrate, 0.1 M oxalic acid, and 0.35 M H_2O_2, with a pH of 4.0. Retreatment in fresh solution for 3 hr gave an additional decontamination factor of 2.4 (total D.F. = 175). Thirteen other loop samples were treated in a 3-hr dishwasher test in the oxalate reagent (2 hr at 95°C, plus heating time of 1 hr), and the average decontamination factor was 212, with a range from 24 to 800. The decontamination of the samples in the bottom of the washer, where liquid impingement was more vigorous, was the highest. At the end of the 3-hr dishwasher test the pH of the solution was 4.5 and the H_2O_2 concentration was 0.22 M, with no adjustments being made during the test. Since the helium circulated in the Brookhaven loop had been contaminated with air, the contamination was not typical of that expected in the helium-cooled EGCR but was sufficiently similar to indicate the effectiveness of the treatment.

The action of hydrogen peroxide in oxalate-citrate at pH 4.0 and 95°C in contact with carbon steel was studied. The solution accelerated instead of inhibiting corrosion at approximately 0.05 M H_2O_2 (1.3 mil/hr with H_2O_2 versus 0.08 mil/hr without H_2O_2). At about 0.07 M H_2O_2 a dark film formed on the steel. At about 0.15 M H_2O_2 the film dissolved and

corrosion inhibition supervened. Corrosion inhibition by hydrogen peroxide was also a function of temperature. At a concentration of 0.1 M, oxalic acid with 1.0 M H_2O_2 can probably be used as a decontamination agent up to 60°C, since the corrosion was only 0.009 mil/hr, but at 65 to 70°C corrosion set in at a rate of 0.65 mil/hr. At the low pH of oxalic acid the oxalate ion was oxidized by the peroxide in a few hours, but the peroxide was otherwise stable for many hours. Corrosion acceleration and inhibition by hydrogen peroxide in oxalic acid have been observed by British workers in the electroplating industry.

As part of the continuing oxalate-peroxide formula improvement program, corrosion rates of eight different metals were measured in six 0.30 M oxalate–0.35 M H_2O_2 solutions at 95°C, with oxalic acid concentrations from 0 to 0.30 M and the balance of the oxalate ion as ammonium oxalate. Carbon steel corrosion was 7 to 19 mil/hr at oxalic acid concentrations of 0.2 to 0.3 M (pH up to 1.5), with inhibition by factors of more than 100 when the oxalic acid dropped to 0.15 M or less (pH over 2.5). Corrosion rates on types 304 and 347 stainless steels and Zircaloy 2 remained at less than 0.001 mil/hr and on titanium at generally less than 0.01 mil/hr. The corrosion rate on aluminum, which was 0.18 mil/hr when the oxalate ion was all furnished by oxalic acid (pH 0.7), dropped to 0.052 mil/hr when the oxalate ion was all provided by ammonium oxalate (pH 6.2) in the oxalate-peroxide mixture.

In a procedure similar to one proposed EGCR decontamination procedure for stainless steel, type 347 stainless steel from the Thorex process cell was decontaminated. The decontamination factor for plutonium was 1000 to 3000 in 30 min at 90°C with acid fluoride inhibited with 1 M H_2O_2 (0.1 M NaF in either 1 M HNO_3, 0.4 M oxalic acid, or 0.3 M H_2SO_4). The corrosion rate of the nitric acid mixture on type 347 stainless steel was only 0.004 mil/hr at 70°C.

At an AEC-sponsored Reactor Decontamination Information Exchange meeting on June 1 and 2, at which eight other active centers of decontamination research were represented, it was learned that Hanford and Argonne have successfully tested oxalate-peroxide buffered with acetate.

In scouting tests at ORNL, chromic acid was found to be impractical as a substitute for hydrogen peroxide as the oxidative component in oxalate mixtures because of corrosion, oxidation of the oxalate, and poor UO_2 dissolution. "Everlube 811," a proposed dry-film lubricant for the EGCR service machine, was partly removed from coated metals by a normal decontamination cycle with oxalate-peroxide. Two inhibited-phosphoric-acid solutions prepared by the Pennsalt Co. showed promise as decontaminants for stainless steel, but they were too corrosive for carbon steel.

Parametric Survey of Axial-Upflow Pebble-Bed Power Reactors

R. B. Korsmeyer

Basis for Evaluating Effect of Size on Investment

In any gas-cooled reactor power plant the three most expensive components of the reactor proper are: (1) the pressure vessel and its internal structure, (2) the fixed-graphite reflector, and (3) the enriched uranium. The uranium and fixed-graphite investments are proportional to the core dimensions in large reactors, and the vessel cost depends on both its size and its design pressure. The size and the limiting design pressure are not independent, however, because of limitations in the thickness of steel that can be field welded.

The most economical pressure vessel of large size is spherical, although the reactor core which is enclosed in it is usually cylindrical and must be surrounded by an adequate reflector. The cylinder of largest volume that can be enclosed in a given spherical vessel has a length-to-diameter ratio of 0.7. Although the maximum neutron economy occurs at a ratio of 0.92 for a cylindrical core, the economy does not change greatly over the range of about 0.7 to 0.92, and it appears to be most economical to use the lower ratio for the core and reflector together in an actual design.

In the fall of 1960 a study of a 330-Mw electrical-output pebble-bed-reactor power station was completed in which an axial-upflow bed was chosen

for the design.[17] The upflow bed was selected in spite of the fact that the axial-downflow bed proposed by Sanderson and Porter[18] is free of the fuel-ball levitation problem, because the core support structure of the latter lies directly in the path of the hot exit gas.

Since the problems of dimensional stability, thermal expansion, and material life are so severe that no way to design a reliable support has been found to date, it is important to evaluate the effects of the ball levitation limitation for the axial-upflow bed as the reactor power is increased to 2000 to 3000 Mw. Increasing the power output may affect costs adversely because (1) the maximum allowable gas pressure decreases with increasing pressure vessel size, (2) thermal stresses in the fuel increase with fuel-ball diameter, and (3) the fuel-ball diameter must be increased as the gas pressure is decreased to avoid bed levitation. The resultant effect of these three factors is to reduce the core power density as the reactor power is increased and thus to offset much of the reduction in the unit cost of investment otherwise realized with increasing reactor size.

The effects of these factors are shown quantitatively in Fig. 2.28, which was constructed on the basis of the following assumptions, using the previous pebble-bed reactor study[17] as the point of departure.

Coolant Conditions. The reactor coolant is helium entering at 550°F and leaving the reactor at 1250°F.

Pressure Vessel. The vessel is a spherical shell with a uniform wall thickness of 4.0 in., and the design stress does not exceed 16 600 psi. Considering the internal structure (excluding graphite) as part of the vessel, the unit cost is constant at $2.30/lb, at an apparent density of 750 lb/ft^3 for the steel in the shell.[17] The high apparent density arises from the fact that the vessel nozzles, reinforcement, and other steel attachments are included in the vessel weight, but the volume of steel is arbitrarily taken as that of the 4-in.-thick shell.

---

[17]A. P. Fraas et al., Design Study of a Pebble-Bed Power Plant, ORNL CF-60-12-5 Rev., May 11, 1961.

[18]Sanderson and Porter, Design and Feasibility Study of a Pebble Bed Reactor Steam Power Plant, SP-1963, May 1, 1958.

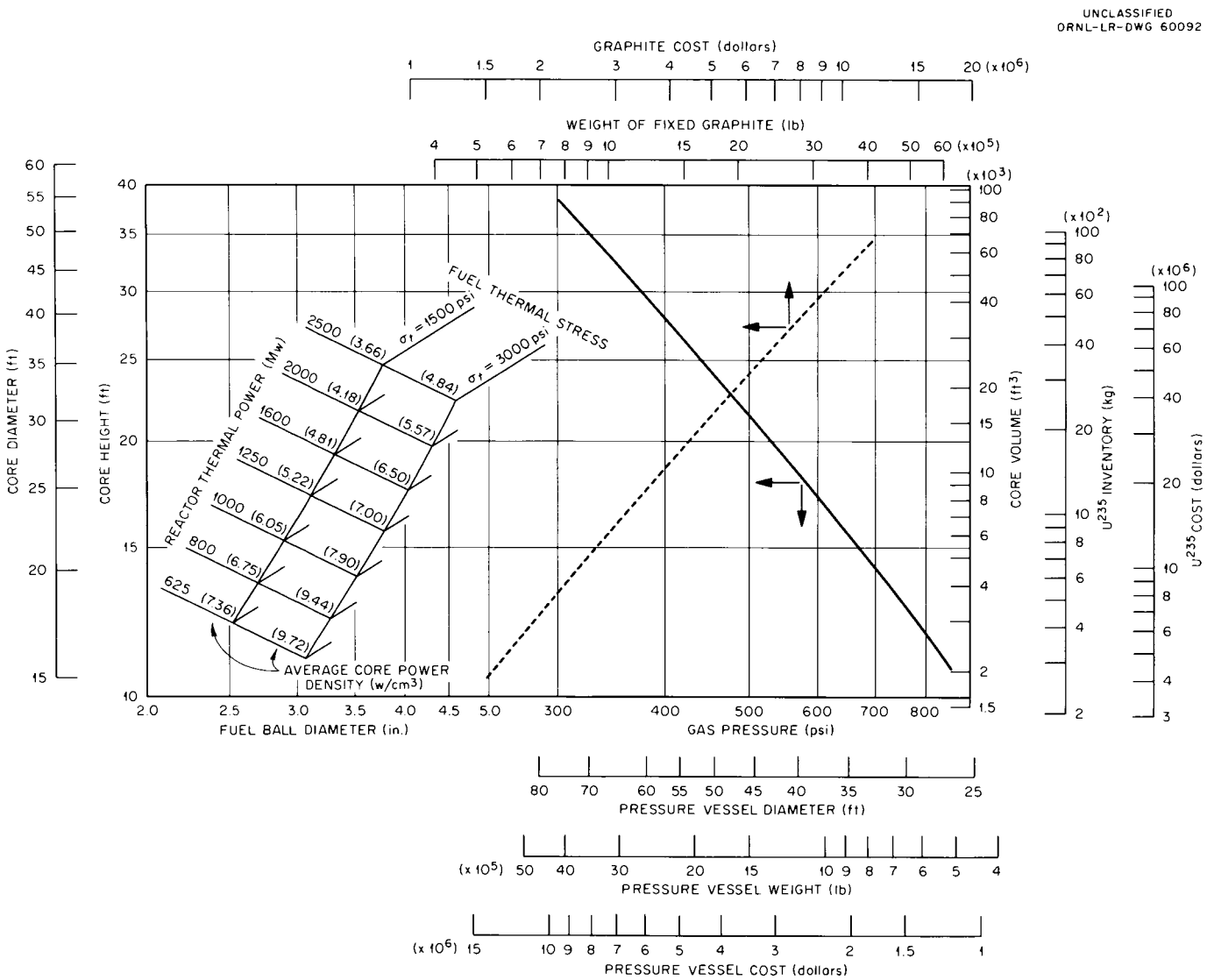

Fig. 2.28. Effect of Power on Minimum Size and Cost of the Reactor Graphite, Pressure Vessel, Uranium Inventory of an Axial-Upflow Pebble-Bed Reactor.

Core. The core is a right-circular cylinder filled with the fuel balls. The core and the fixed-graphite blanket together form a right circular cylinder whose length-to-diameter ratio is 0.7. In an actual reactor the core would not be flat on top and bottom because of fuel loading and unloading requirements.

Fixed Graphite. The fixed graphite is assumed to be equivalent to a layer 3 ft thick surrounding the core on all sides. Thus, the pressure vessel inside diameter is (1.74L + 7) ft, where L is the core height (allowing a 6-in. clearance). A void fraction of 10% was assumed for the top and bottom layers to provide for gas flow passages. The unit cost is \$2.83/lb, and a density of 105 lb/ft^3 was used.

Uranium and Thorium. The uranium and thorium concentration in the fuel does not change appreciably with increasing core size from the values used in the previous study.[17] The uranium and thorium inventories are, therefore, proportional to core volume. The unit cost of U^{235} is \$17.10/g and that of thorium is \$43.00/kg of metal. The fabrication charge is not included because reliable figures are not available. The charge would, however, be proportional to the uranium inventory and therefore would not alter the general conclusions implicit in Fig. 2.28. In the previous study the graphite spheres contained 0.50% UO_2 plus 9.61% ThO_2 by weight. The thorium cost is therefore 4.6% of the U^{235} cost in all cases; it is not included in Fig. 2.28 because its contribution is negligible compared with that of the uranium.

Correlation of Size and Cost

The designer is interested in minimizing capital costs by making the reactor as compact as possible. It may be seen in Fig. 2.28 that for a given thermal power output the core size may be reduced by using larger fuel balls (required by higher gas velocities) and higher gas pressures. The lines of constant total power are shown (Fig. 2.28) for the range of thermal power output from 625 to 2500 Mw. These lines relate the core size to the fuel-ball diameter. At the same time the matching pressure and pressure vessel diameter for that core height may be obtained from

the figure by reflection from the solid line at the right. Pressure vessel weight and cost may be read directly on the auxiliary scales.

For a given fuel ball size, however, the average core power density (taken as 0.5 of the peak core power density) is limited by the allowable thermal stress in the fuel. The allowable stress in highly irradiated graphitic fuels has not been accurately determined, but is probably not very high. The limiting conditions for two values, 1500 and 3000 psi, are shown (Fig. 2.28) as pairs of parallel lines intersecting each constant-power line, along with the corresponding average core power density (w/cm^3) at each intersection. The stresses were calculated for a core voidage of 0.39 and the following fuel properties:

Coefficient of thermal expansion	$3 \times 10^{-6}/°F$
Modulus of elasticity	1.5×10^6 psi
Thermal conductivity	8 $Btu/hr \cdot ft^2$ (°F/ft)
Poisson's ratio	0.3

The loci of these intersections have been drawn to aid interpolation between lines of constant power. The designer must always choose conditions so that the core height lies above both the constant power line and the constant thermal stress line. Both the minimum core height and the fuel-ball diameter are therefore determined by the intersection of these two lines.

The weight and cost of the fixed graphite are obtained from the core height by reflection from the dotted line (Fig. 2.28), and the core volume, U^{235} inventory, and cost corresponding to the core heights are shown on the scales at the right.

The result of decreasing the power density with increasing reactor power is to increase the cost of the large components more rapidly than would otherwise occur. The net effect is that the total unit cost of the structural components approaches a constant rather quickly, while the uranium and thorium inventory costs continue to rise. These effects are shown in Fig. 2.29, where the fuel inventory cost (uranium plus thorium) is plotted separately. It is clear that the economic incentive to develop

a practicable restraint for the upflow core or a reliable support for the downflow core increases with reactor size.

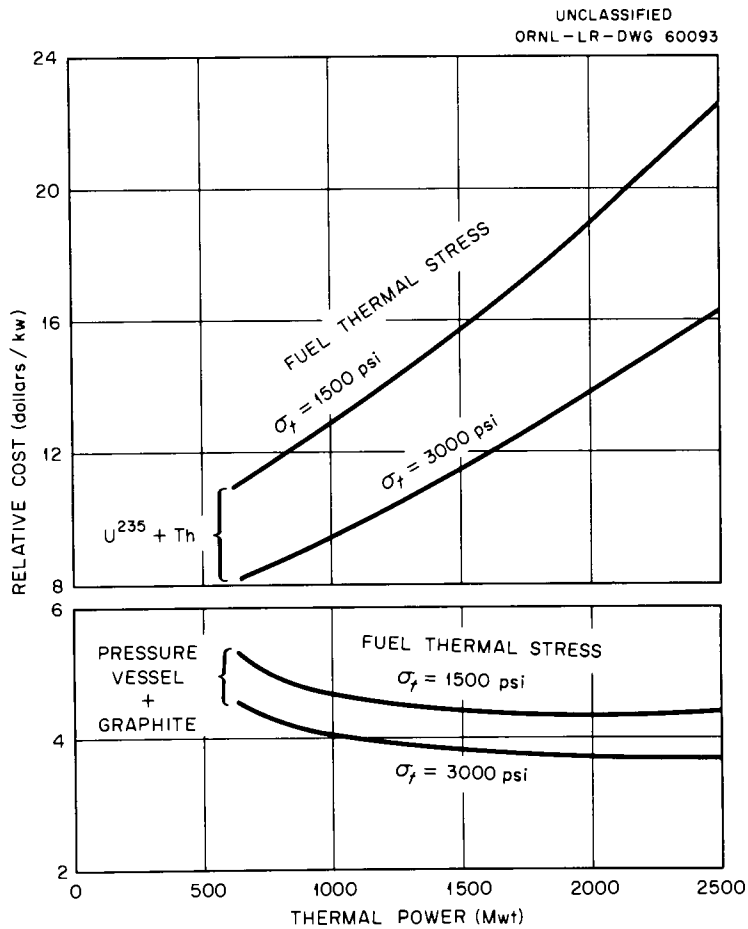

Fig. 2.29. Relative Reactor Cost Versus Power for Axial-Upflow Pebble-Bed Reactor.

3. EXPERIMENTAL INVESTIGATIONS OF HEAT TRANSFER AND FLUID FLOW

H. W. Hoffman J. L. Wantland

Resistance-Heated-Tube Heat Transfer Experiment

W. J. Stelzman

Experimentation with the model 4 heat-transfer apparatus has been initiated. This apparatus, shown in Fig. 3.1, consists of two successive full-scale Title II EGCR fuel-element clusters, each enclosed in a separate 3.00-in.-i.d. Pyrex glass channel. The upstream cluster is electrically connected so that the power generation in the central tube can be controlled separately from that of the six peripheral tubes in which the power generation is essentially uniform. This cluster is not instrumented for tube surface temperature measurements, but it serves to establish the flow and temperature structure of the gas entering the downstream cluster. The power generation in each of the seven tubes of the downstream cluster can be controlled and each tube in this cluster can be probed for the measurement of the local surface temperature throughout the entire length of the cluster in the same manner as was done in the model 3 heat-transfer apparatus.[1] A significant design change from that of the model 3 apparatus is that in this apparatus the flow is upward through the system, that is, through the upstream cluster to establish the flow, through the instrumented downstream cluster, and out through an ample outlet plenum chamber.

In the system there are five transverse planes at which local gas temperature measurements can be made: four in the downstream cluster (three of which are formed by the Micarta collars, Fig. 3.1, which serve as alignment guides, reference surfaces, and seals) and one near the outlet end of the upstream cluster. At each measuring station there is a small hole in the Pyrex channel through which a thermocouple probe can be inserted to a predetermined depth. Since both Pyrex channels can be freely rotated, gas-temperature probing at all but the innermost regions of the

[1]GCR Semiann. Prog. Rep. Dec. 31, 1958, ORNL-2676, pp. 36–45.

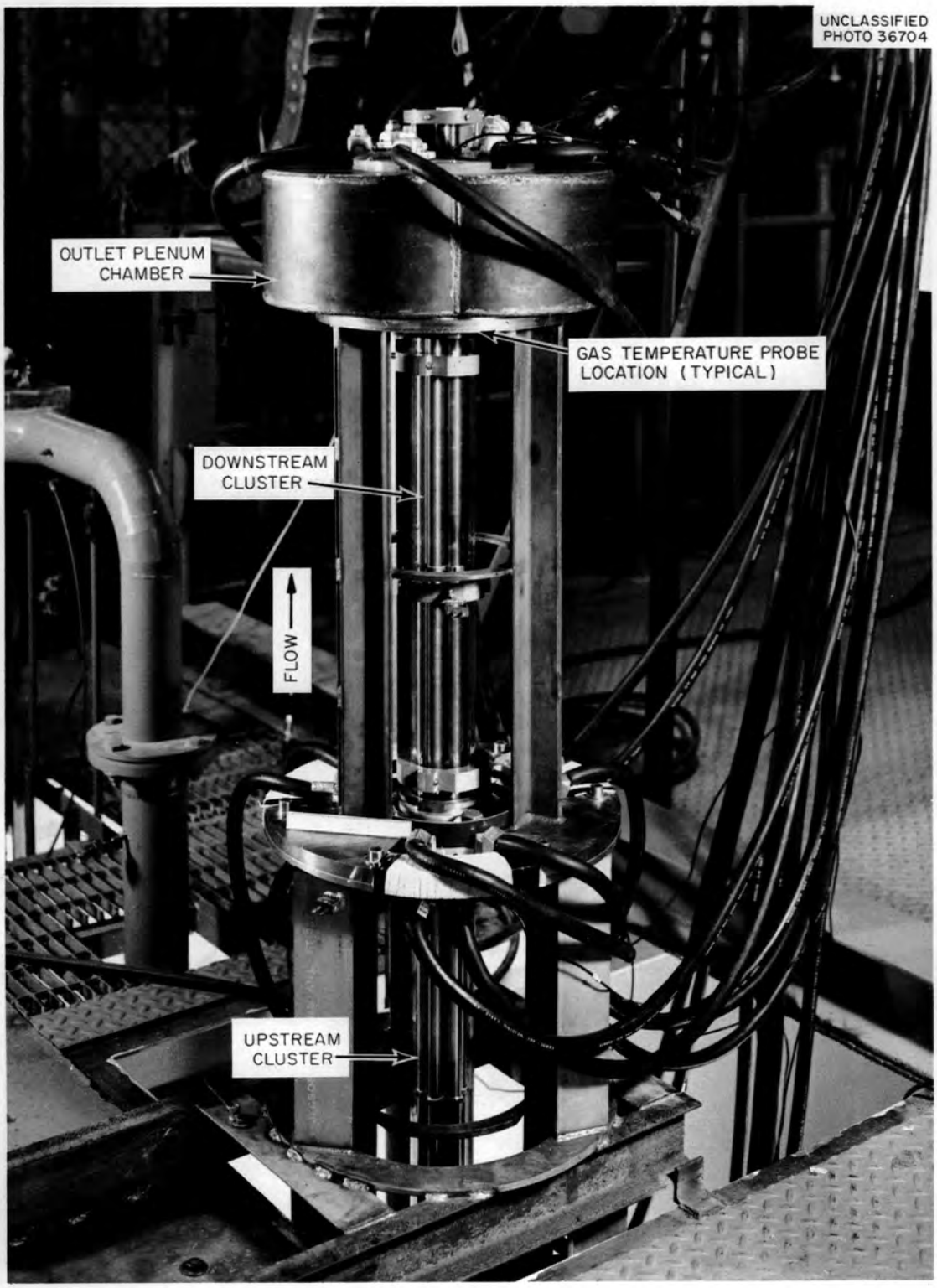

Fig. 3.1. Model 4 Heat-Transfer Apparatus.

flow passage can be accomplished. The upstream cluster can be rotated with respect to the downstream cluster so that the effects of cluster relative orientation on heat-transfer characteristics can be studied.

A series of experiments is in progress (designated as series 4-1) in which the tubes of the two clusters are directly in line (0-deg relative orientation) and the upstream cluster is unheated. It was the intention to operate all seven tubes of the downstream cluster at equal power generation rates; however, during the course of experimentation, it was discovered that because of erroneous voltmeter readings the power generation was not uniform. It was subsequently determined that during assembly of the electrical system, the voltmeter leads had been located so that extraneous voltages were induced in them by the electrical fields surrounding the main power leads. Voltage calibrations have been made so that the correct power determinations can be made and the voltmeter leads are being relocated. Since a considerable portion of the data for the series 4-1 experiments had been collected before the error was discovered, it was decided to complete the series of tests and to analyze the data for uneven cluster power distribution. A second series of experiments with uniform power generation is scheduled.

For the series of tests with uneven power generation, the average bulk Reynolds modulus was 54 000 and the tube heat fluxes ranged from 6500 to 7000 Btu/hr·ft^2, tubes 1 and 2 having 7% higher and tube 5 having 1% higher heat generation rates than tubes 3, 4, 6, and 7. Preliminary results for peripheral tube 5 are presented in Table 3.1. The mean heat-transfer characteristics compare favorably with those obtained with the model 3 heat-transfer apparatus. For example, at $L/d_e = 38$ for tube 5, the Nusselt modulus (based on bulk gas properties at that axial plane) is calculated to be ~124. For tube 4 at the same L/d_e, series 4C on the model 3 apparatus,[2] the bulk Nusselt modulus (corrected to the same Reynolds modulus by $N_{Nu} \sim N_{Re}^{0.8}$) is calculated to be ~126. The difference of the two values is <2%, which is less than the experimental error associated with these data.

---

[2]GCR Quar. Prog. Rep. March 31, 1961, ORNL-3102, pp. 70–76.

Table 3.1. Preliminary Data on Axial Variation of Mean Inside Surface Temperature and Mean Heat-Transfer Coefficient for Tube 5 of the Series 4-1 Heat-Transfer Experiments

Axial Position (L/d_e)	Mean Inside Surface Temperature (°F)	Mean Heat Transfer Coefficient (Btu/hr·ft^2·°F)
1.50	187	>61.7
5.04	242	45.3
10.65	271	39.7
11.20	273	39.3
12.50	278	38.8
13.00	280	38.6
13.58	276	38.3
14.00	282	38.2
15.00	285	37.9
16.00	288	37.7
18.00	294	37.1
21.11	294	37.8
22.00	279	41.7
22.60	245	52.7
23.00	236	57.4
24.00	230	61.2
25.00	249	52.7
26.20	257	50.0
30.00	274	46.2
33.61	287	43.8
35.00	295	42.3
40.23	313	40.0
45.00	322	39.1

The mean surface temperatures of Table 3.1 are plotted in Fig. 3.2 using a dimensionless distance ratio, x/L, as the abcissa. Two peculiarities in the data are apparent. At $x/L = 0.299$ the indicated surface temperature is ~5°F lower than would be predicted from adjacent data points. From $x/L \approx 0.75$ to $x/L \approx 1$ the indicated surface temperatures are 5 to 7°F higher than the trend indicated by the temperatures from $x/L \approx 0.55$ to $x/L \approx 0.75$. Several data reruns at various time intervals have shown the reproducibility of both these phenomena to a precision of ±1°F. The reasons for the inconsistencies is not presently known. It is possible

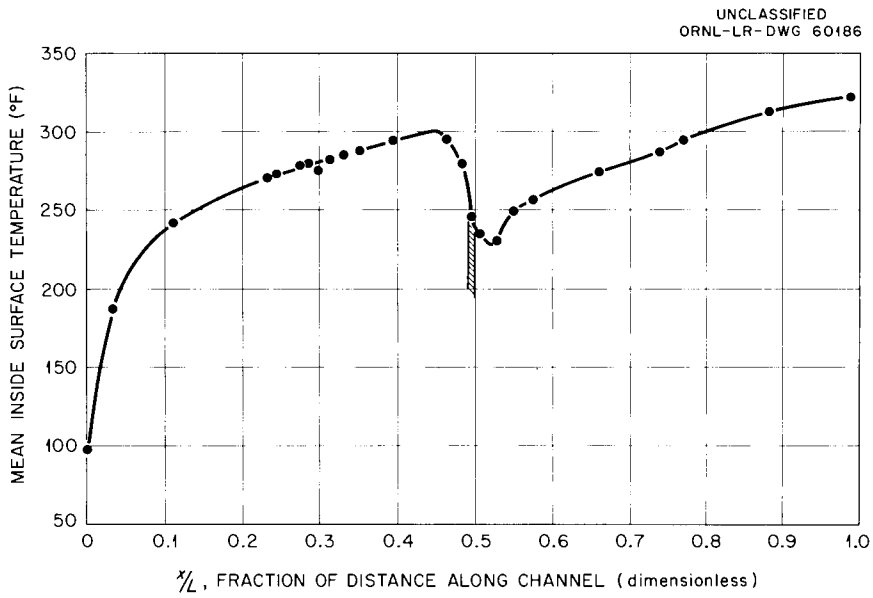

Fig. 3.2. Variation in Mean Axial Surface Temperature of Tube 5 in the Series 4-1 Heat-Transfer Experiments, Preliminary Results.

that the low indicated surface temperature at $x/L = 0.299$ is due to a discontinuity in the metallic structure (or wall thickness) at that transverse plane or to the presence of a thin local layer of silver solder inadvertantly deposited there during fabrication of the element. The difference in surface temperature trends between $x/L \approx 0.55$ to 0.75 and $x/L \approx 0.75$ to 1 could be due to variations in the metallic structure of the tube in this region. This is being investigated in greater detail.

Circumferential surface temperature distributions are shown in Fig. 3.3 for tube 5 at $L/d_e = 17.9$ and $L/d_e = 35.0$ and are compared with typical results obtained during the series 4C experiments using the model 3 apparatus.[2] At $L/d_e = 17.9$ the surface temperature profile obtained in the series 4-1 experiments is more symmetrical than the profile obtained during the series 4C experiments. This is attributed to a more symmetrical flow distribution through the upstream unheated cluster. Comparison at the $L/d_e = 35.0$ level indicates only a slight difference between the two sets of data. This seems to indicate that temperature distributions in the downstream half of the cluster are controlled more strongly by the mid-cluster spacer than by the flow distribution of the gas entering the cluster.

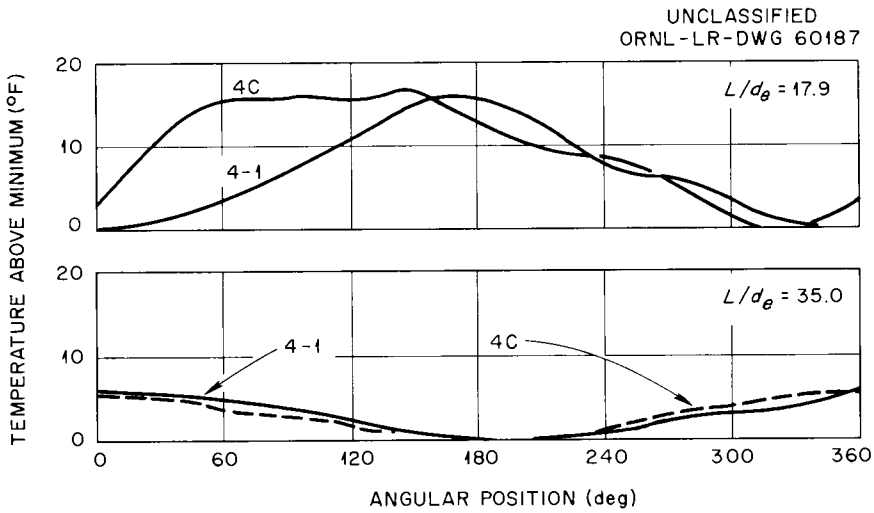

Fig. 3.3. Preliminary Circumferential Temperature Profiles for Tube 5, Series 4-1, Compared with Results of Series 4C on the Model 3 Apparatus.

Velocity Distribution Studies

F. E. Lynch

The accumulation of data for delineating the velocity field in the downstream element of two EGCR clusters[3,4] has been completed. Velocity profiles were determined at $L/d_e = 3.9$ using the model 3 apparatus; at $L/d_e = 11.0$, 26.0, and 44.0 using the model 4A apparatus; and at $L/d_e = 20.9$ and 34.0 using the model 4B apparatus. Relative cluster orientations of 0, 15, 30, 60, and 90 deg (see Fig. 3.4) were studied. A summary of the velocity profiles obtained 0.050 in. from the surface of tube 1 is shown in Fig. 3.5. At $L/d_e = 3.9$ the effects of spider configuration and cluster orientation are clearly discernible. The curves for 0- and 60-deg orientations can be paired, the major differences being due to the different locations of the web supporting the central tube. Also the 30- and 90-deg orientations can be paired. The expected symmetry in the velocity pattern for the 90-deg orientation (see Fig. 3.4) is quite apparent. At $L/d_e = 11.0$ the effects of cluster orientation still persist, but the velocity distribution appears to be more strongly controlled by

[3]Ibid., pp. 79–82.

[4]GCR Quar. Prog. Rep. Dec. 31, 1960, ORNL-3049, pp. 174–81.

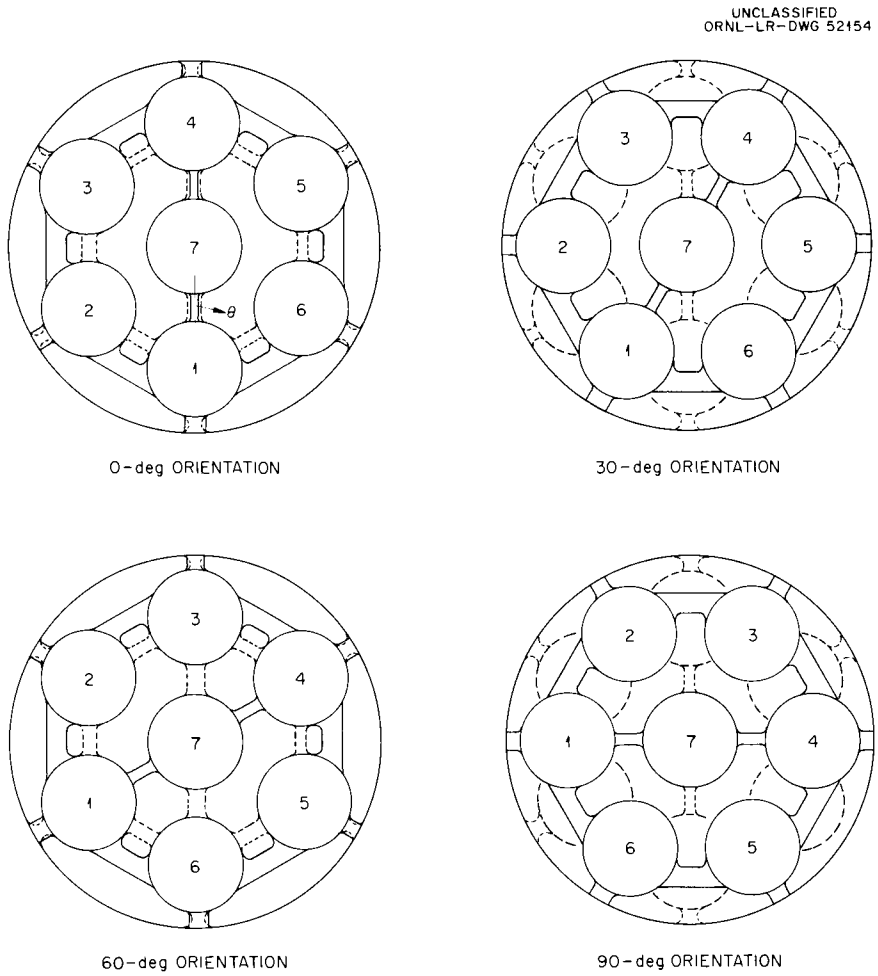

Fig. 3.4. Designation of Rod Positions and Relative Cluster Orientations of Adjacent Title II Design Spiders as Examined in Experimental Studies with EGCR Clusters.

the cross-sectional shape of the flow channel. At $L/d_e = 20.9$ (upstream of the mid-cluster spacer) the effects of cluster orientation are almost negligible, all curves being quite similar in shape. Downstream of the mid-cluster spacer the effects of cluster orientation appear to be completely negligible. At $L/d_e = 26.0$ the local velocity minima caused by the support webs and 60-deg pad on the spacer are evident. At $L/d_e = 34.0$ a slight velocity rise in the region downstream of the 60-deg pad of the mid-cluster spacer is shown. It is thought that this is due to a reentry of the fluid in the region between the tube and the channel wall after having been displaced by the 60-deg pad on the mid-cluster spacer.

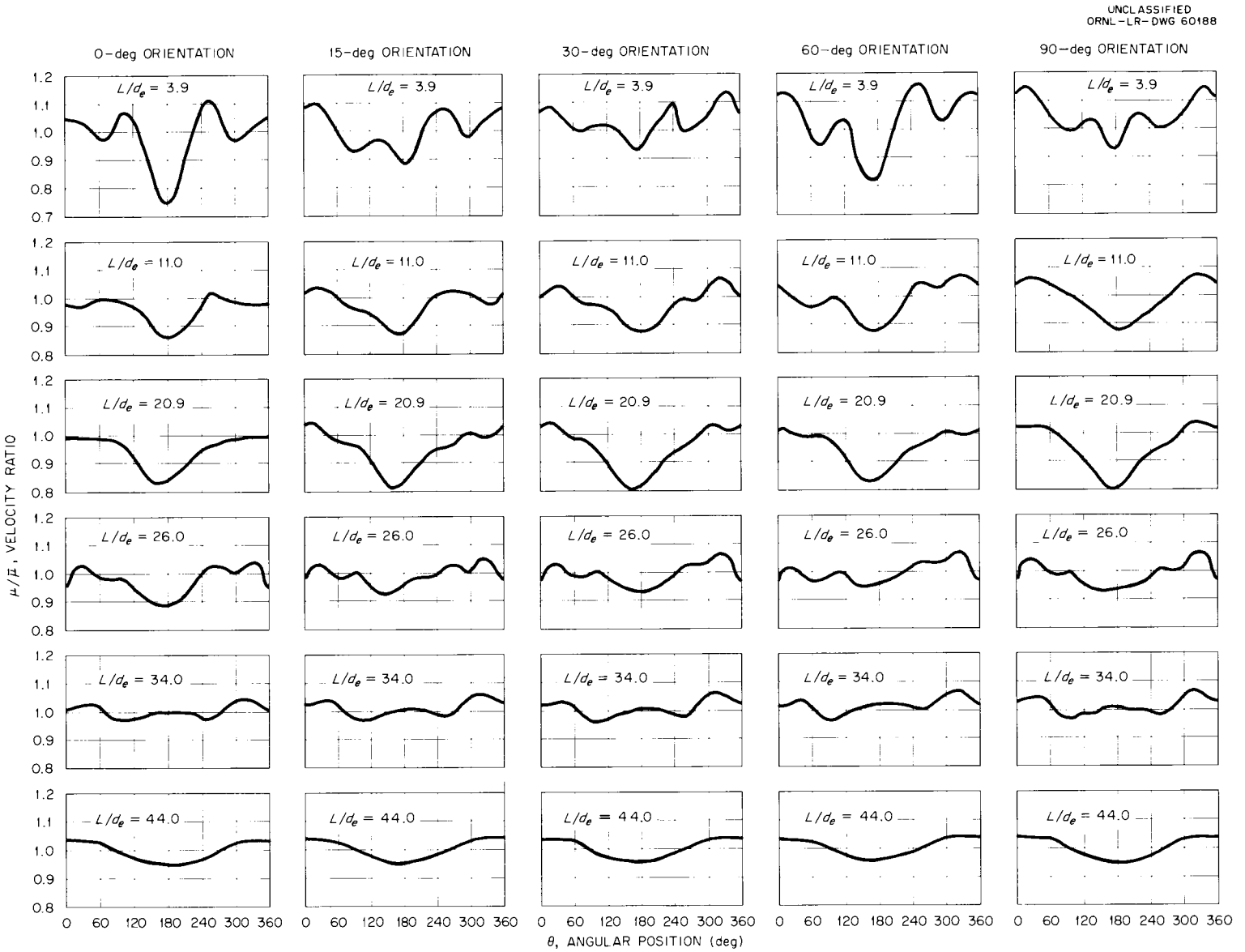

Fig. 3.5. Summary of Velocity Profiles Around Tube 1; Pitot Probe 0.050 in. from Tube Surface, N_{Re} = ~50 000.

At $L/d_e = 44.0$ this velocity maxima has disappeared, and again the profile shapes are beginning to be controlled by the shape of the flow channel rather than by obstructions formed by the spiders and spacers.

Pressure-Loss Measurements in EGCR Clusters

G. J. Kidd, Jr.

Experimentation has been resumed on the three-cluster EGCR pressure-drop apparatus, described previously,[5] to which a few modifications have been made. All piezometer holes were enlarged from 1/32 to 1/16 in. in diameter, since it was found that the surface roughness of the graphite sleeve was of the same order of magnitude as the diameter of the original holes. The outer surfaces of the graphite sleeves were coated with a thin layer of clear epoxy resin to eliminate air leakage. A sensitive inclined manometer was used (in lieu of U-tube manometers) to read the individual pressure drops.

Bare-tube friction factors, hanger-spider pressure-loss coefficients, and mid-cluster-spacer pressure-loss coefficients have been determined in the Reynolds modulus range of 15 000 to 80 000 using the method previously presented.[5] These data are shown in Figs. 3.6 and 3.7. The bare-tube

[5]GCR Quar. Prog. Rep. March 31, 1961, ORNL-3102, pp. 82–85.

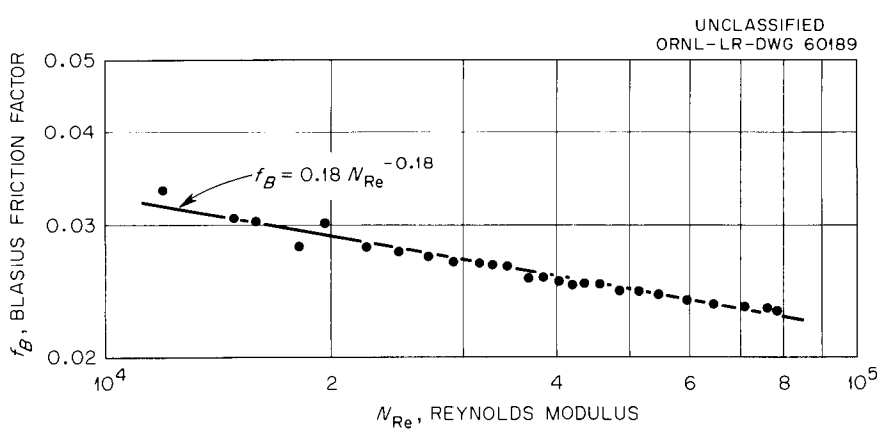

Fig. 3.6. Bare-Tube Friction Factor vs Reynolds Modulus for EGCR Fuel-Element Cluster.

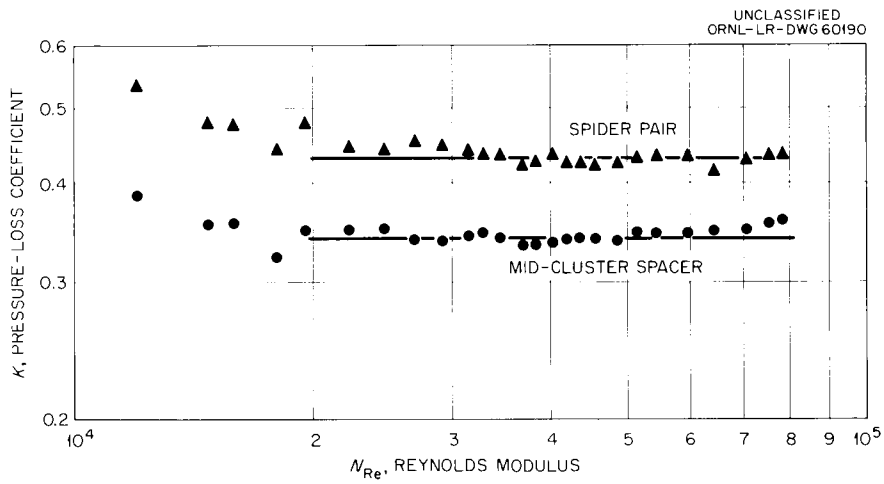

Fig. 3.7. Hanger-Spider and Mid-Cluster-Spacer Pressure-Loss Coefficients vs Reynolds Modulus for EGCR Fuel-Element Cluster.

friction data thus obtained can be correlated in this range by the empirical equation

$$f_B = 0.18\ N_{Re}^{-0.18} \quad ,$$

where f_B is the Blasius friction factor and N_{Re} is the bulk Reynolds modulus.

The hanger-spider and mid-cluster-spacer pressure-loss coefficients were found to be essentially independent of Reynolds modulus above N_{Re} = ~20 000; K for the spider pair was 0.43 ± 5%, and K for the mid-cluster spacer was 0.34 ± 5%. The experimental value of 0.43 for the hanger-spider pressure-loss coefficient is ~13% higher than that calculated by considering that there was a sudden expansion in this region followed by a sudden contraction.[6] This difference is not unreasonable because the form drag of the support webs was neglected in the calculation. For the mid-cluster-spacer pressure-loss coefficient calculation the spacer was considered as a pseudo orifice with

$$\beta = \left(\frac{\text{free-flow area through spacer}}{\text{free-flow area in cluster}}\right)^{1/2} = 0.81 \quad ,$$

[6]Flow of Fluids Through Valves, Fittings, and Pipes, Crane Company Technical Paper No. 409, p. 24 (May 1942).

and the coefficient was calculated using the standard orifice equation with the orifice coefficient, C, taken as unity[7] in the Reynolds modulus range of 25 000 to 75 000. The value obtained (K = 0.34) was identical to that determined experimentally.

---

[7]D. P. Eckman, Industrial Instrumentation, p. 348, John Wiley and Sons, New York, 1950.

Part 2. Materials Research and Testing

4. MATERIALS DEVELOPMENT

J. H. Coobs

Fabrication and Physical Properties Studies of Fuel Materials

Powder Processing and Fabrication of UO_2 (A. J. Taylor, J. M. Robbins)

Additional work was done to prepare miniature UO_2 specimens with large differences in grain size for irradiation in LITR capsules. One group of pellets sintered for 16 1/2 hr at 1750°C in hydrogen had a grain size of approximately 90 μ. A second group of pellets was fired for 1 hr at 1450°C in argon in an attempt to obtain the small grain size desired. The resultant grain size of these pellets was approximately 20 μ; however, definite pitting was found at the contact points where the pellets consisting of high oxygen-to-uranium ratio starting material touched the low oxygen-to-uranium ratio grog on which they were sintered. This result is in line with other recent observations which indicate that the reaction between materials having high and low oxygen-to-uranium ratios when heated in argon is proportional to the difference in oxygen content and that the extent of the reaction increases as the difference in oxygen content increases. Observations also indicate a second type of reaction that is apparently proportional to both increasing oxygen-to-uranium ratio and increasing temperature. This reaction results in removal of material from surfaces and redeposition on the same surfaces, apparently by vapor-phase transport, in the form of layers of small, loosely bonded crystals of UO_2. This effect becomes observable at 1600°C, and for material of a given oxygen-to-uranium ratio it increases with temperature; likewise, for a given temperature the effect increases with increasing oxygen-to-uranium ratio. The small-grain-size pellets will be made by a different technique while the phenomena noted above are being studied.

All the UO_2 specimens for the Be-UO_2 compatibility studies have been prepared, except those having a high oxygen-to-uranium ratio, that is, 2.10. It has been determined that reduction of the high oxygen-to-uranium

ratio of 2.18 in the starting material to 2.01 during sintering, as mentioned previously, was not caused by hydrogen contamination in the inert furnace atmosphere but was, rather, a consequence of gas-solid equilibria in the oxygen-uranium system at elevated temperatures. A furnace is being prepared in which sintering can take place in an atmosphere having a controlled oxygen content.

Thermal-Conductivity Studies (T. G. Godfrey, D. L. McElroy)

The major developmental work on the radial heat flow apparatus was completed and an experimental run was performed using a specimen of INOR-8 alloy. The results given in Table 4.1 indicate that a precision of ±2% was obtained. An error analysis of the technique and apparatus showed

Table 4.1. Thermal Conductivity of INOR-8

Average Specimen Temperature (°C)	Thermal Conductivity[a] [w/cm^2 (°C/cm)]	Average Specimen Temperature (°C)	Thermal Conductivity[a] [w/cm^2 (°C/cm)]
166	0.1226	609	0.1942
166	0.1238	651.5	0.2038
263	0.1360	652	0.2042
263	0.1365	652	0.2048
326.5	0.1451	652.5	0.2040
363	0.1498	680	0.2058
364.5	0.1497	681	0.2068
440	0.1606	681.5	0.2091
441	0.1595	701	0.2175
488	0.1708	740	0.2310
494.5	0.1751	765	0.2350
496	0.1726	766	0.2352
496	0.1718	800	0.2365
497	0.1737	813	0.2400
559	0.1859	814	0.2388
559.5	0.1866	815	0.2383
609	0.1961	816	0.2398
609	0.1944	816	0.2419

[a]Values reported represent average of 24 measurements, 12 based on absolute and 12 on differential determinations of temperature differences.

the results to be accurate to ±5%. This degree of precision requires a relative calibration of all thermocouples in the specimen between successive data points by isothermal operation and intercomparison of all thermocouples. The data obtained during the test run showed that the thermal conductivity of INOR-8 increases linearly with temperature to about 450°C, where a slight change in slope occurs. Near 680°C a second inflection was observed that represented a 10% increase in conductivity.

The major features of the apparatus are shown in Fig. 4.1. The specimen consists of a 9-in.-tall stack of 1/2-in.-thick bushings, 3 in. o.d., and 0.65 in. i.d., as shown in Fig. 4.2. The central 3-in. section of the stack contains the three instrumented disks for temperature difference determinations. Each of the three disks is machined to accept two thermocouples at each of two radii. The thermocouples enter the specimen radially and turn to assume an axial orientation for the last 3/8 in. This arrangement serves to reduce heat loss down the thermocouples. The radial temperature gradient is produced by a double spiral-wound platinum-rhodium core heater powered by a transistorized magnetic-regulated direct-current power supply. The core heater is provided with voltage taps spanning the central 3 in. for determination of the power dissipated per unit length. The absolute temperature of the specimen is controlled by a molybdenum-wound muffle heater, which is shown in position around the specimen in Fig. 4.3. Differential thermocouples between the ends and the center of the specimen are used to control the axial temperature with end guard heaters. This control is critical, since the method requires that all heat flow be in a radial direction. Thermal insulation is provided by bubbled alumina and insulating fire brick (grade K-26). The apparatus is operable in a vacuum, but purified inert gases are normally used. A precision six-dial potentiometer and a millimicrovolt electronic null detector are used to measure and intercompare all thermal emf's.

The UO_2 specimen stack described previously has been installed in the apparatus,[1] and complete characterization of the material as to

[1]GCR Quar. Prog. Rep. March 31, 1961, ORNL-3102, p. 92.

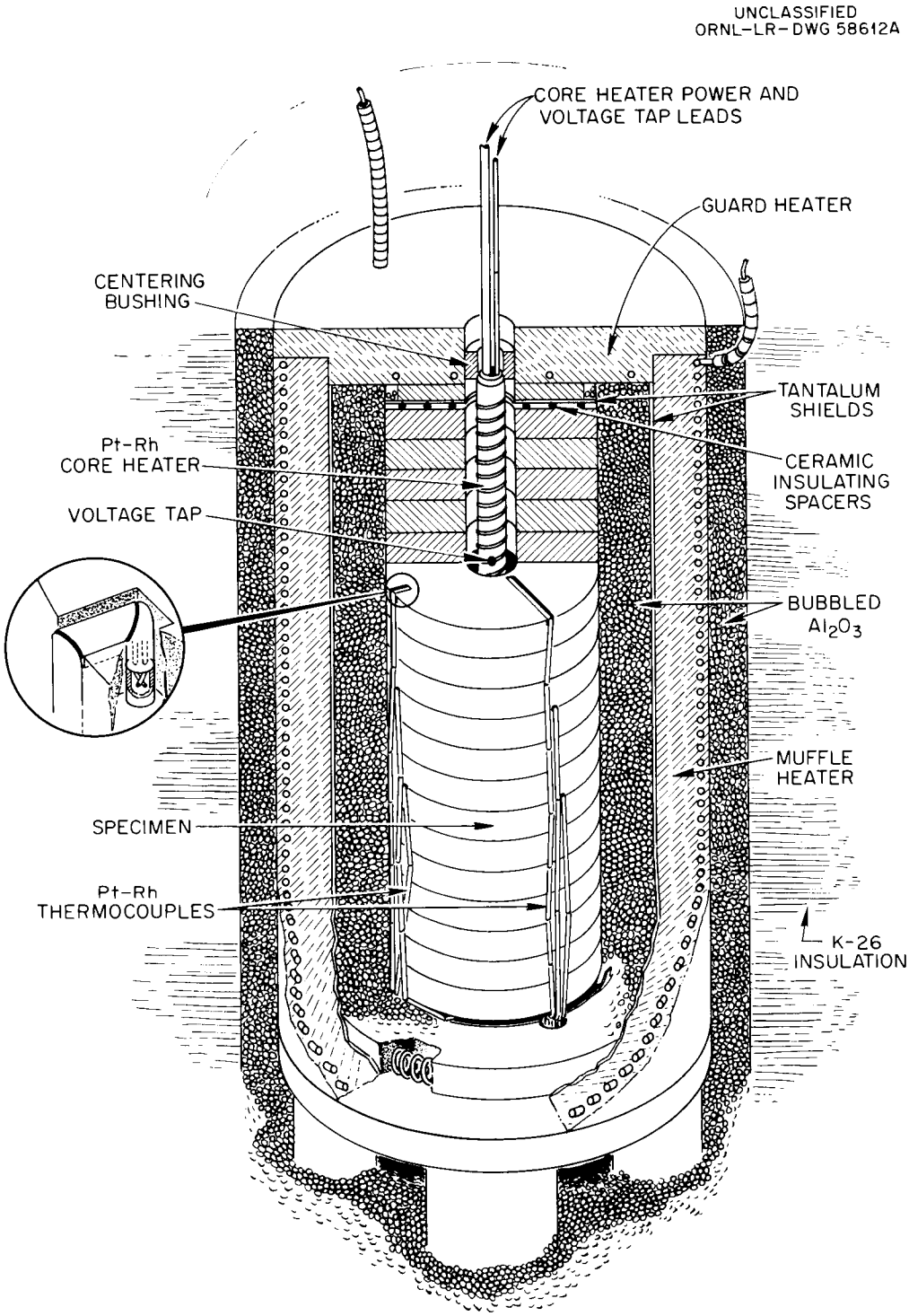

Fig. 4.1. Schematic Diagram of Radial-Heat-Flow Thermal-Conductivity Apparatus.

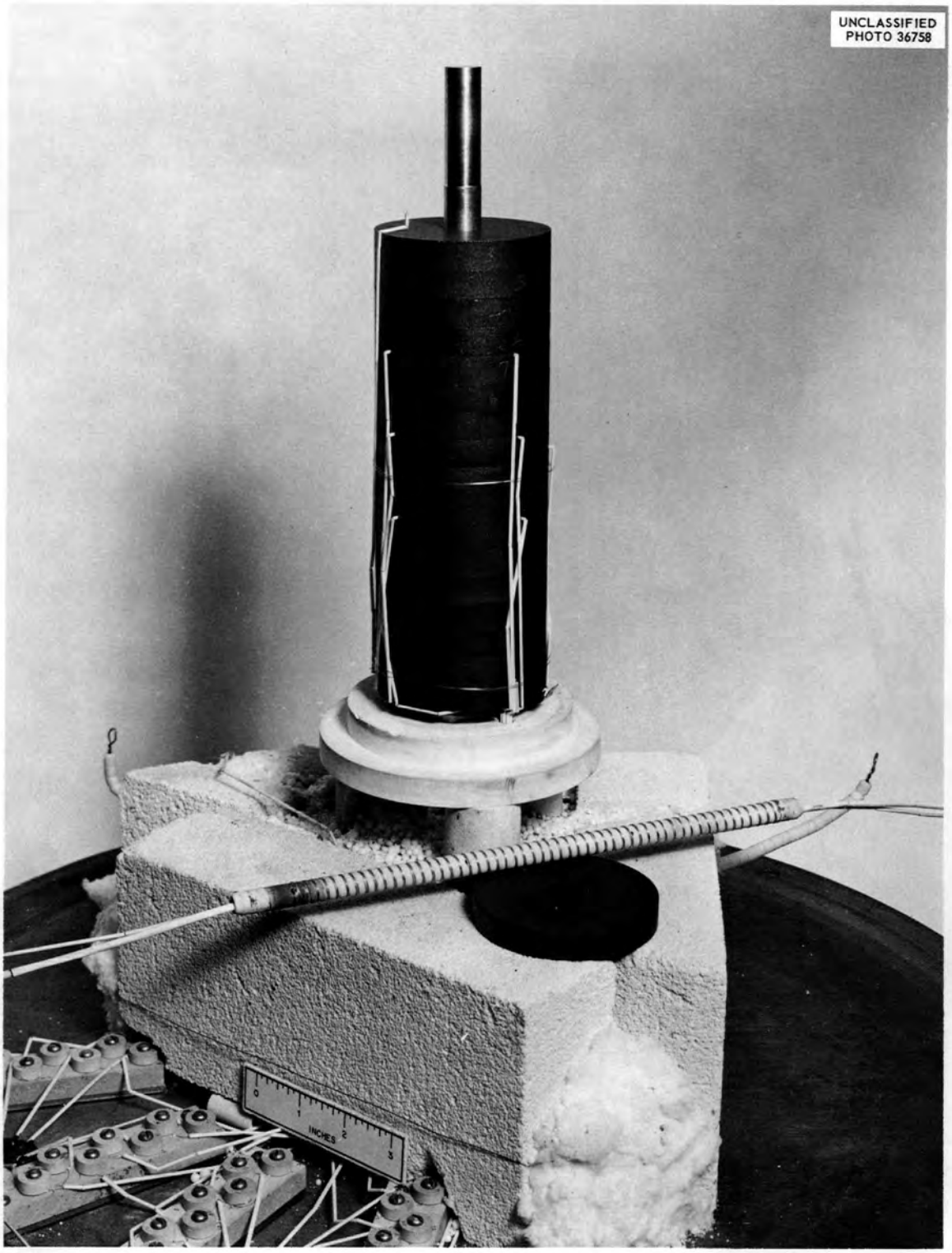

Fig. 4.2. Partially Assembled Specimen Stack for Tests in Thermal-Conductivity Apparatus. Platinum-rhodium core heater is shown with sample disk.

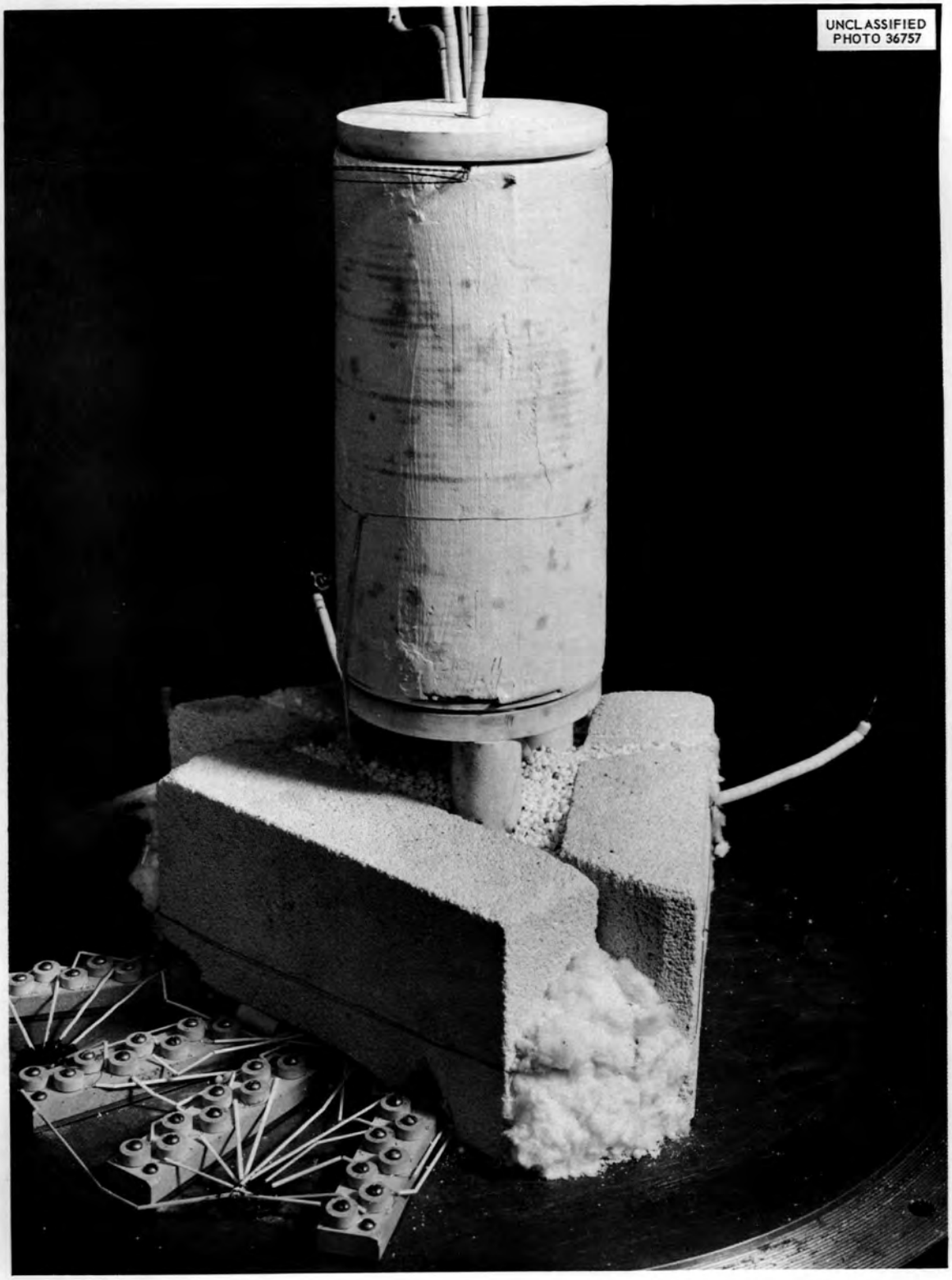

Fig. 4.3. Partially Assembled Thermal-Conductivity Apparatus Showing Muffle and End Guard Heaters in Place.

stoichiometry and purity is in progress. Thermal-conductivity measurements have been initiated near room temperature.

Fabrication of BeO (R. L. Hamner)

Fueled BeO Bodies. Beryllium oxide bodies containing 30 vol % UO_2 as either 100- to 150-μ particles or as 150- to 250-μ particles were fabricated to 95 to 96% of theoretical density by cold pressing and sintering in hydrogen at 1750°C. These specimens were virtually free of the void areas around fuel particles which contributed to the low densities (89 to 93%) previously reported.[2] This reduction in void space was accomplished by holding the green density of the BeO matrix constant and increasing the preshrinkage of fuel particles from approximately 24 to 34%.

Microscopic cracks were noted after sintering in some specimens but were not apparent in others. Reduction in the incidence of microcracks was accomplished by providing additional shielding between the specimens and the furnace susceptor during sintering. Essentially the same results were obtained when the fuel loading was reduced to 20 and 25 vol %.

Fabrication of Unfueled BeO. Developmental work was initiated on the preparation of high-purity BeO bodies to be used in irradiation experiments designed for studying the effects of density, grain size, and temperature at high fast-neutron doses. The small cylindrical specimens required measure approximately 0.25 × 0.25 in. and are to be sintered to densities of 2.7 and 2.9 g/cm^3, with two significantly different grain sizes for each density.

High-density bodies, 2.89 ± 0.02 g/cm^3, were obtained by cold pressing without binder and sintering in hydrogen for 1 hr at 1750°C. The low-density bodies, 2.69 ± 0.02 g/cm^3, were sintered under the same conditions but were pressed with 15% epoxy resin binder, which was removed prior to sintering. It was noted that widely varying the heating rate had a significant effect on the final density. Starting with compacts of the same green density, final densities were lowered from 96 to 71% of theoretical when the time to reach 1750°C was increased from 1 1/2 to 24 hr.

[2]Ibid., pp. 97–98.

The desired variation in grain size was obtained by varying the time of heat treatment at high temperature. After heating the specimens for 17 hr at 1750°C in hydrogen, the grain size in high-density specimens appeared to have increased by a factor of 4 to 5 over the grain size of specimens heated at this temperature for only 1 hr. The grain size in low-density specimens appeared to increase when treated in the same manner, but not as uniformly as in the high-density specimens. No significant grain growth was observed in BeO specimens heated in air for 120 hr at 1500°C after having been sintered in hydrogen at 1750°C.

Coated-Particle Evaluation (J. M. Kerr)

The preirradiation evaluation previously described[3] has been completed on three batches of pyrolytic-carbon-coated UC_2 from two different vendors. The results of this evaluation are given in Table 4.2. As a result of the evaluation, only two batches, 3M-SP-2 from Minnesota Mining and Manufacturing Company and HTM-1 from High Temperature Materials, Inc., were judged suitable for irradiation tests.

The first irradiation capsule containing HTM-1 material (designated LCP-1) is being irradiated in the LITR. The graphite and "Carbocel" capsules for the C-1 facility in the ORR, described previously,[3] have been loaded with HTM-1 particles and are ready for insertion. A second LITR capsule, LCP-2, has been designed that is to be loaded with batch 3M-SP-2 coated particles. The appearance and microstructure of the particles to be used in this capsule may be seen in Figs. 4.4 and 4.5. As illustrated in Fig. 4.4, the coated particles are polygonal rather than spherical in shape. The structure of the uranium carbide particle and the coating shown in Fig. 4.5 is typical of the vendor's product. The material at the interface between the central carbide sphere and the pyrolytic-carbon coating has been identified as primarily graphite.

[3]Ibid., pp. 104–7.

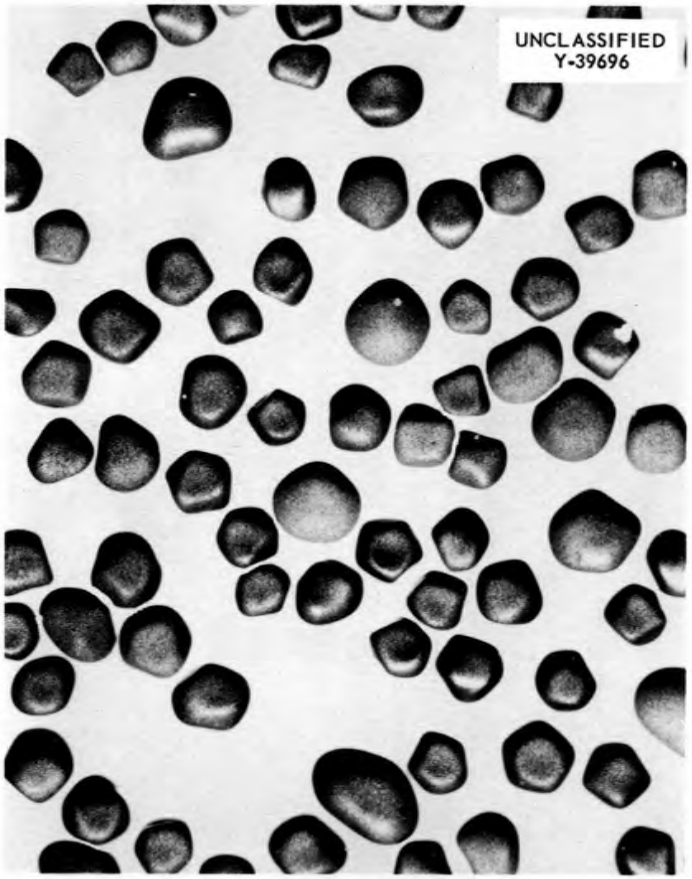

Fig. 4.4. Photograph of 3M-SP-2 Pyrolytic-Carbon-Coated Particles Showing Polygonal Shape. Unmounted, unetched, oblique lighting. 20X.

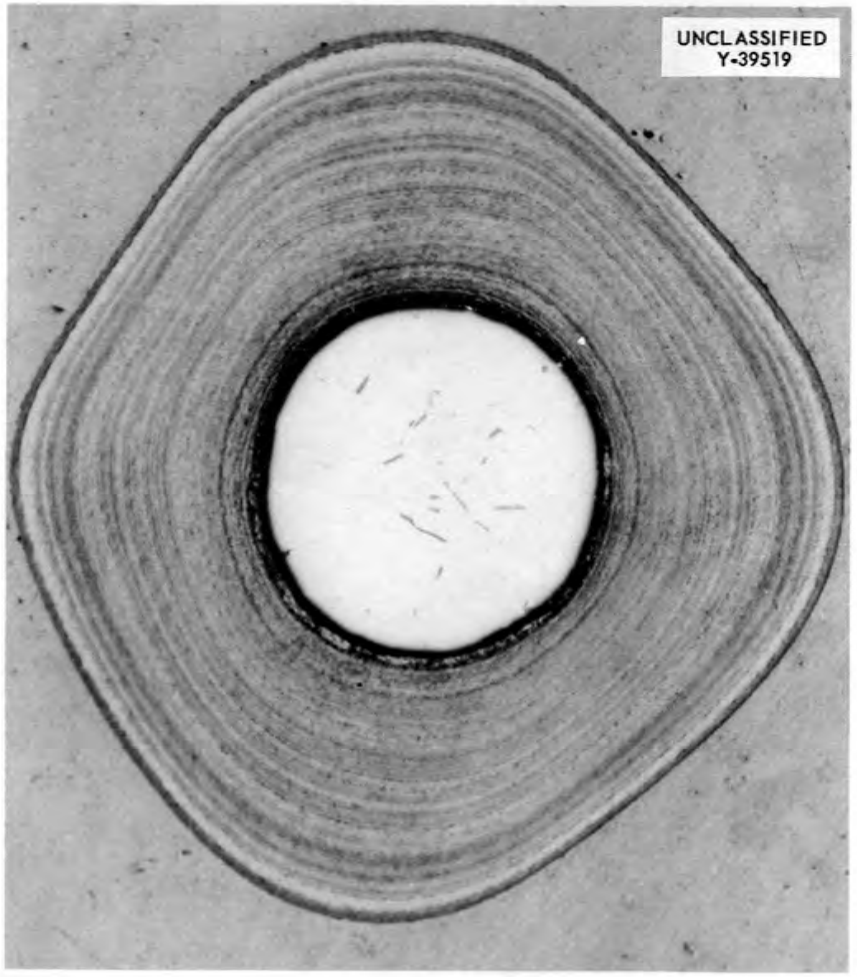

Fig. 4.5. Photomicrograph of a 3M-SP-2 Particle Showing the Carbide Particle and the Pyrolytic-Carbon Shell with Graphite and Unidentified Phases at the Interface. Note nonspherical contour. Unetched, bright-field illumination. 250X.

Table 4.2. Preirradiation Evaluation of Pyrolytic-Carbon-Coated Spherical Uranium Carbide Particles

Sample Designation	Minnesota Mining and Mfg. Co.		High Temperature Materials, Inc. Batch No. 1
	Lot 10695-47	Lot SP-2	
Uranium content, % U/g of particles	50	40	40
Coating thickness, μ	48–96	48–161	109 av
Coated particle diameter, μ	(a)	417–589	417–589
As-received surface contamination, %	9×10^{-4}	$<8 \times 10^{-5}$	$<8 \times 10^{-5}$
Uranium dissolved in acid leaching, as received, %	7×10^{-2}	5×10^{-3}	4×10^{-3}
Surface contamination after three thermal cycles,[b] %	3×10^{-3}	$<8 \times 10^{-5}$	$<8 \times 10^{-5}$
Uranium dissolved in acid leaching after thermal cycling, %	3×10^{-2}	2×10^{-3}	2×10^{-4}
Final surface contamination, %	3×10^{-3}	$<8 \times 10^{-5}$	$<8 \times 10^{-5}$

[a]Polygonal-shaped particles.

[b]Thermally cycled to approximately 1450°C.

Release of Fission Products from Coated Fuel Particles (J. L. Scott, D. F. Toner, R. E. Adams)

Pyrolytic-carbon-coated UC_2 particles from lot No. 10695-47, manufactured by Minnesota Mining and Manufacturing Company, were tested for fission-gas-retention properties after irradiation to a thermal-neutron dose of 6.7×10^{17} neutrons/cm^2 in the ORNL Graphite Reactor. Five individual tests were run between 1400 and 2535°C.

The first specimen was given thermal treatments at the times and temperatures indicated in Fig. 4.6. In this graph the total test time is plotted versus the cumulative release of Xe^{133}. Less than 3×10^{-3}% release of Xe^{133} was detected during the first 90 hr at 1825°C. The sample

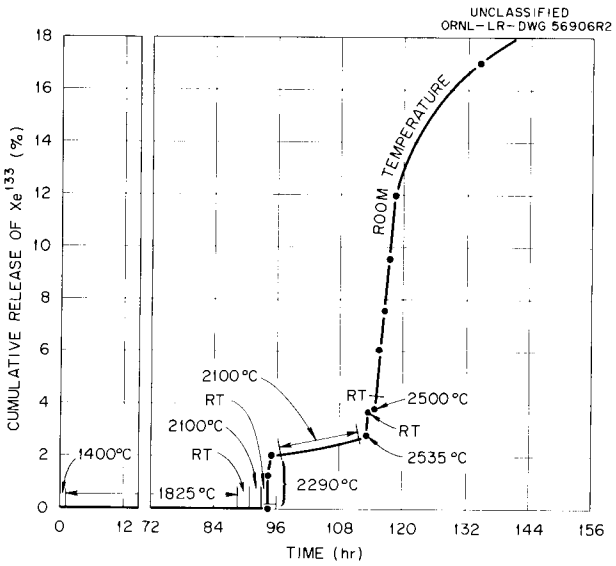

Fig. 4.6. Release of Xe^{133} from 3M Coated-UC_2 Particles (35 Mesh).

was then subjected to a series of thermal cycles between room temperature and the indicated temperatures. Fission gas was not released until the temperature increased to 2290°C. Some of the coatings undoubtedly fractured at this temperature and caused abrupt gas release. Subsequent recycling between room temperature and 2500°C caused additional release. It is interesting to note that in a vacuum of 0.3 μ Hg at room temperature the release of Xe^{133} continued.

In the second test, a second was heat treated at a constant temperature of 2050°C for 103 hr. The results, presented in Fig. 4.7, show that $<3 \times 10^{-3}\%$ of the Xe^{133} was released during the first 37 hr of the test. After 37 hr, the particle coatings started rupturing. The rupture of the third particle occurred at 47 hr. The release associated with this rupture is shown in the inset of Fig. 4.7. An instantaneous release of xenon occurred that amounted to 42.5% of the amount present in the particle. At the end of the test, 29.0% of the total gas in the sample had been released. It is estimated that 53 out of the 101 particles of coated UC_2 had ruptured.

The third test on the coated 3M particles was of 140 hr duration at 1960°C. No Xe^{133} was released, but activity was found on the initially clean furnace. This activity was identified as Ba^{140} and its daughter isotope, La^{140}, in approximately equilibrium quantities. Two additional tests were run to confirm the release of Ba^{140} without concurrent Xe^{133} release. The first was of 22 hr duration at 1900°C; the second was for 1 hr at 1400°C and 2 1/2 hr at 1775°C on sample HTM-1. In both tests Ba^{140} was found. There were also traces of Ru^{103}. No other gamma activity was observed, including Xe^{133}.

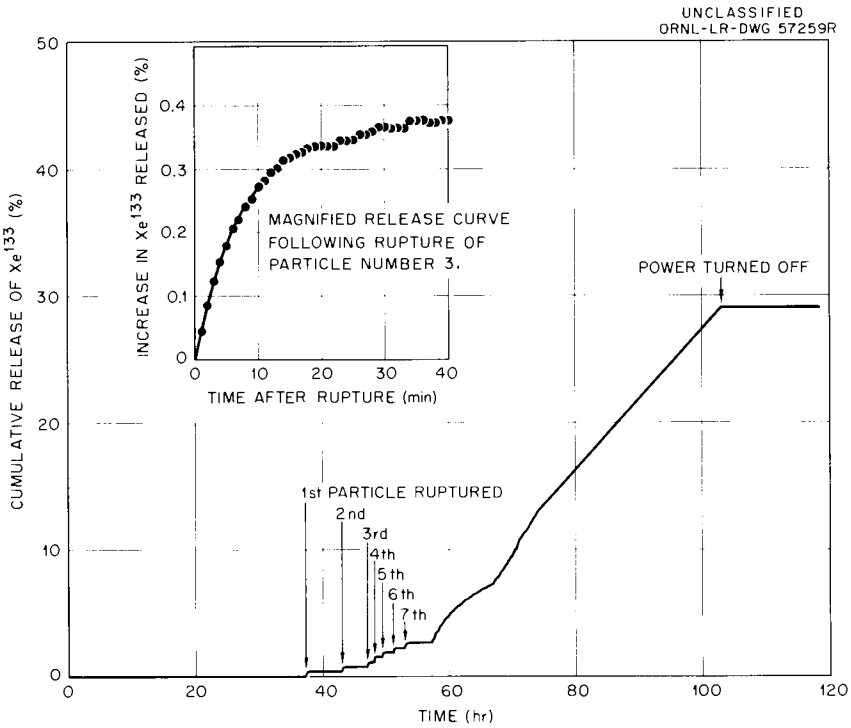

Fig. 4.7. Release of Xe^{133} from Irradiated UC_2 Particles with Pyrolytic Coatings During Heat Treating at 2050°C.

This phenomenon may be due to the preferential reaction of ruthenium with the coatings to form unstable carbides. Barium carbide may melt at a temperature as low as 1770°C, and it has a high vapor pressure.[4] Such a reaction would permit barium ions to go into solution in the carbon coating and pass through the coating by diffusion. Since barium and ruthenium carbides are unstable, the isotopes would be expected to escape when they reach the outer surfaces.

Other elements, such as columbium, molybdenum, and zirconium, form stable carbides and have low vapor pressures. The carbon coatings would tend to retain these fission products as carbides. Since xenon and the other rare gases form no compounds, they are perhaps insoluble in the coating. Thus, only the recoil fraction would enter the coating, and the diffusion gradient is such that most of each isotope would diffuse inward instead of outward.

[4]M. Hansen, Constitution of Binary Alloys, pp. 267–8, McGraw-Hill Book Company, 1958.

Release of Fission Products from Hydrothermal Thoria (J. L. Scott D. F. Toner, R. E. Adams)

Several specimens of a hydrothermal ThO_2–5 wt % UO_2 mixture prepared by the sol-gel process (sample A2177-6) were tested for fission-gas-retention properties in the temperature range 1440 to 2015°C. Individual samples containing 0.2 to 0.6 mg of U^{235} were irradiated to a thermal-neutron dose of 6.77×10^{17} neutrons/cm^2 in the ORNL Graphite Reactor. The specimens were subsequently heated in an induction furnace in a vacuum of about 10^{-3} mm Hg. The fractions of Xe^{133} released at 1440, 1640, 1760, and 2015°C are shown in Fig. 4.8 as a function of the square root of time. These coordinates were used because a straight line on such a plot is indicative of a diffusion mechanism of release. The results show that the amount released increased with increasing temperature and that, with the exception of a small initial burst of gas, the mechanism of release was diffusion. In Fig. 4.9, the log of the diffusion rate parameter D' obtained from these data is plotted versus the reciprocal absolute temperature. From the slope of the curve, the activation energy for diffusion of Xe^{133} from this ThO_2-UO_2 mixture was calculated to be 75.9 kcal/mole, which is to be compared with the 70 to 80 kcal/mole reported for UO_2.

An additional test was then run for 25 hr at 2200°C, and during this test 30.6% of the Xe^{133} in the sample was released. In contrast to the release at lower temperatures, the rate of release was constant, indicating that the mechanism of release was sublimation of the thoria rather than diffusion. For comparison, a sample of UO_2 was tested for 25 hr at 1900°C. All the Xe^{133} was released, and the UO_2 was completely vaporized. The increased stability of ThO_2-UO_2 would be expected as a result of the higher melting point of ThO_2 (3300°C) compared with that of UO_2 (2750°C).

Uranium Carbide Fuels (J. D. Sease, J. P. Hammond)

Uranium monocarbide in comparison with UO_2 offers improved thermal conductivity, higher uranium density, and resistance to thermal shock. At present, however, fabrication of the material is expensive, and its hydroscopic nature imposes practical limitations in handling and storage,

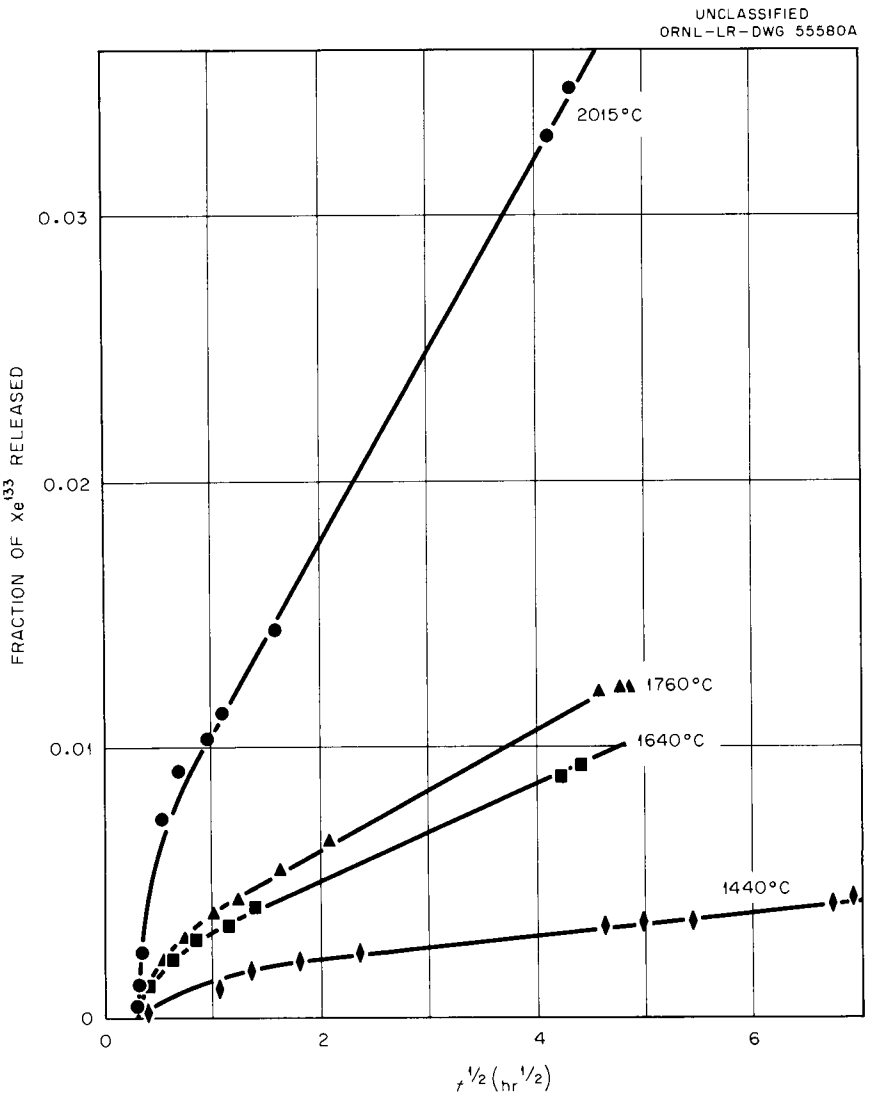

Fig. 4.8. Release of Xe^{133} from a Hydrothermal ThO_2–5 wt % UO_2 Mixture Irradiated to a Thermal-Neutron Dose of 6.77×10^{17} neutrons/cm^2 and then Heat Treated in the Temperature Range 1440 to 2015°C.

even after fabrication into pellets. Sintering temperatures as high as 2000°C may be required to achieve acceptable bulk density, and stoichiometry is disturbed by vapor losses.

Various approaches were investigated for overcoming these disadvantages. One of these involved the use of a permanent cementing agent to lower the fabrication temperature by liquid-phase (eutectic) sintering. Carbides fabricated by this method may take on desirable physical properties, especially when the binder phase assumes a continuous network.

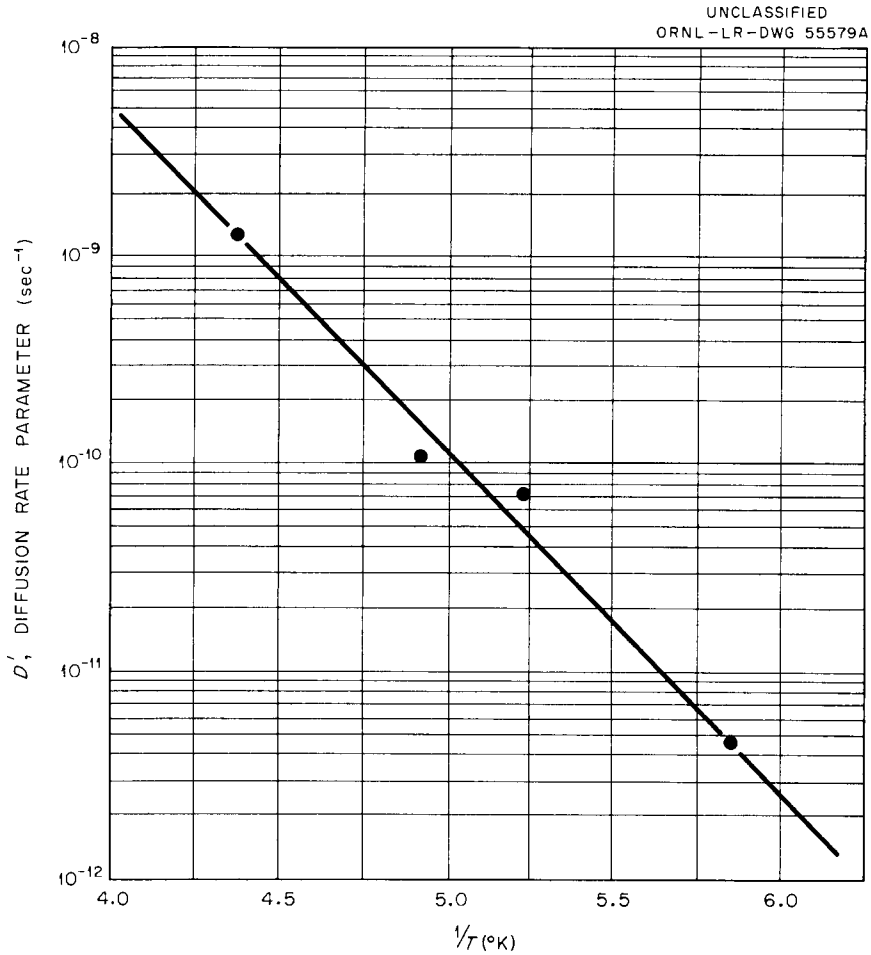

Fig. 4.9. Diffusion Rate Parameter Versus Reciprocal Temperature for a Hydrothermal ThO_2–5 wt % UO_2 Mixture.

Of the various permanent agents examined for cementing uranium carbide (Ni, Cr, U_2Mo, U_3Si_2, and USi_2), the uranium silicides gave the most satisfactory results. An advantage of uranium silicide over the metallic binders is that high fuel density can be maintained while sacrificing little with respect to parasitic neutron capture (σ_a for Si is 0.13 barns/atom). Also, the silicides are readily prepared as very fine, clean powder. The fabrication of the silicide-cemented bodies in general consists of converting arc-cast fingers of UC, U_3Si_2, and USi_2 to powder (<5-μ particles) by crushing and ball milling. After blending the carbide with the silicide, an organic binder (usually camphor) is introduced and the mixture is compacted. These preparatory operations are carried out in argon, and the pellets are fired in a vacuum of 1 to 2 × 10^{-6} mm Hg.

The densities achieved by sintering various compositions of U_3Si_2- and USi_2-bonded UC at several temperatures are given in Table 4.3. It may be seen that good density was achieved for the U_3Si_2-bonded material sintered at 1550°C. A high theoretical density of 97% was recorded for all bodies fired at 1650°C. All pellets were characterized by smooth, lustrous surfaces with sharp edges.

Under certain conditions of fabrication, the U_3Si_2 binder gave a reaction product that appeared as a continuous phase completely enveloping the compact. This structure is shown in Fig. 4.10. The USi_2 binder, on the other hand, usually appeared as equiaxed particles in the final structure, as shown in Fig. 4.11. This difference in microstructure influenced the corrosion resistance of the materials. The U_3Si_2-cemented body, which has a continuous binder phase, gave very substantial resistance to boiling water; however, bodies containing 5, 10, and 15 wt % USi_2 reacted almost as rapidly as arc-cast UC.

Table 4.3. Densities of Sintered U_3Si_2- and USi_2-Bonded Uranium Carbide Pellets

Bonding Material		Theoretical Density[a] (%)			
		Sintering Temperature			
Type	Quantity (wt %)	1500°C	1550°C	1600°C	1650°C
U_3Si_2	9.1[b]	84.5	94.0		
	18.25[b]	89.5	97.5		
	18.25[c]				97.0
USi_2	5.0[d]	81.0	87.0	93.0	97.0
	10.0[d]	70.0	81.0	92.0	97.0
	15.0[d]	72.0	84.0	93.0	97.0

[a]Averaged value determined from values for duplicate specimens.

[b]Pressed with 2 wt % cetyl alcohol at 30 tsi and fired 1 hr at indicated sintering temperature.

[c]Pressed with 2 wt % cetyl alcohol at 30 tsi and fired 2 1/2 hr at indicated sintering temperature.

[d]Pressed with 2 wt % camphor at 10 tsi and fired 2 hr at indicated sintering temperature.

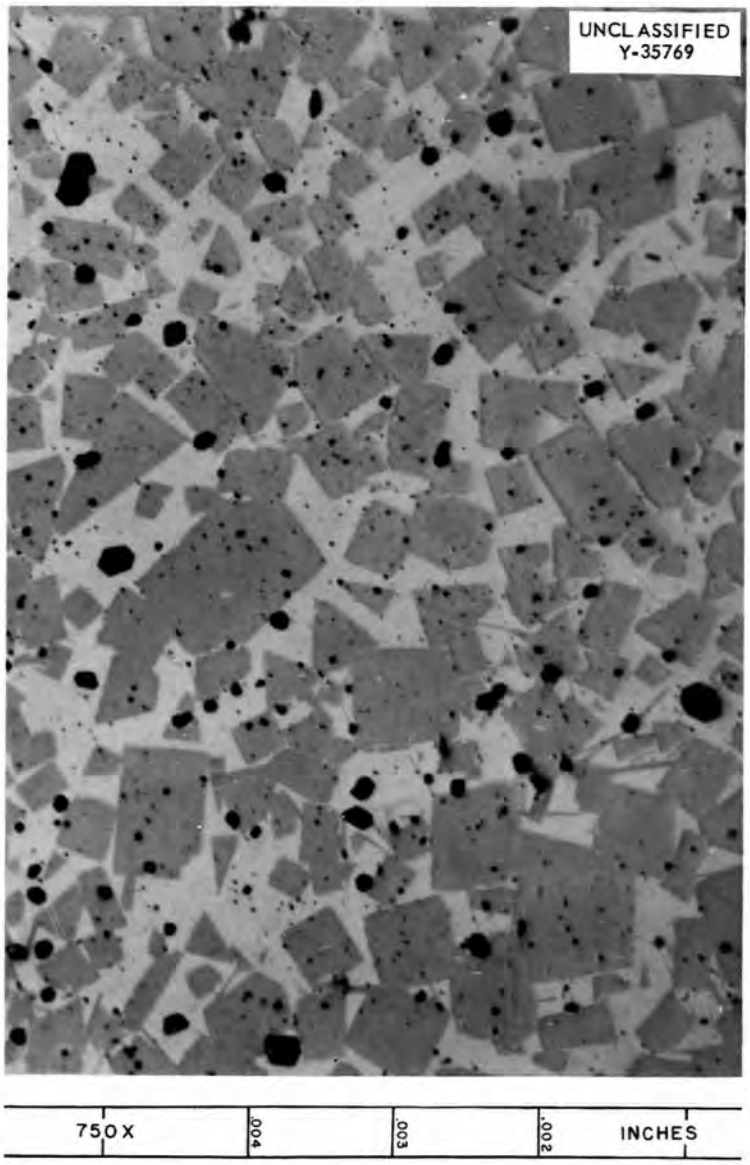

Fig. 4.10. Microstructure of Uranium Silicide-Bonded Uranium Carbide Consisting of UC–18.25 wt % U_3Si_2 and Cetyl Alcohol Binder Fired 2 1/2 hr at 1650°C in Vacuum. As-polished. The light continuous phase is reaction product, the gray material is UC, and the black material has not been identified.

X-ray diffraction analyses of the U_3Si_2-bonded bodies gave evidence of large amounts of UC and small amounts of an unidentified phase or phases resulting from reaction of the U_3Si_2 and UC. Like examinations of the USi_2-bonded materials indicated large amounts of UC and lesser amounts of α-USi_2.

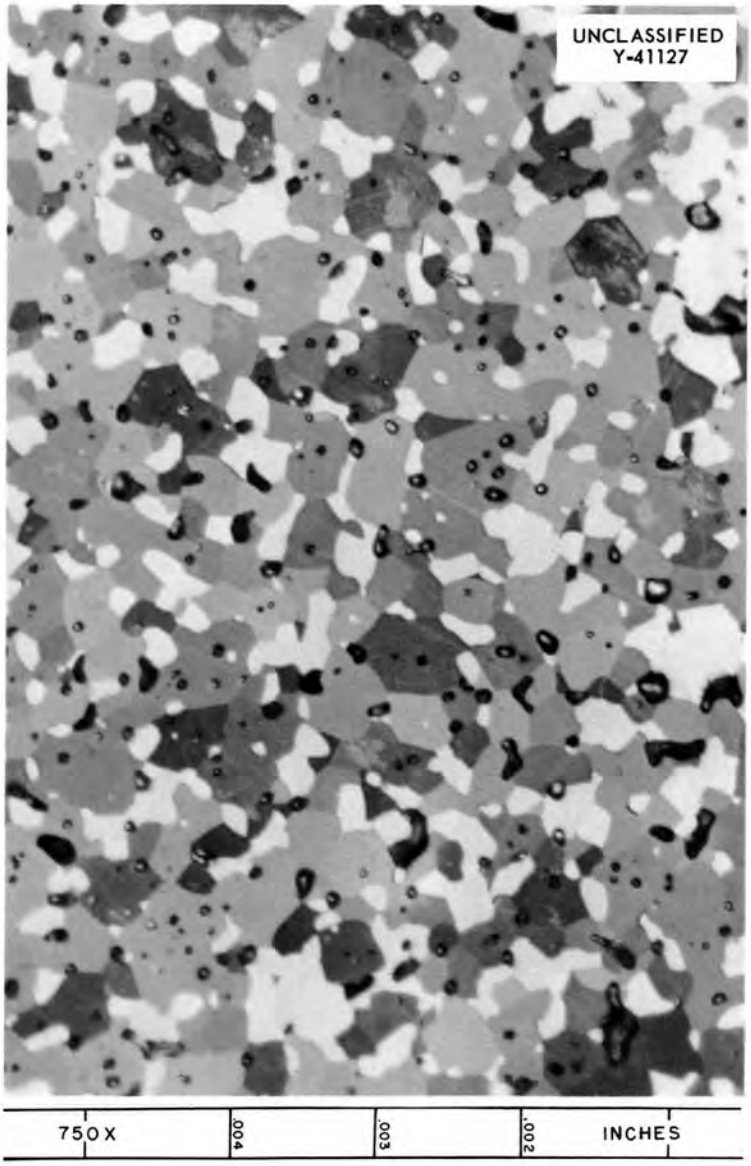

Fig. 4.11. Microstructure of Uranium Silicide-Bonded Uranium Carbide Consisting of UC–10 wt % USi_2 and Camphor Binder Fired 2 hr at 1600°C in Vacuum. Etched with 30% HNO_3–30% acetic acid–30% H_2O. The white phase is USi_2 and the remaining material is UC.

Compatibility of UC with Beryllium (J. F. Murdock)

A series of diffusion experiments was completed for determining the extent of reaction between UC and beryllium at temperatures of 700 to

1000°C. In a preliminary experiment at 1000°C using fragments of UC,[5] extensive reaction was observed at the interface. Polished wafers were used in the diffusion couple in all subsequent experiments to ensure intimate contact. The thicknesses of the intermetallic reaction zones were measured on polished, anodized sections with the use of a precision measuring microscope. A sample of the intermetallic reaction product was removed with an ultrasonic microchisel and identified by x-ray diffraction as UBe_{13}.

A summary of the data obtained in these diffusion experiments is presented in Table 4.4. These data indicate that the reaction between UC and beryllium increases rapidly in the temperature range 750 to 800°C.

Table 4.4. Results of Thickness Measurements on Diffusion Couples of UC and Beryllium

Temperature (°C)	Contact Time (hr)	Average UBe_{13} Thickness (μ)
700	185	7
750	187	27
800	162	115
850	144	106
900	121	150
950	103	131
1000	90	176

Structural Materials Evaluation

Coated Graphite Support Sleeves for EGCR (F. L. Carlsen, Jr., R. W. McClung)

Oxidation Resistance of Coated Sleeves. The oxidation resistance of a pyrolytic-carbon-coated graphite sleeve was determined at 600°C in

[5]GCR Quar. Prog. Rep. March 31, 1961, ORNL-3102, pp. 108–10.

air using the procedure and apparatus previously described.[6] The oxidation rate of the coated specimen was approximately one-half that of the uncoated Speer nuclear grade 2 specimen during the first 2 hr but was nearly the same as that of the uncoated material during an additional 2-hr test. A visual inspection of the surfaces of the coated sleeve revealed that the coating had been burned away in one area on the outer surface; however, the coating on the inner surface was still intact. This difference in behavior was primarily due to the coating on the outer surface being only 0.001 in. thick; further, the outer coating contained many discontinuities, whereas the coating on the inner surface was continuous and approximately 0.010 in. thick.

The evaluation of four sleeves of 901S graphite coated with siliconized SiC by American Lava Corporation was continued. Three of the sleeves were tested for oxidation resistance in the as-received condition by heating in an open furnace at 1000°C for 1 hr. Two of the sleeves lost approximately 1 g and the third lost approximately 8 g. The fourth sleeve was heated at 600 to 800°C for approximately 8 hr in an open furnace and lost 15 g. The original weight of the sleeves was approximately 10 kg. The weight losses were due to oxidation of the graphite through isolated defects in the siliconized SiC coatings. It is anticipated that the results of the tests on the first two specimens will be used as the basis for an oxidation specification for EGCR sleeves.

Samples of seven experimental grades of graphite from National Carbon Company which were completely coated with SiC were tested for oxidation resistance at 600°C. Three of these samples were extruded and four were molded. The particular grades of base graphite chosen for the samples were reasonably isotropic with respect to the coefficient of thermal expansion. The values of this property for the three extruded samples varied between 4.5×10^{-6} and $5.2 \times 10^{-6}/°C$ over the temperature range 20 to 100°C. The four molded samples were said to be "fairly isotropic," but no physical property data were given. Of the molded samples, only sample NT-0056 was completely oxidation resistant after 76 hr of testing

[6]Ibid., pp. 110–15.

in air at 600°C. Of the extruded samples, the grade 927 sample showed a weight gain of approximately 0.08 g after 8 hr at 600°C but a weight loss of 34 g after 72 hr at this temperature. The original weight of the sample was 1671 g. This weight loss was due to oxidation of the graphite through isolated defects, as was shown by the formation of a few low-density regions under the coating. None of the other samples were completely oxidation resistant when tested at 600°C in air.

The oxidation rates of two of the SiC-coated samples submitted by National Carbon Company were determined as a function of time at 600°C in air. The data, which are based on intermittent test periods, are presented graphically in Fig. 4.12, along with the results of similar tests on specimens of uncoated Speer nuclear grade 2 graphite. These data indicate that relative oxidation rates based on 2-hr tests under the conditions indicated are approximately representative of those which would be obtained in tests of much longer duration.

Coating Thickness. Some metallographic measurements have been made of the thickness of the siliconized-SiC coatings on graphite. All the coatings lack uniformity of thickness, with some of the maximum thicknesses being as much as seven times the minimum thickness in the same localized

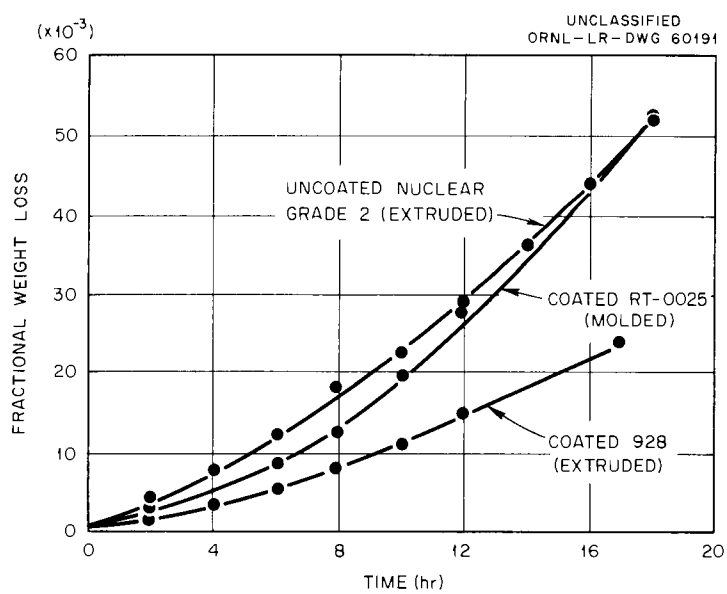

Fig. 4.12. Oxidation of Coated and Uncoated Graphite Specimens in Air at 600°C.

section. In addition there is frequent evidence that discrete coating particles have penetrated the graphite beyond the coating-to-graphite interface. However, average coating thickness measurements were recorded for comparison with eddy-current measurements. As might be expected because of the gross variations of the data, some measurement errors were found. The best agreement seemed to be for the thin coatings, which exhibited the most uniformity. It is evident that the coatings must be much more uniform if measurements are to be meaningful and accurate.

Coating Composition. The chemical composition of the SiC-base material was determined in order to estimate the effect of the coating on the thermal-neutron-absorption cross section, σ_a, for the graphite. The results of spectrographic analyses of the coatings applied to full-size EGCR support sleeves are given in Table 4.5. The increase in the absorption cross section for the graphite sleeve as a result of the addition of the coating was calculated to be approximately 1.6, 8.9, and 1.6 mb

Table 4.5. Impurity Composition of SiC Coatings from Three Vendors

Impurities	Quantity of Impurity in SiC Coating (wt %)		
	American Lava Corp.	National Carbon Co.	Norton Co.
Al	>1	>1	>1
B	5×10^{-4}	5×10^{-4}	5×10^{-4}
Ca	2×10^{-2}	High	2×10^{-2}
Cr	10^{-2}	5×10^{-2}	10^{-3}
Cu	5×10^{-3}	5×10^{-3}	2×10^{-3}
Fe	>0.1	>0.1	5×10^{-3}
Mg	5×10^{-3}	2×10^{-3}	10^{-3}
Mn	10^{-2}	0.1	2×10^{-4}
Mo	2×10^{-4}	Trace	2×10^{-4}
Ni	5×10^{-3}	5×10^{-3}	2×10^{-3}
Pb	10^{-2}	5×10^{-3}	10^{-3}
Ti	10^{-2}	High	10^{-2}
V	10^{-2}	10^{-2}	10^{-2}
Eu[a]	$\leq 1.7 \times 10^{-6}$	$\leq 2.3 \times 10^{-4}$	$\leq 2.7 \times 10^{-6}$
Ash[b]	2.5	14	3.5

[a]Determined by a neutron-activation analysis.

[b]Weight of coating per 100 g of coated graphite.

for the American Lava, National Carbon, and Norton coatings, respectively, based on the analyses and the ash content.

Several coated samples representative of specimens prepared according to process and material variations designed to lower the amounts of impurities in the coatings were obtained from American Lava Corporation. The results of the chemical analyses of these samples are given in Table 4.6. The calculated increase in the absorption cross section for the graphite sleeve as a result of addition of the 1 wt % coating is given in Table 4.7. For these calculations the boron content in samples TP-1, TP-2, and TP-3 was assumed to be 5 ppm. The weight gain after coating

Table 4.6. Results of Chemical Analyses of Coated Graphite Samples

Sample Designation	Ash Content (wt %)	Impurities in Ash (ppm)					Sample Type
		Fe	Mn	Ti	V	B[a]	
Group 1	0.08	60	<60	180	<20	5	Uncoated
Group 2	19.5	3060	980	275	<20	5	Standard process coating
Group 3	24.0	2740	610	195	<20	1	Coating process variation
Group 4	28.0	3440	900	205	<20	1	Coating process variation
901S	0.06	100	<80	320	<20		Uncoated
TP-1	16.1	1320	170	425	<20		Coated (low Fe)
TP-2	22.6	2040	490	445	<20		Coated (low Fe)
TP-3	22.8	205	<5	125	<20		Coated (low Fe)

[a]Determined by spectrographic analysis.

Table 4.7. Calculated Increase in Thermal-Neutron-Absorption Cross Section of Graphite Sleeve As a Result of the Addition of the 1 wt % Coating

Sample	$\Delta\sigma_a$ (mb/wt % coating)		
	Including Impurities	Impurities Only	Boron Only
Group 2	0.777	0.093	0.042
Group 3	0.729	0.047	0.008
Group 4	0.743	0.059	0.008
TP-1	0.745	0.061	0.042
TP-2	0.758	0.074	0.042
TP-3	0.729	0.045	0.042

was used to determine the silicon content. It should be noted from these data that the increase in σ_a is primarily due to the silicon and boron.

Thermal-Neutron-Absorption Cross-Section Measurements. The thermal-neutron-absorption cross section of the standard process coating from American Lava Corporation was measured in the Hanford Test Reactor. These Δih measurements[7] were made on three specimens of EGCR core graphite before and after the application of the coating.

The average thermal-neutron-absorption cross section in millibarns per carbon atom is given by the equation[7]

$$\sigma_a \ (2200 \text{ m/s}) = 4.47 \pm 0.04 - (0.733 \ \Delta\text{ih} \pm 0.03) \quad . \tag{1}$$

The increase in σ_a as a result of the addition of the 1 wt % coating is then

$$\frac{\Delta\sigma_a}{\text{wt \% coating}} = \frac{-0.733 \ (\Delta\text{ih}_{\text{after}} - \Delta\text{ih}_{\text{before}}) \pm 0.06}{\text{wt \% coating}} \quad . \tag{2}$$

The results of the Δih measurements are given in Table 4.8.

The average value of 0.836 mb/wt % coating is significantly higher than the 0.777 mb/wt % coating predicted from the chemical analyses;

[7]A comparative purity measurement in terms of change in reactor period measured in inhours. See P. F. Nichols, Absorption Cross Section of Graphite, Nuclear Sci. and Eng., 7(5): 395–9 (1960).

Table 4.8. Results of Δih Measurements on Coated Graphite Samples

Specimen No.	Amount of Coating (wt %)	Δih		$\Delta\sigma_a$ (mb/wt % coating)
		Uncoated	Coated	
FN-180	4.03	0.614	−4.034	0.846 ± 0.018
FN-151	4.86	0.682	−4.884	0.840 ± 0.018
FN-42	4.38	0.666	−4.256	0.823 ± 0.018

however, an increase of 6 ppm in the boron content would account for the difference.

Dimensional Behavior of the EGCR Fuel Elements at Elevated Temperatures (W. R. Martin)

The study of the dimensional behavior of a simulated EGCR stainless-steel-clad fuel element has been completed.[8] It was determined that the expansion characteristics of the stainless steel cladding and the fuel pellet can be predicted from isothermal-expansion data. Of interest was the depth of the end plenum during the initial heatup in each element to operating temperature as a function of type of pellet, pellet central temperature, average cladding temperature, and the assembled gap between the top end plug and MgO insulator. These data are presented in Figs. 4.13 and 4.14 and are valid only if the pellet is free to move vertically within and relative to the cladding.

[8]W. R. Martin and J. R. Weir, Jr., Dimensional Studies of a Simulated EGCR Fuel Element at Elevated Temperatures, ORNL-3103 (in press).

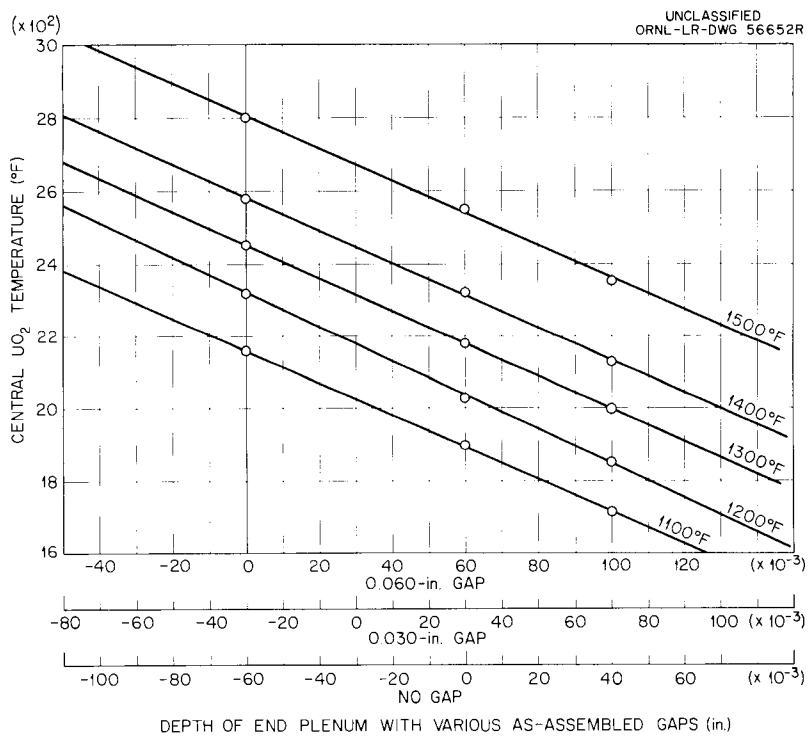

Fig. 4.13. Predicted Depth of End Plenum for Square-End Pellets in EGCR Fuel Element As a Function of Operating Temperature.

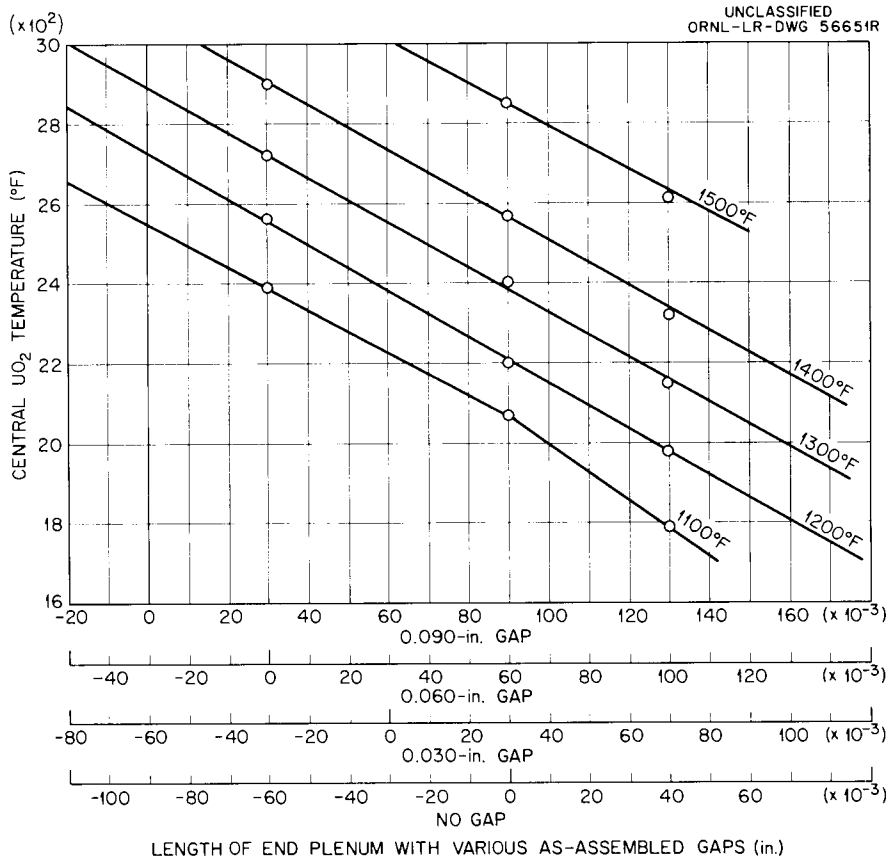

Fig. 4.14. Predicted Depth of End Plenum for Dished Pellets in EGCR Fuel Element As a Function of Operating Temperature.

Thermal cycling of an element that contains a diametral gap causes only the normal thermal expansions, as shown in Fig. 4.15, and only slight degradation of the fuel pellet.[9] On the other hand, thermal cycling of a fuel element that has no diametral gap results in plastic deformation of the cladding. The magnitude of the strain is a linear function of the number of thermal cycles for a given set of thermal and pressure conditions, as shown in Fig. 4.16. A summary of data obtained as a function of both upper and lower temperature limits for a given rate of temperature change and hold time at the upper temperature limit during cycling is presented in Fig. 4.17. The magnitude of the plastic strain per cycle is affected by the heating and cooling rates and by the hold time at the upper temperature limit. Examples of these effects are shown in Figs. 4.18 and 4.19. These cycling experiments demonstrated that one necessary

[9]GCR Quar. Prog. Rep. June 30, 1960, ORNL-2964, pp. 84–90.

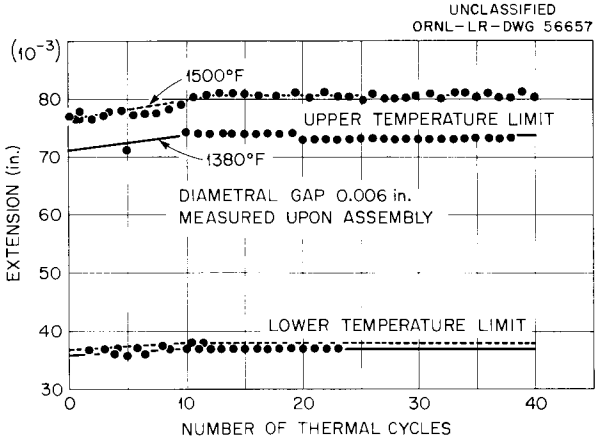

Fig. 4.15. Dimensional Behavior of Uncollapsed Fuel Capsule During Thermal Cycling.

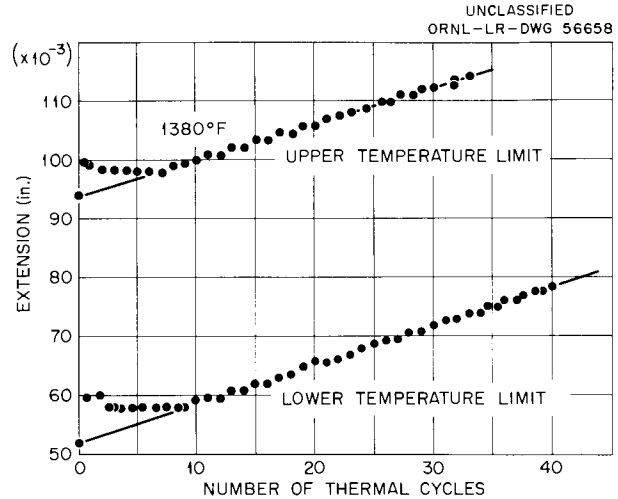

Fig. 4.16. Dimensional Behavior of a Collapsed Fuel Capsule During Thermal Cycling.

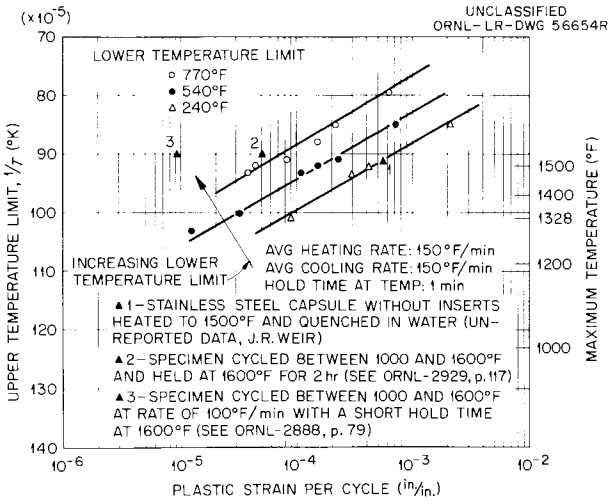

Fig. 4.17. Effect of Temperature Limits on Plastic Elongation of Thermally Cycled Simulated EGCR Fuel Elements.

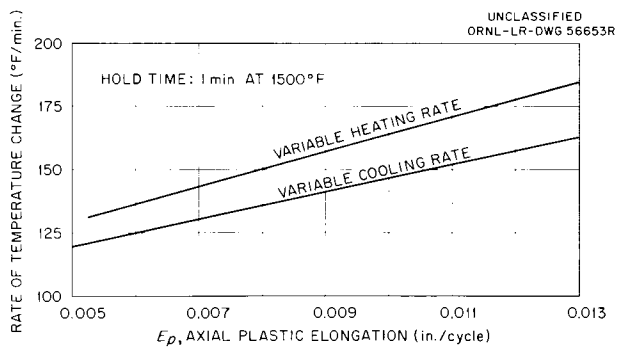

Fig. 4.18. Effect of Heating and Cooling Rate on Deformation of EGCR Fuel Element with no Diametral Gap Between Cladding and Fuel.

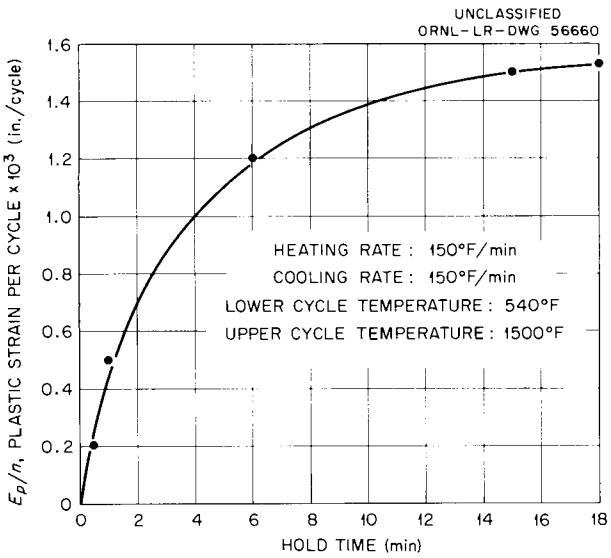

Fig. 4.19. Effect of Hold Time at Top of Cycle on Plastic Strain Per Cycle of EGCR Fuel Element with No Diametral Gap Between Cladding and Fuel.

criterion for axial extension of the fuel element is the absence of the diametral gap between fuel and cladding. Further, the relationship between the parameters which determine the magnitude of the plastic strain suggests that a time-dependent thermally activated deformation process is responsible for the growth. It is noted that there is a critical maximum temperature limit which must be exceeded and a minimum temperature below which the capsule must be cycled before axial elongation is detectable during 50 cycles.

Reactions of Type 304 Stainless Steel with CO and CO_2 in Helium (H. Inouye)

Two more tests on type 304 stainless steel were completed: an 818-hr test in an atmosphere of CO_2 and helium and an 840-hr test in an atmosphere of CO, CO_2, and helium. These tests were run to determine whether pure CO_2 in helium is carburizing at some temperature, to investigate the relationship of the ratio of the partial pressures of CO_2 and CO (P_{CO_2}/P_{CO}) to the oxidation rate, and to study the relationship of the $(P_{CO})^2/P_{CO_2}$ ratio to carburization.

The study of the effect of CO_2 was conducted with CO_2 at a concentration of 0.244 vol %, based on 315-psi helium plus impurities (0.0524 atm), and the only other impurity in the helium carrier gas was 0.02% N_2. As reported previously,[10] it was postulated that the "break-away" oxidation observed at 1800°F would occur in a shorter time if the P_{CO_2}/P_{CO} ratio were increased. This hypothesis was confirmed by the present test with $P_{CO_2}/P_{CO} = \infty$ in which the "break-away" reaction occurred at 120 hr

[10]GCR Quar. Prog. Rep. March 31, 1961, ORNL-3102, pp. 126–8.

compared with 500 hr in the previous test with $P_{CO_2}/P_{CO} = 0.669$. The principal oxide at the gas-metal interface was Fe_3O_4, which grew as oxide whiskers, rather than $3Cr_2O_3 \cdot Fe_2O_3$, which was the oxide found in similar tests at approximately 1400°F.

The phases identified at the surfaces of the specimens oxidized at several temperatures are listed in Table 4.9. It appears from the test results that $3Cr_2O_3 \cdot Fe_2O_3$ is a metastable phase which exists for times of the order of 300 hr. The oxide phase or phases which determined the reaction rates were estimated from the occurrence of inflections in an Arrhenius plot, assuming parabolic oxidation rates. Three such inflections were apparent in the temperature range 800 to 1850°F, from which it was concluded that the rate controlling oxides were Fe_2O_3 up to 1350°F, Cr_2O_3 between 1350 and 1600°F, MnO between 1600 and 1700°F, and Fe_3O_4 above this temperature. The presence of weak chromium lines is not consistent with any theory and is presently assumed to be in error.

Carbon dioxide appears to be both carburizing and decarburizing to type 304 stainless steel. Up to 1300°F no carburization was detected, while between 1300 and 1700°F the carbon content increased. A maximum in the carbon content of 0.24% occurred at 1614°F. Decarburization occurred above 1700°F and increased in extent at higher temperatures.

Table 4.9. Phases Identified on Type 304 Stainless Steel Specimens Oxidized in CO_2 for 818 hr

Specimen Temperature (°F)	Phases[a]	Remarks
1238	α-Fe, Fe_2O_3, Cr_2O_3	Green-brown powdery oxide
1561	α-Fe, Cr_2O_3, MnO, Fe_3O_4	Green-brown powdery oxide
1614	α-Fe, MnO, Cr_2O_3, Fe_3O_4	Gray-tan powdery oxide
1715	α-Fe, Fe_3O_4, MnO, Cr_2O_3	Black crystalline oxide over green-brown oxide
1787	Fe_3O_4, α-Cr	Black crystalline whiskers
1850	Fe_3O_4, α-Cr	Black crystalline whiskers

[a]Listed in order of abundance.

The test conducted with a CO-CO_2 mixture in helium was intended to verify that when protective oxides are formed the reaction rate is independent of the pressure of $CO + CO_2$ and that carburization of the metal is dependent on the concentration. The composition of the atmosphere was 0.0117 vol % CO_2 and 0.111 vol % CO, based on 315-psi total helium pressure (P_{CO_2} = 0.0025 atm, P_{CO} = 0.0238 atm). These concentrations give $P_{CO_2}/P_{CO} = 0.105$ and $(P_{CO})^2/P_{CO_2} = 0.227$.

The reaction rate of type 304 stainless steel in this atmosphere was parabolic at 1800°F. The equation of the rate curve was calculated to be

$$\Delta w = 0.064\ t^{0.477} \quad , \tag{3}$$

where Δw is in milligrams per square centimeter. In a previous test at approximately the same gas ratio but twice the concentration, an 800-hr weight gain of 1.44 mg/cm^2 occurred, which is to be compared with 1.66 mg/cm^2 in the present test. The variations in the reaction rates with temperature in this atmosphere indicated that two oxides were present, as was the case in the previous test. The reaction rates at this low concentration of $CO + CO_2$ were equivalent at temperatures above 1500°F to the reaction rate in a previous test with twice the concentration. Below 1500°F the reaction rates at the lower concentration were higher. It appears from this behavior that lower gas concentrations favor the formation of spinels rather than Cr_2O_3. Carbon analyses are being obtained on samples from this test.

Studies of Pressure-Vessel Steels (ORNL Subcontract No. 1083 at Rensselaer Polytechnic Institute; status reported by G. M. Slaughter and P. Patriarca)

Investigations are continuing in an effort to obtain a better understanding of the brittle-fracture characteristics of the heat-affected zones in welds of ASTM A-212, grade B, pressure-vessel steel. The results obtained from the work being carried out at Rensselaer Polytechnic Institute are summarized in Table 4.10. It may be seen that thermal cycles with peak temperatures of 2400°F in the heat-affected zones of welds made

Table 4.10. Simulated Welding Thermal Cycles and Resulting Transition Temperatures for A-212, Grade B, Steel

Peak welding temperature: 2400°F

Energy Input (joules/in.)	Initial Plate Temperature (°F)	Postwelding Heat Treatment	Transition Temperature (°F)	
			Ductility (10 ft-lb)	Fracture (50% shear)
		1-in. Plate		
As received			−22	70
50 000	80	None	105	
	80	1150°F for 4 hr	−35	25
100 000	80	None	125	230
	80	1150°F for 4 hr	90	210
150 000	80	None	90	220
	80	1150°F for 4 hr	115	213
200 000	80	None	100	233
	80	1150°F for 4 hr	80	203
		4-in. Plate		
100 000	80	None	92	
	80	1150°F for 4 hr	−30	63
	350	1150°F for 4 hr	80	185

in 1-in. plate at energy inputs from 50 to 200 kj/in. drastically lowered the notch toughness of the base material. In 4-in. plate, a thermal cycle with a 2400°F peak temperature associated with an energy input of 100 kj/in. significantly reduced the impact strength of the base plate. A thermal stress relief was effective in improving only those areas in the 1-in. plate exposed to a 2400°F peak temperature that had an energy input of 50 kj/in. At higher energy inputs, postheating failed to improve the as-welded impact properties. However, the impact strength of those areas in the 4-in. plate that experienced a 2400°F peak temperature during welding with an energy input of 100 kj/in. was significantly increased following a 4-hr stress relief at 1150°F.

From the thermal-cycle curves shown in Fig. 4.20, it is evident that the cooling rates associated with a given weld energy input are considerably more rapid in the 4-in. plate than in the 1-in. plate. The larger mass of material involved provides a much larger heat sink and results in correspondingly faster cooling rates. A summary is presented in Table 4.11 of the results of the cooling curve analysis and the hardness measurements associated with the particular microstructures which are generated. It is evident that the cooling curves associated with an energy input of 50 kj/in. in 1-in. plate (initial plate temperature of 80°F) are essentially equivalent to the cooling curves from 100 kj/in. in 4-in. plate, and similar impact behavior would be expected. In addition, Fig. 4.20 and Table 4.10 indicate that the incorporation of a 350°F preheat makes the 100 kj/in. cooling curves approximately equivalent for the two thicknesses.

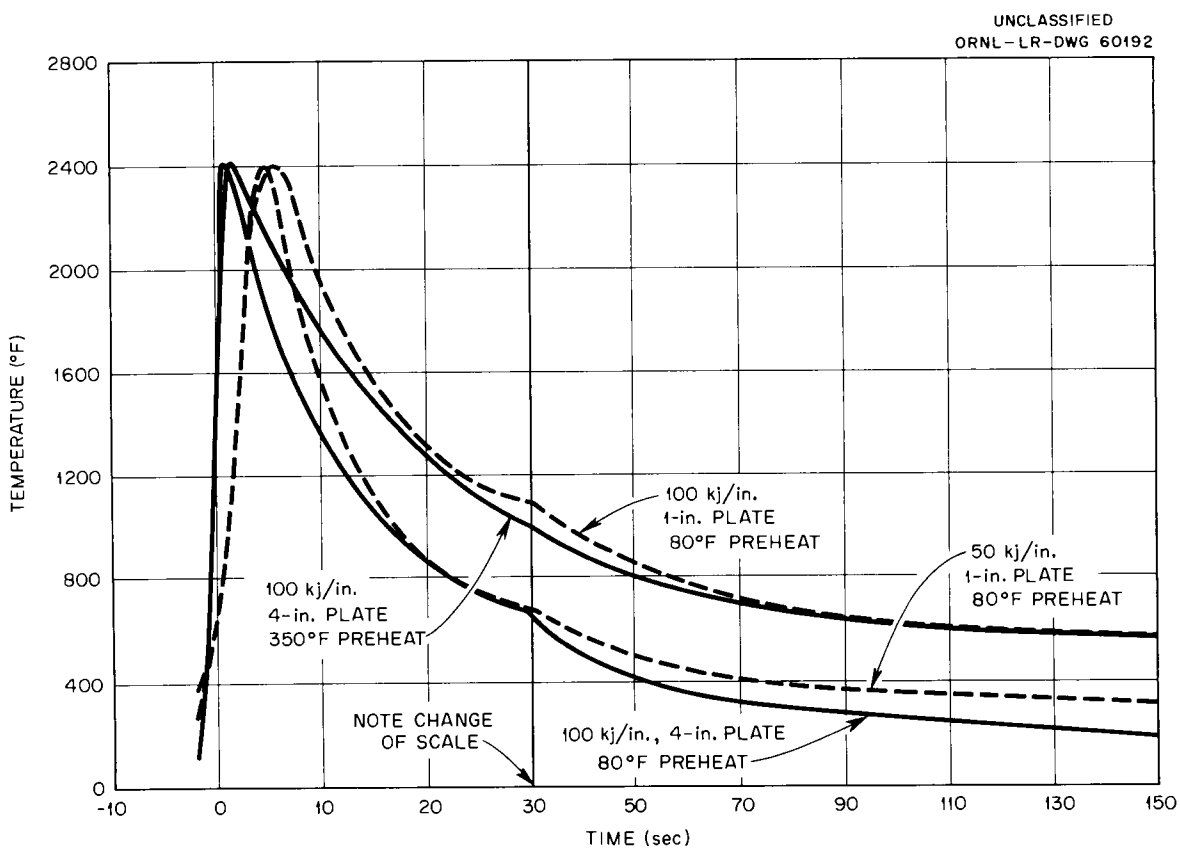

Fig. 4.20. Thermal Cycles Associated with Various Combinations of Plate Thickness and Weld Energy Input.

Table 4.11. Simulated Welding Thermal Cycles and Related Cooling Rates and Hardness

Peak welding temperature: 2400°F
As-received hardness: 164 VPN

Energy Input (joules/in.)	Initial Plate Temperature (°F)	Instantaneous Cooling Rate (°F/sec)		Hardness (VPN)	
		At 1000°F	At 1300°F	As Welded	After Stress Relief
		1-in. Plate			
50 000	80	43.8	83.4	378	280
100 000	80	13.6	31.9	271	220
150 000	80	5.5	15.4	260	236
200 000	80	2.0	7.2	235	227
		4-in. Plate			
100 000	80	37.7	70.6	371	266
100 000	350	15.8	38.0		251

This study is presently being concentrated on the development of a set of suitable welding conditions that will permit an acceptable notch toughness in the heat-affected zone after welding and stress relief. It appears that it would be poor practice to subject weldments of ASTM A-212, grade B, steel welded at low energy inputs to conditions of severe restraint before postheating.

Manufacturing and Inspection Methods Development

Fabrication of Instrumented Fuel Capsules for In-Pile Tests
(E. A. Franco-Ferreira)

Work has been continued on the development of procedures for fabricating instrumented fuel capsules for the irradiation program. The over-all techniques used have been described previously.[11]

[11]Ibid., pp. 131–3.

In the course of the fabrication development, serious limitations in the original capsule design have appeared. For example, after the capsules are fabricated, the external portions of the thermocouples must withstand considerable handling and bending in the process of installing them into the experimental facility. During these handling and bending operations, the 0.040-in.-o.d. thermocouples on the capsule inner surface were subject to breakage. This was due to two causes: (1) the thermocouples were inherently delicate and (2) stress concentrations and localized thermocouple cladding embrittlement existed where the thermocouples were brazed into the end caps with GE-81 (Ni-Cr-Si) brazing alloy.

As a result of these difficulties, a modification was made in the surface thermocouples in order to increase their durability. The modified thermocouple consists of a 0.060-in.-o.d. stainless steel-sheathed Chromel-Alumel unit swaged to 0.038 in. o.d. over the length located inside the capsule. The section of the thermocouple in which the transition from 0.038 in. o.d. to 0.060 in. o.d. occurs is contained inside the end cap. Thus, the part of the thermocouple that is subject to high stress concentrations and bending has a fairly heavy cladding and an o.d. of 0.060 in.

Three capsules have been successfully fabricated using this design; two of these are being irradiated and one was retained as a spare. The central thermocouple wells of the two capsules being irradiated were fabricated from tungsten and Fansteel-82 alloy, while the central well of the spare capsule was fabricated from molybdenum.

Nondestructive Testing of Through-Tube Weldments (K. V. Cook, (R. W. McClung)

Test radiographs were made under conditions which simulated the expected background radiation in order to further test the feasibility of radiographic examination of the EGCR experimental loop through-tube weldments.[12] A 3.1 curie Ir^{192} source located at the axis of the tube was used for the primary radiation source for radiography of the circumferential weld. A 4.5-curie Ce^{137} source located approximately 3.5 ft from the film was used to provide the fogging background. Relative exposure

[12]Ibid., pp. 135–6.

time of each of the sources was adjusted to account for film placement and removal in the reactor and to provide for usage of at least a 10-curie Ir source. No significant loss of detail was observed on the radiographs. Therefore, if the original estimates of the background irradiation are correct, radiographic examination of the welds will be possible. The principal limitation on radiographic quality will be the very poor geometrical relationship between the source, specimen, and film. In addition the accomplishment of the inspection will depend on the development of adequate mechanical fixtures to properly position the source and film.

A preliminary investigation was made of an alternate procedure to overcome some of the fogging background if it exceeds the estimates. A dilute chemical solution of sodium thiosulfate and potassium ferricyanide can be used to reduce the film density on the finished radiograph. A test was performed during which an aluminum step wedge was radiographed to produce a high-contrast film with densities in the range from about 0.5 to 5.7. A uniform exposure was superimposed on the film to produce a density range from about 3.5 to greater than 7.4. This film was subsequently reduced to bring the over-all density down to approximately 1.25 to 5.25. The original film contrast was restored for final film densities up to about 2.0. Beyond this a slightly reduced contrast was observed. Further studies should define more accurately the capabilities and limitations of this technique.

Diffusion of Carbon in Dissimilar-Metal Welds (ORNL Subcontract No. 1444 at Virginia Polytechnic Institute; status reported by G. M. Slaughter)

The diffusion of carbon in dissimilar-metal welds at elevated temperatures is being studied at Virginia Polytechnic Institute. The pertinent results and conclusions for welds of type 304 stainless steel to ASME SA-212 steel are summarized below.

The diffusion coefficients that were obtained are somewhat less than those listed in current literature. When carbon diffuses into the AISI type 304 stainless steel side of the joint, the stainless steel adjacent to the original interface becomes saturated with carbon, and any further diffusion can occur only from this saturated zone. It is generally

accepted that the diffusion rate of carbon is more rapid in ferrite than in austenite, so the diffusion of carbon from the ferrite to the austenite will be controlled by the slower diffusion rate in the austenite. Examination of the type 304 stainless steel side of the interface shows that diffusion is more rapid along the grain boundaries of the austenite than within the grains.

From the calculations it seems that the major part of the carbon diffusion occurred in the early stages of exposure at the temperature investigated and that after prolonged exposures the width of the decarburized zone changed very little. This indicates that the major portion of the property changes in welds between AISI type 304 stainless steel and SA-212 steel would occur within relatively short times.

Beryllium Investigations

Compatibility of Beryllium with Gases (W. J. Werner)

Reaction with Wet CO_2. The rate of reaction of high-purity Pechiney flake beryllium with CO_2 containing approximately 4 vol % $H_2O(g)$ was studied at 650 and 725°C for times up to 600 hr. At 650°C the reaction rate was similar to that observed in dry CO_2; however, at 725°C a "breakaway" reaction occurred after 60 to 70 hr. Analyses of these specimens after testing showed an increase in the carbon content of 0.031% in the 650°C test and 0.1% in the 700°C test. Thus, it is evident that both wet and dry CO_2 are carburizing to beryllium.[13]

The products of the reaction of Brush QMV powders with $H_2O(g)$ and the reaction of Be_2C powder with $H_2O(g)$ and with H_2 have been determined. The specimens were exposed for approximately 24 hr to the appropriate gases at pressures of 25 mm Hg, and duplicate mass-spectrometer gas analyses were obtained for each test. The results of the analyses are presented in Table 4.12. The data support the previous contention that the initial period of rapid weight gain observed for the reaction of Brush powder with wet helium may be the result of decarburization of the sample

[13]Ibid., pp. 136–41.

Table 4.12. Mass-Spectrometer Analyses of Gases Present After Reacting Brush QMV Powder with $H_2O(g)$, Be_2C Powder with $H_2O(g)$, and Be_2C Powder with H_2

Gas	Composition of Gas Present After Reaction Occurs (%)							
	Be Exposed to H_2O			Be_2C Exposed to H_2O		Be_2C Exposed to H_2		
	At 600°C	At 650°C	At 700°C	At 500°C	At 550°C	At 500°C	At 550°C	At 600°C
H_2	99.52	99.78	99.8	41.6	49.6	78.2	84.46	72.62
CH_4	0.04	0.04	0.03	48.2	44.2	10.9	8.68	18.71
H_2O	0.10	0.06	0.06	0.2	0.2	0.3	0.46	0.19
HC	0.01	0.01	0.01	2.1	1.5	3.0	1.40	0.99
N_2 + CO	0.21	0.11	0.09	7.8	4.3	7.5	4.95	7.44
Ar	0.09							
CO_2	0.02	0.01	0.01	0.1	0.2	0.1	0.60	0.05

during the early portion of the test[13] and that Be_2C, either initially present or formed as a reaction product with CO_2, may be one of the factors influencing the "break-away" phenomenon observed in wet CO_2.

Oxidation of a Be-C Alloy in Wet H_2. As a result of the indications that the Be_2C content of beryllium may be one of the factors influencing the "break-away" phenomenon, the reactions of a beryllium-carbon alloy containing 1.65% C with H_2 containing approximately 100 ppm $H_2O(g)$ were studied at 650 and 700°C for times up to 80 hr using a microbalance. At 700°C the reaction was protective for about 16 hr, at which time the "break-away" reaction occurred and continued for the duration of the test. The same "break-away" reaction occurred at 650°C after about 22 hr. The carbon contents after test were 0.93% for the specimen tested at 700°C and 1.05% for the specimen tested at 650°C. Metallographic inspection of these specimens after testing showed the attack to be intergranular, presumably occurring at the sites previously occupied by Be_2C.

Beryllium Pressure Bonding (ORNL Subcontract No. 2029 at Battelle Memorial Institute; status reported by J. T. Lamartine)

A program is being conducted on a subcontract at Battelle Memorial Institute for investigating the gas-pressure bonding of beryllium and

beryllium-UO_2 compartmented fuel plates. Recent work has included studies of the compatibility of UO_2 fuel pellets and spacer materials with beryllium during the pressure-bonding operation.

Components to be pressure bonded are usually sealed in an evacuated stainless steel container with spacers inserted between the specimen and the container walls to prevent container-to-specimen bonding. In order to select spacer materials for use with beryllium components, several potential materials were pressure bonded with beryllium at 1650°F for 4 hr at 10 000 psi. The materials tested included mild steel, chromium-plated mild steel, stainless steel, graphite-coated stainless steel, pyrolytic-carbon-coated stainless steel, thoria-coated stainless steel, nickel, molybdenum, tungsten, tantalum, and columbium. The bonded specimens were then evaluated for ease of separation and reaction with the beryllium. All the materials except nickel reacted with the beryllium during pressure bonding. However, all except nickel separated readily from the beryllium, apparently by fracture through the brittle layer formed at the interface. Based on these results, the practice of using mild steel for spacers has been adopted. The reaction layer is removed by a postbonding pickling treatment.

Other tests on specimens containing fuel bodies showed reactions between beryllium and UO_2 when bonded at 1550, 1650, and 1750°F at 10 000 psi for 1 and 4 hr. In each case the reaction layer was less than 0.001 in. thick and was identified as UBe_{13}. A similar reaction was observed between beryllium and graphite-coated UO_2 when bonded at 1650°F for 4 hr at 10 000 psi. No detectable reactions occurred between beryllium and chromium-coated UO_2 bonded at 1650°F for 4 hr at 10 000 psi or between beryllium and pyrolytic-carbon-coated UO_2 bonded at 1650 and 1750°F for 4 hr at 10 000 psi.

Finned Beryllium Tube Inspection Techniques (R. W. McClung, C. V. Dodd)

Three lengths of finned beryllium tubing manufactured by Nuclear Metals, Inc., were received for use in the development of inspection techniques for use with such tubing.[14] The tubes are each approximately

[14]Ibid., pp. 145–7.

3 ft long, 1/2 in. i.d., and contain 12 identical external fins. The maximum wall thickness at the root of the fin is approximately 0.040 in., and the fin height is about 1/4 in. One of the tubes has a spiral twist on the fins of about 180 deg in 27 in. of length.

Fluorescent penetrants disclosed only small pinhole discontinuities in the outer surface of the tubes. Low-voltage radiography revealed the presence of a number of pits and high-density particles. However, because of the very large changes in section thickness due to the fins, only the root areas between the fins are being examined. Three successive radiographs at 60-deg rotational intervals have proved adequate for complete root coverage on the straight-finned tubing. Approximately 85% coverage is achieved by this technique on the helical-finned tubing. Adequate radiography of the remaining 15% of the tubing is prevented by the coincidence of a projected fin image with a projected groove image. (The radiograph is made through both walls simultaneously.) Approximately 1% sensitivity can be achieved in the groove areas. As was discussed previously,[14] the most realistic eddy-current technique will require a bobbin-type coil to fit inside the tube.

Six longitudinal reference notches have been machined on one of the straight-finned tubes. The smallest outer surface notch was 0.0043 in. and the smallest inner surface notch was 0.0033 in. All the notches, as well as a number of indications, were detected by the eddy-current examination. By using discriminatory instrument adjustments it was determined that a number of the unknown indications were due to discontinuities on the inner surface. The helical-finned tubing exhibited more and larger indications than the other two tubes. It is felt that these may have been due to foreign material (iron) contamination on the inner surface. This tube is being etched to remove the possible contamination, and it will be re-examined.

Correlation of Mechanical Properties of Beryllium Tubing with Nondestructive Testing (J. R. Weir)

The mechanical properties of beryllium tubing at temperatures up to 700°C have been found to vary considerably.[15] Metallographic examination

of the fractures in tubes tested by internally pressurizing to cause failure has disclosed that defects such as die marks and other surface defects may have contributed to early failure of the tubing. As a result, an attempt is being made to correlate the results of nondestructive tests with variations in mechanical properties.

Correlations have been found between the results of radiographic inspection and stress-rupture properties at 600 and 700°C. The results indicate that premature failure of the beryllium tubes in stress-rupture tests may be associated, in most cases, with defects observed during radiographic examination. Thus there is evidence that correlations of this type will be successful.

---

[15]GCR Quar. Prog. Rep. Dec. 31, 1960, ORNL-3049, pp. 234–7.

5. IN-PILE TESTING OF COMPONENTS AND MATERIALS

D. B. Trauger O. Sisman

Fuel Element Irradiation Program

Full-Diameter Prototype EGCR Fuel Capsules (F. R. McQuilkin, V. A. DeCarlo, R. L. Senn, A. W. Longest)

Irradiation of the eight group III experimental capsules, described previously,[1] was completed on May 7. Following withdrawal from the reactor, the units were moved to the ORR south hot cell for disassembly. A summary of the operational data for these capsules is given in Table 5.1, and a graph showing the temperature history of capsule 01A-3 is presented in Fig. 5.1. The central temperature measurements were made with a tungsten-rhenium thermocouple inserted into a tungsten thermowell, as described previously.[2] The pressures on the outer surface of the beryllium capsules and the thermal cycles applied during irradiation are described in Fig. 5.2.

Eight group IV experimental capsules were inserted in the reactor at the beginning of cycle 34; irradiation started May 19. Seven of these capsules are shown mounted in the mockup facility in Fig. 5.3. Design data and the planned operating conditions for these capsules are summarized in Table 5.2.

Each group IV specimen capsule is mounted in a pressurized NaK vessel surrounded by a thermal gas barrier to allow for temperature control similar to that used for previous experiments. Chimney-type cadmium shutters are mounted on capsules 04-4 and 05-4, which consist of beryllium-clad UO_2 pellets from CEA, for manual application of thermal cycles. Also, facility revisions were made to provide for operation of these capsules at outer surface pressures of up to 850 psi at 1112°F.

Gas circulators of the rotary positive-displacement type employing copper-impregnated (25%) Teflon vanes were installed in the thermal-barrier

[1]GCR Quar. Prog. Rep. Sept. 30, 1960, ORNL-3015, pp. 107–12.

[2]GCR Quar. Prog. Rep. Dec. 31, 1960, ORNL-3049, pp. 238–44.

Table 5.1. Summary of Operating Data for Group III UO_2-Fueled Capsule Irradiation Tests in ORR

Irradiation starting date: August 14, 1960
Irradiation ending date: May 7, 1961
Irradiation time normalized to operation at 30 Mw: 205.9 days (capsule 01A-3, 188.6 days)
Reactor power generation during irradiation: ~150 000 Mwhr (capsule 01A-3, ~136 000 Mwhr)

	Capsule Number							
	01A-3[a]	02-3	03-3	04-3	05-3	06-3	07-3	08-3
Specimen identification	OR-2GA	OR-2B3	CEA-03	CEA-08	UK-3009B	UK-2932A	OR-1B2	OR-1G
Reactor position	P-8, P-9	P-8	P-7, P-8	P-7	P-3	P-2, P-3	P-2	P-1, P-2
Perturbed thermal flux, neutrons/cm^2·sec	1.33×10^{13}	2.14×10^{13}	5.00×10^{13}	4.83×10^{13}	1.95×10^{13}	1.53×10^{13}	1.52×10^{13}	0.82×10^{13}
Number of pellets	12	14	9	9	19	19	22	12
Average pellet density, % of theoretical								
Bulk	94.3	95.4	93	93	96.9	96.5	95.1	96.8
Immersion		93.9					98.4	
Pellet enrichment, % U^{235}	2.42	1.82	0.71	0.71	2.42	2.42	2.42	2.42
Oxygen-to-uranium ratio	2.002	2.001			2.006	2.008	2.003	2.003
Average pellet diameters (cold), in.								
Inside	0.3230	0	0	0	0	0	0	0.3225
Outside	0.7059	0.5133	0.5118	0.5157			0.2987	0.7037
Radial clearance between UO_2 and cladding, in.								
Maximum	0.0030	0.0024	0.0071	0.0059			0.0009	0.0044
Minimum	0.0023	0.0008	0.0035	0.0031			0.0002	0.0033
Heat rate, Btu/hr·ft	24 000	22 200	19 100	18 500	8 400	6 600	6 100	14 900
Total heat flux, Btu/hr·ft^2	102 200	118 600	102 000	98 800	80 600	55 400	51 200	63 400
Calculated burnup, Mwd/MT of UO_2								
Total	2093	3130	2657	2574	3583	2821	2615	1420
Rate (per day at full power)	11.1	15.2	12.9	12.5	17.4	13.7	12.7	6.9
Typical irradiation conditions[b]								
Temperature at outer surface of cladding, °F								
Design	1600[c]	1112[d]	1112[d]	1112[d]	1112[d]	1112[d]	1112[d]	1600[c]
Highest	1520	1130	1130	1145	1180	1145	1085	1492
Lowest	1292	980	1098	1015	1100	1080	1082	1058
Average	1429	1048	1114	1072	1140[e]	1112[e]	1084[e]	1300
Pressure on outer surface of cladding, psig	300	f	g	f	300	300	300	300
Shutter thermal cycles	0	20/month	20/month	20/month	1/day	1/day	1/day	0
Number of thermocouples that failed	0	2	5	1	6	3	5	0
Assembly drawing number	D-10014	D-9614	D-9806	D-9806	D-9805	D-9805	D-9615	D-10016

[a] Inserted Sept. 25, 1960; irradiation started Oct. 4, 1960.

[b] Data recorded March 20, 1961.

[c] Maximum operating temperature indicated by any outer surface thermocouple.

[d] Average operating temperature indicated by all outer surface thermocouples.

[e] Temperature oscillations for these capsules were from 30 to 180°F at a frequency of 4 to 10 cpm.

[f] 150, 1 month; 225, 1 month; 300, 4 months; 375, 1 month; 450, 1 month; see Fig. 5.2.

[g] 150, 2 months; 225, 2 months; 300, 4 months; see Fig. 5.2.

Table 5.2. Summary of Design and Planned Operating Conditions for Group IV UO_2-Fueled Capsules in ORR

	Capsule Number							
	01C-4[a]	02-4	03-4	04-4	05-4	06-4	07-4	08B-4[b]
Specimen identification	OR-4G, tube J-2	OR-5S	OR-1S	FR-3B, 38	FR-3B, 39	OR-3S	OR-2S	OR-3G, tube J-1
Origin of specimen	ORNL	ORNL	ORNL	CEA France	CEA France	ORNL	ORNL	ORNL
Type of capsule	Pellets in instrumented stainless steel tube	Tamp-packed powder in stainless steel tube	Hot-swaged powder in stainless steel tube	Pellets in beryllium tube	Pellets in beryllium tube	Hot-swaged powder in stainless steel tube	Hot-swaged powder in stainless steel tube	Pellets in instrumented stainless steel tube
Perturbed thermal flux, neutrons/cm^2·sec	1.66×10^{13}	1.34×10^{13}	1.33×10^{13}	7.86×10^{13}	7.86×10^{13}	1.69×10^{13}	2.29×10^{13}	1.66×10^{13}
Enrichment, % U^{235}	2.30	1.83	2.35	0.71	0.71	2.03	0.71	2.30
Pellet density, % of theoretical	95.44	58.3	93.1	93.44	93.44	89	93.1	96.35
Heat rate, Btu/hr·ft	30 000	7 500	15 325	30 000	30 000	15 600	8 000	30 000
Specific power, w/g of UO_2	13.9	8.9	11.3	20.3	20.3	12.5	5.9	13.9
Cladding temperature, °F	1600[c]	1300[d]	1300[d]	1112[d]	1112[d]	1300[d]	1300[d]	1600[c]
Cladding pressure, psig								
Initial	300	300	300	300	500	300	300	300
Final	300	300	300	300	850[e]	300	300	300
Central temperature measured	Yes	No	No	No	No	No	No	Yes
Thermocouple	Pt vs Pt–10% Rh							Pt vs Pt–10% Rh
Thermowell	Tungsten							Fansteel-82
Cladding inner surface temperature measured	Yes[f]	No	No	No	No	No	No	Yes[f]
Shutter thermal cycles	0	0	0	20/month	20/month	0	0	0
Thermal barrier gas gap, in.								
Hot	0.012	0.026	0.013	0.006	0.006	0.013	0.026	0.012
Cold	0.019	0.032	0.019	0.011	0.011	0.019	0.032	0.019
Assembly drawing number	D-10400	D-10231	D-9521	D-9806	D-9806	D-9521	D-9521	D-10400

[a]Hollow pellets prepared from large-grain (35-mesh) UO_2.

[b]Hollow pellets prepared from fine-grain (100-mesh) UO_2.

[c]Maximum operating temperature indicated by outer surface thermocouples.

[d]Average operating temperature indicated by all outer surface thermocouples.

[e]To be increased 75 psig per reactor half cycle, except final increase, which will be 50 psig.

[f]Thermocouples are 38-mil-o.d. stainless steel-sheathed, ungrounded, Chromel-Alumel units with MgO-insulated junctions prepared from 1/16-in.-o.d. stainless steel thermocouple material by a three-step swaging and annealing process; two such thermocouples are brazed to cladding inner surface and fitted into grooved (50 mils by 50 mils) fuel pellets.

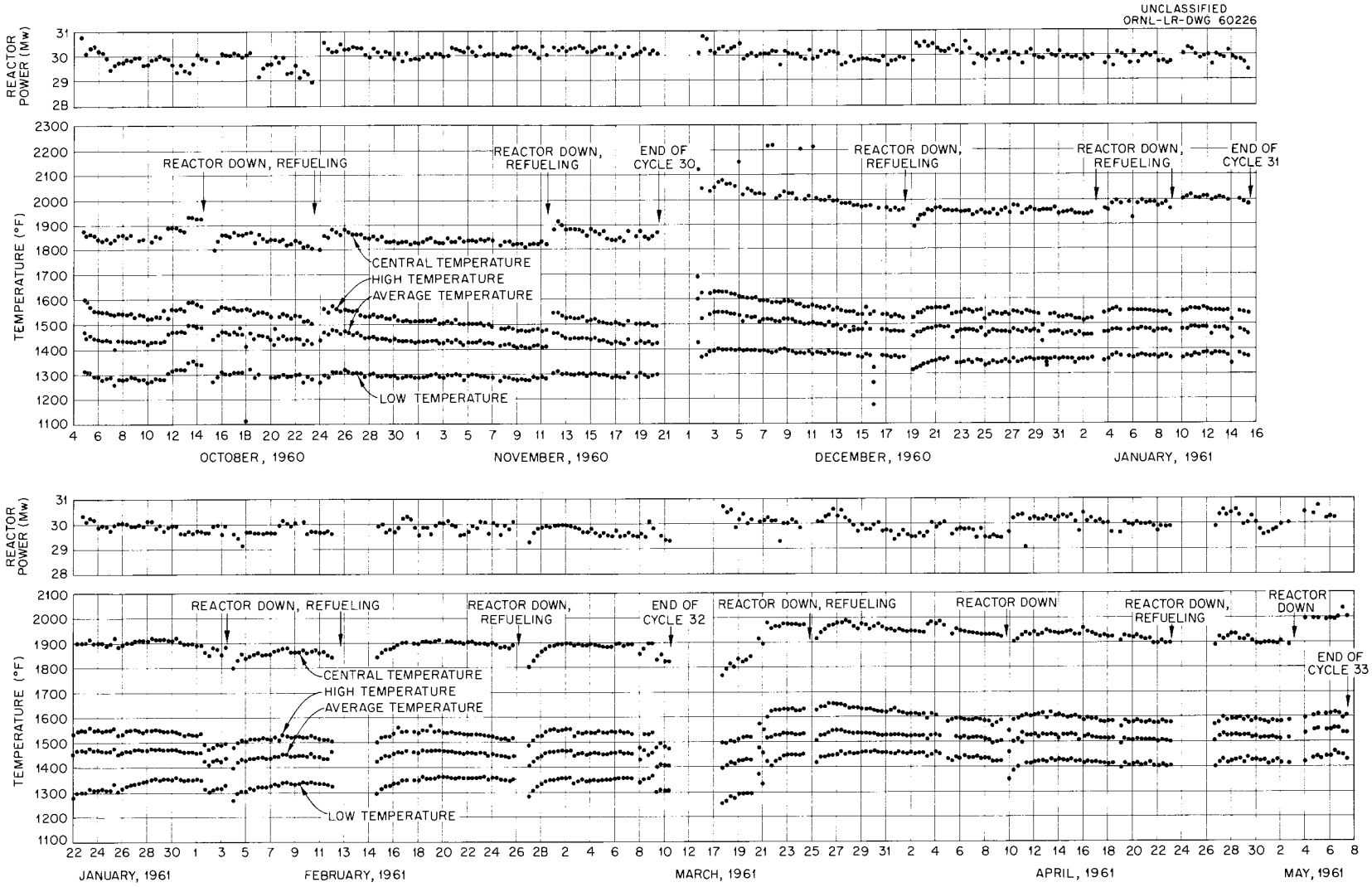

Fig. 5.1. Temperature History of ORR-Irradiated Group III Capsule 01A-3.

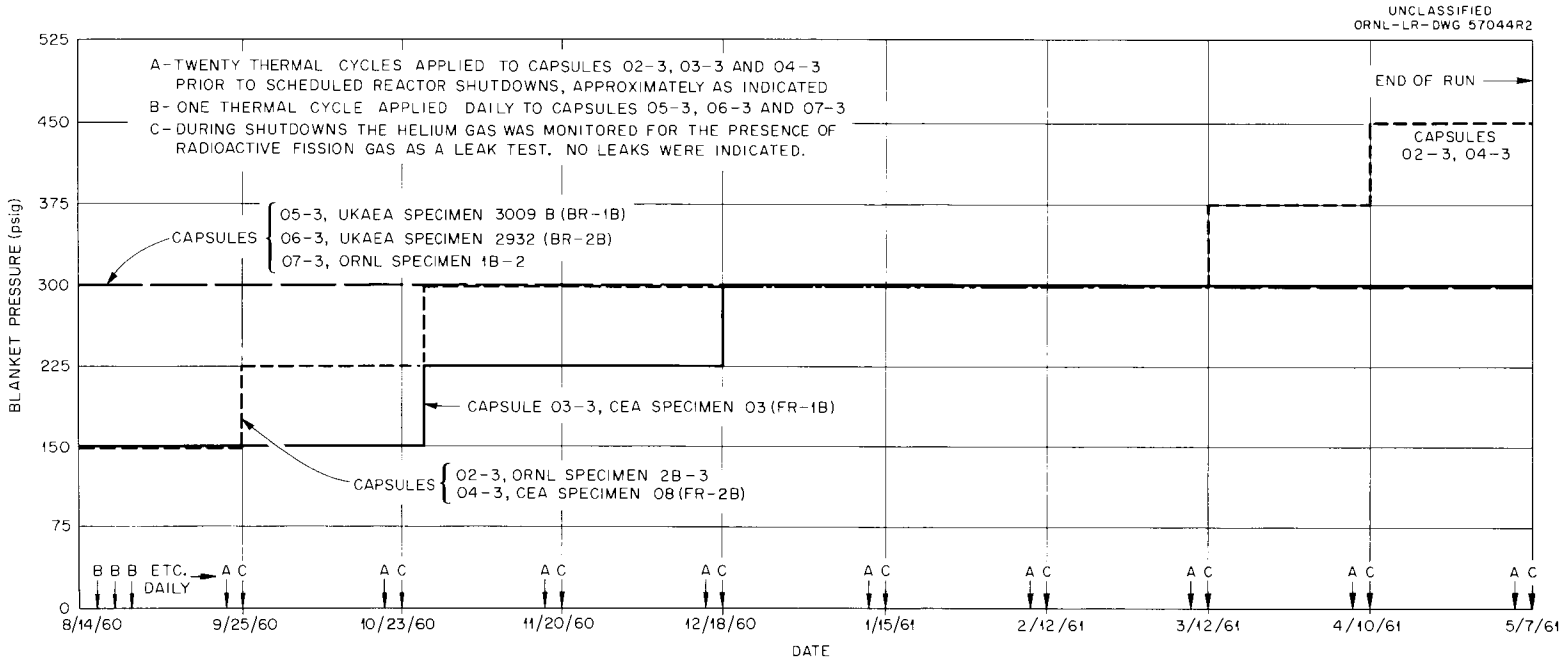

Fig. 5.2. Operating History of ORR-Irradiated Group III Beryllium Capsules.

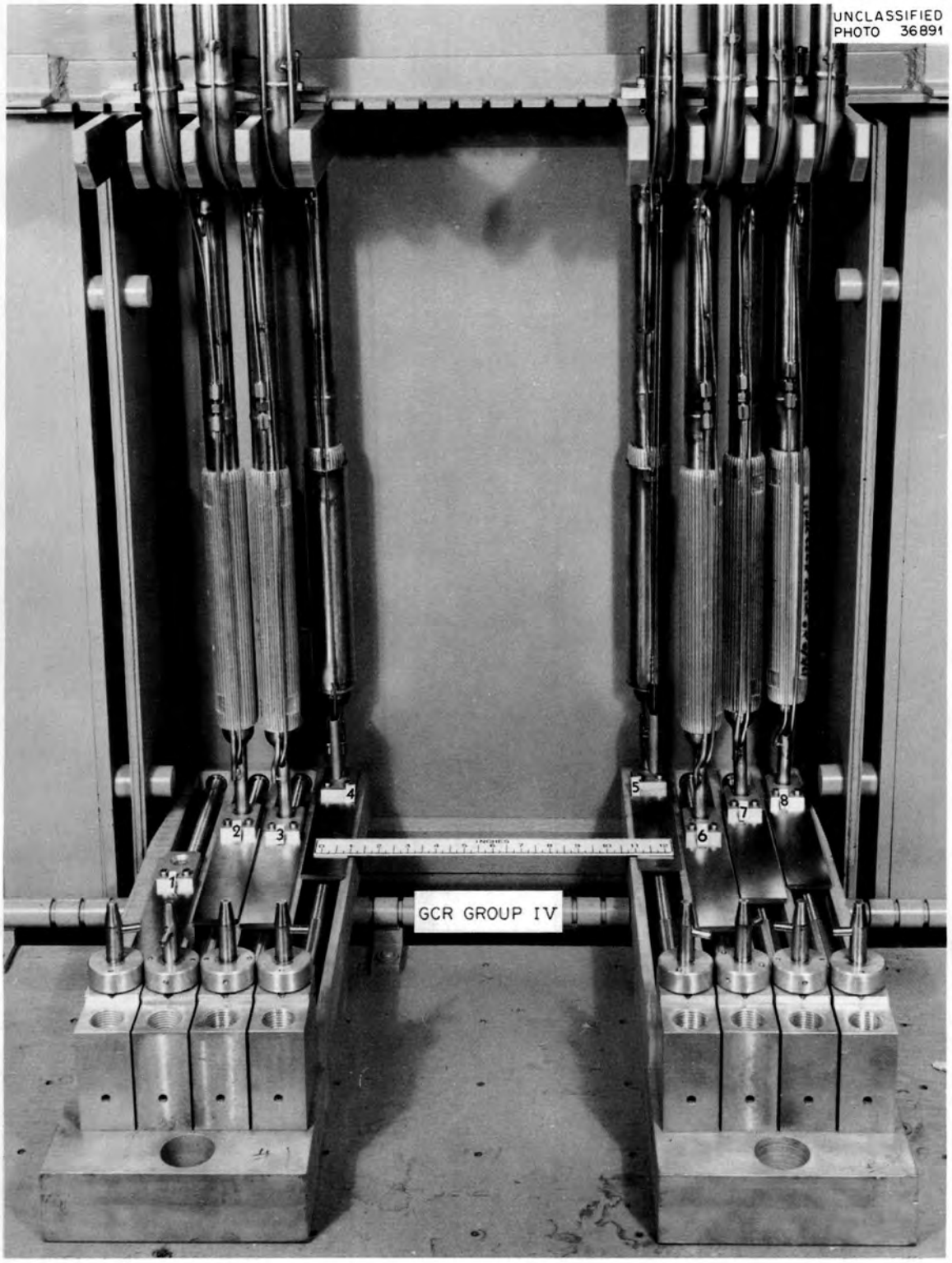

Fig. 5.3. Group IV Capsules Mounted in Mockup Facility.

gas circuits of all the capsules to reduce temperature fluctuations of the type encountered[2,3] with group III capsules. While it appears that circulation of the thermal barrier gas is desirable (when using a mixture of gases) gas circulation alone is probably not the total solution to the temperature oscillation difficulty. Several items of operational experience tend to support the postulation that convective movement of the NaK coolant may result in a channelled flow pattern capable of producing some part of the oscillations.

During the ORR reactor-cycle-34 shutdown, the lower capsule mounting plate and associated brackets were replaced. As shown in Fig. 5.3, the new plate is equipped with remotely operated screw-driven capsule positioners that permit individual adjustment of any experimental assembly within a centerline travel zone of 1 to 8.9 in. from the reactor face at any time. Thus compensating adjustments can be made for neutron flux shifts resulting from burnup and/or changes in core loading (reactor fuel and experiments), and experimental assemblies can be relocated or partially withdrawn.

Two thermopiles for monitoring the thermal-neutron flux have been installed 22 1/2 in. west of the reactor face on the midpoint centerline for each of the north and south groups of capsules. Calibration of these units is in progress.

Miniature-Capsule Irradiation Experiments in the LITR (F. R. McQuilkin, W. E. Thomas)

Operating data for the miniature capsules irradiated in the LITR during this report period are summarized in Table 5.3. It should be noted that the central temperatures reported in this table are somewhat lower than those reported previously[4] for the same experiments. The disagreement results from earlier use of improper reference-junction compensation values for the tungsten-rhenium thermocouples. The corrected values are presented in Table 5.3.

---

[3]GCR Quar. Prog. Rep. March 31, 1961, ORNL-3102, pp. 149–53.

[4]Ibid., pp. 153–4.

Table 5.3. Operating Data for Miniature Capsules Being Irradiated in the LITR

Experimental Assembly No.	Fuel Composition	U^{235} Enrichment (%)	Initial Central Fuel Temperature (°F)		Date Installed	Date Removed	Estimated Burnup (Mwd/MT of UC)
			"a" Capsule	"b" Capsule			
L-M1	$BeO-UO_2$	20	1110	1395	10-20-60	In-pile	
L-M3	$BeO-UO_2-ThO_2$	93	1660	1895	11-22-60	In-pile	
L-M4	$BeO-UO_2$	50	1955	2300[a]	2-8-61	In-pile	
L-M5	$BeO-UO_2-ThO_2$	93	1535	1900	4-11-61	In-pile	
L-C2	UC	10	2000	2370	12-14-60	4-15-61[b]	7600
L-C3	UC	10	2260	2290	12-14-60	3-19-61[b]	6200
L-T1	UO_2	10	1300	1475	12-19-60	3-7-61	4800
L-CP1	Pyrolytic-carbon-coated UC_2	93	1940	2120	3-9-61	In-pile	

[a]Estimated; thermocouple in this specimen was unreliable in operation and failed after eight days of service.

[b]Date of capsule failure and removal from reactor core.

Experimental assemblies L-M1, L-M3, and L-M4, which contain $BeO-UO_2$ and $BeO-UO_2-ThO_2$ fuel mixtures,[4] have continued to operate satisfactorily under the conditions given in Table 5.3. Experimental assembly L-M5, which contains $BeO-UO_2-ThO_2$ fuel, was inserted in the LITR during this quarter; it is scheduled for a burnup of 5 at. % of the total uranium.

During irradiation, experimental assemblies L-C2 and L-C3, which contained UC fuel, developed a series of circumferential cracks on the "b" capsule cladding at approximately the vertical midplane of the fuel specimen. These assemblies consisted of the hollow cylindrical fuel body, 0.111 in. i.d., 0.262 in. o.d., 0.500 in. long, surrounded by a thin (0.010-in.-wall) tantalum tube. The assembly was positioned and centered in the encapsulating Inconel tube by a stepped end spacer. The 0.020-in. radial gap between the tantalum tube outer surface and the Inconel container inner surface was filled with high-purity helium to serve as a thermal-barrier gas. The central temperature in specimen L-C2b remained essentially constant for approximately three months, until March 10, when the thermocouple indication started an upward drift that reached a maximum on March 19, nine days later. Thereafter the drift was downward to

approximately 1900°F on the last day of operation, April 15. The "a" capsule fuel temperature remained approximately constant until March 16. During the following two days, the thermocouple showed a rapid decline and thereafter the temperature indication was erratic until the cladding failure of the "b" capsule.

The indicated temperature behavior for both the "a" and "b" specimens of assembly L-C3 was quite similar to that described above for assembly L-C2. The results of visual examination of these units in the hot cell are presented in the following section of this chapter on "Evaluation of Radiation Effects."

Experimental assembly L-T1, which was irradiated for an in-pile evaluation of 0.020- and 0.040-in.-diam steel-sheathed Chromel-Alumel thermocouples for LITR-capsule service, was removed after 1543 hr of operation. Only one of the four 0.020-in.-diam thermocouples failed. The four larger thermocouples all performed satisfactorily. A postirradiation hot-cell examination of this assembly is in progress.

The first coated-particle experiment was started on March 9, 1961. The experimental assembly, L-CP1, contains loosely packed pyrolytic-carbon-coated UC_2 spheres (~450 μ in diameter) fabricated by High Temperature Materials, Inc. This assembly is scheduled for removal from LITR facility C-47 on July 25, 1961. The expected burnup at that time will be approximately 10 at. % of the total uranium. The particles are contained in tantalum cans positioned by end spacers to give an approximately 0.022-in. radial gas gap between the tantalum can and the encapsulating Inconel tube. The thermal barrier gas for this experiment is high-purity helium. The second coated-particle test assembly, containing pyrolytic-carbon-coated UC_2 spheres fabricated by the Minnesota Mining and Manufacturing Company, was inserted in LITR facility C-42 on June 1, 1961. A burnup of 10 at. % is specified for this assembly also.

Modification of GCR-ORR Loop No. 1 (J. K. Franzreb)

The in-pool, in-pile, and heater sections of GCR-ORR loop No. 1 were rebuilt and installed during the ORR shutdown of May 7. New compressors had been installed prior to this shutdown, and additional instrumentation

was added to control two secondary low-pressure buffer zones in the underwater piping.

Loop operation was started when reactor operation was resumed, and subsequently the loop has been functioning satisfactorily. A set of GCR pressure-vessel-steel weld-metal test specimens is being irradiated at 550°F. Loop operation is being controlled with the automatic cooler flow controller, and the loop has already gone through one reactor setback without the need for manual adjustment.

The major change made in the loop to improve its versatility and containment was the addition of a concentric pipe to the main loop piping to provide a second container and a gas annulus for leak detection. The inner pipe contains the helium coolant at 300 psia and the outer pipe contains helium at 60 psia. Appropriate instrumentation was provided to monitor the pressure in both pipe systems. Also, the piping runs were simplified by the elimination of flanged joints and were arranged for convenient drainage of decontamination solutions. Design work has been completed on a double containment system for the compressors, and, when this work has been accomplished, the loop will be suitable for tests of defective fuel elements.

Fuel Element Testing in MTR (C. W. Cunningham, J. A. Conlin)

The third graphite-encapsulated test fuel element with a UC_2-graphite matrix (ORNL-MTR-48-3), which was removed from the MTR on January 16, 1961, because of excessive fission-gas release,[5] was examined at the General Electric Vallecitos Atomic Laboratory (GEVAL). A leak was located in the silicon seal between the encapsulating graphite bottle and plug.

A similar fuel element was irradiated during test ORNL-MTR-48-4 from March 20 through May 1, 1961. In addition to being encapsulated in a low-permeability graphite can, as was unit 48-3, the individual fueled graphite matrices were coated with pyrolytic carbon. The fission-gas release became excessive after the first few hours of operation, and failure of the encapsulating graphite container was assumed. The test assembly

[5] Ibid., pp. 154–6.

was therefore withdrawn to the fully retracted position to reduce the activity in the purge gas system. Under these conditions, the temperature of the encapsulating graphite wall averaged 1150°F, corresponding to 210 w/cm^3 heat generation in the fuel and a total fission power of 13.7 kw. The element has been transferred to the GEVAL hot cells for examination.

The failures of these two units almost immediately after startup has emphasized the need for improved leak checking techniques for the graphite containers after final assembly. These containers were checked by looking for a change in weight after immersion in carbon tetrachloride. Ordinary helium leak-testing techniques were not considered applicable because of the semipermeable nature of the graphite.

A technique similar to that employed for the OEEC Dragon reactor fuel boxes will be tried. It consists of subjecting the elements to a vacuum for a period of time followed by pressurization with helium, which will fill the element container if leaks are present (undesirably, the pores of the graphite will also be filled). Following this, the element is purged with nitrogen and the effluent sniffed for helium with a helium leak detector. The helium concentration versus time provides a measure of the permeability of the element. After gaining experience with various samples, it should be possible to distinguish leaking elements.

The fission-gas-release-rate data for the ORNL-MTR-48-2 test have been recalculated.[6] Corrections were made based on postoperational calibration of the flow instrumentation, more precise measurement of the gas volume between the test fuel element and the sampling station, and the variation of the ratios of fission gas volume between the test fuel element and the sampling station. The variations of the ratio of fission-gas-release rate to production rate as a function of test duration are shown in Fig. 5.4. It is noteworthy that the ratios appear to be constant after 40 to 60 days from startup. No fission-gas-release data were taken after 148 days (November 21, 1960), when the encapsulating graphite developed a leak at a thermocouple hole.

---

[6]GCR Quar. Prog. Rep. Dec. 31, 1960, ORNL-3049, p. 246.

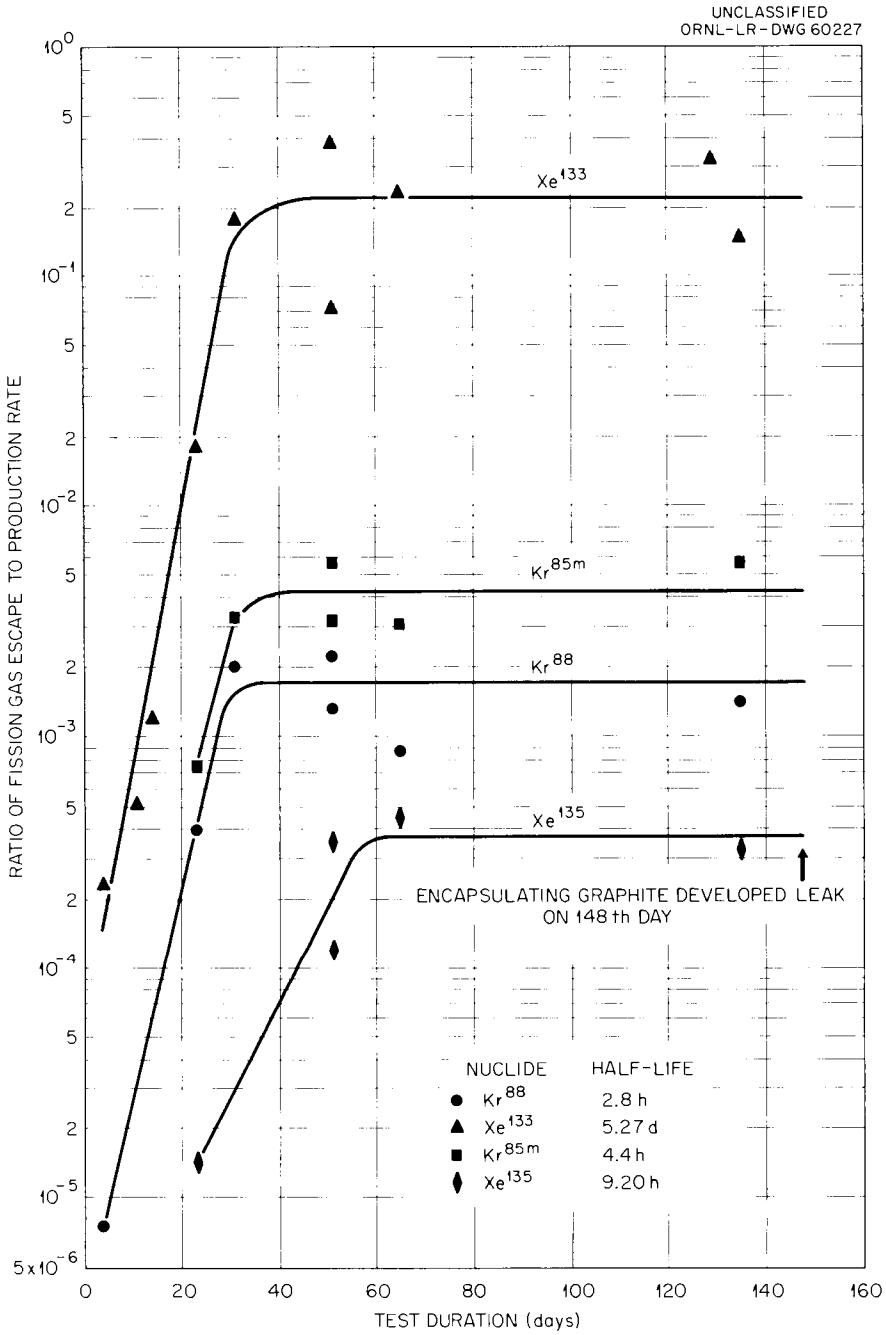

Fig. 5.4. Variations of Ratio of Fission-Gas-Release Rate to Production Rate as a Function of Test Duration for Experimental Assembly ORNL-MTR-48-2.

Evaluation of Radiation Effects

J. G. Morgan
E. L. Long P. E. Reagan
M. F. Osborne H. E. Robertson

ORR- and ETR-Irradiated Prototype Capsules

Capsule Evaluations. Examinations of the group I and group II ORR-irradiated UO_2-fueled capsules described previously[7] have been completed. The results of bulk density measurements made by the mercury immersion technique on UO_2 pellets from eleven of these capsules are presented in Table 5.4. The small decreases in density may be attributed to micro cracks, which were present in most of the pellets. Since the precision of measurement was estimated to be about ±0.07 g/cm^3, these density changes, like those indicated by the previously reported immersion density data,[7] are, in general, insignificant.

Examinations were also completed of ETR-irradiated UO_2-fueled capsule E-9. The irradiation conditions and data obtained from examination of this capsule are given below:

Average operating temperature, °F	
Cladding	1300
Center of UO_2 (calculated)	2700
Burnup, Mwd/MT of U	
From Co monitor	2800
From Cs^{137}	2100
From Ce^{144}	2600
Fission-gas release, % Kr^{85}	3
Gas pressure in capsule at 75°F, mm Hg	1020

The agreement in the burnup data from the various measurements is considered to be fairly good, inasmuch as values based on Cs^{137} are expected to be somewhat low. It is to be noted that these experimental burnup values are somewhat lower than the estimated value presented previously.[7] The fission-gas release appears to have been several times that for comparable ORR-irradiated capsules. The mass spectrometer analysis of the

[7]GCR Quar. Prog. Rep. March 31, 1961, ORNL-3102, pp. 156–74.

Table 5.4. Effect of Irradiation on Bulk Density of EGCR Prototype Fuel Pellets

Capsule No.	Density (g/cm^3)		
	Before Irradiation	After Irradiation	Change
01-1	10.40	10.14	−0.26
02-1	10.28	10.25	−0.03
03-1	10.41	10.31	−0.10
05-1	10.29	10.03	−0.26
01-2	10.51	10.42	−0.09
02-2	10.51	10.52	0
03-2	10.35	10.30	−0.05
04-2	10.35	10.34	0
05-2	10.38	10.10	−0.28
07-2	10.45	10.36	−0.09
08-2	10.44	10.35	−0.09

gas in the capsule indicated (see Table 5.5) the expected volumetric distribution of krypton and xenon isotopes and reasonable purity of the helium fill gas.

Metallographic Examination of ORR-Irradiated Group II Capsules. Slight differences were noted in the hollow UO_2 pellets from capsules 01-2, 02-2, 03-2, and 05-2. One difference was that the pellet from capsule 05-2, which was irradiated at the highest temperature, showed the greatest tendency toward fracturing. All the pellets exhibited various grain sizes across the wall. The pellet from capsule 05-2 was the only one that showed any appreciable grain growth compared with that of the unirradiated control specimen. A small amount of metallic-appearing second-phase material was present in the hollow pellets. Based on chemical analyses, the second phase is probably free iron. This second-phase material was also noted in the unirradiated control samples.

The hollow UO_2 pellets from capsules 04-2 and 06-2, which contained a central BeO rod, were not noticeably different from the hollow UO_2 pellets of capsules without a central BeO rod. A transverse section of a

Table 5.5. Results of Mass Spectrometer Analysis of Gas from Irradiated Capsule E-9

Gas Constituents		Quantity (vol %)
He		88.27
CO_2		0.169
Ar		0.052
O_2		0.47
N_2		1.57
H_2O		0.84
Xe^{136}		2.97
Xe^{134}		2.12
Xe^{132}		1.47
Xe^{131}		0.08
	Total Xe	6.64
Kr^{86}		0.639
Kr^{85}		0.092
Kr^{84}		0.355
Kr^{83}		0.183
	Total Kr	1.27

pellet representative of the pellets irradiated in capsules 01-2 through 06-2 is shown in Fig. 5.5. Most of the voids are believed to be a result of "pull-out" of small grains during polishing. The interface of two UO_2 pellets from capsule 06 was also examined. Small grains were present along the interface, as shown in Fig. 5.6. It was also noted that the pellets were off-set from each other. No microstructural differences were noted in the solid UO_2 pellets from capsules 07-2 and 08-2 as compared with the hollow UO_2 pellets from capsules 01-2 through 06-2.

Cladding samples from capsules 02-2, 05-2, 06-2, and 08-2 were also examined. An end-cap weld from capsule 02-2, as may be seen in Fig. 5.7, showed no deleterious effects of irradiation. However, longitudinal sections of type 304 stainless steel cladding taken at pellet interfaces revealed voids that were not present in the unirradiated control capsule. The voids in the sample from capsule 05-2 are shown in Fig. 5.8. The particular sample was taken at a point in the cladding where a "wrinkle"

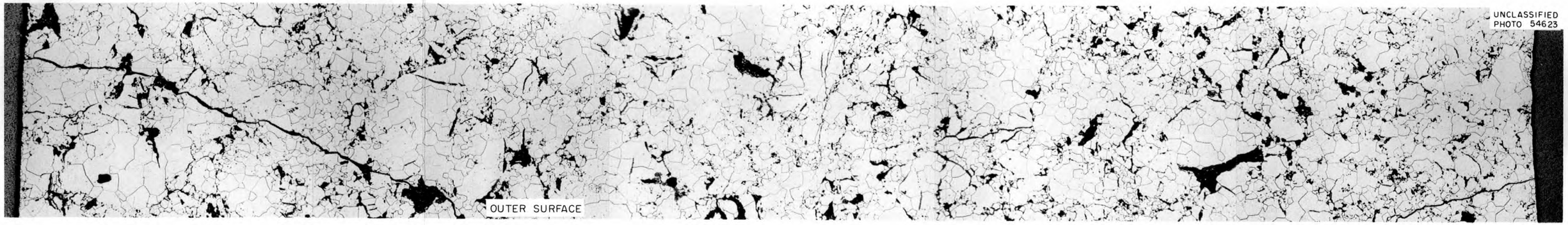

Fig. 5.5. Transverse Section of Pellet No. 5 From ORR-Irradiated Group II Capsule 04-2.

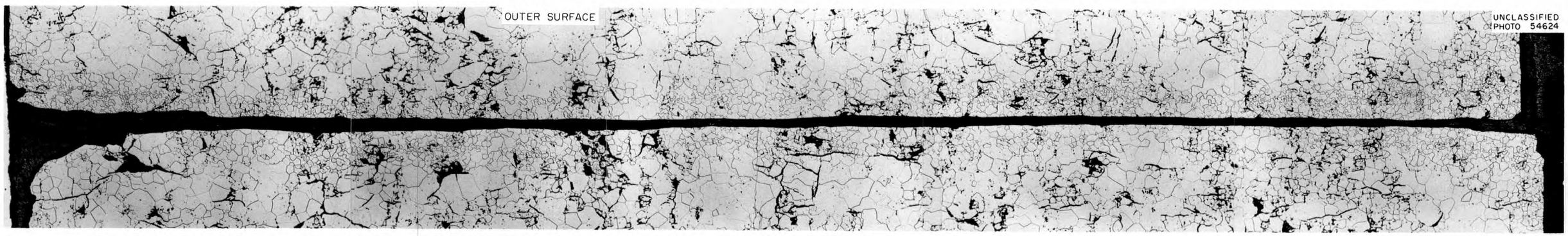

Fig. 5.6. Longitudinal Section Taken at Interface of Pellets Nos. 1 and 2 of ORR-Irradiated Group II Capsule 06-2. Note small grains and off-set of pellets.

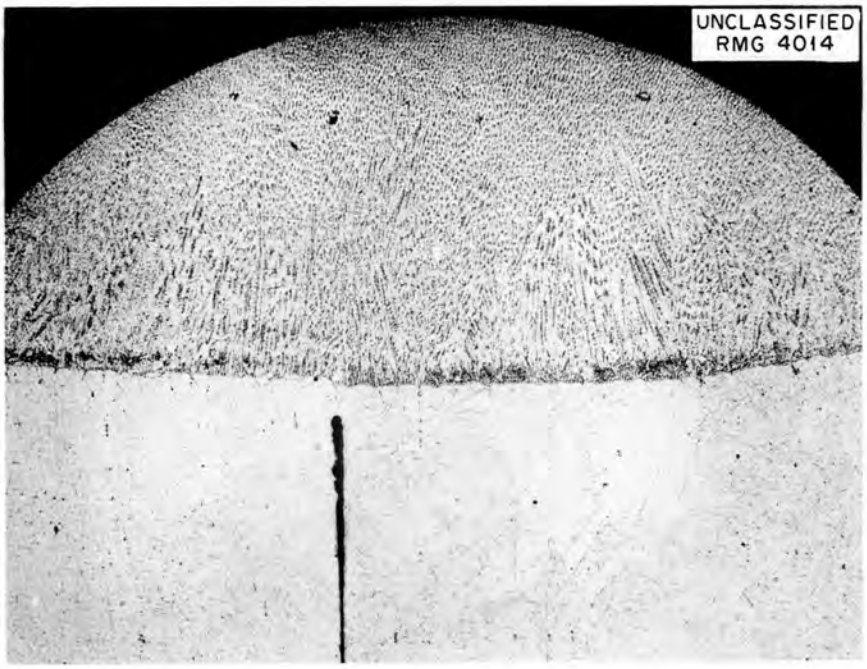

Fig. 5.7. End-Cap Weld from ORR-Irradiated Group II Capsule 02-2. Etched. 100X

Fig. 5.8. Longitudinal Section of Type 304 Stainless Steel Cladding from ORR-Irradiated Group II Capsule 05-2. Note voids and UO_2 imbedded in inner surface. As polished. 100X

was observed during disassembly. The frequency of the voids decreased with an increase in the distance from the pellet interface. Small pieces of UO_2 were imbedded in the cladding at the inner surface, as may be seen in Fig. 5.8.

Examination of the cladding samples from capsules 06-2 and 08-2 showed fewer voids, but a second phase was present in the grain boundaries. In order to emphasize the quantity of the grain-boundary phase, the specimen was electrolytically etched. The specimen is shown in Fig. 5.9 both as polished and after removal of the second phase material by etching. This second phase has been tentatively identified, both metallographically and by x-ray examination, to be the sigma phase. The voids in the cladding adjacent to a pellet interface diminished with an increase in distance from the interface. These voids and the second phase material in the grain boundaries and at grain corners are thought to be the results of the combined effects of thermal cycling and strain during irradiation.

Comparison of Group I and Group II Capsules. There was a pronounced difference in the microstructures of the UO_2 fuel pellets of ORR-irradiated group I and group II capsules, for which the irradiation conditions were similar. The needle-like structure observed in the pellets from the group I capsules,[7] which was believed to be associated with the UN_2 present before irradiation, was not seen in the pellets from the group II capsules. There was no UN_2 in the as-fabricated pellets for the group II capsules. A marked difference in the integrity of the group II pellets compared with that of the group I pellets was noted; specifically, the outer surfaces of the UO_2 pellets from the group II capsules were not fractured.

Metallographic Examination of Capsule E-9. Numerous microcracks were found in the hollow UO_2 fuel pellet from capsule E-9. There was, however, no evidence of gross fracturing of the fuel, as was seen in the hollow pellets from the ORR-irradiated group I capsules, which were tested under similar in-pile conditions,[7,8] even though there was an appreciable quantity of UN_2 nitride in the unirradiated control pellet. Capsule 06-1 of the group I capsules showed the least amount of fracturing of the fuel.

[8]GCR Quar. Prog. Rep. Dec. 31, 1959, ORNL-2888, p. 100.

This capsule contained a BeO bushing in the center of the stack of pellets, as did capsule E-9.

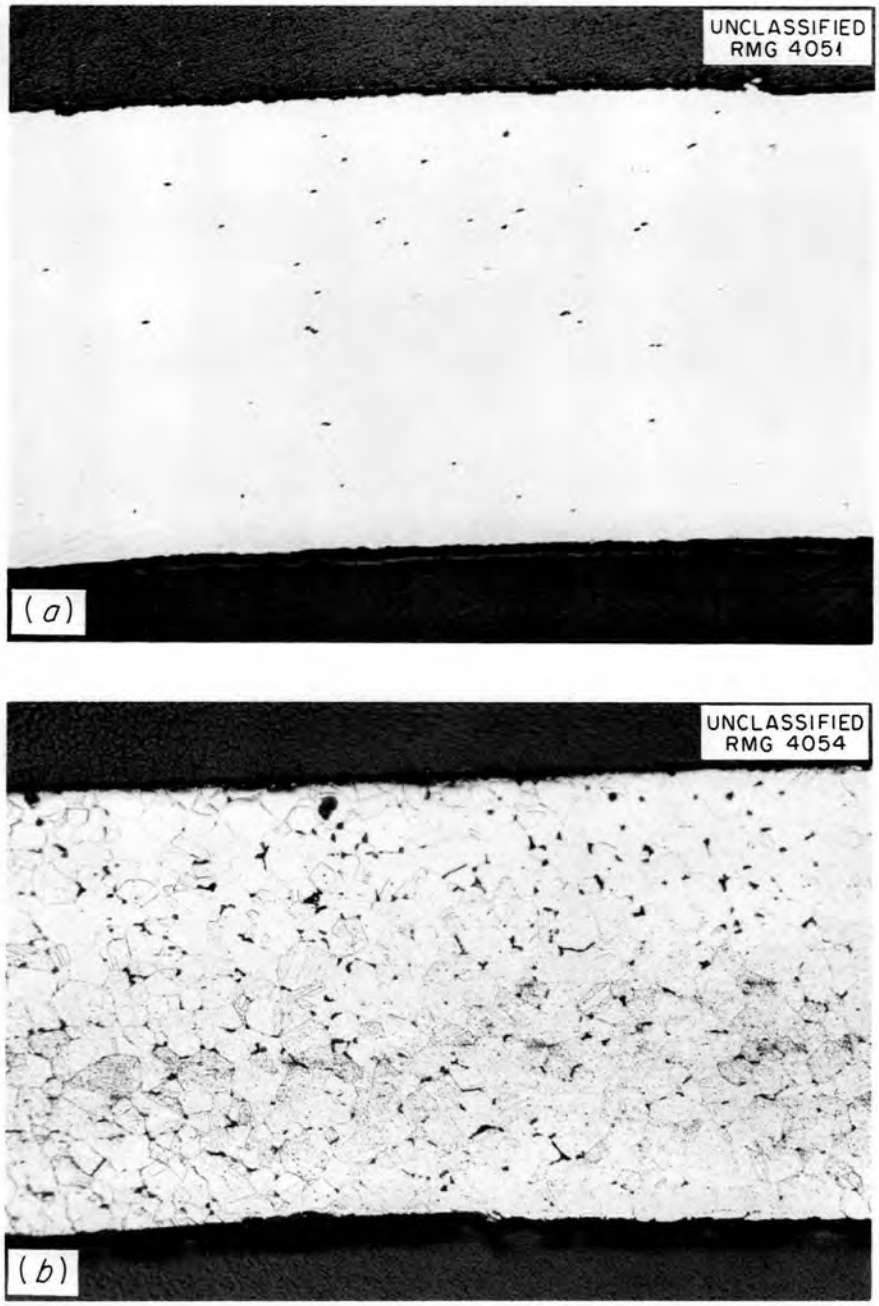

Fig. 5.9. Longitudinal Section of Type 304 Stainless Steel Cladding from Group II Capsule 08-2. (a) As polished. 100X. (b) Electrolytically etched. 100X. Most of the voids resulted from etching out the sigma-phase material.

The acicular structure seen in other pellets that contained appreciable amounts of UN_2 was found again in the irradiated fuel from capsule E-9. There was no measurable change in grain size as a result of irradiation.

LITR-Irradiated UC-Fueled Capsules

Capsule Evaluations. A series of three irradiations of bulk UC has been completed in the LITR, as mentioned in the preceding section. The material was arc melted and cast in a graphite mold in the form of right cylinders, which were ground to an outside diameter of 0.262 ± 0.001 in. and then ultrasonically drilled to produce a cylindrical hole 0.111 ± 0.003 in. in diameter. These pellets required special handling at all stages of processing to prevent attack by moisture or water. The grinding of the solid pellets was performed in nonaqueous oil, and the drilling was done under kerosene. Two pellets were made from each casting. The end surface of the pellet from the bottom of the casting contained equiaxed grains, whereas the other sample surfaces had the characteristic columnar grains of the cast material. The UC used contained 4.8 ± 0.05 wt % carbon, and the bulk density ranged from 95 to 97% of theoretical. The pellets were placed in tantalum foil cans and sealed in helium in the standard LITR double capsules. The pellet central temperature was monitored with tungsten-rhenium thermocouples inserted in the drill holes. There was one pellet 0.5 in. long in each capsule. In addition, a control pellet was sealed in helium in a tantalum can and heated in a vacuum furnace in the laboratory. The control sample, L-CD, was heated at 2300°F for 40 days. An end view of this sample in its tantalum can, Fig. 5.10, shows little evidence of reaction between the carbide and the tantalum can.

The in-pile test conditions for the three capsules are summarized in Table 5.6. The top capsule is designated as "a" and the bottom "b." The gas from capsule "a" was analyzed and the results are presented in Table 5.7. The fission-gas release based on Kr^{85} was 1.7%.

A small reaction area at the UC-tantalum interface was discovered during examination of capsule L-Cla, and there was a more severe reaction between the UC and the tantalum in capsule L-Clb, the bottom capsule. The external surface of the tantalum can of capsule "b" is shown in Fig. 5.11.

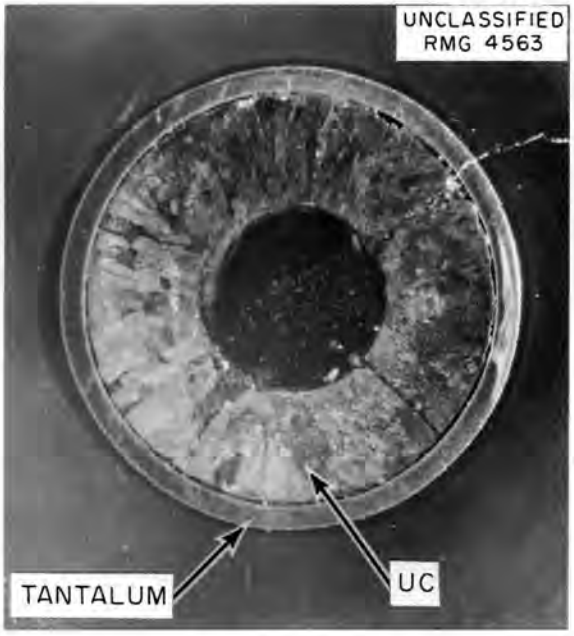

Fig. 5.10. Uranium Monocarbide in Tantalum Can After 985 hr at 2300°F Out-of-Pile. 10X.

There was swelling of the can in the region surrounding the UC pellet. A cross section of the pellet and can is shown in Fig. 5.12. As may be seen, the reaction penetrated the can wall and proceeded into the UC pellet.

Experimental assemblies L-C2 and L-C3 were irradiated at higher temperatures and for longer times than capsules L-Cla and L-Clb (Table 5.6). The thermal histories during these experiments were similar in that after a period at normal operating conditions, the central temperatures rose abruptly and then dropped to below the normal operating temperature. Both experiments were terminated because of rupture of the bottom capsule. It is postulated that the temperature increase occurred because the interface reaction products

Table 5.6. Operating Conditions for LITR-Irradiated UC-Fueled Capsules

Capsule No.	Irradiation Time (days)	Central UC Temperature (°F)[a]	
		First Day	Last Day
L-Cla	39	2095	1950
b	39	2135	1990
L-C2a	121	2000	1700
b	121	2370	1920
L-C3a	100	2260	1915
b	100	2290	1750

[a]Corrected temperatures; see preceding section on "Miniature-Capsule Irradiation Experiments in the LITR."

Table 5.7. Results of Mass Spectrometric Analysis of Gas from Irradiated Capsule L-Cla

Gas Constituents		Quantity (vol %)
He		98.07
N_2		1.11
O_2		0.138
Ar		0.104
CO_2		0.095
Kr^{83}		0.012
Kr^{84}		0.021
Kr^{85}		0.004
Kr^{83}		0.034
	Total Kr	0.071
Xe^{131}		0.046
Xe^{132}		0.065
Xe^{134}		0.131
Xe^{136}		0.173
	Total Xe	0.415

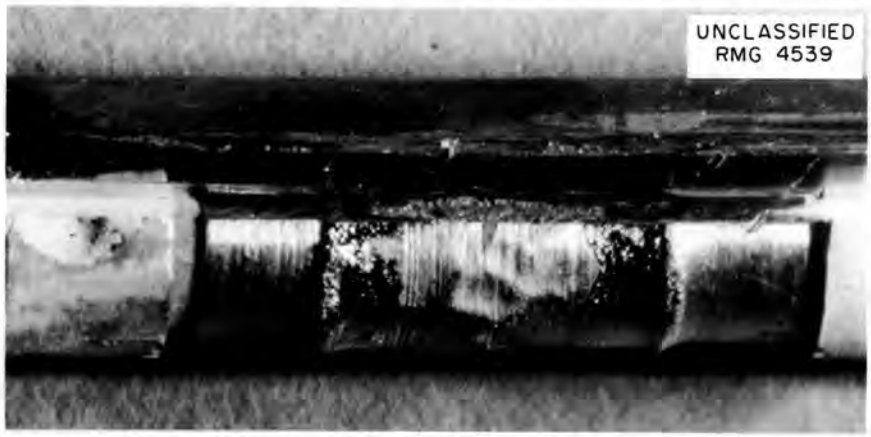

Fig. 5.11. External Surface of Tantalum Can on a UC Pellet After Irradiation in the LITR at Approximately 2000°F to a Burnup of 4000 Mwd/MT of Uranium. Note reaction zones and swelling of can. Capsule L-Clb. 4X.

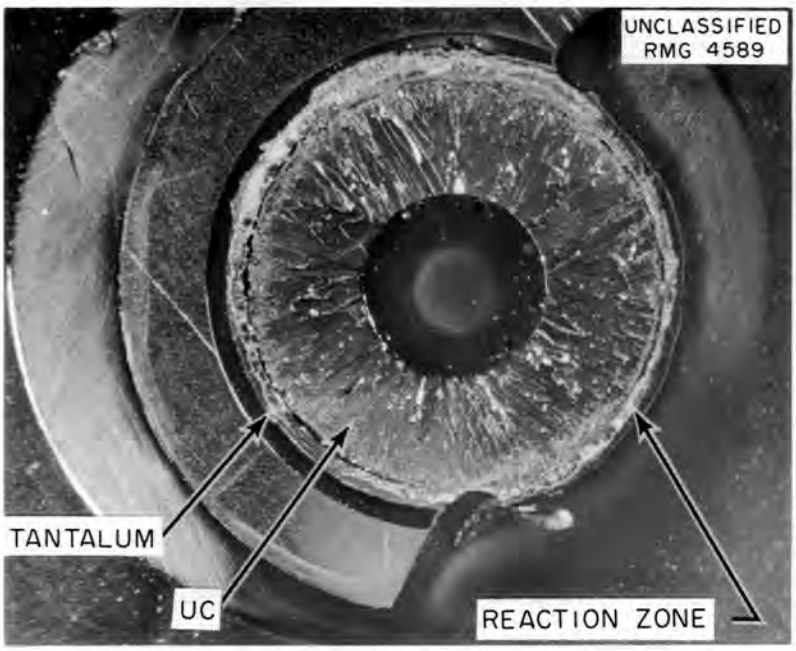

Fig. 5.12. Cross Section of Irradiated Capsule L-C1b Showing Reaction Zone at UC-Tantalum Interface. 10X.

acted as thermal insulation. As the reaction progressed, however, the tantalum can bulged until it touched the inner wall of the Inconel outer capsule. This increased the thermal conductivity and caused the central temperature to decrease.

The bottom capsule of assembly L-C3 is shown after irradiation in Fig. 5.13. The capsule pulled apart during disassembly. The Inconel outer capsule of assembly L-C2 is shown in Fig. 5.14. A bubble test revealed the indicated cracks through the Inconel wall in the region of the bottom capsule. No leaks were found in the "a" capsules of either assembly.

Metallographic Examinations. Both as-fabricated and heat-treated UC pellets of the type irradiated in assembly L-C1 were examined metallographically in order to establish a basis for detecting microstructural changes in the postirradiation examination. Two UC pellets were examined as fabricated and then sealed in tantalum cans under helium and heat treated for approximately 40 days at 2300°F under vacuum, as mentioned above. Examination of the heat-treated UC pellets revealed no noticeable

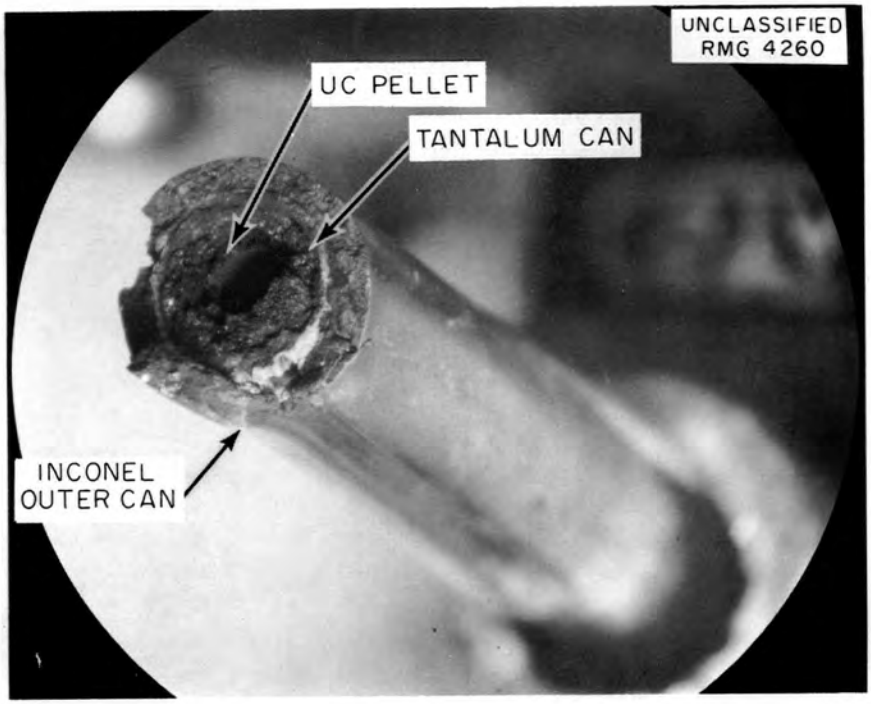

Fig. 5.13. Cross Section of Capsule LC-3b Showing Reaction Area that Resulted in Cladding Failure. 4X.

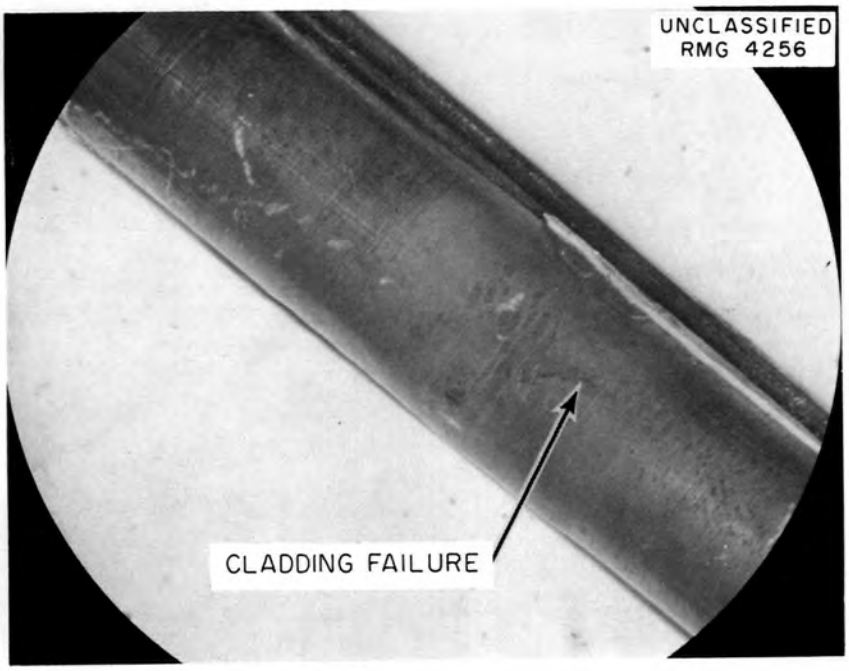

Fig. 5.14. Assembly L-C2 Showing Cracks in Inconel Outer Capsule in Region of "b" Pellet. 4X.

changes in microstructure. A small reaction layer was evident on both the inner and outer surfaces of the tantalum can. Since the reaction layer was present on both surfaces, it is not believed to be a reaction between UC and tantalum. A typical transverse section of the capsule is shown in Fig. 5.15.

Metallographic examinations have also been made of irradiated assembly L-C1. Typical transverse sections of the UC pellets and the tantalum cans of the "a" and "b" capsules are shown in Fig. 5.16. An equiaxed grain structure may be seen in the UC pellet of the "a" capsule, whereas columnar grain structure is evident in the "b" capsule pellet. The differences in grain structure of the UC pellets are due to the orientation of columnar grains in the region of the casting from which the particular pellet was machined, as mentioned previously. The sections taken through a colony of columnar grains normal to the long axis appear to consist of equiaxed grains. An unidentified fine precipitate may be seen uniformly distributed throughout both pellets. Also there are voids in the outer region of the UC and general separation at grain boundaries. The metallographic examinations confirmed the visual evidence of reaction between the UC pellets and the tantalum cans; the reaction was more severe in the "b" capsule than in the "a" capsule, as shown in Fig. 5.16. The reaction layer was apparently in a molten state during a portion of the in-pile time, as evidenced by the shape of the voids and the existence of primary crystals in the outer region. At least three distinct layers may be observed in the reaction zone. An attempt to identify the reaction layers by x-ray diffraction will be made.

MTR-Irradiated UC_2-Graphite Dispersions

Capsule Evaluations. The irradiation histories and descriptions of the MTR irradiations of UC_2-graphite fuel matrices were reported previously[9] and in the preceding section of this chapter. The test capsules consist of pellets of UC_2 dispersed in graphite and canned in low-permeability graphite. There have been four experiments to date. The first

[9]GCR Quar. Prog. Rep. March 31, 1961, ORNL-3102, pp. 176–8.

Fig. 5.15. Typical Transverse Section of a Hollow UC Pellet in a Tantalum Capsule After Heat Treating at 2300°F for Approximately 40 Days. Etched. 100X.

UNCLASSIFIED
PHOTO 54881

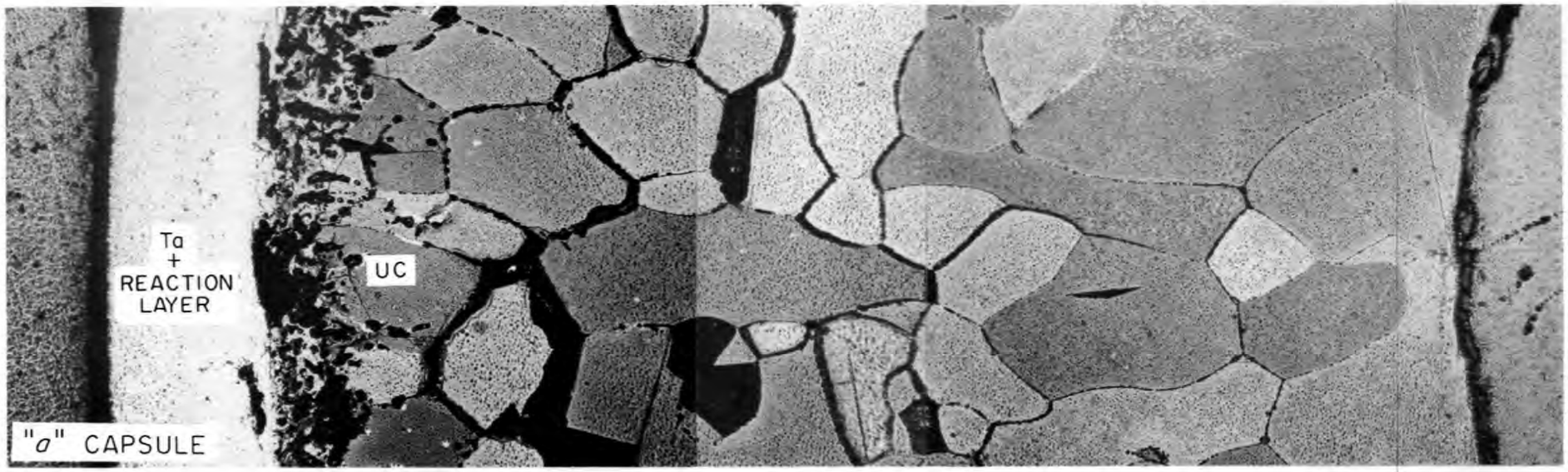

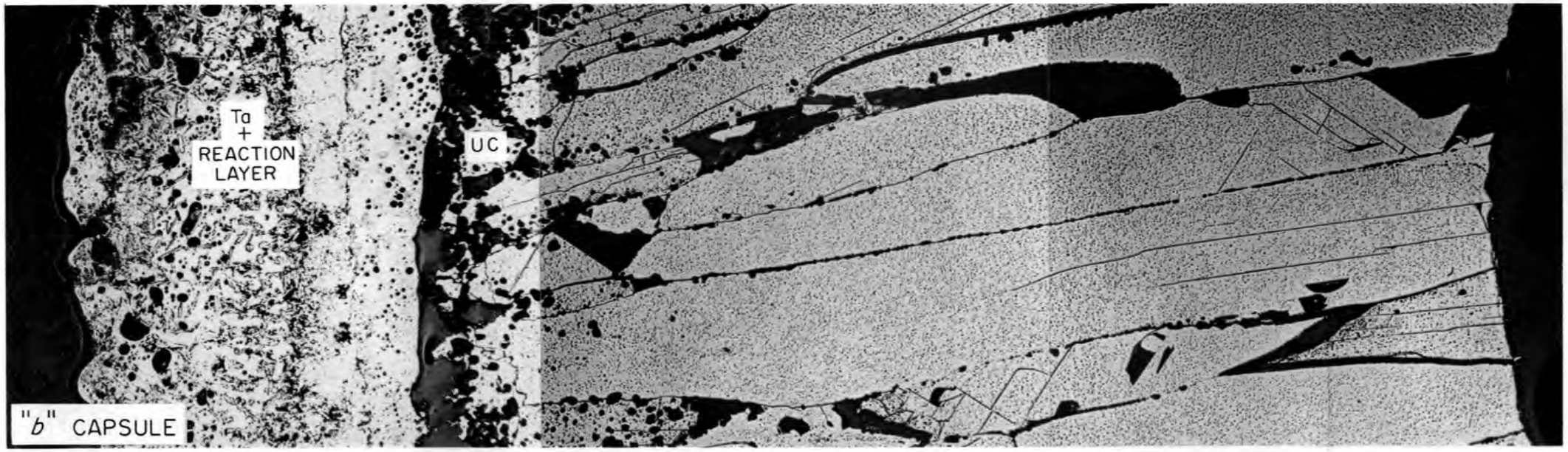

Fig. 5.16. Typical Transverse Sections of UC Pellets and Tantalum Cans of Capsules L-Cla and L-Clb After Irradiation. "a" capsule, etched; "b" capsule, as polished. 100X.

capsule (MTR-48-1) was irradiated in a static atmosphere, but the other three (MTR-48-2, -3, -4) had a sweep gas flowing outside the graphite can so that fission-gas release could be monitored. Capsules 2, 3, and 4 failed during testing under conditions that indicated leakage of the graphite can. Capsules 2 and 3 have been leak tested and the leaking area of the can has been located. Capsule 4 is being examined at GEVAL.

Core drillings were taken in the fuel pellet and the graphite can of capsule MTR-48-1 to help establish fuel and fission-product migration patterns. The data obtained on the uranium concentration in pellets "a" and "b" are presented in Table 5.8. The original uranium loading in fuel pellet "b" was higher than in pellet "a" to compensate for the lower neutron flux in the "b" position. An autoradiograph of an unirradiated control fuel pellet indicated homogeneous distribution of the fuel, but no

Table 5.8. Uranium Concentration in Fuel Pellets of Irradiated Capsule MTR-48-1

Sampling Position (in.)[a]	Uranium Concentration (atoms/mg of graphite[b])
Fuel Pellet "a"	
	$\times 10^{17}$
0	1.78
0.200	2.74
0.340	2.29
0.415	2.05
Fuel Pellet "b"	
	$\times 10^{17}$
0	4.07
0.200	4.01
0.340	3.31
0.415	3.31

[a]Distance of drill from center of pellet.

[b]Graphite matrix material.

core drillings have been taken for direct comparison. Lower uranium burn-up would be expected toward the center of the fuel pellet as a result of the flux depression in that region, so the reason for the low uranium concentration at the center of pellet "a" is not apparent.

The concentration of uranium and fission products in the wall of the graphite can on pellet "a" are listed in Table 5.9. It should be noted that the concentrations of Zr^{95} and Ce^{144}, which form stable carbides, decrease more steeply than the concentrations of Sr^{89} and Cs^{137}, which are more mobile. All values have been corrected for decay. Further work is under way to determine the average distribution of fuel dispersed in an unirradiated sample and whether the unirradiated graphite can contains uranium contamination.

The specimen for the second experiment differed from that of the first experiment in that the two fuel pellets were in a single graphite can rather than in individual cans. The graphite can and end spacers are shown after irradiation in Fig. 5.17. The porous carbon end spacers had changed dimensions as the result of the irradiation and could not be slipped intact from the ends of the graphite can. This was not the case in the first experiment in which a porous graphite spacer was used between the graphite cans. The outside dimensions of the graphite can were

Table 5.9. Uranium and Fission-Product Concentrations in Graphite Can on Pellet "a"

Sampling Position (in.)	Uranium Concentration (atoms/mg of graphite[a])	Fission-Product Concentration (atoms/mg of graphite[a])			
		Sr^{89}	Zr^{95}	Cs^{137}	Ce^{144}
0.508[b]	1.65×10^{16}	1.20×10^{16}	3.38×10^{14}	1.25×10^{16}	5.65×10^{15}
0.598	3.42×10^{15}	9.71×10^{13}	8.02×10^{11}	7.15×10^{14}	2.12×10^{11}
0.698	4.82×10^{15}	1.44×10^{14}	3.88×10^{10}	1.71×10^{14}	2.02×10^{11}
0.798	4.44×10^{15}	2.76×10^{13}	2.26×10^{10}	6.46×10^{13}	1.15×10^{11}

[a]Graphite matrix material.

[b]Distance of drill from center of can; can inner surface at 0.500 in.; can outer surface at 0.938 in.

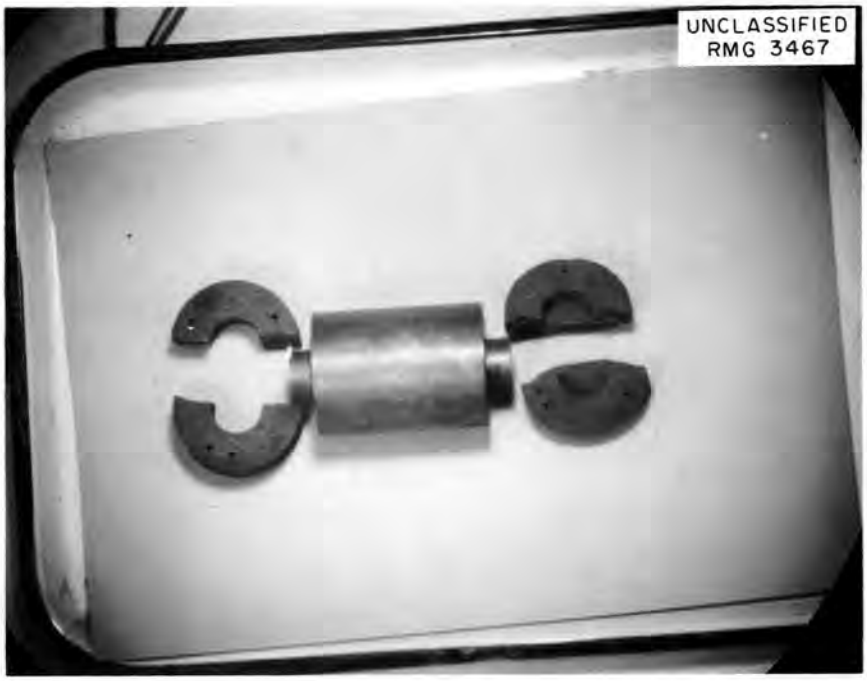

Fig. 5.17. Irradiated Graphite Can and Carbon End Spacers of Experimental Assembly MTR-48-2. 0.25X.

not changed by the irradiation. After the can was opened, the fuel pellets appeared as shown in Fig. 5.18. The short section of pellet had a higher uranium loading to balance out the longitudinal flux gradient. As may be seen in Fig. 5.18, small globules of silvery colored material were found adhering to the surfaces of the fuel pellets. There was also material of this type on the inner surface of the graphite can which housed the fuel pellets. This material has not yet been fully identified. The radioactive constituents were fission products, principally Ce^{144}, as well as uranium. The globules had a semiliquid consistency on the fuel pellet surface, which indicated the possibility that a low-melting-point alloy was formed by a combination of the UC_2 and the fission products. Because of the large amount of this material, a more logical explanation is that foreign material was introduced either during the canning of the fuel or subsequent to hot cell examination when the can, which had a leak, was immersed in hot silicone oil.

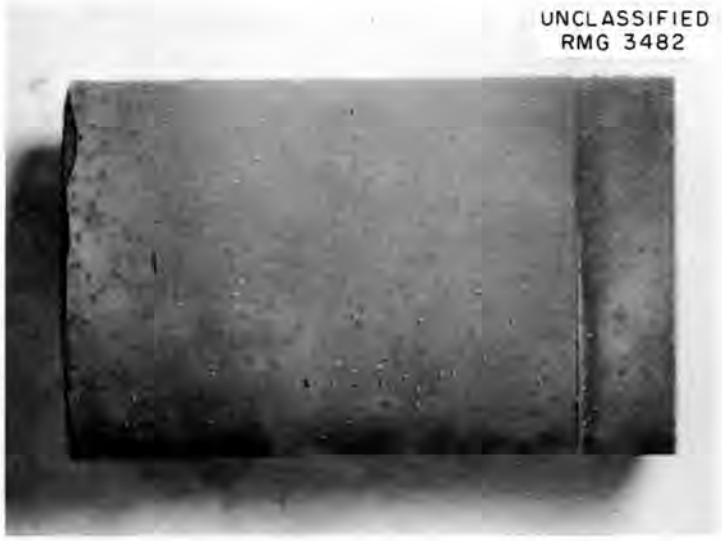

Fig. 5.18. Irradiated UC_2-Graphite Fuel Pellets from Experimental Assembly MTR-48-2.

The fuel pellets underwent dimensional changes similar to those of the first pellets (experiment MTR-48-1). An average decrease in diameter of 4.5% and a length increase of 3% were noted.

Metallographic Examination of Capsule MTR-48-2. An area typical of the UC_2 dispersed in graphite in pellet "a" of experimental capsule MTR-48-2 is shown in Fig. 5.19. The light phase, which is the UC_2, appears to have been in the molten state at one time. It is not possible to determine whether this occurred in-pile because no unirradiated control sample is available.

The type 316 stainless steel-sheathed thermocouple that was included in the low-permeability graphite can was examined. Two transverse sections were taken, one 5 in. from the bead and the other 1 in. from the bead. There was no change in grain size compared with that of an unirradiated control specimen. The section 5 in. from the bead looked like the control specimen except that there was evidence of carbide formation in the grain boundaries. The section 1 in. from the bead was heavily carburized, with practically a continuous carbide phase in the grain boundaries. General pitting of the outer surface was also noted. These transverse sections are shown in Fig. 5.20.

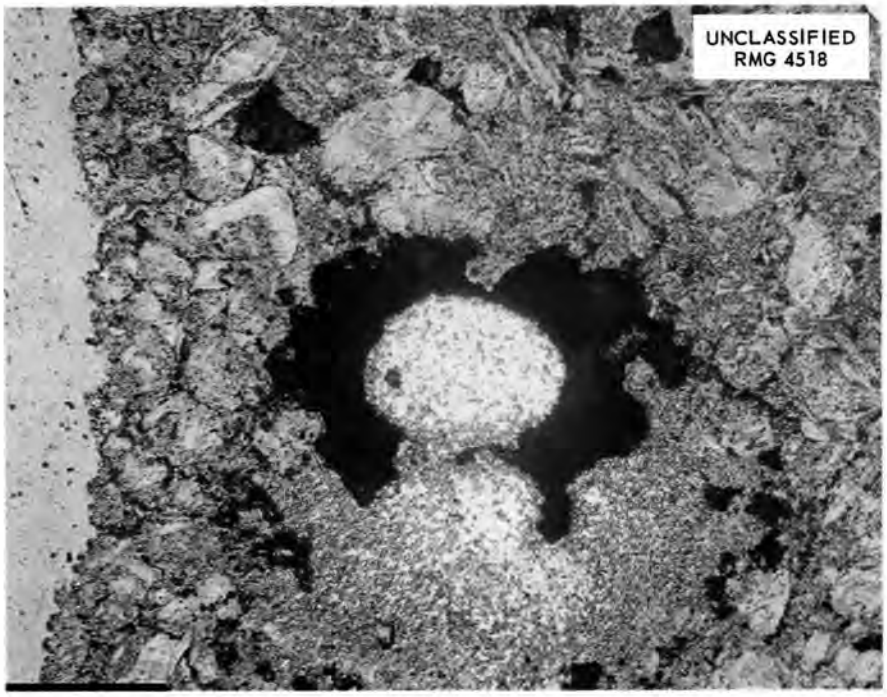

Fig. 5.19. Typical Area of UC_2-Graphite Pellet from Capsule MTR-48-2. The white phase is UC_2. As polished. 250X.

ORR-B9 Facility Irradiations

Facility Modifications. The ORR-B9 facility is being converted from a nitrogen-cooled loop into a single-pass air-cooled system with a helium sweep gas flow to transport fission gases from the test capsule to a gamma-ray spectrometer. A special trap will be used to collect the solid daughters of short-lived fission gases. The modified experimental section is shown in Fig. 5.21, with the air and helium flow paths indicated. Test samples received from High Temperature Materials Company, Inc., consisting of UC_2 spheres with pyrolytic carbon coatings are being prepared for irradiation. The uranium is 93% enriched, and the spheres are 0.040 in. in diameter, including the coating.

Metallographic Examination of Capsules B9-3 and -4. Metallographic examinations have been made of capsules B9-3 and -4 for which the in-pile test conditions and the macro examination results were reported previously.[10]

[10]Ibid., pp. 181–8.

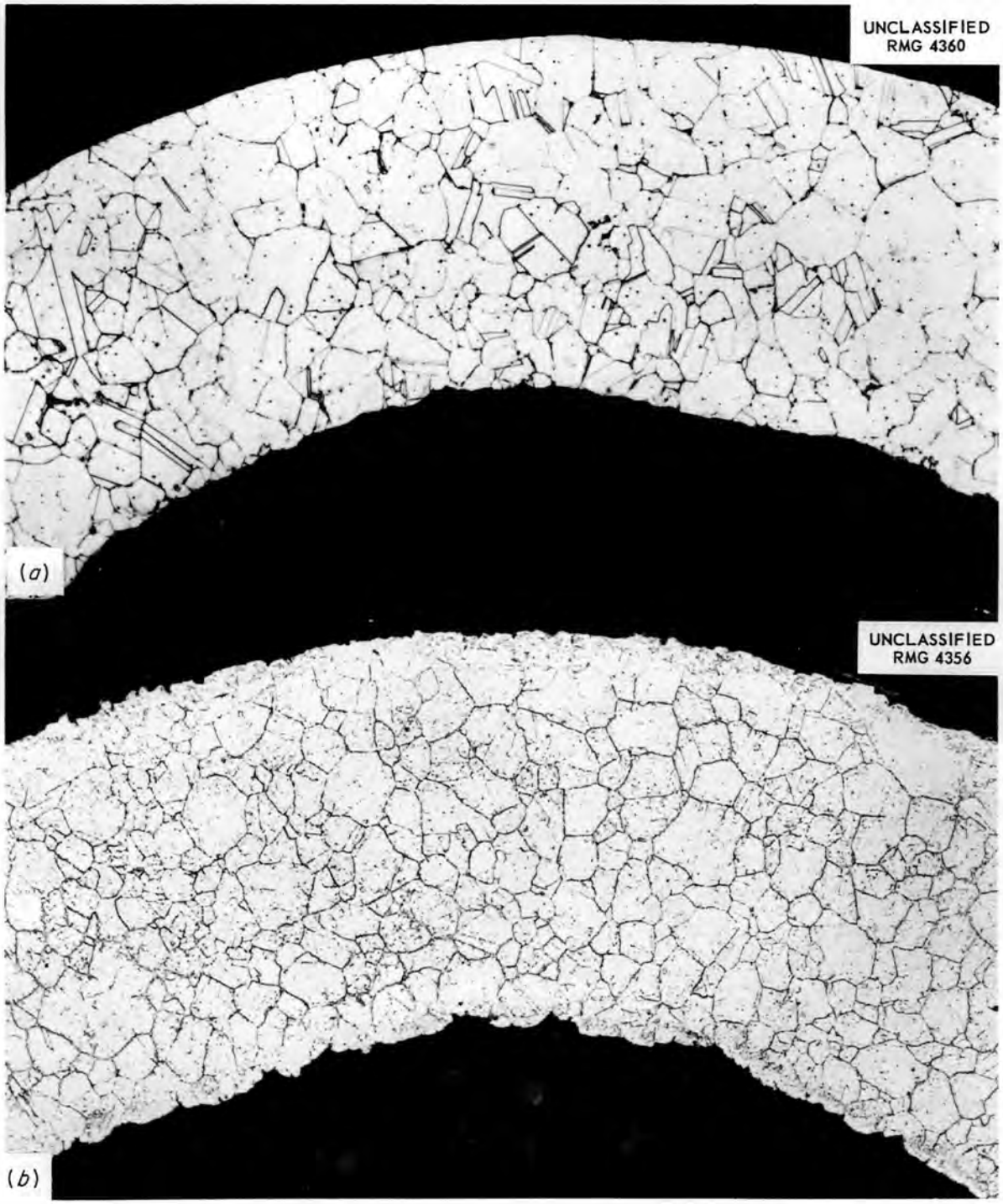

Fig. 5.20. Transverse Sections of Type 316 Stainless Steel Sheath of Thermocouple No. 8 from Capsule MTR-48-2. (a) Section taken approximately 5 in. from thermocouple bead. (b) Section taken approximately 1 in. from thermocouple bead. Note carbide phase in grain boundaries and precipitate in grains. Etched. 250X.

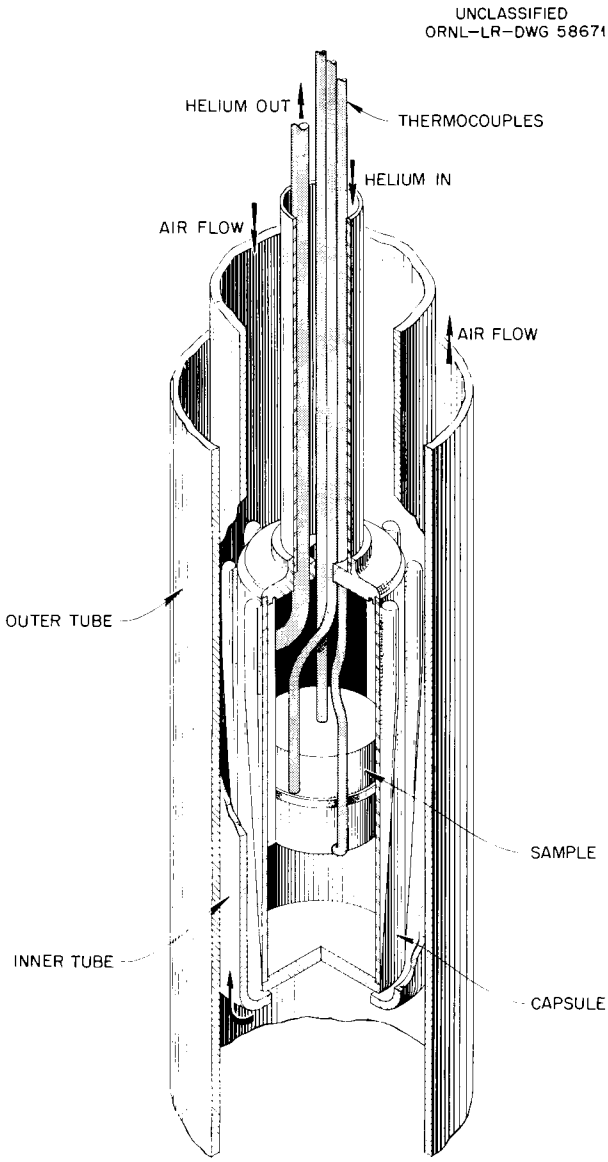

Fig. 5.21. Experimental Section of Modified Assembly for Irradiations in ORR Facility B9.

These capsules consisted of UO_2 pellets clad with low-permeability graphite. The B9-3 specimens were coated with siliconized SiC and the B9-4 specimens were uncoated. A longitudinal section through the hole shown previously in the siliconized SiC coating of the top sample of capsule B9-3 is presented in Fig. 5.22. No fractures were found in the siliconized-SiC-sealed threaded graphite plug in the graphite can. There were, however, fractures in the silicon seals of the two uncoated low-permeability graphite cans irradiated in the B9-4 capsule, such as that shown in Fig. 5.23.

The postirradiation examination of the UO_2 pellets from both sections of capsule B9-3 revealed similar microstructures. As mentioned previously,[9] the ends of the originally hollow cylinders became filled with UO_2 during irradiation. One of these deposited UO_2–graphite interfaces is shown in Fig. 5.24. There is no evidence of a reaction between the UO_2 and the graphite. Long columnar grains were formed in the UO_2 by the migration of "chevron"-shaped voids toward the hotter regions of the UO_2, that is, toward the center of the pellet. The migration of the voids is the result of sublimation of UO_2 from the hotter surfaces followed by a redeposition of the UO_2 vapor on the cooler surfaces. This also explains the shape of the voids. The grains that are

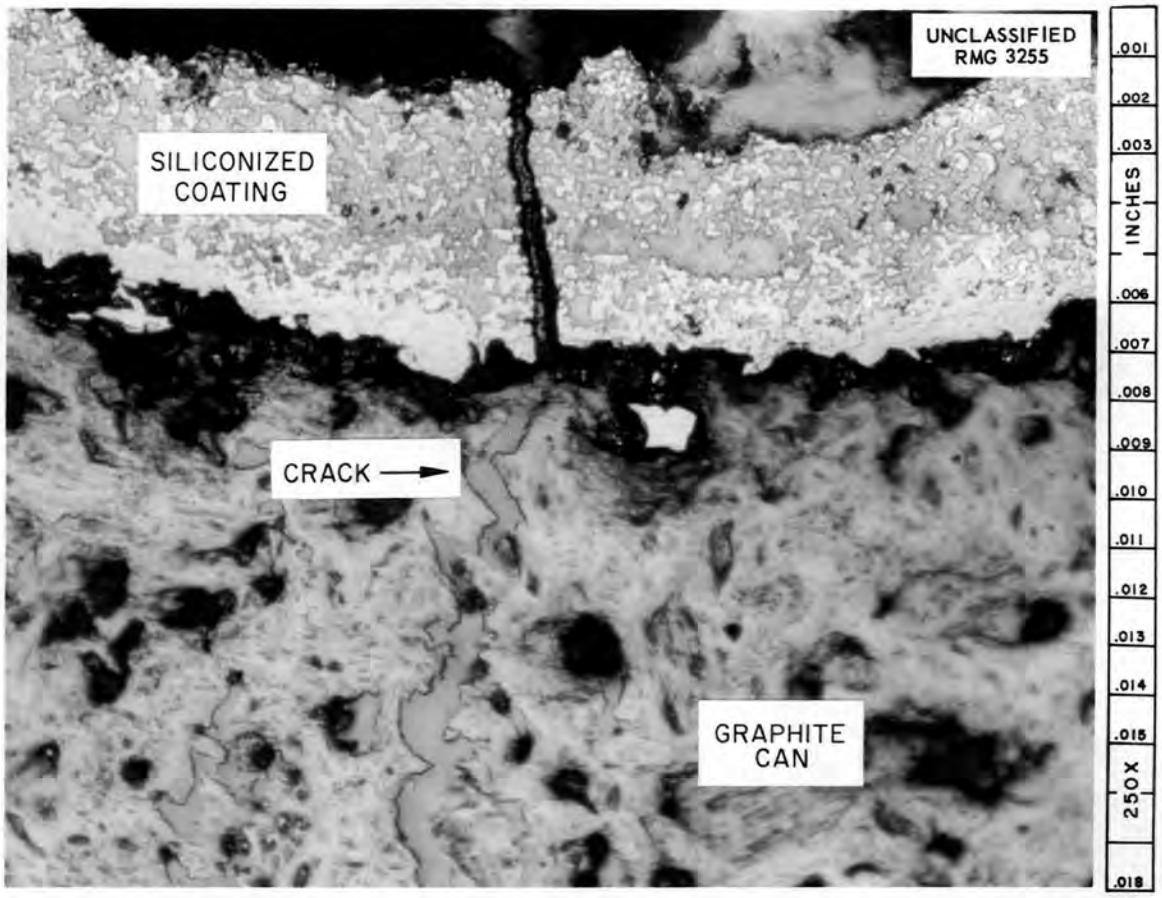

Fig. 5.22. Longitudinal Section at Thermocouple Trench of the Top Sample from Capsule B9-3. The crack began at the inner surface of the graphite can and continued through the siliconized SiC coating. As polished. 250X.

formed by the migration of the voids have a <111> preferred orientation along the columnar axis. Based on the work of Lawson and MacEwan,[11] steep thermal gradients must exist at temperatures between 1700 and 2800°C in order for this phenomenon to occur.

Examinations of transverse sections of the UO_2 pellets from capsule B9-3 revealed an average loss of approximately 25% of the wall thickness. This agreed with the amount of UO_2 deposited in the ends of the pellets. Small crystals of UO_2 were found on the inner surfaces of the pellet that

[11]V. B. Lawson and J. R. MacEwan, Thermal Simulation Experiments with a UO_2 Fuel Rod Assembly, CRFD-915.

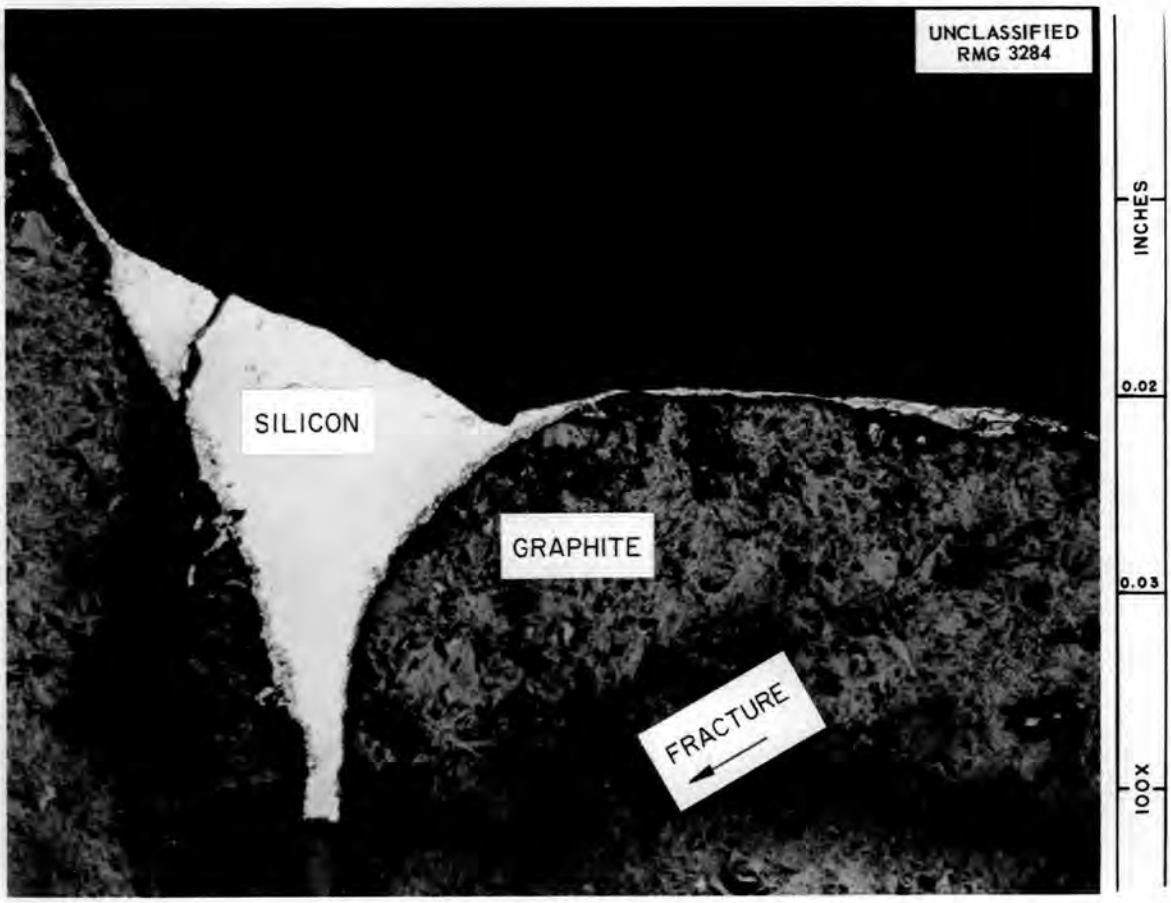

Fig. 5.23. Typical Silicon-Sealed Plug in Low-Permeability Graphite Can from Capsule B9-4. Note fracture extending through the silicon seal and the graphite. Dark areas around the fractures in the graphite are silicone oil absorbed during leak-testing. As polished. 100X

are believed to have been formed as a result of thermal cycling during irradiation. There is no evidence that any portion of the UO_2 had been in the molten state during irradiation; thus the hypothesis that the movement of the UO_2 was a result of a sublimation-redeposition mechanism is substantiated.

No movement of the UO_2 was found in capsule B9-4, and there was no evidence of reaction between the UO_2 and graphite. Radial fractures of the pellet were noted. The microstructure examination showed the UO_2 to be composed of equiaxed grains. The grain size was at least five times that of the unirradiated control sample. Typical sections of the hottest regions near the inner surface are shown in Fig. 5.25. The microstructures

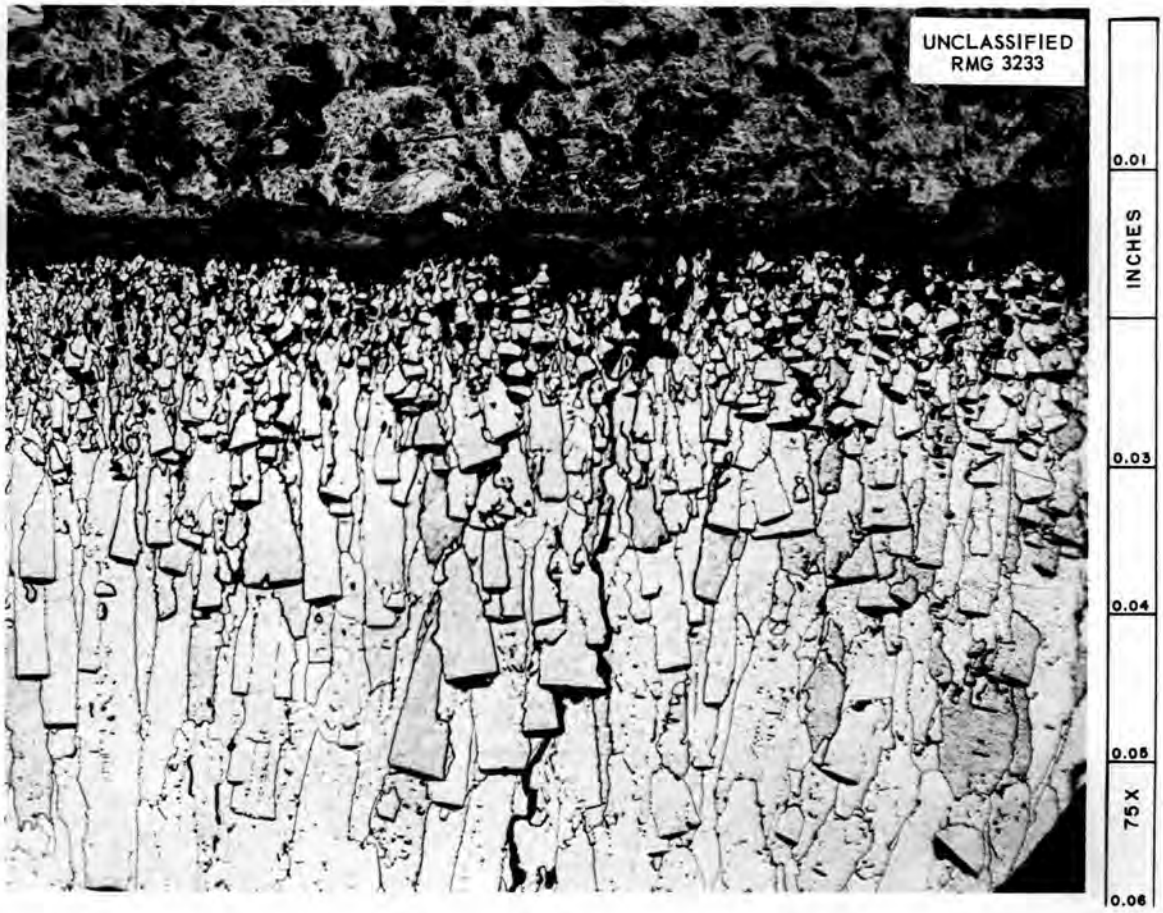

Fig. 5.24. Interface of Graphite Can and Vapor-Deposited UO_2 in Specimen from Capsule B9-3. Note columnar grains formed as a result of the migration of the voids toward the hotter regions of the pellet. Etched. 75X.

of the two pellets were similar in the outer surface regions. Voids in the grain boundaries from the middle of the wall to the inner surface region were noted only in the irradiated pellet at the higher temperature.

Instantaneous Fission-Gas-Release Experiment

R. M. Carroll

Xenon and Krypton Release

The initial results obtained with thin-plate samples of UO_2 sandwiched between ThO_2 plates were reported previously.[12] The UO_2 samples

[12]GCR Quar. Prog. Rep. March 31, 1961, ORNL-3102, pp. 188–96.

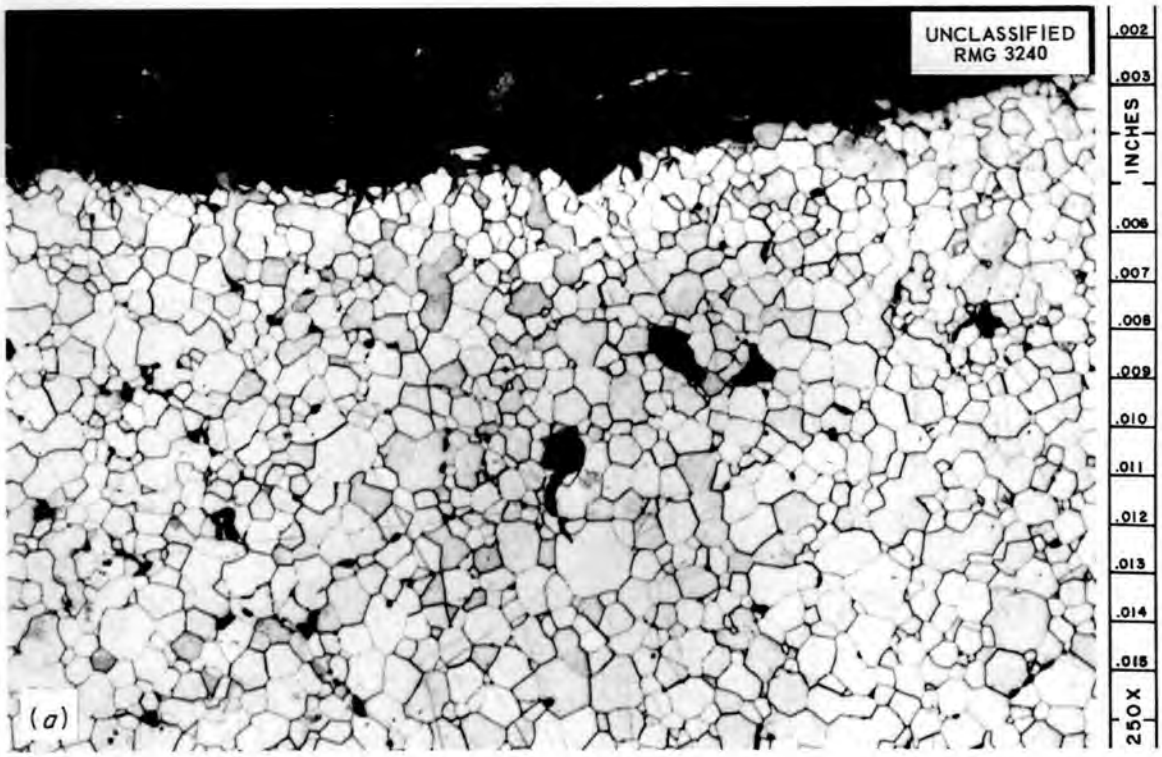

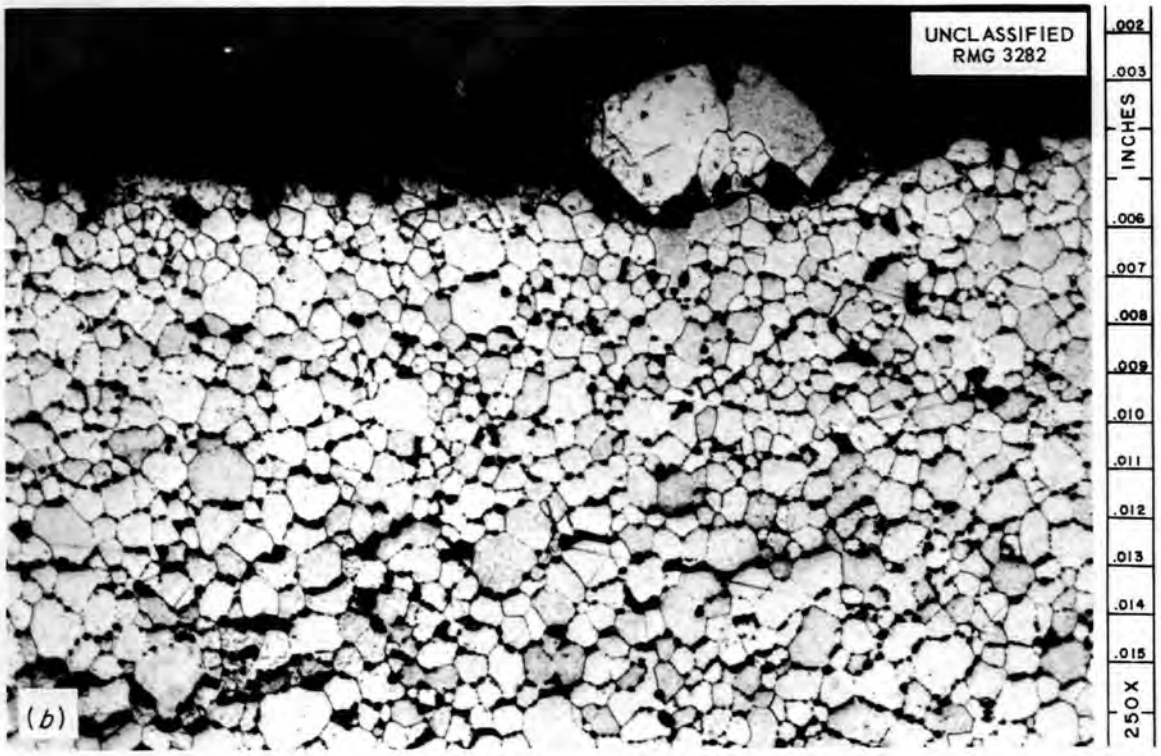

Fig. 5.25. Typical Microstructures at Inner Surface Regions of the Hollow UO_2 Pellets from Capsule B9-4. (a) Pellet irradiated in lower temperature zone. (b) Pellet irradiated in higher temperature zone. Etched. 250X.

had been irradiated at various temperatures until a maximum temperature of 1100°C was obtained. At 1100°C, the gas release continued to increase with time. The sample was then again irradiated at lower temperatures, and it was found that the ratio of release of fission gas to production had been permanently increased by the irradiation at 1100°C. The activation energy had not been altered, however, so the temperature dependence of the gas release remained the same.

Subsequent irradiation at different temperatures disclosed that the rate of release of the fission gases was slowly increasing with time. The cause of the time-dependent increase is not known. The increase was not continuous but, rather, appeared to follow thermal cycles. The samples were removed from the reactor and will be examined for structural changes.

The data obtained from this experiment are being evaluated. The temperature dependence of Xe^{138}, Kr^{88}, and Kr^{85m} release was studied most thoroughly because these isotopes reach equilibrium release within 24 hr. The data divide roughly into two categories, those taken before reaching 1100°C and those taken after this temperature was reached. The release-to-production ratio was increased about an order of magnitude by the irradiation at 1100°C.

When the UO_2 was cooled from operating temperature to around 100°C, there was a burst of fission-gas release. This has been called the cooling burst. A study of such bursts was conducted by allowing the UO_2 to be irradiated under constant conditions until the release rate of Xe^{133} and Xe^{135} was at equilibrium and then cooling the UO_2 rapidly. Samples of the fission gas released during the cooling burst were taken at short time intervals, and the total amount of Xe^{133} and Xe^{135} released in the burst was determined.

At temperatures below 1000°C, only a small fraction of the fission gas being generated is released from the UO_2. The remainder of the gas is trapped in the fuel. If the small escape rate (usually less than 0.1%) is ignored, the amount of any isotope trapped in the fuel is at equilibrium when the decay rate, dN/dt, is equal to the production rate. In this manner

$$\frac{dN}{dt} = N(\lambda + \sigma\phi) = \gamma\Sigma_f\phi \quad , \tag{1}$$

where

N = number of atoms of the isotope,

λ = decay constant of the isotope,

ϕ = neutron flux,

Σ_f = the fission cross section of the UO_2,

γ = the fission yield of the isotope,

σ = the absorption cross section of the isotope.

Since λ, ϕ, Σ_f, γ, and σ are known, the amount of isotope trapped in the fuel, N, can be calculated. The number of atoms of any isotope at radioactive equilibrium in the fuel, neglecting diffusion and recoil escape, is

$$N = \frac{\text{Production rate}}{\lambda + \sigma\phi} = \frac{\gamma\Sigma_f\phi}{\lambda + \sigma\phi} \quad . \tag{2}$$

Except for Xe^{135},

$$\lambda + \sigma\phi \approx \lambda \quad ;$$

when λ of Xe^{135} is used below it is understood to be corrected for burn-up by neutron absorption.

The ratios of two different isotopes trapped in the UO_2 are

$$\frac{N_1}{N_2} = \frac{\gamma_1\Sigma_f\phi}{\gamma_2\Sigma_f\phi}\,\frac{\lambda_2}{\lambda_1} = \frac{\gamma_1}{\gamma_2}\,\frac{\lambda_2}{\lambda_1} \quad , \tag{3}$$

when the isotopes are at radioactive equilibrium.

The time required for radioactive equilibrium is approximately five half lives of the isotope. The fuel is irradiated at constant flux (and therefore constant isotope-production rate) for this length of time. The fuel may be irradiated at different temperatures, but the small escape rate, even at higher temperatures, would have little effect on the amount of trapped isotope. Thus, after equilibrium has been obtained, the amount

of trapped isotopes has the inverse ratio of the decay constants and the direct ratio of the yield, as expressed in Eq. (3).

The amount of isotopes released by recoil from the UO_2 will vary directly with flux and has no temperature dependence. The ratios of isotopes released by recoil are

$$\frac{N_1}{N_2} = \frac{\gamma_1 \Sigma_f \phi}{\gamma_2 \Sigma_f \phi} = \frac{\gamma_1}{\gamma_2} \quad , \tag{4}$$

so the isotopes released by recoil vary directly with fission yield. Isotopes which are released by diffusion follow the general relation

$$f = C \left(\frac{D}{\lambda}\right)^{1/2} \quad , \tag{5}$$

where

- f = fractional release (ratio of rate of release to rate of formation),
- D = diffusion coefficient for the isotope,
- λ = decay constant for the isotope,
- C = a constant that depends upon the diffusion model used.

The ratio of the amounts of two isotopes escaping the fuel by diffusion would be

$$\frac{f_1}{f_2} = \frac{C\left(\frac{D_1}{\lambda_1}\right)^{1/2}}{C\left(\frac{D_2}{\lambda_2}\right)^{1/2}} = \left(\frac{D_1\lambda_2}{D_2\lambda_1}\right)^{1/2} \quad . \tag{6}$$

If the diffusion coefficients are equal

$$\frac{f_1}{f_2} = \left(\frac{\lambda_2}{\lambda_1}\right)^{1/2} , \tag{7}$$

but the fractional release, f, is $R/\gamma\Sigma_f\phi$, where R is the release rate. Therefore

$$\frac{f_1}{f_2} = \frac{R_1\gamma_2\Sigma_f\phi}{R_2\gamma_2\Sigma_f\phi} .$$

The ratio for the equilibrium release rates of two isotopes with the same diffusion coefficients is then

$$\frac{R_1}{R_2} = \frac{\gamma_1}{\gamma_2}\left(\frac{\lambda_2}{\lambda_1}\right)^{1/2} . \tag{8}$$

Two isotopes of xenon, Xe^{133} and Xe^{135}, were studied to find the release rates under various conditions. These isotopes were assumed to have the same diffusion coefficients, and their release rates were corrected for the release of their iodine precursors. The ratio of the production rates and therefore the ratio of the recoil rates is 1.05, from Eq. (4).

During steady-state release, the measured Xe^{133}-to-Xe^{135} ratio was 5.1 (average). The diffusion ratio predicted by Eq. (8) is 4.6. The 5.1 ratio of Xe^{133} to Xe^{135} shows that these isotopes were released by diffusion rather than any form of recoil, which would have given a 1.05 ratio.

When the cooling burst was released, the measured ratio of Xe^{133} to Xe^{135} was 22. Equation (3) gives 22 as the Xe^{133}-to-Xe^{135} ratio for trapped xenon at radioactive equilibrium. This demonstrates that the cooling burst releases a store of trapped gas.

Generally, the same fraction of the total amount of trapped Xe^{133} and Xe^{135} was released in the cooling burst. The amount of Kr^{88} and Kr^{85m} trapped in the fuel is small compared with the trapped Xe^{133} and Xe^{135}, but it appears that the kryptons are also released in the same fraction as the xenons. The burst has the same general appearance as would be expected if a small portion of the fuel were totally emptied of trapped gases.

The cooling burst was found to be temperature dependent, that is, the higher the temperature of irradiation, the larger the cooling burst. The steady-state diffusion release was also temperature dependent and increased with temperature. When the total number of atoms released in the cooling burst is divided by the number of atoms per second released during steady-state release, the resulting time is a constant. The cooling burst was found to release the same amount of Xe^{133} as 18 hr of steady-state release and the same amount of Xe^{135} as 7 hr of steady-state release. Seven bursts were evaluated to obtain these data, which show several hours scatter, but since the size of the bursts varied through two orders of magnitude, these times are considered reasonably constant.

The existence of a region in the fuel in which the gas is trapped has important implications. All models used for calculating diffusion coefficients assume a homogeneous medium in which the gases diffuse until they encounter a free surface where they are liberated. The calculations also assume a concentration gradient through the thickness of the model. In this way, the value of the diffusion coefficient depends upon the distance through which the gas has diffused. The trapped gas implies a nonhomogeneous model, with one zone where gas can be released by diffusion and the other zone in which gas is trapped. It may be possible to evaluate the thickness of the diffusion zone by an analysis of the ratios in which Xe^{138}, Xe^{133}, Xe^{135}, I^{133}, I^{135}, Kr^{85m}, and Kr^{88} are being released. This problem will be studied to attempt to find an adequate model for predicting diffusion release.

The UO_2 sample is physically a two-region body, consisting of grains and grain boundaries. This also implies that a two-region model should be used. The effect of grain boundaries can be evaluated by using a

single-crystal sample. Some single crystals of UO_2 have been obtained, and samples will be prepared for irradiation.

Iodine Release

The iodine precursor of xenon is released from UO_2 with the same temperature dependence as the xenon and krypton. In the 700 to 1000°C temperature range about 80% of the mass 135 and 45% of the mass 133 isotopes which are released emerge from the fuel as iodine or a precursor of iodine. The reason for the different percentage is not entirely clear.

This ratio of iodine to xenon escape is true only in the 700 to 1000°C range. At lower temperatures recoil predominates, and nearly all the isobar is released as iodine. In the 1100°C run, while the fuel was changing release characteristics, 28% of the mass 133 isotope and 46% of the mass 135 isotope escaped as iodine. The 1100°C run cannot be regarded as typical, however, since equilibrium was never attained.

Radiation Effects on Structural Metals

Stainless Steel (N. E. Hinkle, J. T. Venard, J. W. Woods, J. C. Zukas)

Three additional in-pile tube-burst tests of type 304 stainless steel (Superior Tube Co., heat No. 23999x) were completed. The data obtained in these and previous tests are summarized in Table 5.10.

The data indicate a change of about 25% in rupture strength in tests at 1500°F and a change of about 15% at 1600°F. No change in time to rupture occurred at 1300°F. The ductility at rupture was decreased by a factor of 2 to 4 at all test temperatures. There is an indication that at 1500 and 1600°F, the ductility at rupture decreases with increasing time to rupture, although the out-of-pile specimens do not show this trend. Both the in-pile and out-of-pile specimens tested at 1300°F exhibited much lower fracture strain, with the in-pile fracture strain limited to an average of 1%.

Table 5.10. Stress-Rupture and Tangential Strain Data for In-Pile and Control Tube-Burst Specimens of Type 304 Stainless Steel (Superior Tube Co., Heat No. 23999x)

Test Temperature (°F)	Specimen Identification	Stress (psi)	Time to Rupture (hr)	Average Tangential Strain (%)	Maximum Tangential Strain (%)
1300	15-2	13 000	127	1	1.4
	15-3	13 000	217[a]	0.4	0.6
	15-6	13 000	141	1.1	2.1
	15-8	13 000	116	0.85	1.15
	126 control	13 000	144	1.57	2.33
	127 control	13 000	144	2.72	3.49
	15-4	11 000	502	0.9	1
	15-7	11 000	470	1.1	1.9
	15-10	11 000	452	0.8	1.1
	124 control	11 000	470	3.57	4.12
	128 control	11 000	550	2.86	4.21
	15-1	9 000	1642	1	1.1
	15-5	9 000	>1860	0.85	1.1
	15-9	9 000	>1860	0.8	1
1500	9-7	5 000	337	3.3	3.8
	9-8	5 000	518	3.2	3.8
	73 control	~5 250	1130	8.1	9.3
	239 control	~5 250	1025	12.5	15
	9-6	4 000	673	3.8	5.3
	17-3	4 000[b]	851	1.3	3.6
	72 control	~4 200	1670	9.6	11.5
	240 control	~4 200	2450	9.2	12.4
	17-1	3 000	>1600	0.5	0.6
	17-9	3 000	>1600	0.7	0.85
	310 control	~6 300	520	10	15
	537 control	~6 300	184	7	9
1600	17-8	5 000	50	1.1	1.5
	1066 control	~4 600	82	7.5	9.8
	Control	~4 300	175		
	1112 control	~4 200	63	11	17
	Control	~3 800	180		
	Control	~4 100	142		
	360 control	~3 700	265	10.2	13.5
	718 control	~3 200	243	18.5	24.2
	1068 control	~3 200	197		
	17-5	3 000	414	3.3	6.8
	17-6	2 600	870	3.2	5.6
	17-4	2 200	1430	2.2	3.8
	17-7	2 200	>1500	1.5	1.8

[a]Irradiated more than 500 hr at 1300°F and 16 Mw prior to stressing.

[b]Irradiated more than 500 hr at 1500°F and 30 Mw prior to stressing.

Inconel (N. E. Hinkle, J. W. Woods, J. C. Zukas)

Three additional in-pile tube-burst tests of Inconel (INCO heat No. NX-8962) were completed. The strain data and times to rupture at 1500°F in air are given in Table 5.11 for in-pile and control specimens.

It was suggested that the reduction in time to rupture for the in-pile specimens might be caused by the presence of boron in the material, since the boron would give rise to the formation of helium gas during thermal-neutron bombardment. In order to investigate this possibility, six special heats of Inconel were obtained from the International Nickel Company that contained various amounts of natural and/or isotopic boron,

Table 5.11. Stress-Rupture and Tangential Strain Data for In-Pile and Control Tube-Burst Specimens of Inconel Tested at 1500°F (INCO Heat No. NX 8962)

Specimen No.	Stress (psi)	Time to Rupture (hr)	Average Tangential Strain (%)	Maximum Tangential Strain (%)
11-5	5000	173[a]	0.45	0.6
11-6	5000	73	2.7	5
11-7	5000	140[a]	2.5	4.4
11-8	5000	91	1	1.6
9-4	5000	117[b]	0.55	0.8
4-5	5000	109[c]	1.5	2.3
4-6	5000	110[d]	4.7	5.6
35 (control)	5000	473		11.2
41 (control)	5000	487		8.4
28 (control)	5000	410		5.7
43 (control)	4000	801		13.8
44 (control)	4000	797		10.7
4-10	3000	774	0.65	0.8
37-2-71	3000	784		0.8
37-2-73	3000	>870		1.25
48 (control)	3000	>2850		9.6

[a]Stressed 48 hr prior to start of irradiation.

[b]Irradiated more than 1000 hr at 1500°F prior to stressing out-of-pile.

[c]Irradiated 100 hr at 1500°F prior to stressing.

[d]Irradiated 550 hr at 1500°F prior to stressing.

as described previously.[13] The first in-pile test has been completed, and the results, together with out-of-pile data, are presented in Table 5.12. In accordance with the postulation of helium gas generation, the heat of material with the greatest amount of B^{10} present would show the greatest effect of neutron bombardment on the rupture strength, while the heat with high B^{11} content would not show as large an effect as for an equivalent amount of B^{10}. The limited data of this first experiment provide both support and opposition to the argument. All the materials, except heat 6B11, seem to respond to the neutron bombardment in the manner expected; however, the amount of change does not appear to be a direct function of B^{10} content. This might be due to a variation in distribution of the B^{10} in the test material. The B^{10} distribution has not yet been

[13]Ibid., p. 202.

Table 5.12. Effect of Neutron Bombardment on Stress-Rupture Characteristics of "Boron-Adjusted" Heats of Inconel Irradiated at 1500°F in Air

Specimen Heat	Boron Content	Specimen Identification	Stress (psi)	Time to Rupture (hr)	Comments on Effect of Irradiation on Time to Rupture
0B	<10 ppm, natural boron	Control	6000	155	Reduced by a factor of 2 to 3
		Control	5000	320	
		28-6	5000	140	
		Control	4000	1250	
		28-2	4000	473	
		Control	3000	1950	
4B11	40 ppm, 98% B^{11}	Control	5000	105	No change
		28-9	4500	186	
		Control	4000	250	
		28-5	3200	617	
		Control	3000	980	
6B11	60 ppm, 98% B^{11}	28-4	5500	56	Reduced by a factor of 10
		Control	5000	610	
		28-10	4500	133	
		Control	3800	1500	
10B	100 ppm, natural boron	28-3	6000	52	Reduced by a factor of 5 to 10
		28-8	5000	58	
		Control	5000	580	
		Control	4000	1750	
6B10	60 ppm, 95% B^{10}	Control	5000	195	Reduced by a factor of 3 to 5
		28-1	4500	80	
		Control	4000	255	
		28-7	3500	229	

determined. The data in opposition to the proposed radiation damage mechanism were obtained for heat 6B11. These data indicate a factor of 10 reduction in time to rupture on a material which should show little change, as observed on a similar material (heat 4B11).

Beryllium (J. R. Weir, W. W. Davis)

An in-pile stress-rupture (tube-burst) experiment has been performed at 700°C on beryllium tubes manufactured by warm extrusion and by hot pressing and machining. Although the data from eight specimens are somewhat scattered, an effect on the strength was observed.

An attempt has been made to obtain an expression for the effect of integrated flux and temperature on the stress-rupture strength of beryllium for the various materials tested thus far. The relationship between the effect of exposure on the 100-hr rupture stress in-pile and the integrated fast flux is shown in Fig. 5.26. The fractional decrease

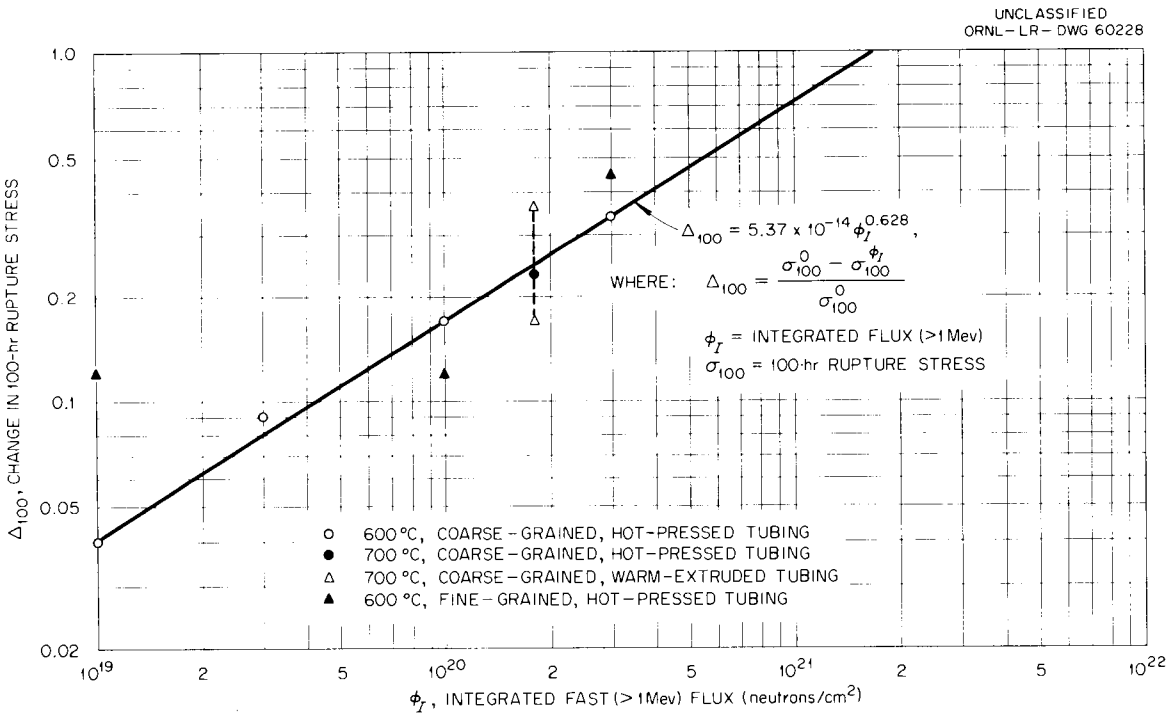

Fig. 5.26. Effect of Irradiation on the Stress-Rupture Properties of Beryllium.

in the 100-hr rupture stress, Δ_{100}, is plotted versus the integrated fast flux for various materials. The most reliable data exist for the coarse-grained, hot-pressed tubing tested at 600°C, and thus the curve is drawn through those points. The limited data for other materials and temperatures exhibit considerable scatter. It is somewhat surprising, however, that the data from tests at 700°C fall on the same curve as that obtained at 600°C, since it would be assumed that, unless helium were diffusing out of the beryllium, it would be more effective in reducing the strength at 700°C than at 600°C.

In addition to the tube-burst specimens, eight swelling specimens were exposed to an integrated fast (>1 Mev) flux of 3.6×10^{20} neutrons/cm^2. The intent of the swelling experiments was to determine the effect of oxygen and carbon content on swelling. The irradiation temperature and the compositions of the beryllium specimens are given in Table 5.13. Under these conditions of irradiation, specimens were found previously to swell 3 to 5%. Postirradiation density measurements on these specimens are under way.

Another experimental assembly is being irradiated that contains 12 tubular swelling specimens as well as specimens of warm-extruded tubing for tube-burst tests. The purpose of these tests is to examine in more

Table 5.13. Composition and Irradiation Temperatures for Beryllium Swelling Specimens

Specimen	BeO Content (wt %)	Be_2C Content (wt %)	Irradiation Temperature (°C)
1	3.75	<0.2[a]	700
2	3.75	<0.2[a]	650
3	~1[a]	1.7	650
4	~1[a]	1.7	700
5	1.2	0.12	700
6	1.2	0.12	700
7	0.6	0.06	700
8	1.2	0.12	700

[a]Estimated.

detail the behavior of Pechiney hot-pressed and warm-extruded tubing at exposures of 1.8 and 3.6×10^{20} neutrons/cm^2 in the temperature range of 650 to 780°C.

Pressure-Vessel Steels (R. G. Berggren)

An experimental assembly (ORR-8) that contained tensile and impact specimens of pressure-vessel steels was removed from the ORR poolside facility after the scheduled two cycles of exposure. Also, experimental assembly ORR-30, which contained impact specimens of ASTM A-212, grade B, steel (base plate and simulated heat-affected zone specimens), was exposed for the scheduled one cycle in the ORR poolside facility and removed. Capsule No. 1, containing ASTM A-212, grade B, steel specimens, was removed from the ORR-GCR loop No. 1 and disassembled in the ORR hot cell. Capsule No. 2, containing E-7016 weld-metal specimens, was installed in loop No. 1 during the May shutdown.

6. OUT-OF-PILE TESTING OF MATERIALS AND COMPONENTS

Compatibility Tests of Graphite, Structural Materials, and Gaseous Coolants

J. H. DeVan B. Fleischer A. M. Smith

Forced-Convection Loop Tests

Forced-convection loop No. 5 containing AGOT graphite, metal test specimens, and helium was operated to study the effects of H_2O inleakage on EGCR materials of construction. Water-saturated helium was injected into the loop over a 1000-hr test period at an average rate of 0.07 cm^3 (liquid)/hr. This injection rate, when corrected for differences in helium volume, was an order of magnitude greater than the maximum inleakage rate stipulated for the EGCR.

Impurity concentrations in the main helium stream as a result of the reactions of the H_2O vapor with graphite in the hot leg of the loop were controlled by means of bypass flow through a small-scale purification system. The amount of H_2 was maintained at or below 2000 ppm (by volume) and the combined total of CO and CO_2 was below 1800 ppm during the test period. The H_2O content of the main stream averaged 20 to 30 ppm; however, on occasions the H_2O concentration rose to 300 to 400 ppm as a result of fluctuations in the injection rate. The main helium stream, which was circulated at a flow rate of 220 lb/hr at 45 psia, was heated to 1400°F in the test section and cooled to 500°F in the cold leg of the loop.

High- and low-alloy steels from the test section of the loop have been examined visually and weight changes recorded (Table 6.1). Oxide films on these specimens tended to be quite superficial, even in the case of lower alloy steels. Weight gains for steels containing less than 7% chromium were generally less than gains recorded in corresponding impurity addition tests at 1100°F.[1] This observation is in accord with thermodynamic predictions of the oxidizing behavior of CO-CO_2 or H_2-H_2O impurities

[1]GCR Quar. Prog. Rep. March 31, 1961, ORNL-3102, p. 212.

Table 6.1. Weight Gain Data on Steel Specimens Tested in Forced-Convection Loop No. 5

Specimen temperature: 1400°F
Test time: 1000 hr

Specimen	Weight Gain (mg/cm^2)
Type 304L stainless steel	0.04
Type 430 stainless steel	0.24
7% Cr–1% Mo–bal Fe	0.15
5% Cr–1% Mo–bal Fe	1.65
3% Cr–1% Mo–bal Fe	0.38
2 1/4% Cr–1% Mo–bal Fe	0.34

in equilibrium with graphite at the respective temperature levels. At the impurity concentrations present in these tests, the oxidizing potential, p_{CO_2}/p_{CO} or p_{H_2O}/p_{H_2}, of mixtures in equilibrium with graphite tends to be higher at 1100°F than at 1400°F.

No evidence of soot deposition was apparent either on the test specimen surfaces or in the cold leg of the loop. The graphite in this loop did not appear to be adversely affected by the test exposure; however, the data collected for these specimens were not sufficiently precise to permit an accurate estimate of effects of a 20-yr exposure under similar test conditions.

Graphite-Metal Diffusion Studies

A test for determining the interaction of graphite and type 304L stainless steel in direct contact at 1300°F was recently concluded after 1000-hr of operation. A vacuum of 8×10^{-5} mm of Hg was maintained over the graphite and stainless steel specimens during the test to minimize effects of gaseous impurities on the interdiffusion of these materials. Several surface treatments had been applied to the type 304L stainless

steel specimens, including preoxidizing, copper plating, and electropolishing. The contact pressures between the graphite and the steel specimens for each surface condition were 500, 1000, and 2000 psi.

Visual examination of the specimen column revealed that uncoated surfaces of the stainless steel had bonded to the graphite at all contact pressures. However, surfaces that had been black oxidized or copper plated showed no indication of bonding. Specimens which had bonded were severely embrittled, as indicated by the nature of the fractures that occurred on bending a 0.005-in.-thick specimen. Preliminary results of metallographic examinations have demonstrated the importance of intimate surface contact on carburization. Heavy carburization of entire grains was evident in areas of the metal surface where there was intimate contact between the graphite and the metal, whereas the areas of the metal surface adjacent to voids in the graphite show only grain-boundary carbides.

The conditions of the next test will be similar to those of the test just completed, except that the temperature of exposure will be 1200°F.

Evolution of Gas from Graphite

L. G. Overholser J. P. Blakely

The degassing behavior of additional samples of needle-coke graphite produced for use in the EGCR and NPR has been investigated. The studies include degassing of specimens to a maximum temperature of 1800°C and determination of the rate of release and composition of the evolved gas at 300, 600, and 1000°C. These materials have been described, and the experimental results obtained with them were presented previously.[2] Another sample of TSX graphite was examined after it was discovered that the sample previously studied was not representative of TSX grade of graphite. The more recent studies of EGCR graphite were made on material from a furnace load not previously examined.

[2]Ibid., pp. 216–24.

For the study of the EGCR graphite, a 6-in. slab was cut perpendicular to the extrusion axis from section No. 4 (a 30-in.-long piece cut approximately 90 in. from an end of the 20-ft-long bar, which came from the furnace load identified as file No. 3; the material for the earlier studies[2] was from a furnace load identified as file No. 16.) Two series of specimens were machined from the 6-in. slab for examination. Series C4C specimens came from a region 1 to 4 in. from the original surface of the bar, whereas series C4B specimens were cut from the central region. The total ash contents were found to be approximately 125 and 250 ppm for series C4C and C4B, respectively. A higher ash content for material from the central portion of the other bar (file No. 16) was also found previously.[2] The densities of series C4C specimens varied from 1.70 to 1.71 g/cm^3 compared with 1.60 to 1.70 g/cm^3 for series C4B specimens. (Only one specimen, C4B-8A, had a density less than 1.64 g/cm^3.) The densities of specimens from the bar examined previously varied similarly.[2]

For the further study of TSX graphite another sample was obtained from Hanford. This second sample had an ash content of less than 10 ppm compared with approximately 500 ppm for the first sample and is believed to be representative of TSX grade graphite.

Data obtained by degassing the graphite specimens to a maximum temperature of 1800°C by induction heating are given in Table 6.2. The total volume of gas evolved by the TSX graphite specimens is approximately one-third that found earlier.[2] The CO concentration of approximately 50% in the evolved gas may be compared with the value of approximately 80% reported previously.[2] Since TSX is a gas-purified graphite, the low ash content and relatively small volume of gas evolved indicate that the second sample received is representative of this grade of graphite. The first sample apparently came from a bar in the furnace that did not attain a sufficiently high temperature to effect the purification expected.

The total volumes of gas evolved by the EGCR specimens are in general comparable to those previously reported.[2] A volume of approximately 50 cm^3/100 cm^3 of graphite appears to be representative for the two bars sampled. The ratios of H_2 to CO are also comparable for the material examined from the two bars. Specimen C4B-8A which evolved 76 cm^3 and had

Table 6.2. Volume and Composition of Gas Evolved by 1 1/4-in.-diam and 1-in.-Long Graphite Specimens at 1000, 1400, and 1800°C

Graphite Sample	Temperature (°C)	Time (hr)	Gas Volume (cm^3/100 cm^3 of graphite)	Gas Constituents												
				H_2		Hydrocarbons		H_2O		CO_2		N_2		CO		Other
				Vol %	cm^3	Vol %	cm^3	Vol %	cm^3	Vol %	cm^3	Vol %	cm^3	Vol %	cm^3	
TSX-2-4A	1000	7	11.0	68	7.5	1	0.1	2	0.2	1	0.1	0.6	0.1	27	2.9	
	1400	7	10.4	57	6.0	1	0.1	0.6	0.1	0.5	0.1	3	0.3	37	3.9	0.1% H_2S
	1800	8	9.3	31	2.9	0.3		2	0.2	0.3		4	0.4	62	5.8	
	Total		30.7		16.4		0.2		0.5		0.2		0.8		12.6	
TSX-2-1A	1800	6	35	49	17	0.6	0.2	0.4	0.1	0.5	0.2	2	0.5	48	17	0.1% H_2S
TSX-2-2A	1800	6	44	52	23	0.5	0.2	0.3	0.1	0.4	0.2	1	0.6	46	20	0.1% H_2S
TSX-2-3A	1800	7	30	51	15	0.6	0.2	0.3	0.1	0.5	0.2	2	0.5	46	14	0.1% H_2S
EGCR C4C-4A	1000	7	18.0	46	8.2	1	0.3	0.7	0.1	1	0.2	1	0.2	50	9.0	0.1% H_2S
	1400	7	19.7	39	7.6	1	0.1	0.3	0.1	0.4	0.1	1	0.2	59	11.6	0.2% H_2S
	1800	7	13.5	24	3.3	0.6	0.1	0.2		0.2		3	0.4	71	9.7	0.3% H_2S
	Total		51.2		19.1		0.5		0.2		0.3		0.8		30.3	
EGCR C4C-3A	1000	3	21.9	48	10.6	2	0.4	0.7	0.2	1	0.3	1	0.2	47	10.2	0.1% H_2S
	1400	7	10.7	35	3.7	2	0.1	0.3		0.4		3	0.3	58	6.2	0.7% H_2S, 1% CS_2
	1800	7	5.8	38	2.2	0.7		0.2		0.2		7	0.4	54	3.1	0.2% H_2S
	Total		38.4		16.5		0.5		0.2		0.3		0.9		19.5	
EGCR C4C-1A	1800	7	56	36	20	0.4	0.3	0.5	0.3	0.6	0.3	0.8	0.5	61	35	
EGCR C4C-2A	1800	6	49	28	14	0.3	0.1	0.7	0.3	0.5	0.2	1	0.6	69	34	
EGCR C4B-10A	1000	7	24.0	37	8.9	0.8	0.2	0.5	0.1	0.8	0.2	2	0.4	59	14.2	0.1% H_2S
	1400	6	10.7	45	4.8	1	0.1	0.6	0.1	0.4		1	0.1	50	5.4	1.3% H_2S
	1800	10	12.0	33	3.9	0.4		0.2		0.2		4	0.5	63	7.5	0.1% H_2S
	Total		46.7		17.6		0.3		0.2		0.2		1.0		27.1	
EGCR C4B-7A	1800	6	48	33	16	0.3	0.1	0.4	0.2	0.4	0.2	2	0.8	65	31	
EGCR C4B-8A	1800	24	76	30	23	0.3	0.2	0.4	0.3	0.3	0.2	0.9	0.7	67	51	0.1% H_2S
EGCR C4B-9A	1800	7	59	33	19	0.3	0.2	0.2	0.1	0.4	0.2	1	0.6	65	39	

a density of only 1.60 g/cm^3 must have been cut from a region containing an inclusion of material not representative of the 6-in. slab.

Data obtained by degassing specimens of the graphite at a maximum temperature of 1000°C using external radiant heating are presented in Table 6.3. Both the total volume and relative composition of the gas evolved by the TSX specimens are typical of a highly purified graphite and are in marked contrast to those reported previously[2] for the first sample of TSX graphite examined.

The results given for the EGCR specimens are in fair agreement with those found earlier[2] for specimens cut from the other bar of graphite (file No. 16). The total volume of gas currently reported is somewhat less. Specimens cut from the inner region (C4B series) evolved slightly more gas than those from the outer region (C4C series). The ratio of H_2 to CO in the evolved gas was found to be somewhat larger for the C4C specimens. The total volumes of gas reported for specimens having various dimensions indicate that the effect of geometry must be only a minor factor, and what little effect it may have is completely masked by variations arising from the nonuniform character of the graphite. Significant amounts of SO_2 were evolved between 300 and 600°C in all cases, with some indication that the sulfur content is higher in the central region than the outer region. Small amounts of CS_2 have been found in some instances.

The results of studies of the volume of gas released by the graphite sample as a function of time at 300, 600, and 1000°C are given in Figs. 6.1 and 6.2 and in Table 6.4. Plots of the log of time versus the volumes of gas released give essentially linear relationships at 300 and 600°C for all the specimens examined over the intervals of time listed in Table 6.4. The values for the constants given in Table 6.4 for the EGCR specimens are in substantial agreement with those given previously.[2] Representative values for the slope of 0.1 and 0.4 to 0.5 for the data obtained at 300 and 600°C, respectively, are indicated from the current and earlier data. Examination of the values given for the slopes of the plots for different specimen sizes again shows that size is an unimportant variable.

Table 6.3. Volume and Composition of Gas Evolved by Graphite Samples at 300, 600, and 1000°C

Graphite Sample	Temperature (°C)	Time (hr)	Gas Volume (cm^3/100 cm^3 of graphite)	Gas Constituents												
				H_2		Hydrocarbons		H_2O		CO_2		N_2		CO		Other
				Vol %	cm^3	Vol %	cm^3	Vol %	cm^3	Vol %	cm^3	Vol %	cm^3	Vol %	cm^3	
TSX-2-1B[a]	300	23	0.4	2		12	0.1	59	0.2	5		18	0.1	5		
	600	20	1.0	20	0.2	26	0.3	26	0.3	7	0.1	5		15	0.2	0.5% H_2S
	1000	45	5.5	75	4.1	2	0.1	2	0.1	1		2	0.1	18	1.0	
	Total		6.9		4.3		0.5		0.6		0.1		0.2		1.2	
TSX-2-3B[a]	300	32	0.5	5		28	0.1	33	0.2	6		24	0.2	5		
	600	10	0.8	20	0.2	33	0.2	12	0.1	8	0.1	7		20	0.2	
	1000	32	4.2	65	2.7	3	0.1	5	0.2	0.7		2	0.1	24	1.0	
	Total		5.5		2.9		0.4		0.5		0.1		0.3		1.2	
EGCR C4C-1B[a]	300	23	0.5	1		4		67	0.4	5		13	0.1	3		5% SO_2
	600	47	1.7	10	0.2	21	0.4	22	0.4	13	0.2	7	0.1	19	0.4	5% SO_2
	1000	20	7.1	38	2.7	3	0.2	0.5		0.9	0.1	0.6		57	4.1	
	1000	24	2.0	59	1.2	2		2		0.2		1		35	0.7	
	Total		11.3		4.1		0.6		0.8		0.3		0.2		5.2	
EGCR C4C-2B[a]	300	23	0.4	10		8		45	0.2	8		19	0.1	7		
	600	43	1.9	19	0.4	16	0.3	18	0.4	10	0.2	6	0.1	16	0.3	4% SO_2
	1000	22	6.1	41	2.5	3	0.2	0.3		2	0.1	0.8	0.1	53	3.2	5% SO_2
	1000	48	2.6	57	1.5	2		4		0.2		2	0.1	35	0.9	
	Total		11.0		4.4		0.5		0.6		0.3		0.4		4.4	
EGCR C4B-8B[a]	300	29	0.5	2		4		75	0.4	5		13	0.1	1		1% SO_2
	600	22	2.0	5	0.1	22	0.4	15	0.3	28	0.6	6	0.1	16	0.3	6% SO_2
	1000	23	9.4	34	3.1	3	0.2	0.6	0.1	1	0.1	1	0.1	59	5.6	1% SO_2
	Total		11.9		3.2		0.6		0.8		0.7		0.3		5.9	
EGCR C4B-9B[a]	300	23	0.8	1		5		50	0.4	13	0.1	17	0.2	6		6% SO_2
	600	17	2.1	5	0.1	17	0.3	23	0.5	22	0.5	6	0.1	17	0.4	10% SO_2
	1000	11	9.2	31	2.8	2	0.2	1	0.1	2	0.2	0.9	0.1	62	5.7	1% SO_2
	1000	31	3.3	58	1.9	3	0.1	0.6		0.1		1		37	1.3	
	Total		15.4		4.8		0.6		1.0		0.8		0.4		7.4	
EGCR C4B-4A[b]	300	24	0.4	1		4		58	0.2	7		22	0.1	2		6% SO_2
	600	21	2.5	4	0.1	18	0.4	18	0.5	30	0.7	5	0.1	18	0.5	8% SO_2
	1000	20	8.5	26	2.2	2	0.1	1	0.1	2	0.1	1	0.1	67	5.7	1% CS_2
	1000	25	1.7	57	1.0	4	0.1	1		0.4		3		32	0.6	3% CS_2
	1000	47	1.7	51	0.9	3	0.1	0.6		0.4		3		39	0.7	3% CS_2
	Total		14.8		4.2		0.7		0.8		0.8		0.3		7.5	

Table 6.3 (continued)

Graphite Sample	Temperature (°C)	Time (hr)	Gas Volume (cm^3/100 cm^3 of graphite)	Gas Constituents												Other
				H_2		Hydrocarbons		H_2O		CO_2		N_2		CO		
				Vol %	cm^3	Vol %	cm^3	Vol %	cm^3	Vol %	cm^3	Vol %	cm^3	Vol %	cm^3	
EGCR C4B-12[c]	300	23	0.5	3		4		51	0.3	8		24	0.1	4		5% SO_2
	600	24	1.9	5	0.1	15	0.3	16	0.3	24	0.5	9	0.2	15	0.3	17% SO_2
	1000	42	10.2	24	2.5	2	0.2	0.8	0.1	0.6	0.1	1	0.1	70	7.2	1% CS_2
	Total		12.6		2.6		0.5		0.7		0.6		0.4		7.5	
EGCR C4B-5[d]	300	19	0.6	1		7		60	0.4	5		19	0.1	3		4% SO_2
	600	22	2.9	5	0.2	20	0.5	28	0.8	17	0.5	7	0.2	16	0.5	6% SO_2
	1000	23	10.1	32	3.2	2	0.2	1	0.1	2	0.2	2	0.2	59	6.0	1% CS_2
	1000	21	1.9	56	1.1	4	0.1	4	0.1	0.4		2		32	0.6	2% CS_2
	Total		15.5		4.5		0.8		1.4		0.7		0.5		7.1	
EGCR C4B-2[d]	300	7	0.7	1		7		63	0.4	3		18	0.1	1		5% SO_2
	600	23	2.6	8	0.2	22	0.6	18	0.5	19	0.5	6	0.2	20	0.5	6% SO_2
	1000	45	11.2	34	3.8	3	0.3	0.8	0.1	1	0.1	2	0.2	58	6.6	1% CS_2
	Total		14.5		4.0		0.9		1.0		0.6		0.5		7.1	
EGCR C4B-11[e]	300	23	0.6	1		3		47	0.3	6		19	0.1	3		7% SO_2
	600	22	1.7	5	0.1	13	0.3	28	0.5	16	0.3	8	0.1	17	0.3	13% SO_2
	1000	36	10.6	28	2.9	3	0.3	1	0.1	2	0.2	1	0.1	66	6.9	1% CS_2
	Total		12.9		3.0		0.6		0.9		0.5		0.3		7.2	
EGCR C4B-13[e]	300	12	0.5	2		3		51	0.3	9	0.1	28	0.2	3		4% SO_2
	600	18	1.7	5	0.1	14	0.3	23	0.4	31	0.5	9	0.2	13	0.2	5% SO_2
	1000	32	10.9	24	2.6	2	0.2	1	0.1	2	0.2	1	0.1	70	7.7	1% CS_2
	Total		13.1		2.7		0.5		0.8		0.8		0.5		7.9	

[a]Specimen 1 1/2 in. in diameter and 2 in. long.

[b]Specimen 2 1/4 in. in diameter and 2 in. long.

[c]Specimen 1 in. in diameter and 1 in. long.

[d]Specimen 1 in. in diameter and 2 in. long.

[e]Specimen 1 in. in diameter and 4 in. long.

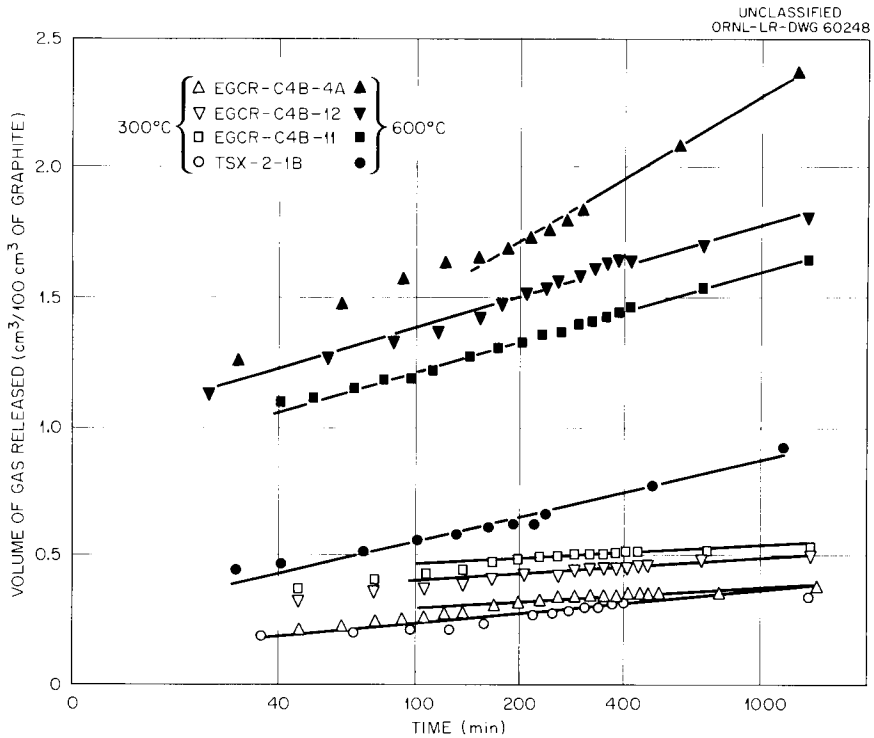

Fig. 6.1. Gas Evolution of Various Graphite Specimens at 300 and 600°C.

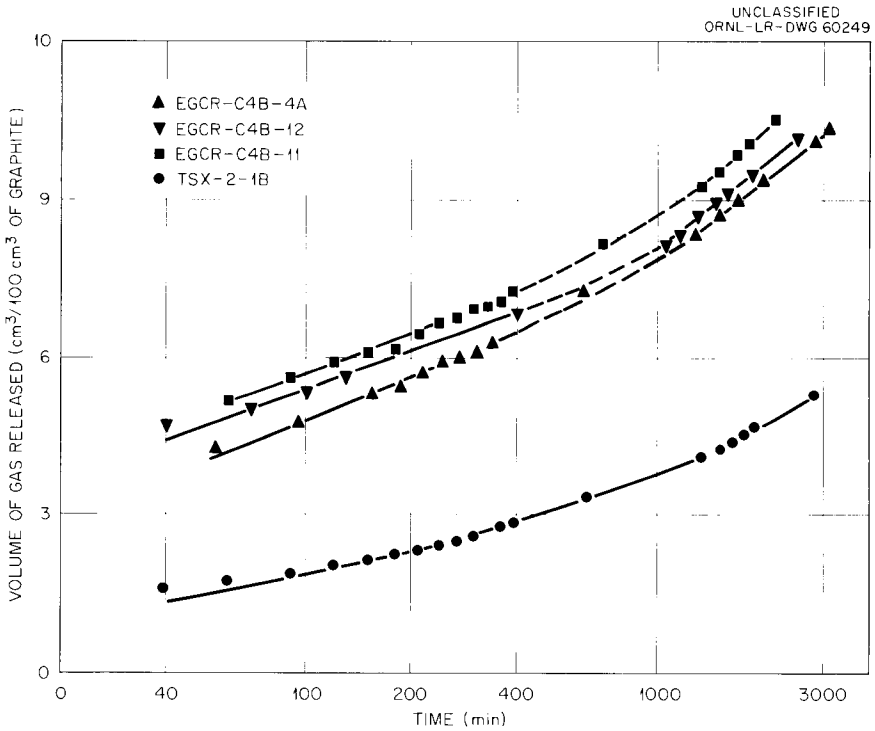

Fig. 6.2. Gas Evolution of Various Graphite Specimens at 1000°C.

Table 6.4. Values for the Constants A and B in the Equation[a] V = A log t + B for TSX and EGCR Graphite Samples at 300, 600, and 1000°C

Graphite Sample	Sample Size		Temperature (°C)	Time Interval (min)	A	B
	Diameter (in.)	Length (in.)				
TSX-2-1B	1 1/2	2	300	35–1350	0.13	−0.03
EGCR-C4C-1B	1 1/2	2	300	60–1400	0.082	0.25
-2B	1 1/2	2	300	50–1200	0.11	0.09
-C4B-8B	1 1/2	2	300	75–1400	0.067	0.22
-9B	1 1/2	2	300	40–1360	0.16	0.26
-4A	2 1/4	2	300	150–1400	0.090	0.11
-12	1	1	300	100–1400	0.090	0.21
-2	1	2	300	50–1400	0.15	0.25
-5	1	2	300	150–1400	0.080	0.34
-11	1	4	300	100–1400	0.090	0.27
TSX-2-1B	1 1/2	2	600	70–1150	0.33	−0.10
EGCR-C4C-1B	1 1/2	2	600	120–2800	0.42	0.18
-2B	1 1/2	2	600	100–4000	0.42	0.13
-C4B-8B	1 1/2	2	600	120–1300	0.46	0.50
-9B	1 1/2	2	600	75–1000	0.39	0.78
-4A	2 1/4	2	600	150–1250	0.75	−0.01
-12	1	1	600	25–1350	0.39	0.60
-2	1	2	600	100–1375	0.53	0.70
-5	1	2	600	70–1330	0.82	0.21
-11	1	4	600	65–1350	0.40	0.40
-13	1	4	600	50–1100	0.28	0.91
TSX-2-1B	1 1/2	2	1000	90–270	1.2	−0.55
			1000	270–1300	2.3	−3.2
			1000	1300–2800	3.5	−6.8
-3B	1 1/2	2	1000	50–400	1.1	−0.81
			1000	1050–2500	2.6	−4.7
EGCR-C4C-1B	1 1/2	2	1000	120–300	2.7	−1.8
			1000	1200–2600	5.5	−9.8
-2B	1 1/2	2	1000	150–400	2.2	−1.3
			1000	1200–4100	4.6	−8.0
-C4B-8B	1 1/2	2	1000	50–440	2.1	1.2
			1000	1125–1380	7.0	−12.8
-9B	1 1/2	2	1000	100–420	3.2	−1.0
			1000	1080–3020	7.0	−12.0
-4A	2 1/4	2	1000	150–350	3.0	−1.4
			1000	1250–5600	5.5	−8.8
-12	1	1	1000	60–400	2.3	0.85
			1000	1050–2500	5.0	−6.9
-2	1	2	1000	50–350	2.4	1.0
			1000	350–1200	3.7	−2.2
			1000	1300–2700	5.8	−8.7
-5	1	2	1000	50–300	2.6	0.66
			1000	300–1375	4.4	−3.8
			1000	1400–2750	6.2	−9.5
-11	1	4	1000	50–400	2.5	0.73
			1000	1300–2200	6.0	−9.5
-13	1	4	1000	60–375	2.2	2.0
			1000	1050–2500	4.7	−4.9

[a]Volume expressed as cm^3 (STP) of evolved gas per 100 cm^3 of graphite and time in minutes. Samples were degassed at 300°C prior to degassing at 600°C and degassed at 300 and 600°C before degassing at 1000°C. The intercepts do not include the gas removed at the lower temperatures.

A similar treatment of the data collected at 1000°C for the EGCR graphite results in curves from which slopes of 2.1 to 3.2 are obtainable during the early stages of the degassing. Following a time interval during which the slope increases rather rapidly, slopes of 4.4 to 7.0 were obtained over an extended period of time during which a linear relationship prevailed. As mentioned previously,[2] the increase in slope with time of degassing appears to be associated with an increase in the H_2 and a decrease in the CO concentration of the evolved gas. The values given for the slopes obtained at 1000°C for different size specimens indicate that the effect of geometry is unimportant.

Transport of Gases Through Graphite

R. B. Evans J. Truitt

An experimental investigation of the interdiffusion and forced-flow behavior of helium and argon in Speer moderator No. 1 graphite has been completed. This material is of the same general classification with respect to flow behavior as National Carbon Company AGOT-grade graphite. Comparative characterization data are given below:

	Speer Moderator No. 1 Graphite	AGOT-Grade Graphite
Permeability coefficient at 20°C and 1 atm, cm^2/sec	0.82	1.40
Permeability coefficient at 20°C and a mean pressure approaching 0, cm^2/sec	0.24	0.41
Porosity based on helium absorption, vol %	17.8	22
Total porosity based on density of 2.25 g/cm^3, vol %	23.2	26

These data were employed to determine a mutual diffusion coefficient and to verify certain superposed flow equations.[3] In addition, two series

[3]R. B. Evans, III, et al., Superposition of Forced and Diffusive Flow in a Large-Pore Graphite, ORNL-3067, Feb. 24, 1961.

of experiments were conducted to investigate the validity of the proposed back-diffusion mechanism at high values of the forced-flow component.

At small forced-flow rates, normal diffusion was the controlling diffusion mechanism, while Knudsen effects were negligible. The average, normalized (1 atm and 20°C), mutual diffusion coefficient is 2.47×10^{-3} cm^2/sec. The flow equations employed previously[3] are applicable to these data; however, experiments conducted at high forced-flow rates show that the superposed equations used previously are not valid. Attempts to modify the superposed flow equations are being made at this time. It might be speculated, however, that this anomoly is caused by either the small channel contributions, which were of no significance at low forced-flow rates, or parallel diffusion through the manometer fluid. Additional tests are in progress to either confirm or eliminate the significance of parallel diffusion through the manometer fluid. At high flow rates, the back diffusion (argon against helium) appears to follow a Knudsen diffusion mechanism, with a D_K of 5.68×10^{-6} cm^2/sec. It was found that a helium sweep rate of 2.5×10^{-4} mole/sec was critical with respect to the back diffusion mechanisms. Extending these findings to applied situations, it may be concluded that, if the sweep rate is lower than the critical value for a given graphite, the fission-product contamination will increase, whereas sweep rates greater than the critical value would require large reprocessing capacities without additional decrease in contamination.

Development of Instruments for Analyzing Helium

J. C. White A. S. Meyer, Jr.
J. E. Attrill

A systematic study of the factors affecting the reproducibility of the Greenbrier Process Chromatograph analyses has been carried out on the Model 312 instrument. This chromatograph, which has been modified to permit changes in sample volume and the analysis of "grab samples" was described previously.[4] In current operations, samples of 5- or

[4]GCR Quar. Prog. Rep. Sept. 30, 1960, ORNL-3015, pp. 143–5.

25-cm^3 volume are resolved by dual-column techniques using a 40-in. silica-gel column for the separation of carbon dioxide and a 20-ft column of 5A molecular sieves for the resolution of hydrogen, oxygen, nitrogen, methane, and carbon monoxide. The concentration of the eluted components is measured by comparison with the helium reference gas in a thermal conductivity cell which utilizes a high-sensitivity bridge circuit equipped with 30-K thermistors. The detector, columns, and chromatographic valves are located within the inner thermostatted compartment, which is stated by the manufacturer to be maintained at a temperature that is constant to ±0.01°C. The outer compartment of the analyzer section is thermostatted to ±0.2°C by injection of a stream of air whose temperature is controlled by mixing the required proportions of room temperature air with air from a heater chamber.

As indicated in a previous report,[5] the reproducibility of the measurement of concentrations is limited primarily by fluctuations in the base line, and some improvement has been achieved by screening the thermistors to reduce the effects of minor fluctuations in flow rate of reference and carrier gases to the detector. The principal source of the remaining fluctuations has been found to be associated with the control of temperature.

Some of the chromatographic components were in physical contact with the walls of the inner compartment, so a fluctuation in the temperature of the outer compartment changed the temperature of the gas to the sample thermistor more rapidly than that of the gas to the reference thermistor. By insulating the chromatographic components from the compartment walls, the sensitivity of the base line to changes of temperature in the outer compartment was reduced by a factor of 3. Improvement in the stability of the temperature of the outer compartment was effected by setting the sensitivity of the thermoregulator to its maximum value, reducing the temperature of the heated air to increase the proportion of heated air for more precisely controllable flows, and connecting a constant voltage transformer to the air heater to eliminate effects of variation in line

[5]GCR Quar. Prog. Rep. March 31, 1961, ORNL-3102, p. 227.

voltage. Additional improvements in stability were made by replacing temperature-sensitive elements, resistors, and potentiometers in the unthermostatted control section.

With these modifications the absolute standard deviations in the measurement of impurities at the 100-ppm concentration level are: 6 ppm for hydrogen; 1 ppm for oxygen, nitrogen, and carbon; 2 ppm for methane; and 3 ppm for carbon monoxide. Since, on the basis of several weeks observation, this reproducibility can be obtained without frequent readjustment of the instrument, these results correspond to at least a fivefold improvement in precision. In order to effect additional improvements, a heat exchanger for the sample and reference gases has been fabricated. The exchanger consists of parallel coils of 0.040-in.-o.d., 0.003-in.-wall stainless steel tubing imbedded in a block of silver. The exchanger will be installed immediately ahead of the detector during the next period when the instrument is not in use.

A third process chromatograph has been ordered for monitoring the blanket gases in in-pile loop tests. This instrument, while similar in function to the two existing instruments, will be substantially modified to accomodate fission gases in the samples. The modified instrument will include a leaktight analyzer cabinet that can be operated at reduced pressures for secondary containment and an additional multicolumn valve for separation of the argon and krypton peaks to exclude these fission gases from the detector and route them to the disposal system, or if desired, through a radiation detector.

Investigation of Adsorbers for Removing Fission-Product Gases from Helium

G. W. Keilholtz R. D. Ackley
W. E. Browning R. E. Adams

Removal of Iodine Vapor

Studies of various materials and methods for the removal of radioactive iodine vapor from high-temperature helium are continuing, with current emphasis on iodine removal and retention by Whetlerite charcoal,

type ASC, 12/30 mesh. This charcoal, manufactured for use in gas masks to afford protection against war gases, is produced by impregnating Pittsburgh BPL charcoal with salts of silver, copper, and chromium. Initial short-term screening tests on various charcoals and silver surfaces indicated, as mentioned previously,[6] that Whetlerite charcoal is superior to the other materials for removing iodine vapor from helium at 325°C. Consequently, an effort is being made to determine the migration rate of iodine through relatively deep beds (4 in.) of Whetlerite charcoal as a function of temperature. The first test of this series was terminated after operation for 468 hr at 325°C with a helium velocity of 38.8 fpm. The radioiodine was contained by the first 0.5 in. of Whetlerite charcoal, and total iodine migration, over the term of the test, was less than 0.06 in. Over-all iodine retention in the 4-in.-deep bed was determined to be 99.99+%. The second test was terminated after operation for 897 hr at 425°C with a helium velocity of 53 fpm. Over-all iodine retention was 99.99+%, with the radioiodine contained by the first 0.75 in. of the charcoal. Iodine migration over the 897-hr period was no more than 0.07 in. Preparations are being made for a long-term test at 550°C.

Removal of Radioactive Noble Gases

The investigation of the removal of krypton and xenon from carrier gases was continued. Experimental measurements were made of the retention of krypton from helium by charcoal at liquid nitrogen temperature, and further consideration was given to the transport of fission-product gases through adsorbers by diffusion.

Operation of adsorbers at liquid nitrogen temperature, or approximately -196°C, is being investigated because equilibrium or static adsorption data indicate that dynamic holdup times for krypton or xenon at that temperature should be extremely long. The adsorbent being studied is 40 g of Columbia HCC, 12/28X, activated carbon occupying a space 8.25 in. long in a trap with an inside diameter of 0.95 in. at a temperature of approximately -196°C. The carrier gas is helium at 1 atm and a flow rate of 360

[6]Ibid., pp. 229–31.

cm^3 (STP)/min. The amount of krypton injected for the test was about 7.5 cm^3 (STP), including 800 mc of Kr^{85} to provide high counting sensitivity. The test has now been in progress for eight weeks with no evidence of breakthrough of Kr^{85}. For comparison, the average krypton hold-up time at room temperature for such a trap and flow rate would be 5 min.

The importance of the transport of krypton and xenon by longitudinal diffusion in adsorbers where the carrier gas is moving at low velocity has been discussed, and, in addition, experimental apparent or effective diffusion coefficients for krypton in Pittsburgh PCB, 12/30, activated carbon, with stagnant helium at 1 atm as the predominant component of the gas phase were presented for 0, 25, and 60°C.[7] Some effort has now been made to provide a method for estimating these coefficients from available or more readily obtainable information. The approach employed was to assume that the effective diffusion coefficient, D_e, could be represented by

$$D_e = D_{12} R_D E_D \quad , \tag{1}$$

where D_{12} is the gas-phase diffusion coefficient for krypton (or xenon) and the carrier gas, R_D is the ratio of the amount of gaseous krypton to that of adsorbed krypton (neglecting the contribution of gaseous krypton to the denominator of the actual ratio involved), and E_D is an efficiency factor to allow for the effect of tortuosity and for the diffusivity in small pores being lower than that for ordinary gas-phase diffusion. The effects constituting E_D have been discussed in related literature.[8,9] Also, R_D is independent of pressure when the adsorption isotherm is linear, a condition practically realized with krypton on charcoal at these temperatures, that is, for krypton pressures not greatly in excess of a few millimeters of mercury. If Eq. (1) is applicable and

---

[7] GCR Quar. Prog. Rep. Dec. 31, 1960, ORNL-3049, pp. 304–5.

[8] A. I. M. Keulemans, Gas Chromatography, 2nd. Edition, Reinhold Publishing Company, New York, 1959.

[9] Ahlborn Wheeler, Reaction Rates and Selectivity in Catalyst Pores, Chap. 2 in Catalysis, Vol. 2, Reinhold, 1955, P. H. Emmett (ed.), pp. 126–31.

E_D does not vary too much with temperature, a plot of D_e versus $T^{0.75}\ k^{-1}$, where T is absolute temperature and k is the adsorption coefficient, should yield a straight line. This power of T results from D_{12} being approximately proportional to $T^{1.75}$ and the amount of gas in the gas phase being proportional to T^{-1}. Such a plot for the aforementioned experimental D_e values is shown in Fig. 6.3, where the points approximate a straight line. The k-values used, as previously obtained,[10] were 142.5, 60.1, and 31.1 cm^3 (STP)/g·atm at 0, 25, and 60°C, respectively. The observed value of E_D was 0.43 based on (1) the straight line in Fig. 6.3, (2) a D_{12} value for the krypton-helium mixture at 298.2°K and 1 atm of 0.645 cm^2/sec, and (3) charcoal with a void fraction of 0.75 and a bulk density of 0.5 g/cm^3. Since this E_D value is considerably less than unity, surface diffusion appears to have been unimportant. The data of Fig. 6.3 may be represented by

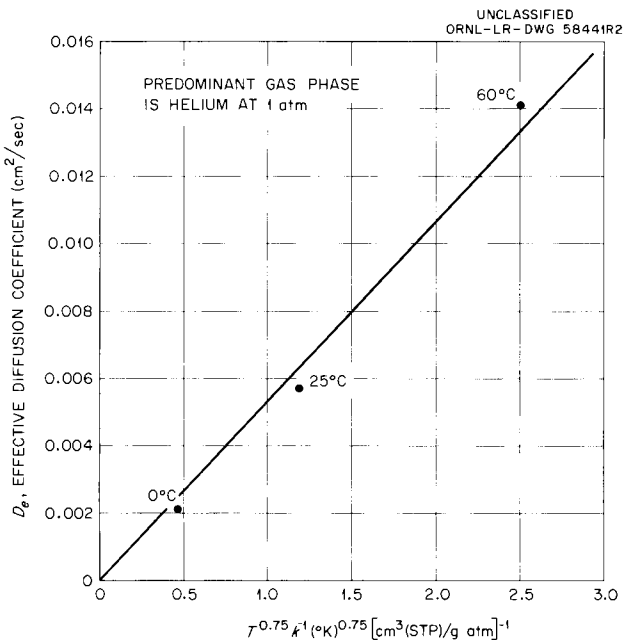

Fig. 6.3. Apparent Diffusion Coefficient for Krypton in Pittsburgh PCB Activated Carbon, 12/30, vs a Function of the Adsorption Coefficient and Temperature.

$$D_e = 0.0053\ T^{0.75}k^{-1} \quad . \qquad (2)$$

If the value of E_D for krypton is also applicable to xenon, as is probably true, approximately, the corresponding equation for xenon would have 0.0045 in place of 0.0053, based on a D_{12} value for the xenon-helium mixture of 0.547 cm^2/sec at 298.2°K and 1 atm. However, because xenon isotherms deviate appreciably from linearity, use of R_D values constant with

[10] R. D. Ackley and W. E. Browning, Jr., Equilibrium Adsorption of Krypton and Xenon on Activated Carbon and Linde Molecular Sieves, ORNL CF-61-2-32, Feb. 14, 1961.

pressure will introduce more error from this source than is the case with krypton; consequently, a more detailed analysis, based on Eq. (1), might be necessary in certain instances, as might also be true with krypton at lower temperatures or at pressures higher than a few millimeters of mercury. In addition, surface coverage with krypton in the experimental diffusion measurements was $\sim 10^{-4}$ monolayer; at some higher but as yet undetermined extent of surface coverage, surface diffusion could no longer be neglected. The D_{12} values given here were calculated by the method described by Hirschfelder et al.[11] The effect of carrier gas pressure on D_{12} is predictable at the fairly high pressures that might be encountered in some applications. From the preceding observations, it appears that effective diffusion coefficients for krypton or xenon in adsorbers can be estimated sufficiently accurately for most situations utilizing available data and theory.

Measurement of High Temperatures

G. W. Keilholtz R. L. Bennett
W. T. Rainey H. L. Hemphill

Drift Studies in a Stagnant Helium Atmosphere

As reported previously, large negative emf drifts have been measured when using Chromel-P as a thermocouple leg in a stagnant helium atmosphere at about 1000°C. The studies have shown the emf errors to be due to intergranular selective oxidation of chromium in the thermal gradient region of the furnace (usually between 700 and 900°C).

Tests have therefore been conducted using a group of chromium-nickel alloys which have been recommended[12] as being more resistant to attack than Chromel-P. The thermocouples prepared from 24-gage bright wire of the recommended materials showed the following average drifts when tested in unpurged thermocouple protection tubes with a stagnant helium atmosphere at 1000°C for 600 hr:

[11] J. O. Hirschfelder, C. F. Curtiss, and R. B. Bird, Molecular Theory of Gases and Liquids, Wiley, New York, 1954, p. 539.

[12] GCR Quar. Prog. Rep. March 31, 1961, ORNL-3102, p. 235.

Thermocouple Alloys	Average Drift in Electrical Output (mv)	Temperature Drift (°C)
Special Chromel-P versus special Alumel	−2.33	−58
Regular Chromel-P versus regular Alumel	−1.76	−44
Chromel-AA versus alloy 875	+0.07	+25
Chromel-A versus alloy 875	+0.05	+5

The comparatively large temperature drift of the Chromel-AA versus alloy 875 thermocouple for a slight emf drift is due to the very low thermoelectric power of this couple in the 1000°C range. When coupled with platinum, Chromel-A and Chromel-AA showed about the same temperature drift (+4.0°C and + 6.0°C, respectively).

Thermal-gradient emf profiles of the wires were plotted by slowly withdrawing the wires from an isothermal tube furnace. The profiles of the Chromel-A and Chromel-AA wires were similar and indicated only very small composition changes. A slight, positive emf error developed in the region of the wires exposed to the thermal gradient during the drift test and increased slowly toward the hot junction. Special and regular Chromel-P wires were similar in profile and showed large negative emf errors in the sections exposed to the furnace thermal gradient. This type of profile has been associated with selective chromium oxidation in past experiments. Since these experiments were conducted in systems containing slight amounts of air, it is not surprising that the drifts were noted even when using bright-annealed wires.

The special Alumel wires showed only slight positive emf errors in profile, and the wires appeared to be physically sound. The regular Alumel wires were severely oxidized, even though they showed only slight positive errors in profile. The insignificant emf drifts were to be expected because only minor changes in composition can occur in Alumel and the emf output of Alumel is almost the same as that of pure nickel.

Alloy 875 is an aluminum-chromium-iron alloy which was recommended as the negative leg for use with Chromel-A and Chromel-AA under reducing

atmospheric conditions. It appeared physically sound after use in the drift tests described above. Emf error profiles showed that no appreciable composition changes occurred.

It is concluded that the 80% Ni–20% Cr type of alloy (Chromel-A and -AA and Geminol-P) is a more suitable type than the 90% Ni–10% Cr (regular and special Chromel-P) type for high temperature use under marginally oxidizing conditions. This is especially important when the system geometry is such as to allow development of atmospheric gradients around the wire, as in long protection tubes of small bore. It is also concluded that the special Alumel alloy was much more resistant to oxidative attack than the regular Alumel under these test conditions.

Bare, dull Chromel-P wires have been studied at lower temperatures than previously reported.[12] The drift tests were carried out in the same assemblies as used in the 1000°C tests. The hot junction temperatures used in these tests were 995, 955, 857, and 770°C. The wires were tested at temperature in a stagnant helium atmosphere for the specified times, removed, and checked for thermal-gradient emf profile. The results of these tests are presented in Fig. 6.4. The thermal-gradient region of the furnace was in approximately the same position for all the tests. The sharp-gradient region extends from 9 to 13 in., as measured from the thermocouple hot junction position. In all cases negative emf drifts were measured during exposure of the couples. Unfortunately there were slight differences in amounts of wire in each assembly, so quantitative comparison of the data is not valid.

In each case the nonhomogeneous section developed in the thermal-gradient region. For the three upper temperatures the maximum error developed within a 29°C range (781 to 810°C). In the 770°C test selective oxidation occurred even deep in the isothermal region of the furnace.

These tests substantiate data obtained previously which indicated that the selective oxidation of chromium occurred predominantly in sections of wires exposed to stagnant helium atmospheres at temperatures between 700 and 900°C. The selective oxidation of chromium occurred mainly in the thermal gradient region of the assembly when the isothermal region was kept above 750°C. Otherwise partial oxidation occurred even in the

isothermal region. This pattern of behavior has been predicted by means of thermodynamic calculations on a simplified system containing oxidizing

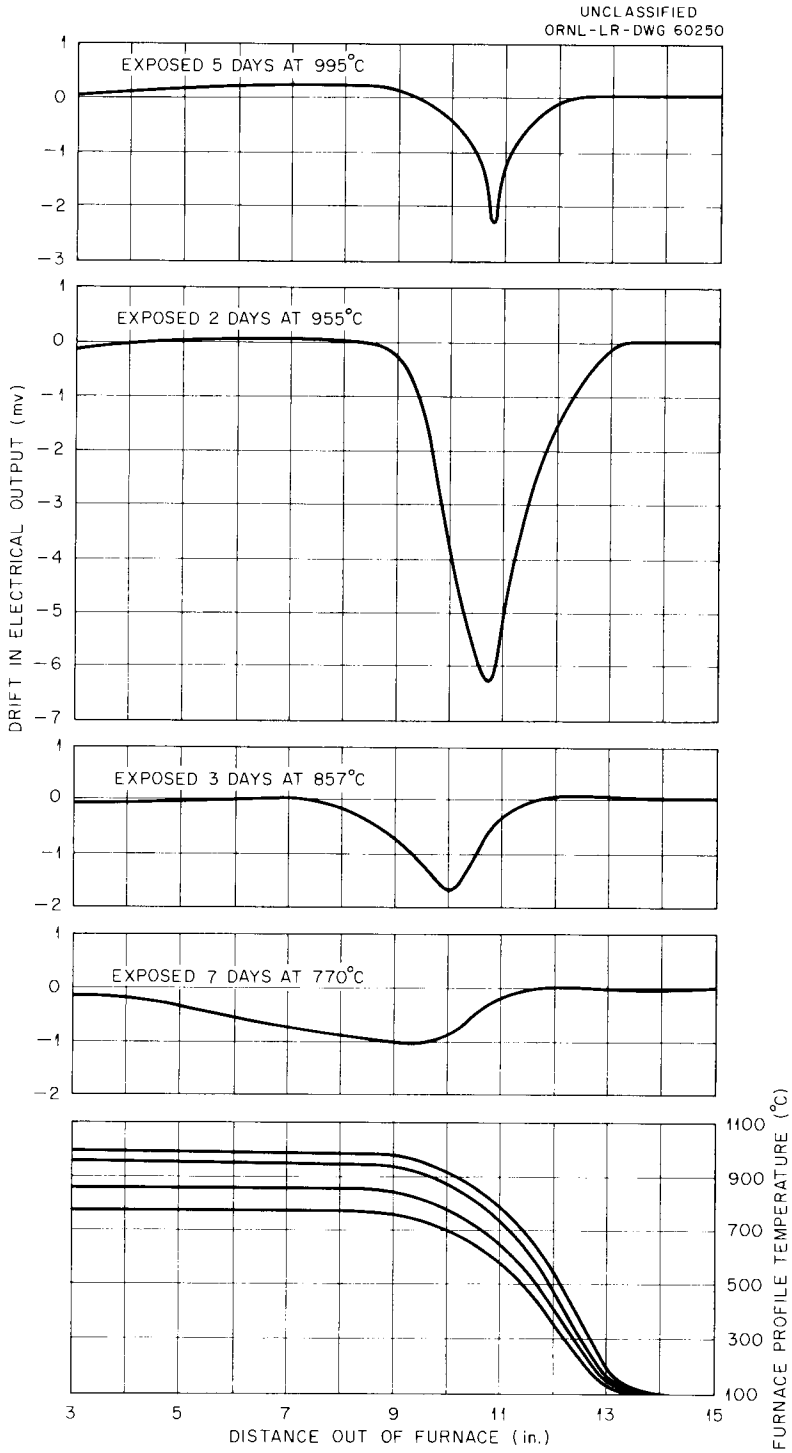

Fig. 6.4. Chromel-P EMF Profiles After Exposure in Stagnant Helium.

and reducing impurities at equilibrium with nickel-chromium solid solutions. In the actual case the effect was probably enhanced by concentration gradients set up in the tube that resulted in a greater supply of oxidizing material in the colder section of the tube. The wires exposed in the thermal-gradient region were also in contact with air and other gases expelled from the tube when first heated. These gases were forced back into connecting tubing and could diffuse slowly back into the assembly, reacting first with wire in the thermal-gradient region. Under reaction conditions such as used in these tests it would be inadvisable to use Chromel-P as a thermocouple alloy at temperatures above about 700°C.

Drift Studies in a Graphite-Helium Environment

Long-term drift tests are being made to determine the emf stability of stainless-steel-sheathed Chromel-P versus Alumel thermocouples in a graphite-helium atmosphere. These tests are carried out by insertion of thermocouples into a graphite cylinder enclosed in a stainless steel can. A static pressure of 7-psig helium is maintained throughout a test. The temperature of the graphite cylinder is controlled at 871°C (1600°F). Control thermocouples are exposed to the same thermal conditions as the test couples but in an air atmosphere.

Thermocouples sheathed with types 304, 310, and 347 stainless steel have been tested to date. The types 304 and 310 stock were 0.063 in. o.d., and the type 347 stock was 0.125 in. o.d. Two vendors furnished type 304 stock to the same specifications. The results from the experiments are presented in Fig. 6.5. Curve 1 illustrates the slow positive drift found in air with type 304 stainless-steel-sheathed couples from vendor A. The same stock gave a rapid negative emf drift in a graphite-helium environment, as is shown by curve 5. A temporary increase in rate of drift was observed when a fresh cylinder of graphite was inserted at 82 days. Note that the negative drift totaled about −50°C after six months. Curve 4 shows the results of inserting the same stock into a graphite cylinder which had been thoroughly outgassed. A positive drift was observed for about three weeks. After the fresh graphite was inserted, a rapid negative drift started. Curve 3 shows typical results

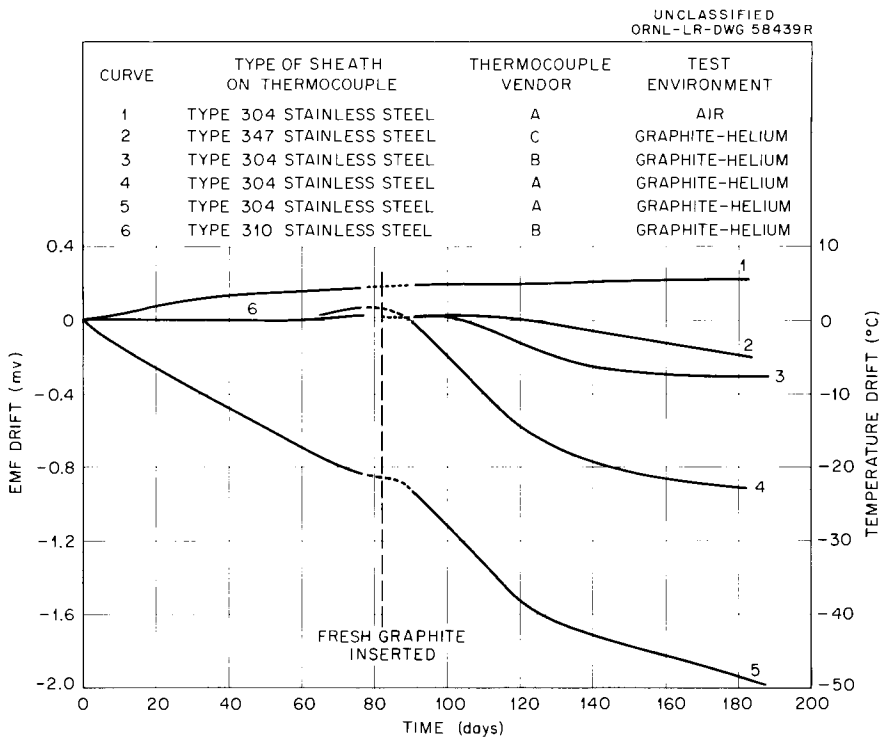

Fig. 6.5. Drift Data for Stainless-Steel-Sheathed Chromel-P Versus Alumel Thermocouples.

obtained with type 304 stock obtained from vendor B. The rate of drift in a graphite-helium environment was only one-third of that for the stock from vendor A. Only a slow positive drift was observed in air.

Curves 2 and 6 show data on types 347 and 310 stock, respectively. It is possible that smaller diameter type 347 stock would show a more rapid drift; however, the curve for type 310 stock should be comparable to the curves for type 304 stock.

The results obtained thus far indicate that the negative emf drift is closely associated with the gaseous products desorbed from the graphite. Experiments now under way indicate that the type 304 stainless-steel-sheathed couples drift slightly positive in a CO atmosphere. These tests will be followed by tests in a hydrogen atmosphere. It is suspected that hydrogen penetration was responsible for generation of the marginally oxidizing atmosphere inside the sheath. Differences in manufacturing techniques may be responsible for the different rates of drift. It appears, for example,

that the magnesia insulation is less densely packed in the stock manufactured by vendor A than in that of vendors B or C. This may result in greater longitudinal diffusion of gases so that concentration gradients conducive to selective oxidation can be set up. In addition, the purity of the magnesia, the inclusion of air or moisture, and the method of fabrication might have influenced the results.

7. DEVELOPMENT OF TEST LOOPS AND COMPONENTS

H. W. Savage

EGCR In-Pile Loops

F. H. Neill

Through-Tube Design (R. E. Helms, W. S. Chmielewski)

The Title II detailed fabrication drawings for the top nozzle tee sections were completed, and design criteria for the through-tube nozzle cooling system were prepared. A design analysis was completed for determining the effect of individual nozzle cooling line failures on the nozzle tee section carbon steel and reactor nozzle extensions, since there is a design temperature limit of 650°F for these sections. With the loop outlet temperature at 1050°F, the time required to heat the nozzle to 650°F is a function of the initial temperature of the nozzle. The initial nozzle temperature is approximately equal to that of the nozzle coolant. The maximum nozzle extension temperature during steady-state operation is 450°F. The following tabulation gives the time required for the nozzle extension to reach 650°F as a function of the initial temperature with the loop temperature constant at 1050°F:

Initial Nozzle Temperature (°F)	Time to Reach 650°F (min)
150	26.6
300	18.3
450	11.8
550	6.5
650	0

It is apparent that ample time is available in which to scram the reactor after a nozzle cooling line failure before the maximum allowable nozzle temperature of 650°F is reached.

Drawings and specifications for the top Bridgman closure and shield can drawings for the biological shielding around the top and bottom nozzle

tee section were completed. The closure for the bottom nozzle tee was redesigned to eliminate rotation and indexing to lock the closure to the tee. The design is based on using the ball-lock feature.

Reactions on the lower reactor nozzles of the four EGCR experimental loops as a result of reactor pressure, component weight, and loop thermal expansions were calculated based on the final Title II pipe stress analysis. The bending moments were below the allowable values of 260 000 lb-in. for the 5 1/2-in.-loop nozzles and 330 000 lb-in. for the 9 1/2-in.-loop nozzles. These allowable values are conservative and are based on an allowable primary-plus-secondary stress intensity of 90% of the yield strength of the piping.

Component Design

Mainstream Filter. (E. R. Schmidt) The allowable radial force and circumferential and longitudinal moments which may be applied to the filter vessel have been determined. These calculations indicate that the latest one-cell piping layout results in reactions at the filter vessel which are too large. Since the detailed loop design work has been deferred, the cell piping layout will not be revised until the project is reactivated. The effect on the allowable reactions of increasing the vessel wall thickness was also determined.

Several absolute filter elements have been received from the manufacturers for testing. Considerable difficulty has been encountered with damage during shipment. Two elements had to be returned and new ones made.

Cooler. (A. W. Culp, E. R. Schmidt) The evaporative cooler has been modified during the last quarter. The heat removal rate of the unit has been decreased from 1750 to 1550 kw, and the steam design temperature has been reduced from 400 to 240°F. These modifications have reduced the length from 11 ft to 5.9 ft, with a substantial saving in gas-side pressure drop and in the estimated cost of the unit. A preliminary stress analysis of the mainstream gas cooler has been completed. The analysis includes primary and secondary stresses in the pressure vessel and tube sheet.

Auxiliary Gas System. (A. W. Culp, W. S. Delicate, L. C. Fuller) Design criteria for the mainstream pressure-relief devices were prepared. Four in-cell devices, located as follows, are required:

Location	Set Pressure (psig)
Bristol Siddeley compressor discharge	985
Emergency bypass compressor discharge	1035
Downstream side of mainstream cooler	1035
Mainstream heater	1035

These pressure relief devices must be back-pressure compensated and have across-the-seat helium leakage of less than 150 cm^3 (STP)/min at operating conditions.

The need for flow restrictors in the mainstream piping to prevent overpressurization of the experimenters' cell was re-evaluated using new design information. The maximum pressure in the cell following double-ended failures of both the mainstream in-cell piping and the in-pile portion of the through-tube was calculated to be 11.4 psig. Therefore, no flow restrictors other than the top and bottom nozzles were required.

The proposed gas-sampling system is designed to obtain gas samples on the main loop piping in the cell. The system utilizes a pneumatic-transfer system to move the sample bomb from the sample station to a chamber mounted on the loop piping, where the sample bomb and chamber are charged with loop gas at pressure and temperature. The chamber is then depressurized and purged, and the bomb is again pneumatically transferred to the sample station, where it is removed for subsequent analysis. The sample bomb contains a small high-temperature, high-pressure check valve that prevents depressurization of the bomb once it has been charged. The system is designed to deliver 4 to 5 cm^3 of loop gas at operating conditions, which correspond to more than 50 cm^3 at standard temperature and pressure.

Design analyses were completed for the decontamination system, the loop offgas system, the purification system, and the mainstream pressure-relief devices. Title I approved process flowsheets for the decontamination system, the loop offgas system, the sniffer gas system, and the CO_2 supply system were prepared. The Title II process flowsheets for the plant and instrument air system were completed. Final design criteria were established for the CO_2 supply system, the dummy stringer, the experimental stringer, the top dummy shield plug assembly, the experimental-assembly-removal cooling system, the experimental assembly insertion system, the loop safety system, and the sample gas and loop containment system.

Storage Hole Facility. (E. R. Schmidt) The assembly and layout drawings of the storage hole vessel, the gas separation tank, the valve rack and control, the gas storage rack, and the miscellaneous equipment containment vessel were completed, as well as the instrumentation drawings and specifications. Auxiliary O-ring seals have been provided in the storage hole primary closure. These seals, with a buffer connection between them, are provided to permit replacement of the Bridgman closure gasket while maintaining the storage hole at an elevated pressure.

Mainstream Piping and Monitors. (W. S. Chmielewski) Engineering work on the out-of-cell mainstream piping (inlet and outlet) has been completed. The Title II drawings and design analysis were prepared. Analysis of transient pressure buildup in the secondary piping as a result of a single-ended failure of the primary piping was made with a program written for the IBM 610. The calculations indicate that the maximum pressure that will be attained in the inlet secondary piping (following the primary failure) is 800 psi. The maximum pressure in the outlet secondary piping is 600 psi, which provides a satisfactory safety factor.

Pressure-drop tests were made on the Unibestos mineral insulation to be used in the outlet mainstream piping to determine the credibility of an "insulation blockage." The insulation was found to be over 90% porous, and it offered little resistance to gas flow.

Modifications to the GS3812 pipe stress program have been completed by the Central Data Processing Group to adapt the program for use on the IBM 7090 and also to enable a revision of the program to handle problems larger

than the original 1300 words of input data. A memo describing the various modifications and revisions has been completed.

Engineering work on the pipe-chase air-cooling ducts was completed. Heat transfer calculations were made with a program written for the IBM 7090. The calculations were made with helium, hydrogen, or steam as the loop coolant.

Engineering work on the out-of-cell radiation monitors was completed. The following locations of the monitors were established: (1) two activity-deposition monitors will be located in the pipe-expansion loop of the top chase (chase between the top nozzle tee and the cooler), (2) one monitor will "look" at the cooler, (3) one activity-deposition monitor will be located in the vertical chase below the cooler, and (4) one delayed-neutron monitor will be located in the pipe expansion loop of the top pipe chase. The actual installation of the monitors will be deferred; only access holes for the monitors and lead conduits will be provided at the present time.

Design and Hazards Report (C. Michelson, R. G. Mallon, A. W. Culp)

A draft copy of the "Preliminary Design and Hazards Summary Report" was issued for review by Reactor Division personnel and the ORNL Reactor Experiment Review Committee. Work is continuing on several supporting documents which will give more detailed information concerning preliminary design drawings, design criteria, design analyses, and specifications for the loops.

Analyses were made of the hazards of missile production in the cell. It appears that the cell liner is more than adequate to contain any credible missiles that might result from the loop piping.

Loop Fabrication (W. F. Ferguson)

The type 347H stainless steel billet material required to fabricate the nozzle tee sections was delivered to Baldwin-Lima-Hamilton Corporation, and the fabrication of all bottom tee section components from the billets is in progress. Deliveries of the bottom and top tee assemblies are scheduled for August 1, 1961, and October 1, 1961, respectively.

Invitations to bid have been mailed to prospective vendors for the fabricated pipe subassemblies, which are being purchased by ORNL and are to be installed by H. K. Ferguson Company concurrent with construction of the EGCR. The delivery schedule, requested in the bid invitation, requires that delivery of fabricated subassemblies start by August 1, 1961, and be completed by November 1, 1961.

Cost estimates for the loops were prepared. These estimates included costs for both the deferred loop program and a program involving completion of the two small loops, with provisions for eventual completion of the large loops.

EGCR Component Tests

R. E. MacPherson

EGCR Valve Tests (J. C. Amos)

Tests of a 6-in.-IPS packed-stem Y-globe valve furnished by the Wm. Powell Valve Company for helium service were terminated after 104 thermal cycles between 200 and 1000°F with the valve in the open position, 265 open-close cycles with the valve body at 1000°F, and 100-hr steady-state operation at 1000°F with the valve in the closed position. Seat and stem leakage were essentially unaffected by thermal cycling, but both seat and stem leakage increased substantially during open-close cycling. Evidence of deterioration of the packing material was found (see Fig. 7.1). The maximum packing-gland helium leakage during open-close cycling was 175 cm^3 (STP)/sec (22.4 cfh). This measurement was taken with the valve body at 1000°F and 1000 psig with 1100-psig pressure in the buffer zone between the upper and lower packing. Seat leakage measured with a pressure of 300 psig upstream and atmospheric pressure downstream increased from a minimum of 1×10^{-4} cm^3 (STP)/sec (1.3×10^{-5} cfh) to a maximum of 7.7 cm^3 (STP)/sec (0.98 cfh) during open-close cycling with the valve body at 1000°F. When the valve was cooled to room temperature, seat leakage further increased to approximately 500 cm^3 (STP)/sec (64 cfh). Both stem and seat leakage substantially exceeded the specified maximum allowable

Fig. 7.1. Wm. Powell Valve Co. 6-in.-IPS Packed-Stem Y-Globe Valve Showing Packing Damage That Occurred During Open-Close Cycling.

limits for this type of valve. Stem leakage is considered the more serious problem, however, since leakage at the rates indicated would not only require excessive makeup gas for the buffer zone but could result in leakage of contaminated system gas to the atmosphere through the stem seal.

A 6-in.-IPS PK-Paul valve manufactured by General Kinetics Company has been returned by the vendor for additional testing after repair of the damage which occurred during the initial tests previously reported.[1]

A 6-in.-IPS hermetically sealed gate valve manufactured by Darling Valve Company, shown in Fig. 7.2, has been given initial shakedown tests in the presence of the manufacturer's representatives and is currently being prepared for elevated-temperature tests. This valve is equipped with a canned-rotor motor drive manufactured by the Chempump Division of the Fostoria Corporation. Valve operation is controlled by high-speed (30 counts/sec) electric counters operated by switches actuated by permanent magnets embedded in the motor shaft. The valve control circuit can be set to stop the valve operation after any predetermined number of revolutions of the motor in either direction.

A 1-in.-IPS hermetically sealed globe valve, shown in Fig. 7.3, equipped with a hand-operated harmonic drive mechanism is currently being prepared for elevated-temperature helium tests. This valve was furnished for testing and evaluation on a "no charge" basis by the United Shoe Machinery Company.

Through-Tube Bearing Test (A. M. Smith)

Two tests have been completed in the EGCR experimental through-tube bearing test rig. This facility is a mockup of the area of the EGCR pressure vessel lower tee sections at which journal bearings are provided to accommodate the movement of the through-tubes as a result of differential thermal expansion between the tubes and the reactor pressure vessel. The equipment is pictured in Fig. 7.4.

In each of the two tests the bearing material on both the sleeve, which simulated the tee sections, and the block, which simulated the

[1]GCR Quar. Prog. Rep. Dec. 31, 1960, ORNL-3049, pp. 333–5.

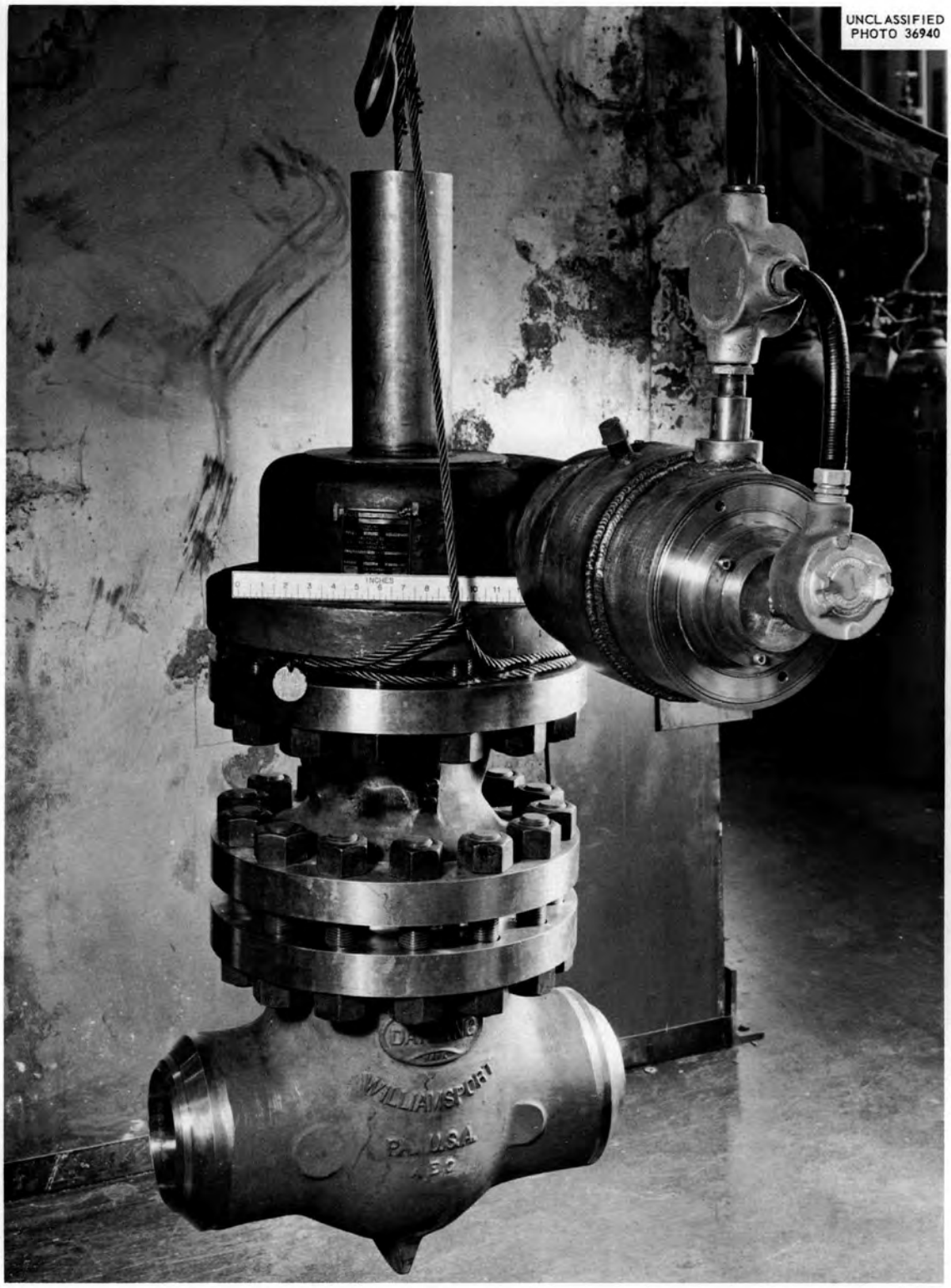

Fig. 7.2. Darling Valve Co. 6-in.-IPS Hermetically Sealed Gate Valve Equipped with a Canned-Rotor Motor Drive.

Fig. 7.3. United Shoe Machinery Co. 1-in.-IPS Hermetically Sealed Globe Valve Equipped with a Hand-Operated Harmonic Drive.

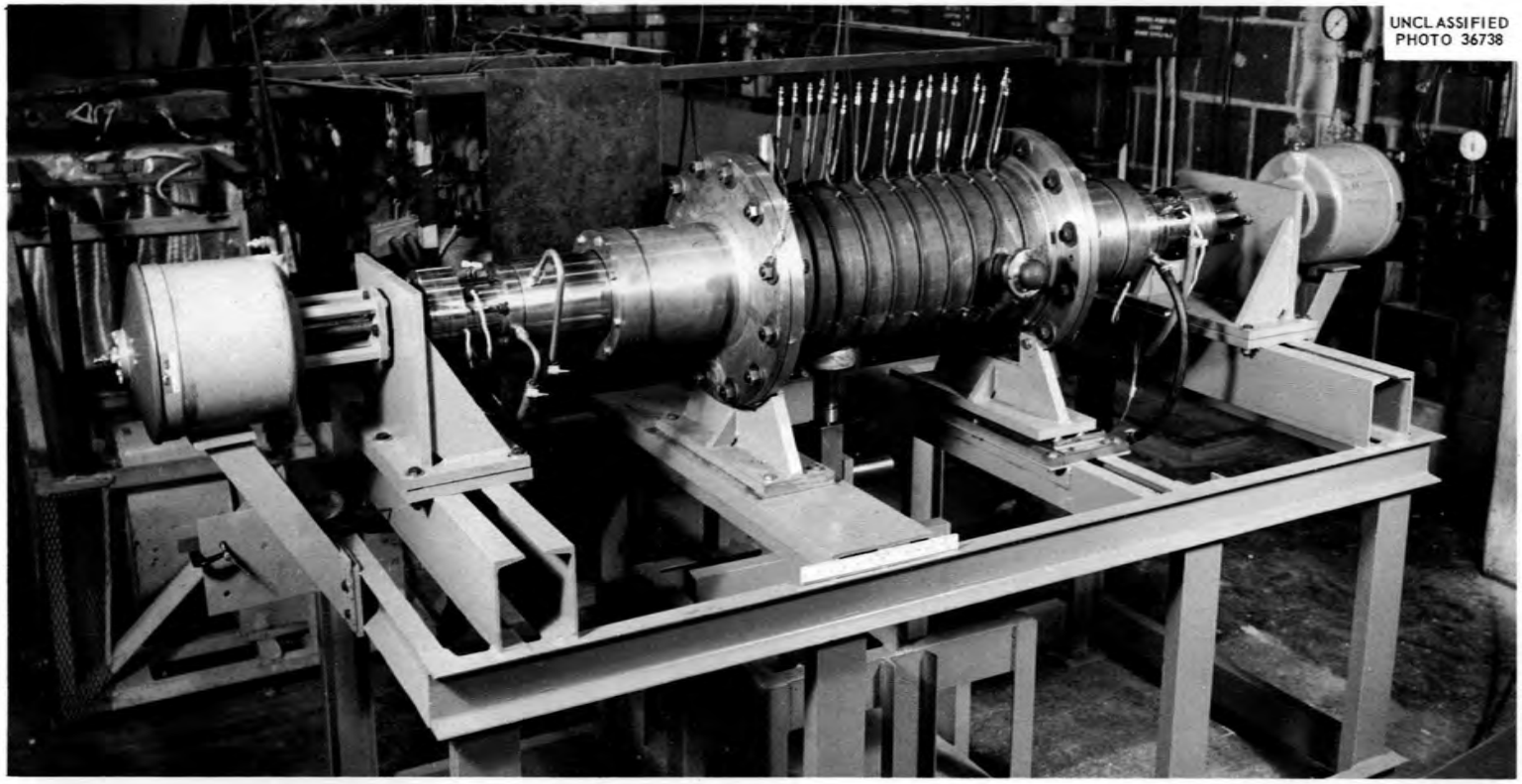

Fig. 7.4. EGCR Experimental Through-Tube Bearing Test Rig.

through-tube, was Stellite No. 6 approximately 1/16 in. thick. The surfaces were maintained at 950 ± 25°F during cycling, and loading was applied to simulate the thrust and bending moment loads that will exist in the reactor application.

The first test was run for 220 cycles before seizure between the two parts occurred. Inspection of the parts revealed longitudinal scoring of the Stellite on both pieces, as well as an area of circumferential scratches that were made during disassembly. In this initial test there was a relatively sharp edge on the block that simulated the through-tube, and it was felt that this could have initiated the galling. Consequently, the leading edge of the block was ground to produce a curved edge with a 1/8-in. radius, both parts were rotated to a new bearing surface, and the test unit was reassembled.

The second test was terminated after completion of the desired 1000 cycles at 950°F. Considerable galling, as shown in Fig. 7.5, was again noted. Spectrographic analysis of the metallic particles which could be brushed from the test pieces showed approximately 5% nickel, which indicates that the Stellite had been completely removed from some areas and that scoring of the stainless steel test piece had occurred. Additional parts coated with Linde Flame Plate LW-IN30 and Stellite No. 12 are presently being fabricated in preparation for further tests.

Through-Tube Orifice-Plate Development Test (F. A. Flint)

Pressure-drop tests have been performed on four through-tube orifice-plate configurations with air at 15 psia and 80°F over a flow rate range of 0 to 400 lb/hr,[2] which is equivalent to a helium flow rate range of 0 to 670 lb/hr at reactor operating conditions. The four orifice-plate configurations were similar in that each was an annular 1/8-in.-thick steel plate having semi-circular scallops equally spaced about the outer periphery. The cross-sectional flow area was varied from plate to plate by varying the number and diameter of the peripheral scallops. Configuration data, air flow rates, and the predicted helium flow rates are given for

[2]GCR Quar. Prog. Rep. March 31, 1961, ORNL-3102, p. 257.

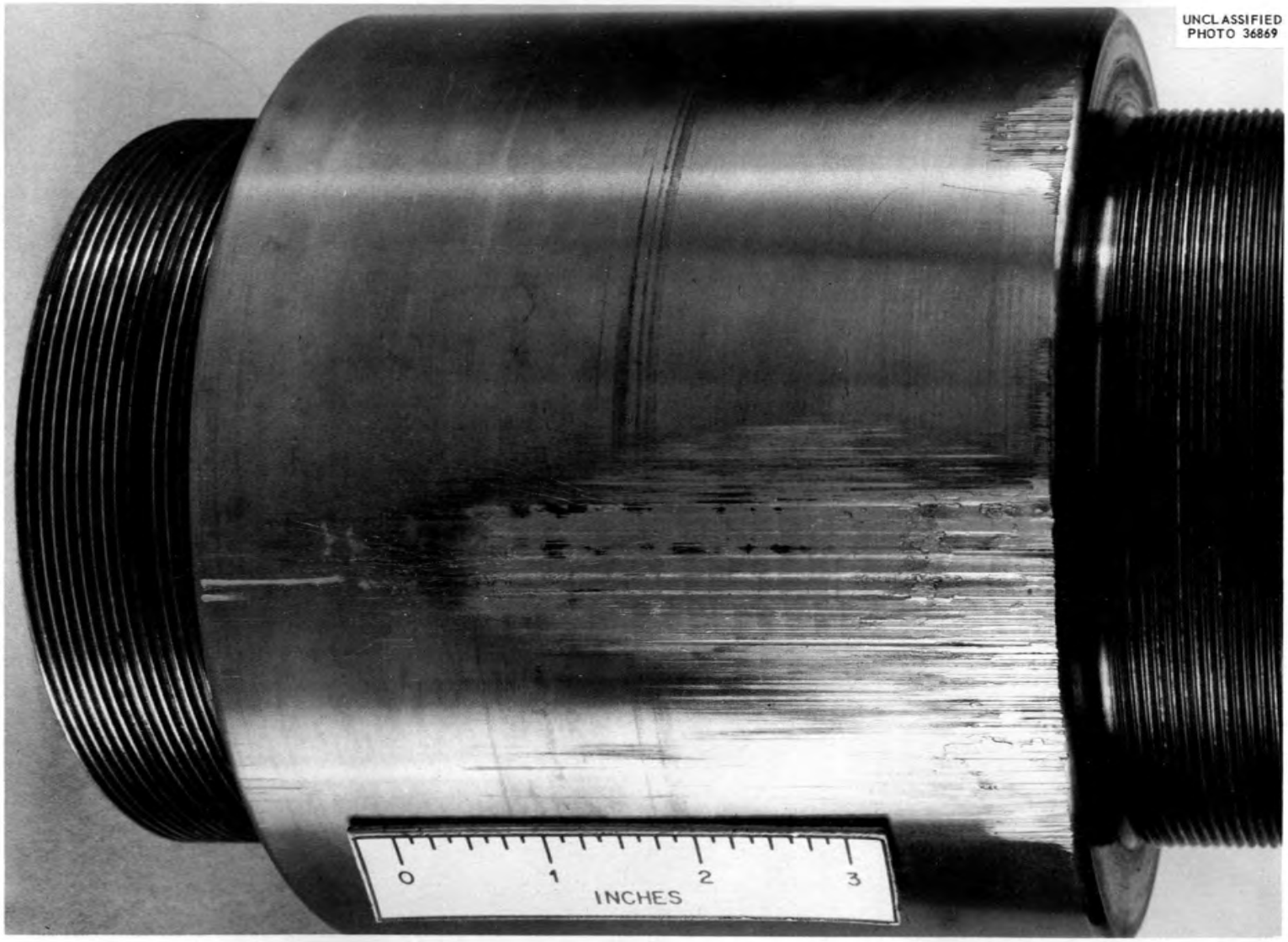

Fig. 7.5. Simulated Through-Tube Bearing Fabricated of Stellite No. 6 After 1000 Cycles Under Anticipated Thrust and Bending Moment Loads While at 950 ± 25°F.

the various plates in Table 7.1. The tabulated results are based on an orifice pressure drop of 9.48 in. Hg with air. The predicted helium flow rate will produce a 10-psi pressure drop across each orifice configuration at EGCR operating conditions.

Table 7.1. Results of Through-Tube Orifice-Plate Development Tests

Plate	Number of Scallops	Scallop Diameter (in.)	Flow Area (in.^{2})	Air Flow Rate (lb/hr)	Predicted Helium Flow Rate (lb/hr)
1	4	0.125	0.12	205	338
2	8	0.125	0.15	218	360
3	8	0.187	0.20	340	560
4	8	0.25	0.29	410	670

Mechanical Joint Service Testing (J. C. Amos)

Proof tests of 5-in.-IPS double-seal Conoseal joints and 6-in.-IPS double-seal Grayloc joints were completed. After successful completion of thermal cycling, mechanical cycling, pressure cycling, and open-close cycling at the rated internal helium pressure of 300 psig, one 5-in.-IPS double-seal Conoseal joint was exposed to helium at 1000 psig and was thermal cycled 100 times between 200 and 1050°F. Although these conditions are substantially in excess of the 700°F and 300-psig rating of this unit, seal leakage during operation at 1050°F remained below 1×10^{-6} cm^3 (STP)/sec for both the inner and outer seals. Leakage tests at 200°F indicated, however, that the outer seal leakage was substantially above the specified allowable leak rate of 1×10^{-2} cm^3 (STP)/sec when the internal pressure was increased to above 750 psig. While this increase in outer seal leakage at higher internal pressures has no direct bearing on the adequacy of this unit for containing helium at its rated pressure of 300 psig, it is interesting to note that the vendor has experienced similar seal leakage at pressures above 300 psig during room-temperature tests of

Fig. 7.6. Grayloc 6-in.-IPS Double-Seal Flange Showing Scoring of the Sealing Surface Which Occurred During Thermal-Cycling Tests.

6-in.-IPS double-seal Conoseal joints designed for 1050°F, 1100-psig operation. The vendor has increased the width of the gaskets for the 6-in. units in an effort to remedy the situation.

A 6-in.-IPS double-seal Grayloc joint using the modified seal ring described previously[3] was disassembled after successfully completing 50 thermal cycles between room temperature and 500°F and 50 cycles between 200 and 1050°F. Scoring of the flange sealing surfaces, as shown in Fig. 7.6, was observed and subsequent attempts to reseal this unit were unsuccessful. The flanges were therefore remachined in accordance with the vendor's recommendations in an effort to eliminate flange scoring; however, adequate sealing was not obtained with the remachined flanges and the seal rings available from previous tests. These results indicate that additional developmental work will be necessary to produce a reusable double-seal Grayloc joint for elevated-temperature helium service.

Tests were also conducted on a spherical seal, shown in Fig. 7.7, and a test fixture furnished on a "no charge" basis for evaluation by Flight Refueling, Inc. The tests indicated that satisfactory seals could

[3]Ibid., p. 262.

Fig. 7.7. Spherical Seal Rings Fabricated by Flight Refueling, Inc.

be obtained at room temperature, but helium leakage increased beyond acceptable limits during the first or second thermal cycle between room temperature and 500°F. This increase in leakage during very limited thermal cycling may be due to seal geometry, material selection, or both. It was concluded that without further developmental work this type of seal would not be suitable for elevated-temperature helium service where extreme leaktightness is required.

GCR-ORR Loop No. 2

J. Zasler

Loop Design and Construction (I. T. Dudley, P. A. Gnadt, W. R. Huntley, S. Kress, J. LaGraff, E. E. Wade)

The preliminary leaktightness test of the GCR-ORR loop No. 2 cell has been completed. The cell inleakage rate was 26 ft^3/day with a cell pressure of 1.86 psi below atmospheric. The design criterion for inleakage is 40 ft^3/day with a pressure of 1.5 psi below atmospheric.

The contracted work on the loop is 99% complete. This work includes installation and/or construction of the cell walls and liner; the piping and electrical penetrations to the cell; the cell lighting, cooling, evacuation, and drainage systems; the fission-gas trapping systems; the loop auxiliary buffer gas fill and evacuation systems; the electrical supply systems; and the 50-ton crane and associated carrier removal facilities. The cell viewing window has been installed.

The 5-ton in-cell crane and the movable rack and associated operating mechanisms have been installed. The main loop components have been set in place, and installation of the prefabricated pipe sections between the components is in progress. The cell interior is shown in Fig. 7.8 prior to rack installation.

All shielded components, except the filters, have been installed in their respective shields. The procedure for installing the components in their shields is shown by Figs. 7.9, 7.10, and 7.11. The new filter cartridges have been received from the vendor and are to be pretested

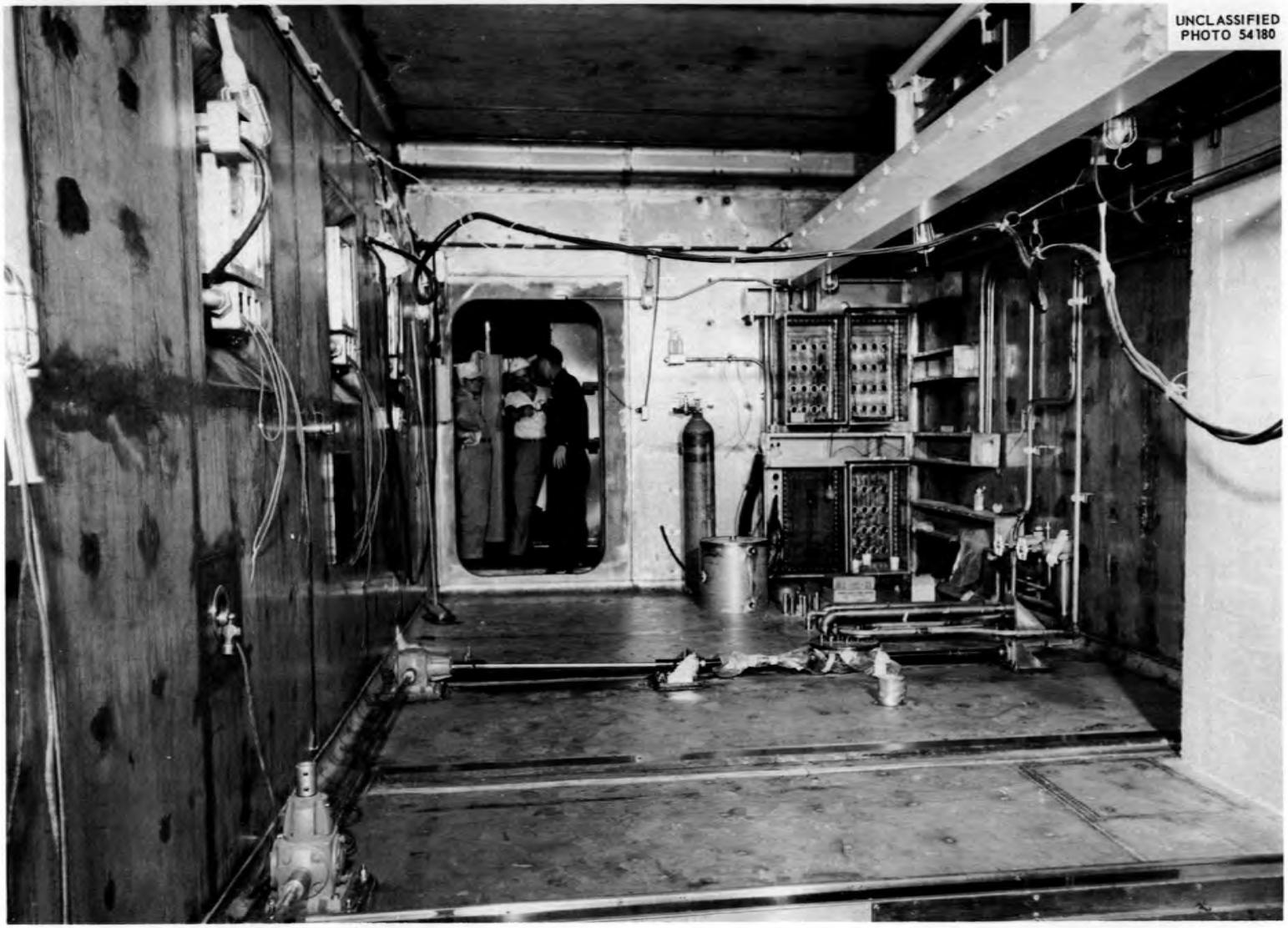

Fig. 7.8. Interior of Cell of GCR-ORR Loop No. 2 Prior to Rack Installation.

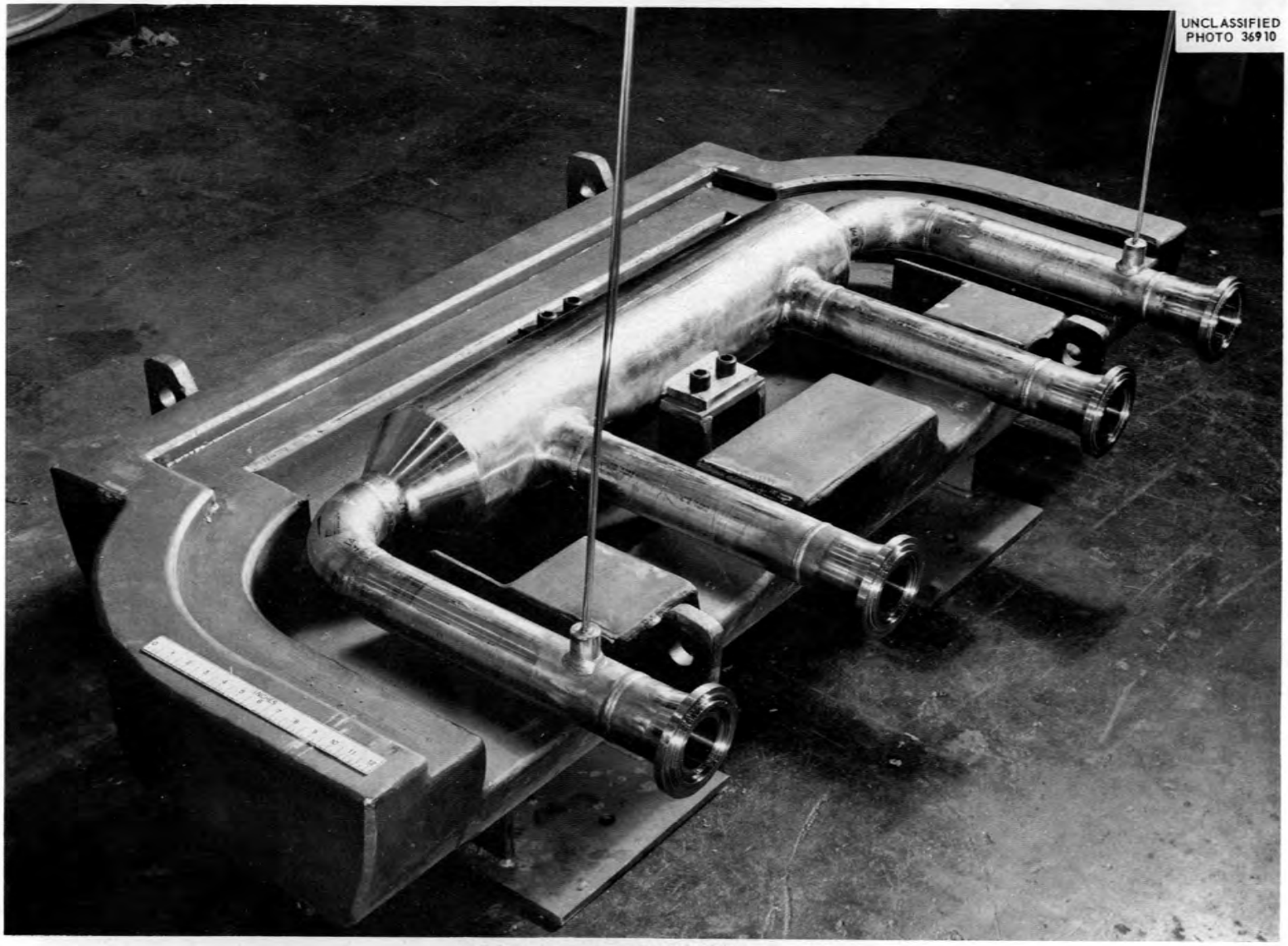

Fig. 7.9. Regenerator in Portion of Shield Prior to Installation of Insulation.

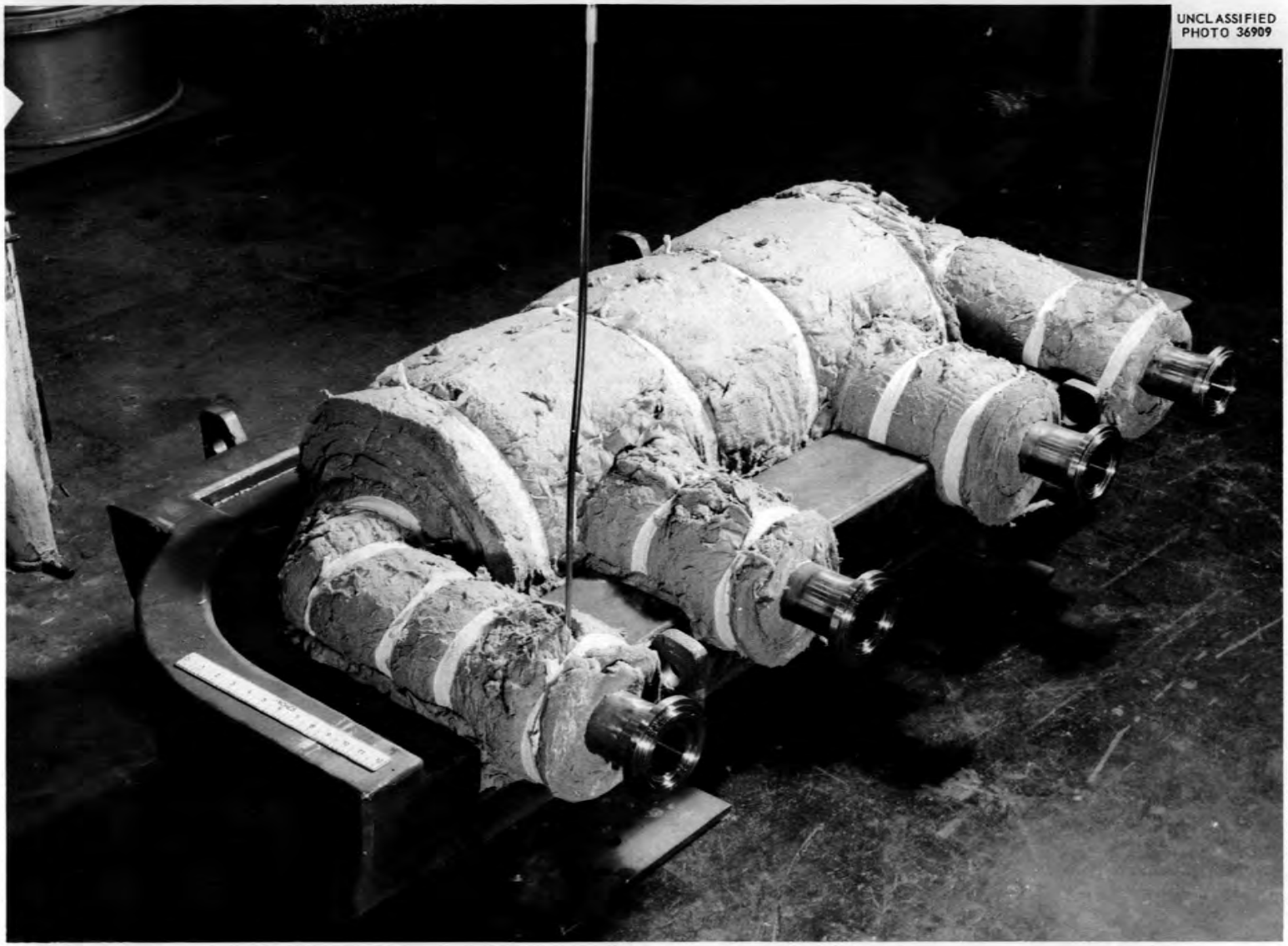

Fig. 7.10. Regenerator with Thermoflex Insulation Installed.

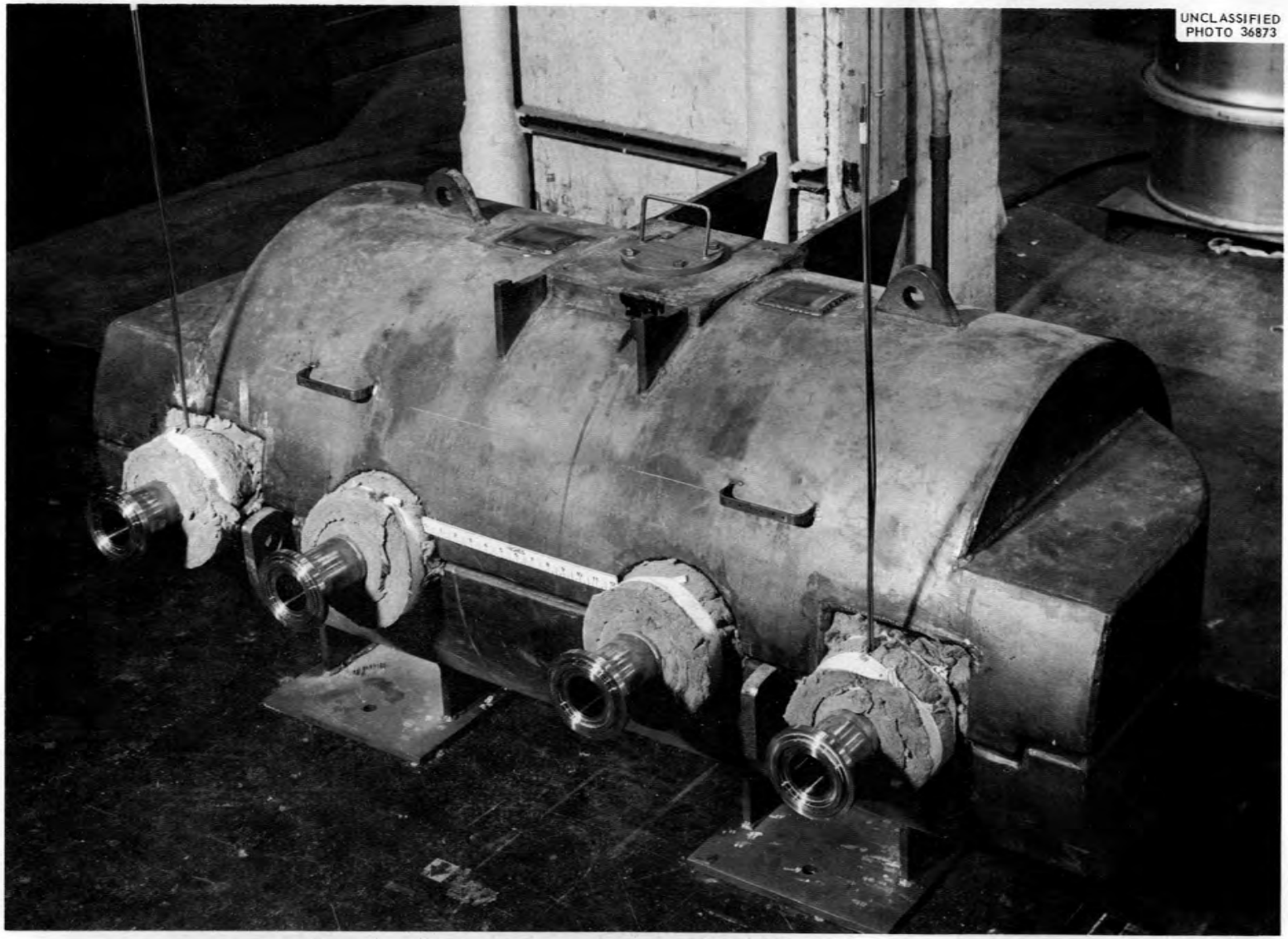

Fig. 7.11. Shielded Regenerator.

to determine filtering efficiency prior to installation in the filter pressure vessel.

Detailing of most of the 2 1/2-in.-IPS main-loop helium piping has been completed. Some modifications are still in progress to accommodate installation of the ORNL-designed compressor with grease-lubricated bearings that will be used for initial loop operation. It has been necessary to substitute these compressors temporarily for the originally planned gas-bearing compressors because of delivery delays by the vendor. Since the compressors will be run in parallel rather than in series, as planned, it has been necessary to design and build a low-pressure-drop check valve to prevent bypass flow when one compressor is inoperative.

Detailing of the 24-in. shielding plug is 95% complete, and detailing of the 18-in. pressure piping plug is under way. Preliminary bills of material were prepared on these two items and the fuel test tube to expedite procurement. The design of the carrier for the pressure piping plug has been completed. This large carrier will have a 19-in. cavity and will weigh approximately 35 tons.

A pipe cutting and sealing die for 1 1/2-in., sched.-80, type 347H stainless steel pipe has been made and tested on commercial-grade pipe. Preliminary tests indicate that the sealing die will permit cutting pipes containing high activity without releasing more than traces of activity to the atmosphere. Performance tests are in progress on type 347H stainless steel pipe, and a specification is being prepared for the hydraulic shear.

Two heaters of the new design have been fabricated, on schedule, and one has been installed in the components test stand. The performance tests now in progress are described in the following section of this chapter.

The IBM 7090 heat transfer code TOSS was extended to provide data for predicting the transient temperatures in the test section during a loss of flow accident. The stress-time-temperature-rupture data obtained are being used to predict whether the pressure shell will fail during the transient. Code input and operational procedures have been established

for studying the condition of fuel "meltdown", that is, loss of flow with the ORR not scramming.

Analyses were made of the general hazards of the loop involved in failure of the evaporator bypass valve, failure of condenser water flow, and loop rupture into the evaporator. The results of these studies were incorporated in an interim design report.[4]

Component Tests (F. A. Flint, R. E. MacPherson)

Operation of the modified GCR-ORR loop No. 2 component test facility was initiated. Testing of the heaters with all three groups in simultaneous operation was completed at a helium flow rate of 450 lb/hr, two thirds completed at 265 lb/hr, and one third completed at 600 lb/hr. All data taken thus far indicate excellent heater performance. The heater power input, the helium temperature at the heater outlet, the maximum heater cartridge surface temperature, and the temperature differential are given for each helium flow rate in Table 7.2. It is significant that the maximum heater cartridge surface temperature occurred at the same thermocouple in all cases.

[4]Interim Design Report — GCR-ORR Loop No. 2, ORNL CF-61-5-39, May 15, 1961.

Table 7.2. Results of Tests of Heaters for GCR-ORR Loop No. 2

Helium Flow Rate (lb/hr)	Heater Power (kw)	Helium Temperature at Heater Outlet (°F)	Maximum Cartridge Temperature, Fourth Pass (°F)	Temperature Differential Across Heater (°F)
265	33	700	809	109
265	42	850	975	125
450	41	700	753	53
450	52	850	908	58
450	72	1000	1151	151
600	45	700	790	90

Special Compressors

W. F. Boudreau

Compressors with Grease-Lubricated Bearings (I. K. Namba)

The two regenerative compressors installed in GCR-ORR loop No. 1 operated satisfactorily for a total of 3300 hr before they were removed while the loop was being renovated for more flexible operation. Subsequent inspection of the ball bearings (Barden 107H) indicated that the front (impeller end) bearings were in better condition than the rear (motor end) bearings. The grease lubricant had some contamination and some apparent loss of lubricity. The ball bearings have been sent to the manufacturer (Barden Corporation) for inspection and evaluation. Two replacement regenerative units have been installed in ORR loop No. 1, and loop operation has been resumed.

A decision was made to provide three regenerative compressors and their containment vessels for use in GCR-ORR loop No. 2. The pressure vessels have been ordered from the Nooter Company. In order to match the ORR loop No. 2 motor-generator set, several sets of two-pole shaftless motors were procured in lieu of the existing four-pole motors.

A small regenerative compressor has been designed for use in the control-rod-drive test facility. This compressor is to be operated with helium at 300 psi and 150°F. Because of the low temperature, the fabrication of this compressor will be relatively inexpensive. A duplicate unit will be built for aerodynamic testing of various impeller and housing configurations in order to develop design data.

Compressors with Gas-Lubricated Bearings (D. L. Gray)

Bristol Siddeley Experimental Compressor. Bristol Siddeley has tested bearings of Meehanite, chrome-plated steel, and silver-plated steel of the conventional British type (plain bearing with anti-whirl groove in the top) without overcoming the instability which occurs at approximately 11 000 rpm in the experimental ("one-off") gas-lubricated compressor.

A new proprietary bearing has been operated in the "M" type test unit at Bristol Siddeley at speeds up to 21 000 rpm. This bearing, which has an adjustable loading device on a top pad, has been adapted to the "one-off" compressor. During initial aerodynamic performance tests, speeds up to 15 000 rpm, temperatures up to 715°F, and pressures up to 350 psi were achieved. A seizure of the rear bearing terminated the tests after approximately one-half the performance runs had been completed. The seizure caused the shaft to bend. The shaft has been straightened and reground, and the compressor has been reassembled with a silver-plated mild steel bearing of the top-pad type. Tests have been resumed, and preliminary reports indicate that compressor operation has been successful at full pressure (405 psi) at temperatures up to about 650°F. Bristol Siddeley engineers are unwilling at the present time to exceed this temperature because they feel that the thermal stresses in the area of the barrel between the flange and the water jacket will become excessive. This belief is the result of calculations based on measured temperatures in the critical areas of the barrel.

ORNL Experimental Compressors. The ORNL-designed GABE I compressor was operated several times for short periods. In all cases the runs were terminated because of bearing touching, as indicated by either audible or electrical detection methods. The final run was terminated by shaft seizure after 27 min of operation. Examination of the bearing surfaces revealed that the thrust bearing was completely unscored, the rear bearing was lightly scored, and the forward bearing was lightly scored, except in the 1/8-in.-wide band where the seizure occurred. The bearing was damaged during disassembly. An attempt was made to repair it with Stellite No. 1 hard-facing material, but shrink cracks spoiled the surface. The repair is now to be attempted with Stellite No. 19 material.

Continental Bearing Research Corporation Experimental Compressor. The Continental Bearing Research Corporation has completed approximately 65% of phase I of their contract to design, fabricate, and test a gas-bearing-supported high-temperature electric motor. The cold test is scheduled to start June 16, 1961.

Compressors for GCR-ORR Loop No. 2 and EGCR Experimental Loops.
(H. C. Young)

The new delivery date for the Bristol Siddeley compressors is July 31, 1961. A Bristol Siddeley stress analyst spent two weeks at Oak Ridge reviewing the thermal stress problems of both the ORR loop No. 2 and the EGCR compressors, and agreements were reached on a procedure for resolving the problems. An experimental method is to be used to verify the actual thermal stress in the region of high stress in each compressor. It is expected that electric heaters will be required to reduce the thermal stress to the allowable value for the EGCR compressors.

Two loop No. 2 compressor pressure vessels have been modified to accommodate thermal stresses, and tests of a bearing assembly in the compressor casing have been resumed. In one test at 160 psia and a low temperature, the gas bearings operated satisfactorily up to 17 000 rpm. In subsequent tests, bearing rubbing occurred at below design speed and pressure when the gas temperature was increased. The third loop No. 2 compressor vessel was scrapped during attempts to repair a crack, and a new vessel is being fabricated.

Completion of welding on the first EGCR compressor vessel was held up pending agreement on modifications to the water jacket to relieve the thermal stress problem. Welding has been resumed and testing of this compressor is expected to be started early in the next quarter.

Agreement was reached on a revised performance testing procedure for tests of all compressors (subsequent to the first three) at full temperature, pressure, and speed. Increased compressor nozzle loadings from thermal expansion of the loop piping have made it necessary for Bristol Siddeley to redesign the EGCR compressor mounting stand.

Previous reports in this series are:

ORNL-2500	Parts 1-4, issued April 1, 1958
ORNL-2505	Issued June 19, 1958
ORNL-2510	Issued September 18, 1958
ORNL-2676	Period Ending December 31, 1958
ORNL-2767	Period Ending June 30, 1959
ORNL-2835	Period Ending September 30, 1959
ORNL-2888	Period Ending December 31, 1959
ORNL-2929	Period Ending March 31, 1960
ORNL-2964	Period Ending June 30, 1960
ORNL-3015	Period Ending September 30, 1960
ORNL-3049	Period Ending December 31, 1960
ORNL-3102	Period Ending March 31, 1961

INTERNAL DISTRIBUTION

1. G. M. Adamson
2. S. A. Beall
3. M. Bender
4. D. S. Billington
5. E. P. Blizard
6. E. G. Bohlmann
7. C. J. Borkowski
8. G. E. Boyd
9. R. B. Briggs
10. W. E. Browning
11. F. L. Carlsen
12. C. E. Center (K-25)
13. E. L. Compere
14. J. H. Coobs
15. W. B. Cottrell
16. J. A. Cox
17. F. L. Culler
18. J. H. DeVan
19. D. A. Douglas
20. R. B. Evans
21. D. E. Ferguson
22. J. L. Fowler
23. A. P. Fraas
24. J. H. Frye, Jr.
25. A. E. Goldman
26. B. L. Greenstreet
27. W. R. Grimes
28. J. P. Hammond
29. W. O. Harms
30. M. R. Hill
31. H. W. Hoffman
32. A. Hollaender
33. A. S. Householder
34. W. H. Jordan
35. C. P. Keim
36. M. T. Kelley
37. P. Lafyatis
38. J. A. Lane
39. R. S. Livingston
40. H. G. MacPherson
41. W. D. Manly
42. R. W. McClung
43. C. J. McHargue
44. H. J. Metz
45. J. G. Morgan
46. K. Z. Morgan
47. F. H. Neill
48. M. L. Nelson
49. N. Ozisik
50. P. Patriarca
51. A. M. Perry
52. D. Phillips
53. M. E. Ramsey
54. M. W. Rosenthal
55. G. Samuels
56. H. W. Savage
57. A. W. Savolainen
58. J. L. Scott
59. O. Sisman
60. E. D. Shipley
61. M. J. Skinner
62. G. M. Slaughter
63. A. H. Snell
64. E. Storto
65. J. C. Suddath
66. J. A. Swartout
67. E. H. Taylor
68. D. B. Trauger
69. C. S. Walker
70. J. L. Wantland
71. G. M. Watson
72. A. M. Weinberg
73. J. R. Weir
74. J. C. White
75. C. E. Winters
76. J. Zasler

77-80. ORNL – Y-12 Technical Library
Document Reference Section

81-150. Laboratory Records Department

151. Laboratory Records Department,
ORNL R.C.

152-154. Central Research Library

EXTERNAL DISTRIBUTION

155-157. W. F. Banks, Allis-Chalmers Mfg. Co.
158-160. P. D. Bush, Kaiser Engineers
161-162. David F. Cope, Reactor Division, AEC, ORO
163-164. R. W. Coyle, Vallecitos Atomic Laboratory
165. E. Creutz, General Atomic
166-168. R. B. Duffield, General Atomic
169. D. H. Fax, Westinghouse Atomic Power Division
170. T. Jarvis, Ford Instrument Co.
171. Richard Kirkpatrick, AEC, Washington
172-173. H. Lichtenburger, General Nuclear Engineering Corp.
174. J. P. McGee, Bureau of Mines, Appalachian Experiment Station
175. S. G. Nordlinger, AEC, Washington
176. H. B. Rahner, Savannah River Operations Office
177. Corwin Rickard, General Atomic
178. S. T. Robinson, Sanderson & Porter
179. M. T. Simnad, General Atomic
180. Donald Stewart, AEC, Washington
181. G. W. Tompkin, Mallinckrodt Nuclear Corporation
182. Philip L. Walker, Pennsylvania State University
183. R. E. Watt, Los Alamos Scientific Laboratory
184-185. W. L. Webb, East Central Nuclear Group, Inc.
186. Division of Research and Development, AEC, ORO
187-788. Given distribution as shown in TID-4500 (16th ed.) under Reactor Technology category (75 copies – OTS)